UNIVERSITÀ DEGLI STUDI DI NAPOLI
FEDERICO II

DOCTORAL THESIS

Desing Guidelines, Experimental Investigation and Numerical Analysis of a New Twin Engine Commuter Aircraft

Author:
Salvatore CORCIONE

Supervisor:
Prof. Luigi DE LUCA

Co-Supervisor:
Prof. Fabrizio NICOLOSI
Eng. Claudio CARUSO

A thesis submitted in fulfillment of the requirements for the degree of Doctor of Philosophy

in the

Doctor of Philosophy School in Aerospace, Naval and Quality Engineering

March 31, 2015

Declaration of Authorship

I, Salvatore Corcione, declare that this thesis titled, 'Desing Guidelines, Experimental Investigation and Numerical Analysis of a New Twin Engine Commuter Aircraft' and the work presented in it are my own. I confirm that:

- This work was done wholly or mainly while in candidature for a research degree at this University.
- Where any part of this thesis has previously been submitted for a degree or any other qualification at this University or any other institution, this has been clearly stated.
- Where I have consulted the published work of others, this is always clearly attributed.
- Where I have quoted from the work of others, the source is always given. With the exception of such quotations, this thesis is entirely my own work.
- I have acknowledged all main sources of help.
- Where the thesis is based on work done by myself jointly with others, I have made clear exactly what was done by others and what I have contributed myself.

This PhD thesis has been defended in a public dissertation on May, 11th 2015 under the judgement of a specialized commission composed by:

- Prof. Piero Gili, Dipartimento di Ingegneria Meccanica e Aerospaziale, Politecnico di Torino;
- Prof. Antonio Viviani, Dipartimento di Ingegneria Industriale e dell' Informazione, Seconda Università degli Studi di Napoli.
- Prof. Lorenzo Trainelli, Dipartimento di Scienze e Tecnologie Aerospaziali, Politecnico di Milano;

Signed: _____

Date: _____

"Research is what I'm doing when I don't know what I'm doing"

Wernher von Braun

UNIVERSITÀ DEGLI STUDI DI NAPOLI
FEDERICO II

University of Naples FEDERICO II

Abstract

Faculty of Aerospace Engineering
Doctor of Philosophy School in Aerospace, Naval and Quality Engineering

Doctor of Philosophy

Desing Guidelines, Experimental Investigation and Numerical Analysis of a New Twin Engine Commuter Aircraft

by Salvatore CORCIONE

At the end of the year 2011, statistical data reports that the average age of general aviation registered aircraft is 46 years for single-engine piston powered aircraft and 15 years for single-engine turboprop aircraft. The average age for twin-engine 8-12 seats aircraft is 42 years for piston powered models and about 29 years for twin-engine turboprop commuter aircraft. These data show the need of a new aircraft model, also characterized by the application of new technologies like composite, light structures, new engine(with lower weight and fuel consumption), new avionics and flight control systems and new and advanced aerodynamics (i.e. optimized airfoil and winglet). Therefore, since the beginning of the year 2012, Tecnam Aircraft Industries and the Department of Industrial Engineering of the University of Naples Federico II are deeply involved in the design of a new commuter aircraft that should be introduced in this market with good opportunity of success. This research work provides some general guidelines on the conceptual design of a new twin-engine commuter aircraft with eleven seats highlighting some general features that are directly coming from market requirements. Aircraft configuration and cabin layout choices are shown and compared to similar solutions adopted by main competitors. The preliminary design has been accomplished through the classical semi-empirical approaches, under the guidance of Prof. Luigi Pascale, designer of all Tecnam aircraft. The preliminary design has been also supplied with aerodynamic analyses performed with a 3-D panel code solver with the aim to verify the aircraft longitudinal and lateral-directional stability. To improve aircraft flight performance, in particular for the climb

phase, winglets have been specifically design for this aircraft in order to reduce the wing induced drag. The aerodynamic analyses have been also addressed to a preliminary estimation of the wing loading, highlighting the effect of fuselage, nacelles and winglets. Identified the final layout and sizing of the aircraft, a 1:8.75 scale model has been build by Tecnam Aicraft Industries, and a wide wind tunnel test campaign has been fulfilled in the main subsonic wind tunnel facility of the Department of Industrial Engineering. Wind tunnel test have been focused on the estimation of the general aerodynamic characteristics of the aircraft. Several aircraft configurations have been tested in order to estimate the contribution of each aircraft component to the whole aircraft longitudinal and lateral-directional stability and control characteristics. To take into account the wind tunnel scaling effects providing more reliable data dealing with the free flight conditions, a wide numerical investigation through a Navier-Stokes equations solver has been performed. The reliability of the numerical investigation has been preliminary validated performing simulations at the wind tunnel conditions and comparing results with the available experimental data. The numerical analyses have been also useful to supply data not available form the wind tunnel tests, such as the accurate estimation of the wing span loads and stall path at free flight conditions (both in flap up and full flap configuration), a complete drag breakdown estimation (useful for aircraft performance estimation) and in order to predict the aircraft maximum lift coefficients(both in clean and flapped configuration). A preliminary investigation about the benefits that could be provided by the wing-fuselage fairing in terms of drag reduction, has been assessed through Navier-Stokes solver. Finally, an estimation of the aircraft flight performance has been fulfilled and effects of drag reduction in terms of maximum achievable cruise speed and fuel consumption an a typical possible mission profile has been presented.

Acknowledgements

A PhD research work needs the sustain of many people and I am greatly indebted to a lot of people that helped me to fulfil this work.

First of all I want express my gratitude to Prof. Fabrizio Nicolosi for offering me this great opportunity. I am very grateful for the chance he gave me to gain so much experience in aircraft design, experimental and numerical aerodynamics. I am so proud to have been able to share this experience standing shoulder to shoulder whit him, "breathing" his passion for the "flight vehicle".

Thanks to Eng. Claudio Caruso for introducing and supporting me in the everyday life of a real company. I want to thank him for sharing with me his work experience and for showing me what the word "work" means outside the academic experience.

Thanks to Costruzioni Aeronautiche Tecnam for the opportunity to be a part of the P2012 Traveller project. Thanks for giving me the chance to "feel and touch" my passion for the flight vehicles.

Thanks to Prof. Luigi Pascale for sharing with me his huge experience and passion for aircraft. I will never forget the time, when discussing about experimental data, he stated these words: "La macchina aeroplano è carogna per definizione". Few words that resume all his experience in the aircraft design. I want also thank him for all the talks we had, that I have always felt as lessons and opportunities to learn as much as possible from his words.

Thanks to Danilo, Elia, Vincenzo (in rigorous alphabetical order) not only for the technical support, but also for making our group a pleasant and exciting place to work.

"Last but not the least", there are no words to thanks Pierluigi, without his motivation I am sure that I never decided to start this work. He was an essential reference to me, he was always able to give me all the practical, technical and motivational support I needed to overcame each obstacle i have found on my path.

Salvatore Corcione

Contents

List of Figures

List of Tables

Abbreviations

AEO	**A**ll **E**ngine **O**perative
CAD	**C**omputer **A**ided **D**esign
CFD	**C**omputetional **F**luid **D**ynamic
CPU	**C**entral **P**rocessing **U**nit
DII	**D**ipartimento di **I**ngegneria **I**ndustriale
EASA	**E**uropean **A**viation **S**afety **A**gency
FAR	**F**ederal **A**viation **R**egulations
MATLab	**M**atrix **L**aboratory (a MathWorks software)
N-S	**N**avier **S**tokes
NACA	**N**ational **A**dvisory **C**ommittee for **A**eronautics
NASA	**N**ational **A**eronautics and **S**pace **A**dministration
OEI	**O**ne **E**ngine **I**noperative
SCoPE	**S**istema **Co**perativo
	Per **E**laborazioni Scientifiche Multidisciplinari
B	isolated **B**ody configuration
BFL	**B**alanced **F**ield **L**enght
BH	**B**ody and **H**orizontal tail configuration
BHV	**B**ody, **H**orizontal and **V**ertical tail configuration
BV	**B**ody and **V**ertical tail configuration
STOL	**S**hort **T**ake **O**ff and **L**anding
V	isolated **V**ertical tail configuration
V.L.A.	**V**ery **L**ight **A**ircraft
WB	**W**ing and **B**ody configuration
WBN	**W**ing, **B**ody and **N**acelles configuration
WBV	**W**ing, **B**ody and **V**ertical tail configuration
WWB	**W**ing, **W**inglet and **B**ody configuration

WWBN	**W**ing, **W**inglet, **B**ody and **N**acelles configuration
WWBN	**W**ing, **W**inglet, **B**ody and **N**acelles configuration
WWBNHV	complete aircraft configuration

Symbols

AR_h	horizontal tail aspect ratio
AR_v	vertical tail aspect ratio
AR_w	wing tail aspect ratio
C_D	3-D Drag coefficient
C_L	3-D Lift coefficient
C_{roll}	3-D Rolling moment coefficient
C_M	3-D Pitching moment coefficient
C_N	3-D Yawing moment coefficient
C_Y	3-D Sideforce coefficient
C_f	friction coefficient
C_l	2-d Lift coefficient
C_p	pressure coefficient
RC	rate of climb
S_w	wing surface
S_h	horizontal tailplane surface
S_v	vertical tailplane surface
S_{TO}	take-off distance
S_{LAN}	landing distance
SHP	shaft horsepower
VEF	engine failure speed
VMC	minimum control speed
V_{TAS}	true airspeed
VSL	landing stall speed
$VSTO$	take-off stall speed
W/P	aircraft power loading

W/S	aircraft wing loading
W_E	aircraft empty weight
W_{TO}	aircraft maximum take-off weight
Λ_h	horizontal tail sweep angle weight
$\Lambda_{c/4}$	sweep angle at half chord
Δx_{ac}	longitudinal shift of the aerodynamic centre
λ_h	horizontal tail taper ratio
η_h	horizontal tail dynamic pressure ratio
α	aircraft incidence angle
η_v	vertical tail dynamic pressure ratio
c_e/c_h	elevator chord to horizontal tail chord average ratio
z_h	horizontal tail vertical position
x_{ac_v}	vertical tail aerodynamic centre longitudinal position
z_{ac_v}	vertical tail aerodynamic centre vertical position
$\delta_{r_{max}}$	maximum rudder deflection
l_T	thrust axis location along wing span
b_v	vertical tail span
a_v	vertical lift curve slope
τ_r	rudder effectiveness
$C_{N_{\delta_r}}$	yawing moment coefficient derivative with respect to the rudder deflection
C_{roll_β}	rolling moment coefficient derivative with respect to the rudder deflection
C_{M_α}	pitching moment coefficient derivative with respect to the aircraft incidence angle
C_{L_α}	lift coefficient derivative with respect to the aircraft incidence angle
C_{N_β}	yawing moment coefficient derivative with respect to the aircraft sideslip angle
C_{D_0}	aircraft zero lift drag coefficient
S_f	fuselage lateral surface area
l_f	fuselage length
w_f	fuselage maximum width
Re	Reynolds number
M	Mach number
mcg	mean geometric chord
c	wing local chord
i_{t_0}	horizontal tail incidence angle
e	aircraft Oswald's factor

x_{cg}	centre of gravity longitudinal position
z_{cg}	centre of gravity vertical position
δ_e	elevator deflection angle
l/h	fuselage fineness ratio
b_h	horizontal tail plane span
τ_e	elevator effectiveness
$\tau_e, \delta_{e_{max}}$	elevator effectiveness at its maximum deflection
$d\epsilon/d\alpha$	wing downwash angle derivatives with respect to the aircraft angle of attack
β	aircraft sideslip angle
$\delta_{r,eq}$	required rudder angle for the equilibrium in yaw
$2r$	fuselage diameter at vertical tail aerodynamic centre
b	wing span
b_H	horizontal tailplane span
b_V	vertical tailplane span
b_{v1}	vertical tailplane span extended on fuselage centreline
c	wing chord
$cant_w$	winglet cant angle
c_{mac}	mean aerodynamic chord
c_v	vertical tailplane chord
d_f	fuselage diameter
e	Oswald's factor
e_w	wing induced drag factor
h_w	winglet height
r_w	winglet radius
r_f	fuselage half equivalent diameter
toe_w	winglet toe angle
z_w	wing position
Δ_w	winglet sweep angle
Λ	wing and tailplane sweep angle
α	angle of attack

β	angle of sideslip
ϵ_w	winglet twist angle
η_p	propeller efficiency
θ	fuselage upsweep angle
λ	taper ratio
λ_w	winglet taper ratio

To my Family and my Love...

Chapter 1

Introduction

1.1 A Brief General Aviation Market Review

Many in the industry had anticipated 2011 to be the year when the General Aviation manufacturing industry would begin to recover. However, the demand for business airplanes and services, especially in the established markets of Europe and North America, remained soft and customer confidence in making purchase decision in these regions remained weak. This inactivity, nonetheless, was offset in part by demand from the emerging markets of China and Russia. While a full resurgence did not take place in 2011, the year finished with signs of recovery and reason of optimism. After all at the end of year 2011 over 320000 small aircfrat were flying worldwide, from 2 seats up to the business jet and the general aviation contributed only in the US for 150 billion of dollars, as shown by GAMA, see Fig. 1.1.

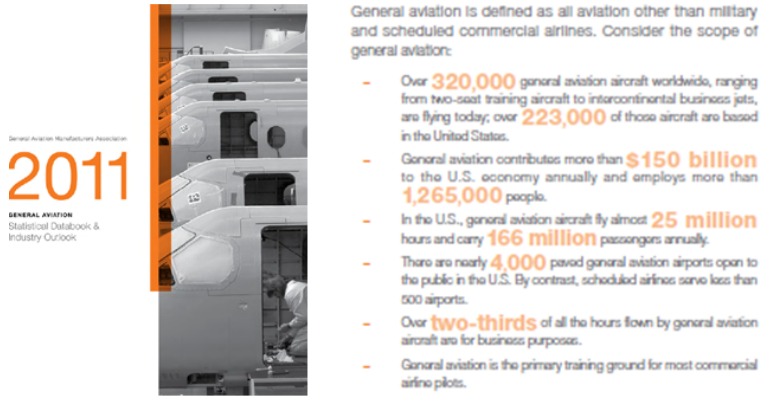

FIGURE 1.1: GAMA General Aviation Market Review, 2011, source: GAMA [1].

Commuter aircraft market is today related to old model. The major airlines in this segment have been demanding a replacement for many hundreds of "heritage" airplanes in the FAR23 and CS23 [5] category currently in

service around the world - as many are now coming to the end of their useful commercial life[1]. GAMA (General Aviation Manufacturer Association) 2011 Statistical Databook & Industry Outlook [1],which is usually a very useful and impressive source of data and statistics for general aviation, reports that the average age of general aviation registered aircraft is 46 year for single-engine piston powered aircraft and 15 years for single-engine turboprop aircraft. The average age for twin-engine 8-12 seats aircraft is 42 years for piston powered models and about 29 years for twin-engine turboprop commuter aircraft, as clearly outlined in Fig. 1.2, where the average age of registered general aviation aircrafts is shown. These impressive data dramatically show the need of new aircraft model which should be characterized also by the application of new technologies like composite, light structures, new engines (with lower weight and lower fuel consumption) and new avionics and flight control systems. Many relevant guidelines in the design, design process and its costs can be found in [6], where the experience of Embraer Company is reported and many important considerations on other general aviation producers during the 90s are shown. Embraer experience shows how a critical feature in aircraft design is the establishing its aerodynamic coefficients, in particular concerning the wings and their junction with the fuselage, highlighting that the definition of the aircraft geometry is often approached by a method of successive approximations. The geometry of the wind tunnel model defined ex-ante could be modified by the results of the wind tunnel experiments. Many improvement in this way can be afford by the computational approaches that could also provide to minimize reliance on costly and time-consuming wind tunnel testing. The computational approach (the finite element method) could also have a relevant benefit in the definition of the structure and for the planning of static, dynamic and vibration and noise tests, reducing the required time for such analyses. The Embraer experience also outlines how the improvement of aircraft performance is increasingly dependent on the use of lighter and more resistant material such as composite and carbon fibres that allows substantially greater flexibility, specific resistance and tenacity to fracture; they also results in lower empty weight and improved range for aircraft. Other considerations can be afford about the avionics that should closely follow the movement of the international technological frontiers, because of its importance for the marketing of the aircraft and in order to be consistent with what it is available at the current time. Finally Embraer experience also points out some economical aspects of the development of a new commuter aircraft. Ref. [6] highlights how on one hand, increased aircraft size and complexity have led to an escalation of development costs; on the other, the market has become more crowded, with

[1]Andrew Bonney, Cape Air's vice-president of planning, said: "We are the largest commuter airline in the US with a fleet of 67 Cessna 402s and Piper Navajos, as well as two ATR 42s, given our ageing fleet, we feel there is an urgent requirement for a new nine-passenger commuter aircraft in this market - no [FAR Part 23 aircraft] has been produced for this sector for about 25 years."
http://www.flightglobal.com/news/articles/aero11-tecnam-unveils-three-new-aircraft-355536

a greater degree of product overlap. At the same time, firms are being pushed to develop and offer not one, but families of aircraft characterised by a communality in order to reduce users' operational costs. This compels the producers to be under competitive stress and many have posted losses. Those linked to or supported by Government funds are claiming large infusions of capital to sustain their position on the market. Thus to approach the development of a new aircraft firms must first find partners. Here the flexibility is the key. Within a well- articulated strategy, they should be willing to share development projects, enter co-production arrangements to minimize costs and risk Also in NASA-SP460 [7] some very important technologies to be introduced for commuter aircraft are well described and defined as main design drivers for commercial success and effectiveness of these machines. This NASA studies, fulfilled in the early years of the 80s, pointed out how the main goals to afford better commercial success and to enable significant advances in the future commuter aircraft, are a 20% reduction of the operating costs, a fuel savings of 35%, increased reliability and safety, a higher level of passenger comfort and reduced maintenance. This study recommended numerous specific technology objectives that included improved aerodynamic performance, increased propulsion efficiency and reduced structural weight(primarily through the application of composite materials). The study also suggested that improvements be sought also in systems for flight management, pilot workload reduction, icing protection and engine condition monitoring and fault detection. The propulsion system improvement is an important ingredient in developing a more fuel-efficient and economic future small transport aircraft. Thus the NASA study addressed the need on appropriate engine and propeller technology choice. Studies about small aircraft transport have indicated that the application of advanced materials and manufacturing techniques, particularly dealing with composites, could contribute to improving future small transport aircraft through a reduction of the structural weight, smoother aerodynamic surfaces, reduced manufacturing costs. Advanced aerodynamics technology provides the basis for the developing the future small transport aircraft designs with increased performance, improved efficiency and better handling qualities.

Aircraft Type	Engine Type	Seats	Average Age in 2005 in Years	Average Age in 2006 in Years	Average Age in 2007 in Years	Average Age in 2008 in Years	Average Age in 2009 in Years	Average Age in 2010 in Years
Single-Engine	Piston	1-3	37	38	38	48.1	-	-
		4	35	36	36	38.2	-	-
		5-7	30	31	32	33.5	-	-
		8+	44	44	43	49.3	-	-
		All	-	-	-	-	42.2	46.3
	Turboprop	All	13	10	14	13.6	16.1	15.2
	Jet	All	34	34	35	44.4	44.0	44.1
Multi-Engine	Piston	1-3	32	32	33	48.9	-	-
		4	35	35	35	36.0	-	-
		5-7	36	36	39	39.3	-	-
		8+	38	39	40	41.6	-	-
		All	-	-	-	-	41.2	39.0
	Turboprop	All	25	26	27	28.8	28.0	27.0
	Jet	All	16	16	16	16.2	17.0	16.2
All Airplanes			**34**	**35**	**35**	**39.3**	**39.5**	**37.3**

FIGURE 1.2: Average Age of Registred General Aviation Fleet, 2005-2010, source: GAMA [1].

A new concept commuter airline should ensuring that not only passenger demands for comfort and safety are met, but that potential operators should be able to deal with an airplane with significantly improved direct operating costs and more efficient maintenance procedures. Nowadays, also global environmental considerations such as the need for lower fuel burn and lower noise emissions are of great importance. As it can been seen in Fig. 1.3 and Fig. 1.4, all the major commuter aircrafts within a segment of 6-15 seats was introduced more than 30 years ago and they are still in use today. These aircraft, still in operation, are characterized by old engine models with high fuel consumption and emissions, by relevant internal and external noise, by all-aluminum alloy heavy structures (no composites), by rough aerodynamic configuration (strut-braced wing without winglet and not streamlined fuselage) and by very old avionic and control systems (only mechanical control and analogical cockpit interface). Also the manufacturing cost can be substantially reduced due to the modern tools and production systems. It can be clearly noticed that almost all commuter aircraft in operation are characterized by a twin-engine arrangement, being the Cessna Caravan the only single-engine aircraft of this category with a certain commercial success.

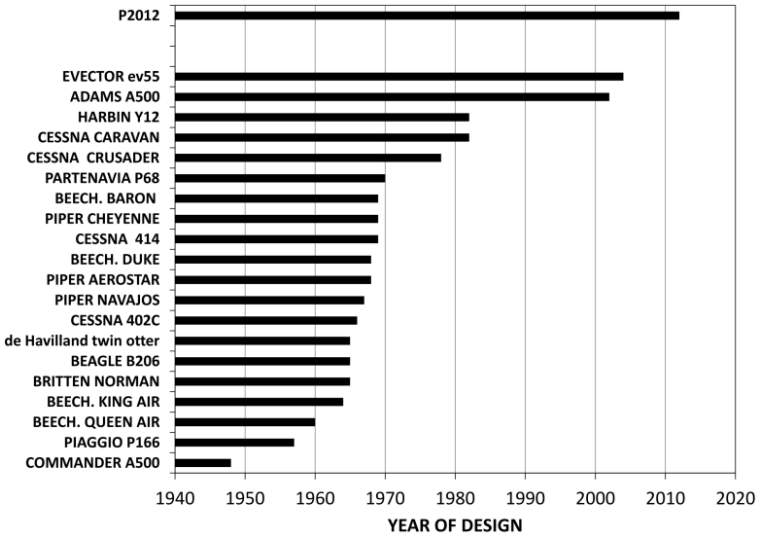

FIGURE 1.3: Year of design of several commuter aircfrat, source: Jane's [2].

1.2 Some Typical Existing Commuter Aircraft

As already discussed in section 1.1 the small aircraft transport scenario is characterized by many hundreds of "heritage" airplanes, in this section an overview of the most successful airplanes model for the small aircraft transport is presented.

Model Specifications		CESSNA 402	CESSNA CARAVAN	PIPER NAVAJOS	BRITTEN NORMAN B2N	BEECH. Baron	BEECH. Duke	PARTENAVIA P68	TECNAM P2012
Year		1966	1982	1967	1965	1969	1968	1970	**2012**
Wingspan	m	13.45	15.87	12.4	14.94	11.53	11.97	12	**14**
Wing area	sqm	21.00	25.96	21.30	30.20	18.50	19.78	18.60	**25.40**
Aspect ratio AR		8.61	9.70	7.22	7.39	7.19	7.24	7.74	**7.84**
Lenght	m	11.09	11.46	9.94	10.86	9.09	10.31	9.55	**11.70**
Height	m	3.49	4.53	3.96	4.18	2.97	3.76	3.40	**4.10**
Cabin height	m	1.27	1.30	1.17	1.30	1.27	n.a.	1.20	**1.37**
Cabin width	m	1.42	1.57	0.76	1.10	1.07	n.a.	1.04	**1.50**
Cabin lenght	m	4.98	5.28	4.42	4.60	3.84	n.a.	4.05	**4.32**
Landing gear type		tricycle - retractable	tricycle- fixed	tricycle - retractable	tricycle- fixed	tricycle - retractable	tricycle - retractable	tricycle -retr. or fixed	**tricycle- fixed**
Engine									
Manufacter		Continental	Pratt-Wittney	Lycoming	Lycoming	Continental	Lycoming	Lycoming	**Lycoming**
Model		TSIO-520-VB	PT 6A-114A	TIO-540-A	I0-540	IO-550-C	TIO-541-E1C4	IO-360-A1B6	**TEO-540-A1A**
Horsepower	hp	2*325	1*675	2*310	2*300	2*300	2*380	2*200	**2*350**
Propeller									
Manufacter - Type		McCauley 3 blade	McCauley 3 blade	McCauley 3 blade	Hartzell 2/3 blade	Hartzell 3-blade	Hartzell 3-blade	Hartzell 2-blade	**Hartzell or MT 3-blade**
Diameter	m	2.25	2.69	2.03	1.98	1.93		1.83	
Design Weight									
Max. gross weight	kg	3107	3629	2948	2994	2495	3073	1990	**3290**
Std. empty weight	kg	1845	1832	1990	1667	1901	1990	1230	**2110**
Useful load	kg	1262	1722	958	1128	682	n.a.	680	
Seating capacity		9	8 to 13	7	9	5	5	6	**9**
Fuel capacity	liters	780	1257	708	492	528	1223		
Wing loading	lb/ sqft	30.30	28.63	28.35	20.31	27.62	31.82	21.91	**26.95**
Power loading	lb/hp	10.54	11.85	10.48	11.00	9.17	8.91	10.97	**10.36**
Performance									
Max. speed VNE	kts	230	186 @FL100	226	183 IAS	223	230	193	**220**
Cruise Speed	kts	213	175 IAS	201	139 @FL70	202	199	165 @FL75	**200 @FL10**
Min. contr. speed VMC	kts	80.0 IAS	n.a.	74.0 IAS	n.a.	n.a.	80.0 IAS	n.a	**73.0 IAS**
Stall speed, flaps up	kts	80.0 IAS	75 CAS	69.7 IAS	50.0 IAS	84.0 IAS	71.0 IAS	68 IAS	**78.0 IAS**
Stall speed, flaps down	kts	71.0 IAS	61 CAS	63.2 IAS	40.0 IAS	73.0 IAS	62.5 IAS	57.0 IAS	**62.3 IAS**
Best rate of climb	ft/min	1450	1234	1395	860	1670	1601	1240	**1600**
Range max	nmi	1273	1295 @FL200	1011	503	1559	1227	1598 @FL70	**662**
Take off distance	m	670	626	695	371	701	632	400	**640**
Landing distance	m	757	505	554	299	762	402	600	**549**

FIGURE 1.4: Year of design of several commuter aircfrat, source: Jane's [2].

1.2.1 Beechcraft

Beechcraft Corporation[2] is an American manufacturer of general aviation and military aircraft, ranging from light single-engined aircraft to twin-engined turboprop transports, and military trainers. Four Beechcraft aircraft models should be mentioned for this category:

- Beechcraft Baron: it is a twin-piston aircraft first designed and manufactured in the name of Beechcraft Baron in 1969 by Beech Aircraft Corporation, which became a subsidiary of Raytheon Aircraft Company in 1980. The Beech Model 95-55 Baron, first flown on 29 February 1960, was developed from the earlier Modet 95 Travel Air. It differed primarily in having more powerful engines, but also in design refinements that included swept vertical tail surfaces, and improved all-weather capability. Deliveries began in November 1960, and ready acceptance of this new twin-engined four/five-seat aircraft resulted in further improvement and development of the type. The Model B55, introduced in 1963, had

[2]Beechcraft official website. http://www.beechcraft.com/.

four-seat and optional five/six-seat accommodation, and in 1965 an additional Model C55 was made available with more powerful 213kW Continental IO-520-C engines. The Model C55 incorporated a number of other improvements, including increased tailplane span and an extended nose baggage compartment, and was developed later as a separate Baron model distinct from the B55. A few months before the introduction of the C55, the US Army announced that the Model 95-B55 had been chosen for military service as an instrument trainer, which was ordered in an initial quantity of 55 under the designation T-42A Cochise. Ten more were procured for US Army service plus, in 1971, five for delivery to the Turkish army under the Military Assistance Program. By 1984, production of civil and military 95-B55 Barons was in excess of 2,400 and 1,201 examples of the Model E55 (formerly C/D55) had been delivered when production ended. In September 1967 deliveries began of a new Model 56TC Baron. This introduced turbocharged power, in the form of two 283kW Avco Lycoming TIO-541-E1B4W engines, providing much improved performance. Air-conditioning was available as an option, Beech claiming this to be the first time that such a system had been offered on a lightweight twin. However, the higher cost of this version of the Baron attracted only 93 sales, and production ended in December 1971. Before that date the range was extended when, in late 1969, Beech introduced the larger Model 58 Baron. First flown in June of that year, it had the fuselage lengthened by 0.25m to provide a more spacious cabin, and related to this was an extension of the wheelbase. Double doors on the starboard side of the fuselage gave easy access to baggage/cargo space behind the rear seats, and powerplant consisted of two engines as installed in the Model E55. Ready acceptance of this improved Baron, with delivery figures that have averaged about two per week for more than 12 years, resulted in the introduction of a pressurised Model 58P, with first deliveries in late 1975. It was something of a matched airframe, combining Model 95-B55 wings. Model 58 tail unit, a strengthened Model 58 fuselage to cater for pressurisation, and main landing gear units as developed for the Model 60 Duke. Power was provided by two Continental turbo-charged engines, currently TSIO-520-WB units with propeller synchrophasers as standard. The most recent addition to the range came with initial deliveries in June 1976 of the Model 58TC which, apart from being unpressurised, is generally similar to its immediate predecessor, and retains its turbo-charged powerplant. The Baron has proved to be a popular twin, and by January 1989 2,182 Model 58s had been delivered. In addition to these Beech production Barons, at least two turboprop conversions have been developed by other constructors. These include the SFERMA Marquis, produced in small numbers in France, and combining Beech-built Baron airframes with 328kW Turbomeca Astazou engines; and the American Jet Industries Turbo Star

Baron powered by two 298kW Allison 250-B17 turboprops. In 2004 Raytheon upgraded the aircraft with a fully integrated glass cockpit along with a Garmin G1000 avionics suite. The aircraft's name was changed to Beechcraft Baron G58 in April 2005, and it was certified in December 2005. The Raytheon Aircraft Company was acquired by Hawker Beechcraft Corporation, US (HBC) in 2007. The aircraft is currently manufactured by HBC. The upgraded Beechcraft Baron G58 made its public debut at the 36th annual Sun 'n' Fun Fly-in Expo held between 13th and 18th April 2009 in Lakeland, Florida, US. On 21 June 2010, the Beechcraft Baron G58 was certified by the Civil Aviation Administration of China (CAAC). In July 2010, the Beechcraft Baron G58 became the first aircraft of HBC to be approved for operations at the London City Airport. Fig. 1.5(a) shows the Beechcraft B58 model, some of its characteristics and flight performance are summarized in Fig. 1.4. The Beechcraft Baron was originally developed for the civil general aviation market, but its characteristics have suggested its use on the military market. As matter of fact Beechcraft Baron is in service of many military agencies all over the world, such as the United States Army, Spanish Air Force, Mexican Air Force and Naval Aviation and Turkish Army and Air Force. The production of the Beechcraft Baron started in 1961 and is still in progress today. More than 6991[3] copies have been built and the unit cost was $ 1,095,000[4] in the year 2012.

- Beechcraft Duke: it is an American-built twin-engine fixed-wing aircraft created by Beechcraft. The aircraft has a nose-wheel, retractable landing gear and a pressurized cabin. The two piston engines are turbocharged and the turbochargers also pressurize the cabin with bleed air. The development of the Beechcraft 60 began in early 1965 and it was designed to fill the gap between the Beechcraft Baron and the Beechcraft Queen Air. On 29 December 1966 the prototype made its first flight [2]. On 1 February 1968 the FAA issued the Type certificate. Distribution to customers began in July 1968. The passenger cabin is fitted with club seating and entry is by means of a port-side airstair entry door in the rear fuselage [8]. The Beechcraft A60, which came onto the market in 1970, represented an advancement over the Baron, with an improved pressurized cabin utilizing advanced bonded honeycomb construction, lighter and more efficient turbochargers, and improved elevators. The last variant, the B60, was introduced in 1974. The interior arrangement was renewed and the engine efficiency again increased by improved turbochargers [9]. The Beechcraft 60 was, despite its very good performance, only a moderate seller, principally because the complicated

[3] Beechcraft Serialization, 1945 thru 2014.
https://www.beechcraft.com/customer_support/technical_publications/docs/nontechnical/serializationL

[4] Beechcraft Berlin aviation GmbH, Flughafen BER.
http://beechcraft-berlin.com/maintenance/.

technology demanded a high expenditure on maintenance. Production was stopped in 1983 [10]. Most of the Duke B-60s still flying have retained their original equipment. Electro-mechanical systems, which were highly advanced when the aircraft was introduced, were superseded in other aircraft with simpler I/C controlled mechanical parts. The aircraft design uses turbocharged Lycoming TIO541-B4 engines that develop 380 hp each. Other systems, parts, and FAA certified technicians are increasingly difficult to locate. Normally, pilots figure 45 US Gallons/hour, plus another 40 gallons for each takeoff and climb as typical fuel consumption for cross country planning. One area of particular maintenance concern involves the original construction of the tail section from a magnesium alloy, making that portion a common and expensive target of corrosion if not detected and treated quickly. Some Dukes have been modified by Rocket Engineering of Spokane, Washington, replacing the Lycoming reciprocating engines with Pratt & Whitney Canada PT6A-21 or -35 turbine engines. The modification increases fuel capacity by 28 gallons and the maximum useful load by 400 lbs. The take-off length required is shortened by over 1,500 feet to only 1,000 feet and the landing distance is reduced by over 2,000 feet to only 900. The maximum rate of climb is increased from 1,600 feet per minute to 4,000 feet per minute, reducing the time to climb to 25,000 feet from 25 minutes to 9 minutes. The cruise speed is increased to 290 knots at 29,000 feet. The modification does have some disadvantages as it increases fuel burn from 56 US gal/hr to 66 and lowers the certified ceiling from 30,000 feet to 28,000[5],[6] The supplemental type certificate was issued on May 12, 2006[7]. The Duke was purchased by corporate and private pilot owners. Most were registered in the United States but examples were exported to many countries including Argentina, Australia, Brazil, Canada, Croatia, Finland, France, Germany, Honduras, Iceland, Serbia, Slovenia, Sweden, Switzerland, South Africa and the United Kingdom. One Duke was flown by the Jamaica Defense Force. Many remain in service in the early twenty-first century. The quarter rear view of the Beechcraft Duke is shonw in Fig. 1.5(b), some of its characteristics and flight perfromance are shown in Fig. 1.4. The Beechcraft Duke was introduced in the 1968 and its production stopped in th 1983, 593 unit were produced[3].

- Beechcraft King Air: The Beechcraft King Air family is part of a line of twin-turboprop aircraft produced by Beechcraft. The King Air line comprises a number of models that have been divided into two families;

[5]Royal Turbine (2010). Performance.
http://www.royalturbine.com/content/performance.

[6]Royal Turbine. Comparison (2010).
http://www.royalturbine.com/content/comparison.

[7]Federal Aviation Administration. November 20, 2008. Retrieved October 15, 2014.
http://rgl.faa.gov/Regulatory_and_Guidance_Library/rgstc.nsf/0/3edaf2d749717989862575120007fe844/$FILE/SA016

the Model 90 and 100 series are known as King Airs, while the Model 200 and 300 series were originally marketed as Super King Airs, with "Super" being dropped by Beechcraft in 1996 (although it is still often used to differentiate the 200 and 300 series King Airs from their smaller stablemates). The Beech Model 100 King Air was added to the range of Beech corporate transports when initial deliveries were made in August 1969. It differed from the earlier King Airs in several respects: reduced wing span, a lengthened fuselage to provide accommodation for a maximum of 15 persons, increased elevator and rudder areas, twin-wheel main landing gear, and more powerful engines. The new wing was generally similar to that developed for the Model 99 Airliner. In October 1971 Beech began deliveries of the improved King Air A100, this variant incorporating detail improvements, and the first five were supplied to the US Army under the designation U-21F. Examples have been procured by the Spanish air force, and a Universal Aircraft Com/Nav Evaluation (UNACE) configured version, for the rapid inspection and calibration of air navigation systems, has been supplied to countries that include Algeria, Belgium, Canada, Indonesia, Malaysia, Mexico, and the USA. Beech also produces specially modified camera-equipped versions of the King Air for aerial survey, and examples are in service in this role in Canada, Chile, France, Jamaica, Saudi Arabia, Thailand, and the USA. In parallel with A100 production since late 1975, Beech has produced a complementary King Air B100 offering higher performance. It differs by the installation of 533kW Garrett TPE331-6-252B turboprop engines, and of equipment directly associated with the engine installation. In addition to its use by military and government users, the King Air is also used by many non-governmental organizations, as well as by corporate and private users. This includes commercial use by air-taxi and air charter companies[8]. The King Air was the first aircraft in its class and has been in continuous production since 1964. Nearly 6000 Beechcraft King Airs of 17 variants have been sold since the product line was introduced in 1964, making this the most successful series of twin turbine-powered business aircraft ever built.The cost per unit of a King Air C90GTi is $ 3.4 million.

- Beechcraft Queen Air: The Beechcraft Queen Air is a twin-engined light aircraft produced by Beechcraft in several different versions from 1960 to 1978. On 28 August 1958 Beech flew the prototype of the new Beech Model 65 Queen Air business aircraft. Designed to meet the requirements of what the company considered to be a growing market, this seven/nine-seat low-wing monoplane had retractable tricycle landing gear, and was powered by two 254kW Avco Lycoming IGSO-480-A1B6 flat-six

[8]Nexant Pacific. Retrieved 3 February 2015 . http://www.nextantpacific.com/uses/.

engines. Full IFR instrumentation was standard, and optionally available equipment, such as an autopilot, and navigation and weather-avoidance radar, could provide the Queen Air with the capability of a contemporary airliner. In the following January Beech flew the first of three Model 65s that were to be used by the US Army for evaluation. This resulted in orders totalling 71 of these aircraft, under the designation L-23F Semi-nole, an identification chosen because of the general similarity between the Twin Bonanza and Model 65 Queen Air, the latter differing primarily by its deeper section fuselage and more powerful engines. In 1962 the L-23F was rede-signated U-8F, and some modified at a later date to provide improved interior accommodation became U-8Gs. A number of commercial Queen Airs were acquired by the Japan Maritime Self-Defence Force, for use in navigation trainer and transport roles, and others went to the air forces of Uruguay and Venezuela. An improved Model A65 Queen Air, introduced at a later date, had swept vertical tail surfaces and greater fuel capacity; and a version with a high-density seating arrangement for a crew of one or two, with 10 or nine passengers respectively, was known as the Queen Airliner. A Model 65 Queen Air was provided with two 373kW Pratt & Whitney PT6A-6 turboprop engines. Identified initially by the company as the Model 65-90T Queen Air, this was evaluated by the US Army, from 17 March 1964, as the NU-8F. Expansion of the Queen Air line came on 22 June 1961 with a first flight of the Model 80 Queen Air. This had more powerful engines (283kW), but the Queen Air A80, introduced in January 1964, had increased wing span that allowed for operation at a higher gross weight. Final version was the Queen Air B80, incorporating a number of design and equipment improvements, and 11-seat Queen Airliners were available for each of these basic versions. A pressurised version of the Model 80 was introduced in August 1965: generally similar to the Queen Air B80, it differed by having structural modification of the fuselage to cater for pressurisation, and by the incorporation of circular cabin windows. Identified as the Model 88 Queen Air, it was taken out of production during 1969 after 45 had been built. A third member of the Queen Air family was introduced in 1968. Known as the Model 70 Queen Air, this was basically an A65 with the increased span wing of the B80. Manufacture of the Models 65 and 70 was terminated at the end of 1971, at which time production figures totalled 404 (including U-8Fs) and 42 respectively. Production of the Model 80 Queen Airs continued until the end of 1978, at which time approximately 510 had been built. The unit cost was $ 135000 (Model 80 in 1962), $576000 in 2012 USD.

(a) Beechcraft Baron.

(b) Beechcraft Duke.

(c) Beechcraft King Air.

(d) Beechcraft Queen Air.

FIGURE 1.5: Some Beechcraft commuter aircrafts.

1.2.2 Britten-Norman Islander/Defender

Britten-Norman[9] (often referred to as BN) is a British aircraft manufacturer and aviation services provider beneficially owned by a consortium which includes two members of the Zawawi family from the Sultanate of Oman. The company is the sole independent commercial aircraft producer in the UK. The company manufactures such aircraft as the Islander and the militarised Defender both of which are capable of short take-off and landing (STOL) operations. The three-engined Trislander is still operating but is not currently being manufactured. The aircraft are typically used for inter-island schedules. The Britten-Norman BN-2 Islander is one of the best-selling commercial aircraft types produced in Europe. Although designed in the 1960s, over 750 are still in service with commercial operators around the world. The aircraft is also used by the British Army and Police forces in the United Kingdom and is a light transport with over 30 military aviation operators around the world. The Islander is also known for servicing the two airports joined by the shortest scheduled flight in the world, a leg of Loganair's inter-island service,

[9]Britten-Normal official website.
http://www.britten-norman.com/.

Loganair Flight 353, from Papa Westray Airport to Westray Airport. The distance is 1.7 mi (2.7 km) and the scheduled flight time including taxiing is two minutes[10]. Desmond Norman and the late John Britten had started their association in the development of crop-spraying equipment, and in 1964 began detail design work on a new lightweight feederline transport. Envisaged as a new-generation replacement for the ageing de Havil-land Dragon Rapide and other aircraft in this class, the Britten-Norman BIM-2 Islander soon attracted considerable interest, and construction of a prototype was initated in September 1964. This aircraft flew for the first time on 13 June 1965, powered by two 157kW Rolls-Royce/Continental IO-360-B engines, and with wings that spanned 13.72m. A number of changes resulted from flight testing, the most important being a 1.22m increase in wing span, and the installation of 194kW Avco Lycoming O-540-E engines, and this has remained the standard powerplant of the Islander, still being installed in production aircraft in its O-540-E4C5 version. Initial production aircraft were BN-2 Islanders, of high-wing monoplane configuration with a functional rectangular-section fuselage, conventional tail unit, non-retractable tricycle-type landing gear with twin wheels on the main units, and accommodation for a pilot and nine passengers. This 'high-density' seating arrangement had been contrived in a cabin that was only 1.09m wide at its maximum by installing 'wall-to-wall' seats, with access via two doors on the port side, and one on the starboard side, making an aisle unnecessary. Exit in emergency can be made by removing the door windows. The first production example of the BN-2 made its initial flight on 24 April 1967, and the first Islander entered service less than four months later, on 13 August. The BN-2 Islander was superseded in mid-1969 by the improved BN-2A Islander, which introduced detail aerodynamic and equipment improvements, in addition to a new side-loading baggage facility. Since 1978 the standard production version has the designation BIM-2B Islander II. This differs primarily by having an increased maximum landing weight, improved internal design, and smaller diameter propellers to reduce the cabin noise level. Various items of alternative equipment have become available over the years to extend the usefulness of the Islanders. These include 224kW Avco Lycoming IO-540-K1BS piston engines, or 239kW Allison 250-B17C turboprop engines, and aircraft with this latter powerplant installation are designated BIM-2T Turbine Islander. Other options include an extended nose to provide an additional 0.62m3 of baggage space, raked wingtips containing auxiliary fuel tanks, and a Rajay turbocharger installation to enchance performance. In addition to operation in a passenger-carrying capacity, the Islander can be used as a freighter with the passenger seats stored in the rear baggage bay, as an ambulance carrying three stretchers and two medical attendants, and for a variety of utility purposes when suitably equipped. Defender and Maritime Defender military versions are also available, and these can be adapted for

[10]Westray & Papa Westray Tourist Association website.
http://westraypapawestray.co.uk/getting-here/.

casualty evacuation, patrol, transport, and search and rescue operations. The success of this aircraft, which from the outset was intended to provide a low-cost reliable aircraft that could, if desired, be used in a number of differing roles, is highlighted by worldwide sales in approximately 120 countries, and which in late 1989 were past the 1100 mark. Of this total more than 300 had been built under licence in Romania, and 35 were assembled in the Philippines from components that had been manufactured by Britten-Norman. Financial problems for Britten-Norman during the early 1970s led to the takeover by The Fairey Group in 1972. During the following year production of the Islander was transferred from Bern-bridge to Gosselies in Belgium. But in 1977 The Fairey Group itself went into receivership, and the Britten-Norman part of the Group was bought by Pilatus, and in the form of Pilatus Britten-Norman Ltd the company continues to complete aircraft in the Isle of Wight after their basic manufacture in Romania. The Britten-Norman Islander production started in 1965 and is still progress today, more than 1280 units have been built. Islander/Defender series are in daily use with some 500 companies and organisations in over 120 countries[11]. Fig.1.6(a) and Fig.1.6(b) show the Britten-Norman Islander and Defender respectively, main characteristics and flight performance are shown instead in Fig.1.4.

(a) Islander. (b) Defender.

FIGURE 1.6: The Britten-Norman Islander.

1.2.3 Cessna

The Cessna Aircraft Company[12] is an American general aviation aircraft manufacturing corporation headquartered in Wichita, Kansas. Best known for small, piston-powered aircraft, Cessna also produces business jets. The company is a subsidiary of the U.S. conglomerate Textron. In March 2014

[11] List of Britten-Norman Islander Operators.
http://en.wikipedia.org/wiki/List_of_Britten-Norman_Islander_operators

[12] Cessna official website.
http://cessna.txtav.com

Cessna became a brand of Textron Aviation[13]. Two of Cessna aircfrat must be cited within a segment o 6-15 seats: the Cessna 402 and teh Cessna 208 Caravan.

- Cessna 404: When flown for the first time on 18 July 1962, the Cessna Model 411 then represented the company's largest business aircraft. Generally similar in configuration to the Model 310, it differed by having slightly increased wing span and area, a lengthened fuselage, more powerful 254kW Continental GTSIO-520-C flat-six turbocharged engines and accommodation for a crew of two and four to six passengers. Production of the Model 411 was discontinued in June 1978, afterthe production of 400 examples, a small number of which were supplied to the French air force. On 26 August 1965 Cessna flew the prototype of a generally similar aircraft which served for two new aircraft, the Model 401 and Model 402, and when FAA certification of the Model 401 prototype was awarded on 20 September 1966 it covered also the Model 402. These two aircraft represented lower-cost versions of the Model 411, differing primarily by having two 224kW Continental TSIO-520-E flat-six engines and some reduction in basic installed equipment. The Model 401 accommodated a crew of two and four to six passengers, but the Model 402 had a cabin layout which permitted a quick change from nine-seat commuter use to an all-cargo configuration. Production of the Model 401 was phased out in mid-1972, with development then being concentrated on the Model 402 which, in December 1971, had been named Utiliner. At the same time a new version of the Model 402 was introduced as the Businessliner. Both versions, powered by 242kW TSIO-520-VB engines, were progressively improved and remained in production for some time, as the 10-seat Utiliner II small convertible passenger/ cargo airliner and the Businessliner II executive transport able to carry 2-6 passengers. The final version was the Businessliner III corporate transport fitted with more sophisticated avionics, including weather radar. A downturn in sales led to production ceasing in 1986 by which time a total of 1,540 Cessna 402 variants had been built, including 12 delivered to the Royal Malaysian Air Force in 1975. The Cessna 402 has proven to be very dependable over the years, which, along with its range and passenger capacity, has made it a popular choice for many small regional airlines worldwide. The aircraft are generally flown on short, thin routes to hubs where passengers can connect to higher density routes. The largest operator of the type is Cape Air[14], which as of September, 2013 has a

[13]Textron 14 March 2014.
http://investor.textron.com/newsroom/news-releases/press-release-details/2014
[14]Cape Air official website.
https://www.capeair.com

fleet of over 75 402s operating in the Caribbean and United States[15]. Fig.1.7(a) and Fig.1.7(b) show the Cessna 402 with the colours of Cpae Air Company and the Cessna Caravan respectively. Main characteristics and flight performance are summarized in Fig.1.4.

- Cessna Caravan: Designed to replace extensive fleets of ageing utility aircraft still in wide service throughout the world such as the DH Canada Beaver, Otter and Cessna 180, 185 and 206 types, the Model 208 was conceived in 1980/81 as the first all-new turboprop powered general aviation aircraft. The prototype Cessna 208 Caravan I flew for the first on 9 December 1982, and the first production aircraft rolled out in August 1984. FAA certification followed in October 1984 and the type is now in service with military air arms in Brazil, Liberia, Thailand and with the Royal Canadian Mounted Police as amphibians. The higher gross weight Model 208A, ordered in December 1983 by the US small parcel airline Federal Express and called Cargomaster by them, is fitted with more comprehensive all-weather avionics and an under fuselage pannier, but has the fuselage windows deleted. Following experience with the 208A, Federal Express ordered the Model 208B Super Cargomaster with the fuselage stretched by four feet, also built without windows and equipped with a pannier. Flight testing began on 3 March 1986, followed by certification and first delivery to Federal Express[16], who have ordered 210, in October the same year. By the end of 1989 more than 370 variants of the Model 208 had been delivered. In 1985 Cessna released details of a quasi-military/special mission version of the Caravan I designated U-27A by the US Department of Defense and marketed as the Low Intensity Conflict Aircraft (LICA). Equipped with six hardpoints under the wing plus another on the fuselage centreline able to carry either a General Dynamics F-16 reconnaissance pod, or a cargo pannier, the LICA also has a electrically operated 'roll up' cargo door with slipstream deflector, that could be opened in flight, and bubble windows for downward surveillance and observation. Cessna are also offering a similarly equipped version of the stretched Model 208B for special mission. The Cessna 208 Caravan was introduced for the fist time in 1984 and over 2000 unit have been built, the price per unit is about $2,022,450 (2011 price USD). The Cessna 208 is used by governmental organisations and by a large number of companies for police, air ambulance, passenger transport, air charter, freight and parachuting operations. Fedex Feeder[16] is the largest operator of the Cessna 208, with over 250 aircraft.

[15] Cape Air (2010), Our Story.
http://www.capeair.com/about_us/our_story.html

[16] FedEx Corporation is an American global courier delivery services company headquartered in Memphis, Tennessee.The name "FedEx" is a syllabic abbreviation of the name of the company's original air division, Federal Express, which was used from 1973 until 2000.
www.fedex.com

(a) Cessna 402.

(b) Cessna Caravan.

FIGURE 1.7: Cessna 402 and Caravan.

1.2.4 Partenavia P68

Partenavia Construzioni Aeronautiche was an Italian aircraft manufacturer from 1957 to 1989. The company was formed shortly after the war by Professor Luigi Pascale of Naples University. Pascale had designed and flown a number of designs, in 1957 a factory was acquired at Arzano. Partenavia became a limited company in 1959. The first major aircraft to be produced was the P.57 Fachiro, a four-seat high wing aircraft for flying club use. A later all-metal version the Oscar replaced the Fachiro on the production lines. In 1981 the company became part of the Aeritalia group and concentrated on the production of over 100 of P.66C Charlie for the Aero Club d'Italia. The most recognised design was twin-engined P.68 first flown in 1970. In 1993 Alenia sold the company to Aercosmos and, in march 1998, was declared bankrupt and Vulcanair bought all the assets, design rights and trademarks. The Partenavia P.68 is an Italian six-seat, twin-engined, high-wing monoplane built by Partenavia and later Vulcanair. Designed by Professor Luigi Pascale and originally put into production in 1972, it was intended for private or business use but has also seen use as both a training and a transport aircraft. It was originally named the Victor, although this name was not used for the production aircraft. The P.68 Observer, which was an Italian/German development, has a transparent nose for use in police work and observation duties. First flown on 25 May 1970, the prototype P.68 was built at Arzano, Italy. It was powered by two 200 hp (149 kW) Lycoming IO-360 piston engines. Production of the P.68 began in 1972 with 14 pre-production aircraft at new facilities in Casoria, Italy. These were followed in 1974 by the P.68 B with the fuselage lengthened by 6 in (15.2 cm) to create more space in the cockpit. It was superseded in 1979 by the P.68C which had a lengthened nose to accommodate a weather radar. A turbocharged version (the P.68C-TC) was available in 1980. The type license was obtained by Vulcanair, which is still producing the P.68C. With the help of Aeritalia, development began of a nine-seat turboprop version. The first aircraft, an AP.68TP, first flew in 1978 using Allison 250

turboprops. Although the prototype had a retractable undercarriage, the production aircraft, named the Spartacus, had a fixed undercarriage. Later, a retractable undercarriage version was built as the Viator. The German company Sportavia-Putzer modified the P.68 by replacing the nose section with a transparent structure, marketing it as an observation aircraft for law enforcement. Initially, Observers were simply conversions of existing aircraft, but later, they were entirely new aircraft built by Partenavia.

(a) Partenavia P68. (b) Partenavia P68 Observer 2.

FIGURE 1.8: Partenavia P68.

1.2.5 Piper Navajos

Piper Aircraft, Inc.[17], is a manufacturer of general aviation aircraft, located at the Vero Beach Municipal Airport in Vero Beach, Florida, United States and owned by the Government of Brunei. Along with Beechcraft and Cessna, it was at one time considered one of the "Big Three" in the field of general aviation manufacturing[11]. On 30 September 1964 Piper flew the prototype of a new twin-engine executive aircraft which was then the largest built by the company. Identified at first as the Piper PA-31 Inca, the aircraft had been redesignated as the PA-31 Navajo when deliveries began on 17 April 1967. A six/eight-seat corporate/ commuter transport of cantilever low-wing monoplane configuration with retractable tricycle landing gear, it was powered by two 224kW Avco Lycoming IO-540-K flat-six engines, and was available in optional Standard, Commuter and Executive versions with differing interior layouts. Made available at the same time was the optional PA-31T Turbo Navajo, which differed only by having two 231kW TIO-540-A turbocharged engines, and the range was extended in 1970 by introduction of the PA-PA-31P Pressurized Navajo with a fail-safe fuselage structure in the pressurised section and two 317kW Avco Lycoming TIGO-541-E1A engines. Production of the PA-31 Navajo ended during 1972 and at the same time the company introduced for 1973 the PA-31-350 Navajo Chieftain which, by comparison

[17]Piper Aircraft official website.
http://www.piper.com

with its predecessor, had the fuselage lengthened by 0.61m and was powered by two 261kW TIO-540-J2BD turbocharged engines driving counter-rotating propellers. A significant advance in the Navajo family came on 22 October 1973 when Piper flew the first production example of the PA-31T Cheyenne, which combined an airframe generally similar to that of the Pressurized Navajo with two 462kW Pratt & Whitney Aircraft of Canada PT6A-28 turboprop engines. In the following year an additional model of the Turbo Navajo was made available, the PA-31-325 Turbo Navajo C/R, which introduced a 242kW version of the counter-rotating engines installed in the Chieftain. Production of the PA-31P Pressurized Navajo ended during 1977, at which time a total of 248 had been built, but at the same time the company introduced a new version of the Cheyenne, the PA-31T-1 Cheyenne I, the original Cheyenne then becoming re-designated PA-31T Cheyenne II. Deliveries of the new Cheyenne I, which differed primarily from its predecessor by having 373kW Pratt & Whitney Aircraft of Canada PT6A-11 turboprop engines, began towards the end of April 1978. The Cheyenne range was extended for 1981 by introduction of the PA-31T-Cheyenne IIXL, with the fuselage lengthened by 0.61m and 559kW Pratt & Whitney Aircraft of Canada PT6A-135 engines flat-rated to 462kW. In 1982 production of the PA-31 Navajo terminated after 1,317 had been built. Later production versions of the Navajo family include the PA-31-325 Navajo C/R, PA-31-350 Chieftain and the PA-31T-1 Cheyenne I, PA-31T Cheyenne II and PA-31T-2 Cheyenne IIXL. However, the loss of the Navajo was compensated for in 1983 by introduction of the PA-31P-350 Mojave, which basically combined the airframe of the Cheyenne II with the power-plant of the PA-315-350 Chieftain. The Piper Navajo was produced from the 1967 to 1984 and 3942 copies were produced. Fig.1.9 shows two different arrangement of the Piper Navajo, main characteristics and flight performance are shown in Fig.1.4.

(a) Piper Navajo PA 31.

(b) Piper Navajos PA 31 Mojave.

FIGURE 1.9: Piper Navajo.

1.3 Some Typical New or Future Commuter Airplanes

The brief overview about some of the main successful airplanes within a segment of 6-15 seats presented in section 1.2 has shown the old-fashioned year of design of these aircraft. Currently only a couple of new aircraft are under development in this category.

- Evektor EV-55 Outback: Evektor-Aerotechnik[18] is manufacturer of general aviation aircraft, based in Kunovice in Czech Republic. The company produces range of light sport aircraft, training and advanced ultralight aircraft that are exported to 40 countries worldwide. Evektor-Aerotechnik is actively engaged in project of twin engine turboprop airplane for 9-14 passengers - the EV-55 Outback. Evektor EV-55 Outback is a twin-engine turboprop aircraft and the prototype first flew on 24 June 2011. In 2004 the company announced its plan to design and construct a two-engined utility aircraft that would carry up to 14 passengers or 4000 lb (1800 kg) of cargo, and operate from unimproved fields and at high-altitude airports. The aircraft will have three configurations: passenger transport, cargo transport and combined operations with space in front for cargo and passenger accommodation aft. The EV-55 is of conventional high-wing utility design, with its horizontal stabilizer mounted near the top of its fin. The prototype aircraft is powered by two Pratt & Whitney PT6A-21 turboprop engines (536 shaft horsepower each), driving a four-blade propeller. The wing is mounted atop a nearly-square fuselage, which has five windows per side. The trailing-link tricycle landing gear retracts into the nose section or pods on the lower fuselage. Expected maximum cruise speed is 220 knots (407 kph). The first prototype, an EV-55M (military version), flew from Kunovice Airport in June 2011, with company pilot Josef Charvat and military pilot Maj. Jiri Hana at the controls. Czech general aviation aircraft manufacturer Evektor is hoping to fly its second EV-55 Outback - the first production-conforming aircraft - later this year. The company is also seeking to secure a tranche of investment to complete development and bring the twin-engined turboprop to market in 2016. The Kunovice-headquartered company has secured 11 deposits to date, including nine from Russian launch customer AeroGeo[19]. Some of the specifications, dimensions and flight performance are summarized in Tab.1.1. Fig.1.12 shows two possible cabin arrangement for Evektor EV-55 Outback passenger and cargo version, Fig.1.10(a) shows instead the first prototype in flight while Fig.1.10(b) illustrated the airplane three views.

[18] Evektor Aerotechnik official website.
http://www.evektoraircraft.com

[19] Evektor builds first production-conforming EV-55, 7 Jan 2014.
http://www.flightglobal.com/news/articles

(a) Evektor EV-55 Outback first flying prototype.

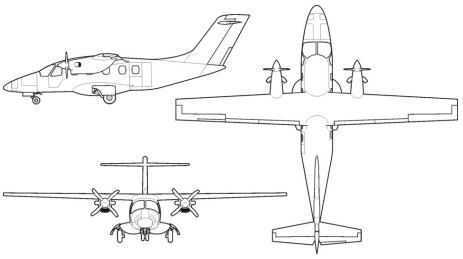

(b) Evektor EV-55 Outback three views.

FIGURE 1.10: Evektor EV-55 Outback.

TABLE 1.1: Evektor EV-55 Ouback Characteristics.

Specification	
Wing span	16.10 m (52.82 ft)
Lenght overall	14.35 m (47.47 ft)
Height	4.68 m (15.28 ft)
Passengers	9 (14)
Cabin length	5.02 m (197.5 in)
Cabin width	1.61 m (63.4 in)
Cabin height	1.37 m (54 in)
Volume	9.47 m^3 (334 cu.ft)
Maximum Take-Off Weight	4600 kg (10140 lbs)
Empty Weight(passenger)	2658 kg (5860 lbs)
Engine	2x Pratt & Witney PT 6A-21 (536 shp each)
Propeller	4 blade constant speed (AVIA AV-844)
Max Speed at 10000ft	408 km/h TAS (220 KTAS)
Stall speed 0° Flaps	143 km/h (77 KEAS)
Stall Speed 38° Flaps	118 km/h (64 KEAS)
Rate of Climb AEO	8.5 m/s (1673 fpm)
Rate of Climb OEI	2.3 m/s (453 fpm)
Take-Off Distance (50 ft at s.l.)	420 m (1378 ft)
Landing Distance (50ft at s.l.)	510 m (1673 ft)

Source: http://www.evektor.cz

- Geci Skylander: For 30 years, GECI International has been a dominant specialist in high technology engineering, with a presence heavily focused on the aeronautics sector. Working in the four corners of the world, the 950 staff, engineers and researchers of GECI International are constantly at the ready to meet the technological challenges of today and the future. Combining excellence, passion and innovation, GECI International is active on two fronts: GECI Engineering, offering expertise and solutions

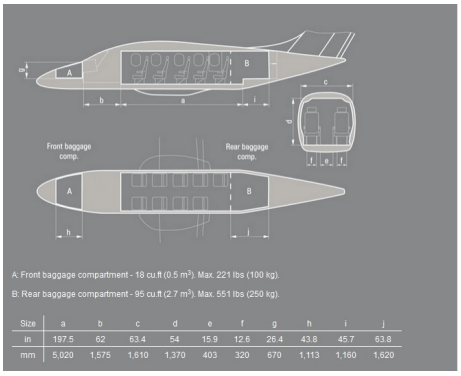

(a) Evektor EV-55 Outback cabin arrangment for passenger version.

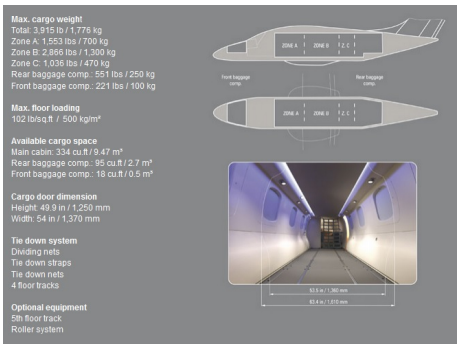

(b) Evektor EV-55 Outback cabin arrangment for cargo version.

FIGURE 1.11: Possible cabin arrangment for Evektor passenger and cargo cabin.

in the sectors of aeronautics, transport and infrastructures, and its subsidiary GECI Aviation, held at 88.58%, with its range of twin turboprop aircraft: the F406 and the Skylander SK-105. The F406, produced by Reims Aviation Industries, is a world-renowned aircraft, especially well suited for surveillance missions. The Geci Skylander was announced on 17 October 2001 at the Seoul Air Show. Design supervision was by the late Desmond Norman, co-designer of the Britten-Norman Islander. The Skylander was concepted to transport up to 19 passengers or 2.7 tons of payload and to be certificated under C23/FAR23 regulations. The concept design was addressed to achieve a maximum cruise of 235 knots and a long range cruise speed of 180 knots, a range of 600 nm, a landing distance (ground roll) of 255 m. Its maximum take-off weight was estimated to be 8260 kg and the aircraft was thought to be powered with 2 Pratt & WhitneyPT6-65B. The first metal cut was scheduled in January 2004. The first two prototypes expected to fly in May 2005, but this has been postponed, pending adequate funding. By December 2007, plans were in hand for the formal programme launch in April 2008 following the signature of letter of intent by Turkish freight carrier ACT Airlines Group for 15 aircraft to be delivered between 2011 and 2021. Simultaneously there was an announced partnership agreement for distribution of the Skylander in Bulgaria, Hungary, Macedonia, Turkey and several Middle East countries. Progress was slowed by a change of manufacturing plant from Portugal to France during 2008, and the target in-service date remained 2011. The program was structured for joint funding (initially USD 120 million) by three risk-sharing partners. In October 2009, a new design of the aircraft was presented and the new target date of entry in service was announced to be the last quarter of

2012. After another change of manufacturing plant location (Chambley-Bussières Air Base in Lorraine) the target date of entry into service was postponed year after year. On October 2012 Geci International's Sky Aircraft was placed under creditor protection and in April 2014 the Commercial Court of Briey decided for the wind up of Geci Aviation[20].

(a) Geci Skylander mockup at Paris Air Show 2009 .

(b) Rendering of the conceptual design of the Geci Skylander.

FIGURE 1.12: Geci Skylander Conceptual Design.

1.4 Typical Commuter Characteristics

Most successfully commuter designs(see section1.2) and the market requirements lead to identify the main specifications for a commuter aircraft to be the following:

- High wing twin-engine airplane in order to to provide an easy cabin access and a better clearance. The choice of high wing configuration facilitates the installation of the engines since the propeller clearance is higher(increased safety) compared with a low wing.
- All aluminium alloy main structure to create a robust yet light airframe easy to be inspected and maintained.
- Fixed landing gear to reduce both maintenance and direct operative costs. However also retractable landing gear version can be designed.
- Piston/Turboprop powered to lead to low flight costs and easy and cheap maintenance.
- Reduced take-off and landing run to guarantee possible take-off and landing from short or not prepared and grass runways.
- Low cost(operative and maintenance)

[20]Wind up of Geci Aviation,18 June 2014.
http://www.geci.net

Fig.1.4 shows some typical characteristics of several commuter aircraft still flying nowadays. The average maximum take-off weight is about 3000 kilograms while the standard empty weight is about 1800 kilograms, the ratio between the empty and maximum take-off weight is about 0.6 while the typical weight on power ration is 10.5 lb/hp and the wing load is between 22-32 lf/sqf. The average useful load is about 1200 kg. A typical commuter aircraft within a range of 7-9 passengers has a wing span of about 13.5 meters and a wing area of about 22 square meters, has an average length of about 11 meters with a fuselage finesess ratio of about 2.5. The typical ratio between the tail and wing area is about 0.2 and 0.12 for the horizontal and vertical tail respectively.

1.5 Goal and Structure of the Research Work

The market analysis discussed above constitutes the motivation behind the will to design a new commuter aircraft that could replace ageing designs such as Cessna 402, Britten-Norman Islander or the Piper Navajo. Tecnam Aircraft Industries and the Department of Industrial Engineering (DII) of the University of Naples "Federico II" have been deeply involved in the design of a new commuter aircraft that should be introduced in the market with very good opportunities of success. One of the goals of this work consist into providing some general guidelines for the design of a twin-engine commuter aircraft within a range of 6-11 seats. Design guidelines are focused mainly on the sizing of tailplanes, and in particular the vertical tail surface sizing, which is a very crucial aspect for this aircraft category commercial success(the vertical tail size determines the minimum aircraft control speed which directly affects the take-off and landing distances). Main goals of this research work are indeed the estimation of both longitudinal and lateral-directional static stability and control characteristics of a new commuter aircraft design. The estimation of the aerodynamics characteristics has been accomplished through all the nowadays available approaches, such as the classical semi-empirical methods, widely used in order to accomplish a very fast and reliable estimation of the goodness of a preliminary project; the numerical analyses through the application of fast and reliable 3-D panel code solver and finally the goodness of preliminary design has been also checked through Computational Fluid Dynamics simulations performed with a Navier-Stokes equations solver, and through a wide experimental tests campaign performed at the main subsonic wind tunnel of the DII.

The description of the work has been structured as follows:

Chapter 2 In this chapter the preliminary design of a new 11 seats commuter aircraft, named P2012 Traveller, is presented. Some general design guidelines, useful to accomplish with the commuter aircraft market specifications, are drown. Aircraft configuration and cabin layouts choices are shown and compared to similar solutions adopted by main competitors. The preliminary design phase has been also supported by aerodynamic analyses

focused on some particular effects such as the wing-fuselage interference and the winglet and nacelle lift contribution and their effect on wing span loading. The aerodynamic analyses have been also essential to validate the preliminary estimation of aircraft stability and control derivatives (both longitudinal and lateral-directional) and to lead to a right sizing of tail surfaces. These analyses have been carried out through the use of a 3-D panel code.

Chapter 3 This chapter is fully dedicated to the wide wind tunnel investigation performed on 1:8.75 scale model of the aircraft. Wind tunnel tests led to the estimation of both longitudinal and lateral-directional stability characteristics, highlighting the contribution of each aircraft component, in particular those of the fuselage and nacelles. Experimental tests allowed to check the goodness of the aircraft trim capabilities also in both most critical centre of gravity position and flap deflection (full flap deflection, landing conditions). These tests have therefore also helped to choose the final incidence for the horizontal stabilizer in order to ensure good equilibrium and trim capabilities. Lateral-directional tests allowed to check the vertical tail sizing in order to grant the minimum control speed. It is clear that Balance Field Length (BFL) (which depends on minimum control speed) is one of the most crucial aircraft performance to have good opportunities of commercial success.

Chapter 4 This chapter is dedicated to the numerical analysis performed with a Navier-Stokes solver software. CFD computations have been performed both at the wind tunnel and free flight conditions. The investigations at the wind tunnel conditions have been used to validate the CFD reliability into predicting aerodynamics characteristics of a complete and complex configurations(i.e. control surfaces, flap deflections and gaps). Numerical investigations at free flight conditions have provided reliable data at higher Reynolds number supplying the lack of experimental data arising from the scaling effect(the maximum available wind tunnel Reynolds was about $6e^5$ while the maximum free flight Reynolds number is about $9.5e^6$). The performed analyses have been also useful to have an accurate estimation of wing loads and stall path at both clean(flap up) and landing conditions. Wing span loads are a very useful and curial data for the sizing of the wing structure and for the planning of wing static loading tests. The numerical investigation have been also useful to perform an accurate drag breakdown(crucial to fulfil a more accurate flight performance estimation) and to highlight each aircraft contribution to the aerodynamic characteristics. Numerical investigation led also to a better understanding of how the contribution to the stability derivatives of each aircraft component changes with respect to the other components, being affected by several interferences factors.

Chapter 5 An estimation of most significant flight performance is illustrated, highlighting the improvements due to winglets and wing-fuselage fairing in terms of drag reductions.

Chapter 6 Finally in this chapter the main achievements of this research work are summarized, some conclusions are drown and area for further research activities are shown.

Chapter 2

Tecnam P2012 Traveller Design Guidelines and Preliminary Aerodynamic Analysis

2.1 Introduction

Costruzioni Aeronautiche Tecnam[1] is an aeronautics manufacturer founded in 1986, based near Naples in Italy. The company has two primary activities: it makes aircraft parts for other manufacturers, and makes its own range of light aircraft. For over 60 years Tecnam has been committed to serving the General Aviation community. Be it the 6th generation Tecnam P92, the best selling P2002 or the P2006T Twin, Tecnam are firmly established as the aeroplanes of choice with General Aviation customers and operators. Be they private pilots enjoying flying for leisure or some of the world's leading Flight Training Organisations. The recent introduction into service of the P2008 and development of the advanced technology, four-seater, single engined P Twenty Ten, ensures that Tecnam continue to offer the widest range of General Aviation aeroplanes. With over 3500 Tecnam aeroplanes operating around the world today, Tecnam customers and operators are supported by a global network of over 60 dealers and 100 Tecnam Service Centres. The Tecnam teams passion for flying has undoubtedly resulted in Chief Designer, Professor Luigi Pascale, creating some of the most innovative and stylish aeroplanes. More importantly Tecnam's wide range of aeroplane models afford its customers and operators superb value for money, from the low initial purchase price to unbeatable operating costs.

[1] Costruzioni Aeronautiche Tecnam official website.
http://www.tecnam.com

As discussed at section 1.1 the commuter aircraft market requires for a new nine-passenger commuter aircraft. This drives Tecnam to take on the design of a new twin-engine eleven seats aircraft. Really the Tecnam idea to develop such a new aircraft model token place from an "expression of interest" request from Cape Air[2]. Andrew Bonney, Cape Air's vice-president of planning said:"We are the largest commuter airline in the US with a fleet of 67 Cessna 402s and Piper Navajos, as well as two ATR 42s, given our ageing fleet, we feel there is an urgent requirement for a new nine-passenger commuter aircraft in this market - no [FAR Part 23 aircraft] has been produced for this sector for about 25 years. Cape Air issued a request for information to all the major airframes and Tecnam produced the best and most comprehensive response" . The two companies have collaborated on the aircraft's design, with Cape Air playing an advisory role[3]. The new Tecnam aircraft was launched at the Aero Friedrichshafen aviation show conducted in Germany in April 2011. The aircraft is being jointly developed with the funding from private capital and the Italian government.

2.2 Sizing and Configuration

The sizing of the P2012 has been accomplished through the use of classical methodologies and approaches, like these ones suggested by Roskam [12], Torenbeek [13], Perkins [14], McCormick [15], Raymer [16]. In the current section all results about the performed study and development of the configuration will be presented. The design of the aircraft has been accomplished starting from the following design requirements:

- Easy cabin access and cabin comfort;
- Spacious luggage compartment,
- Reduced take-off run (<900 ft) and take-off from not prepared runways;
- Cruise flight speed of about 200 kts at altitude of 10000 ft;
- Range higher than 600 nmi.

The easy cabin access and a better aircraft clearance have led to the necessity of high-wing configuration. Other considerations to be taken carefully

[2]Cape Air is an airline head quartered at Barnstable Municipal Airport in Barnstable, Massachusetts, United States. It operates scheduled passenger services in the Northeast, the Caribbean, Midwest, Eastern Montana and Micronesia.
Cape Air official website.
https://www.capeair.com

[3]"Through our extensive knowledge of the commuter airline market, we have been able to offer technical and marketing advice Tecnam which will help to boost Traveller's appeal to a wide audience", Andrew Bonney, Cape Air's vice-president of planning.
http://www.flightglobal.com/news/articles/aero11-tecnam-unveils-three-new-aircraft-355536/

into account are aircraft CG positions and certification problem arising from propeller longitudinal position. Both FAR 23 and CS23 [5] state that two lines at $\pm 5^{\circ}$ from propeller disk do not have to intersect pilot position or pilot flight command. This leads to the fact that the two propellers have to be located well behind or in front of pilot position. As additional design requirements the choice of a fixed landing gear has been adopted to reduce both maintenance and direct operative costs. The choice of high-wing configuration facilitates the installation of engine on the wing, since the engine (and propeller) clearance is higher (increased safety), compared with a low-wing configuration. This aspect is particularly critical if the aircraft should be able to operate from not prepared and grass runways. The low-wing configuration would clearly bring to very high and heavy landing gear structure to guarantee same level of safety and efficiency for the propeller. Also considerations of easy-access on board leads to a high-wing configuration as was done for P2006T, Ref. [17]. The problem of relatively short take-off run is also strictly linked to the minimum control speed which influences the accelerate-stop distance, known as critical problem for the twin-engine configuration. The application of restrictions on power loading and wing loading coming from take-off, landing and cruise performances defined in the design requirements and all necessary climb characteristics for CS23 [5] certifications rules leads to the graph represented in Fig.2.1, which shows the available area in which the design point (max. wing loading and engine power loading) for the aircraft can be chosen. The procedure to obtain take-off, landing, climb and cruise limitations is the classical Roskam approach usually adopted in aircraft preliminary design [12]. The P2012 power loading (about 10 lb/hp), that is similar to other aircraft (also presented in 1.4) leads to even higher cruise performances (about 210 kts) than those considered in the design requirements. In the calculation of design limitations concerning take-off run (1800 ft) and landing run (2000 ft), a maximum lift coefficient of about 1.9 (take-off) and 2.2 (landing) have been considered as reliable and achievable values with a single-slotted flap high-lift system, see Fig. 2.6 where the lift coefficient estimated through the ADAS software is shown at three flap deflections. For climb and cruise limitations, a parasite drag coefficient of about 300 drag counts (0.030) has been assumed also considering the fixed landing gear. An Oswald factor of about 0.83 (achievable through the use of winglets, see also [18]) has been considered. In Fig.2.3 the fuselage design and the cabin arrangements are presented. Easy cabin access and high level of cabin comfort leads to an internal design shown in Fig.2.3. Fig.2.4 presents some possible internal cabin arrangements which will enhance the commercial success of the aircraft through easy re-configuration for different possible applications. A spacious luggage compartment has been considered by Tecnam in the rear part of the cabin (see also Fig.2.3). From aerodynamic point of view, the P2012 fuselage has a streamlined shape both in the nose and in the rear zone. As shown in Fig.2.5 the fuselage fineness ratio l/h is about 7.5, very close to that one of major competitors. As shown in Torenbeek [13],

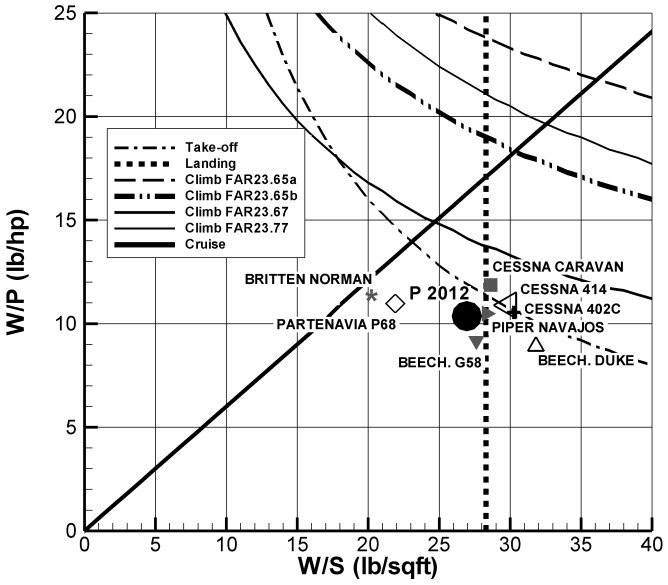

FIGURE 2.1: Power loading (W/P) and wing loading (W/S) of several commuter aircraft.

the choice of fuselage fineness ratio is critical in order to obtain low aircraft drag. From the analysis of the design point described in Fig.2.1, the aircraft is characterized by a wing area of about 25 square meters and a wing span of about 14 m. The wing area has been estimated considering a maximum take-off weight of about 3300 Kg. The maximum take-off weight has been estimated through statistical approach (class-II weight, weight of each aircraft component estimated based on statistical weight of each aircraft part) and the weight of some component has been also estimated through the analysis of 3-D CAD drawings. The P2012 preliminary weight estimation leads to an empty weight with respect to WTO (Max Take-Off Weight) ratio that lies exactly in the average value (about 0.60), see Fig.2.2. The preliminary design of the aircraft has been accomplished also considering the necessity to use all-aluminium alloy structure and fixed landing gear to achieve the goal of a low cost aircraft (in terms of production, operative and maintenance costs). The possibility to use piston engine will lead also to low flight costs and easy and cheap maintenance. The concept of commonality of a family of aircraft could also lead in the future to different versions from 10 up to 19 passengers.

2.2.1 Tailplanes design and sizing

Tailplane design has been performed to accomplish with stability and flight quality characteristics. All required data and assumption for the horizontal

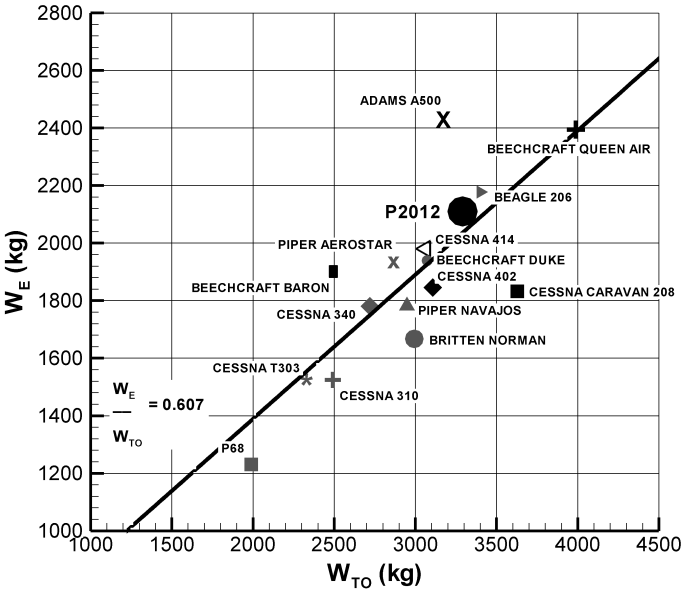

FIGURE 2.2: Empty weight (WE) vs maximum takeoff weight (WTO) of several commuter aircrafts.

and vertical tail planes design are summarized in Tab 2.1 and 2.3 respectively.

TABLE 2.1: Data and assumption for the horizontal tail plane preliminary design.

	Value
AR_h	5.32
$\Lambda_{c/4}$	12.5°
λ_h	0.66
η_h	0.9
c_e/c_h	0.3
i_{t_0}	-2°
$x_{cg}/\bar{c}$	0.25
$z_{cg}/\bar{c}$	0.25
Landing equilibrium	V=VSL; δ_e=-25°
Take-Off equilibrium	VR=0.9 VSTO;δ_e=-25°

For the general aviation aircraft and in particular for commuter aircraft, the right positioning of the horizontal tail is one of the most relevant design goals. The horizontal tailplane position can have a relevant influence on aircraft stability and control and can also involve aircraft ground operation in taxing. Considering also the case of body-mounted tail, the horizontal tailplane

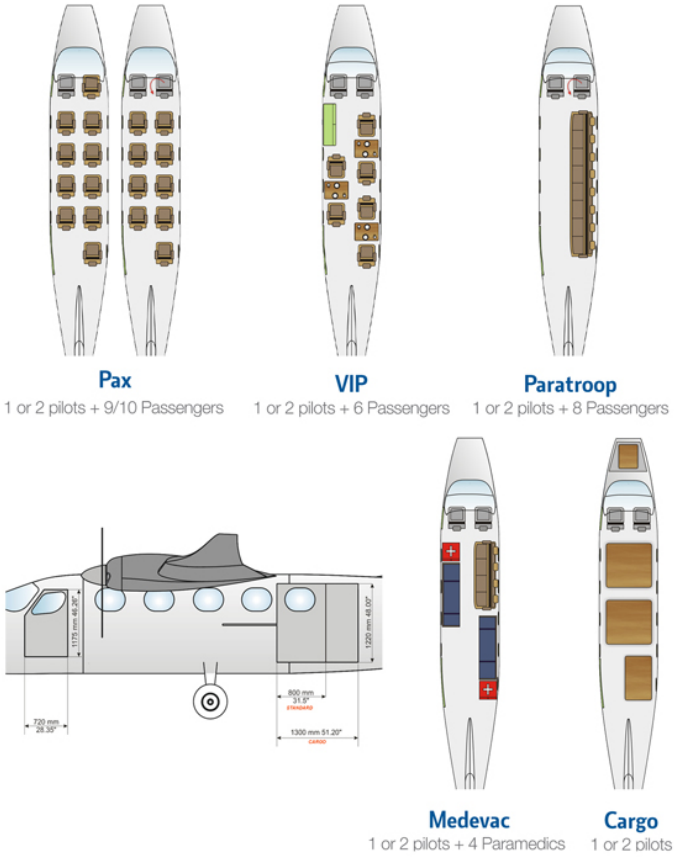

FIGURE 2.3: Cabin arrangement and internal design (courtesy of Tecnam).

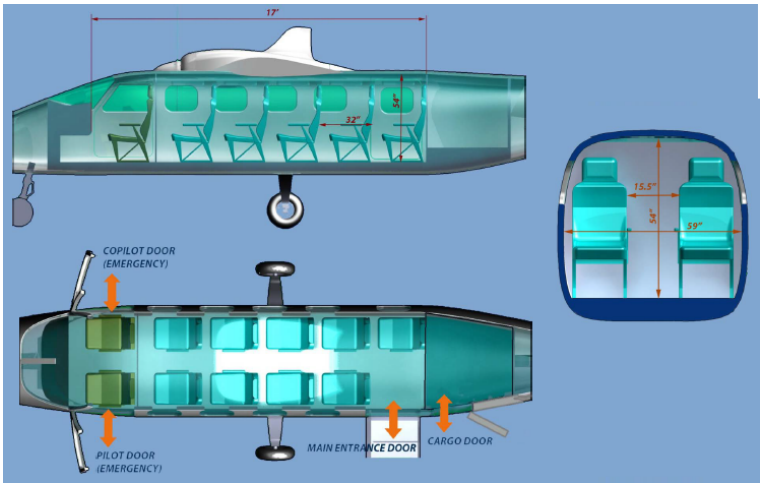

FIGURE 2.4: P2012 Cabin arrangement for all possible versions (courtesy of Tecnam).

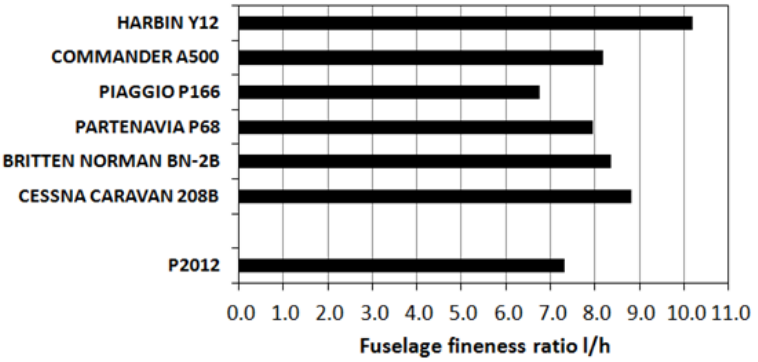

FIGURE 2.5: Fuselage fineness ratio comparison (source: Jane's [2]).

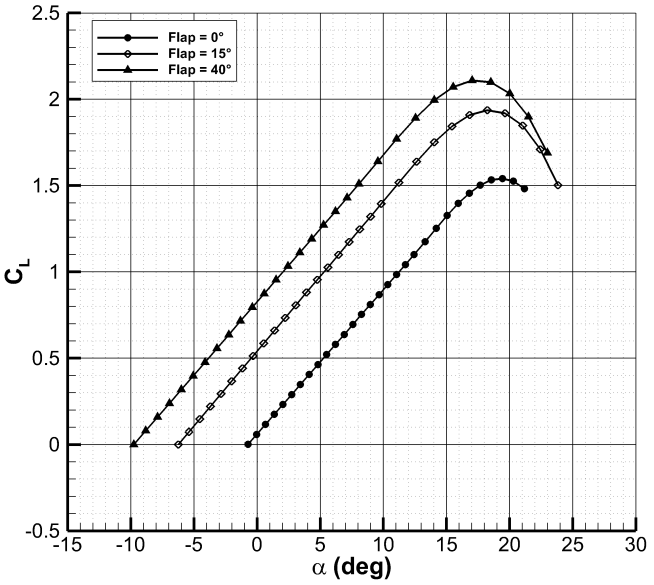

FIGURE 2.6: ADAS estimation of Wing-Body lift coefficient at three flap deflections.

position could also lead to fuselage tailcone shape that are not optimized in terms of drag (high upsweep angles) or that involves low possible rotation angles, especially if a stretched version of the cabin should be implemented. Usually, from the aerodynamic point of view, the horizontal tail vertical position can lead to problems or different stability characteristics in relation to its distance from wing wake. It is well known and it is usually considered in preliminary design, that the wing downwash at tail is dependent on the vertical distance from the wing wake, Ref. [3]. If the horizontal tailplane is invested by the wing wake at some particular angles of attack, this turns to be a possible

dangerous condition, leading to possible stick buffeting and structural fatigue for the horizontal tailplane structure. Usually some semi-empirical method like those of Ref. [3] can be also used to check the chosen position and to avoid these phenomena. Therefore one of the goals of the preliminary sizing has been the identification of the best vertical positioning for the horizontal tail plane, in order to guarantee the minimum interference of the wing wake on the horizontal tail plane, leading to the best longitudinal stability and avoiding both buffeting problems due to the wing wake interaction with the horizontal tail plane and reduction of the longitudinal stability due to the loss in the dynamic pressure on the horizontal tail plane. A preliminary investigation about the wake displacement and downwash angle has been carried out through the application of the methodology developed in the NACA report No. 648, Ref. [3], Fig. 2.7 shows the preliminary estimated wing wake displacement at three flap conditions, highlighting the considerations discussed above. Higher positions of the horizontal plane, which would provide that it is mounted in the vertical plane, in cruciform T-tail configuration, have not been investigated, since they constitute configurations with higher complexity and require heavier structure with consequent increase in aircraft structural weight. Instead lower positions have not been tested in order to not reduce the upsweep angle required for take-off and landing performance. The design of the tail planes

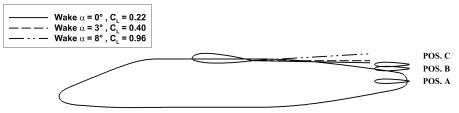

(a) Wing wake displacement in flap up condition.

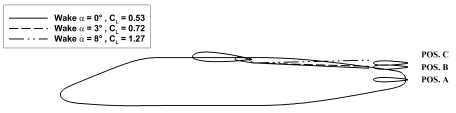

(b) Wing wake displacement in take-off flap condition.

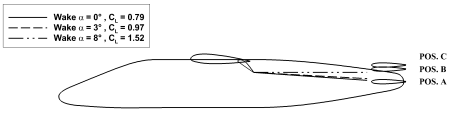

(c) Wing wake displacement in landing flap condition.

FIGURE 2.7: Preliminary estimation of the wing wake displacement through methodology of Ref. [3].

has been carried out using "ADAS" software [19], which is a software for aircraft preliminary design developed at the DII, the software implements all the classical methodologies and approaches like those suggested by Roskam [12], Torenbeek [13], Perkins [14], McCormick [15] . The horizontal tail plane is body mounted almost in the centre of the fuselage tail-cone. The chosen horizontal tail vertical position (slightly lower respect to the wing) leads to a possible choice of a symmetrical fuselage tail-cone, characterized by reduced drag. In order to perform the right sizing of the horizontal tail surface the equilibrium in landing condition, with maximum forward position of the centre

of gravity, the take-off rotation equation (including the thrust effects during the take-off phase) and the minimum static margin in stick-free condition has been considered. An incidence of -2° for the horizontal stabilizer respect to fuselage reference line has been assumed. The above mentioned conditions lead to the limitations depicted in Fig.2.8, where it can be seen how the choice of a ratio S_h/S_W of about 0.24 (the thick solid line) guarantees aircraft stability and control in the $x_{cg}/\bar{c}$ range that goes from 0.15 up to 0.4.

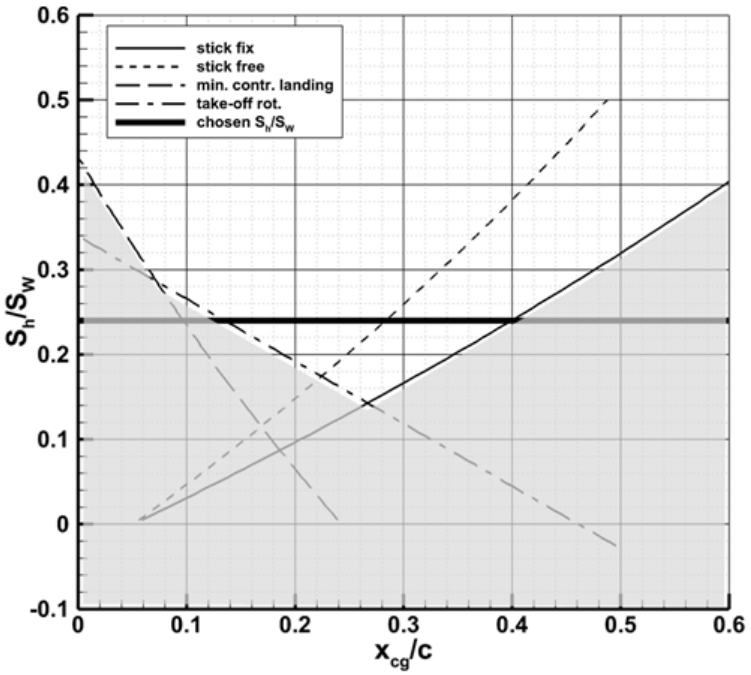

FIGURE 2.8: P2012 Traveller, $x_{cg}/\bar{c}$ range evaluation.

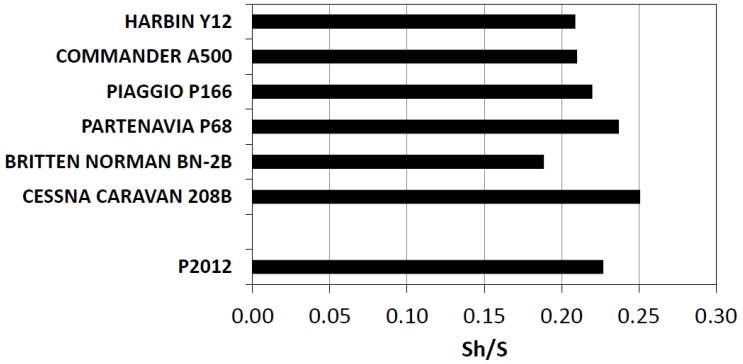

FIGURE 2.9: Horizontal tail surface ratio comparison (source: Jane's [2]).

This horizontal tail size ratio is close to the respective value for aircraft of the same category (see Fig.2.9). The elevator control surface is full-span

extended and could also have a horn balance, thus a sensible reduction of the aircraft trim range occurs at free stick condition as shown in Fig. 2.8. However the stick-free condition could also be avoided on this aircraft category by introducing assisted controls or tab surface as secondary control. A deep and complete semi-empirical aerodynamic analysis for aircraft longitudinal aerodynamics has been performed through ADAS software [19], Fig. 2.10 illustrate the aircraft three views framework panel. The software estimates the contribution of each aircraft component. Concerning the horizontal stabilizer contribution to longitudinal stability and control, the software carefully takes into account the detailed estimation of wing downwash and dynamic pressure ratio at tail (which depends on horizontal stabilizer distance from wing wake). The software take also into consideration non-linear conditions, considering wing and tail lift and moment coefficient in non-linear range up to lifting surface aerodynamic stall. Fig. 2.11 shows the estimated contributions of each aircraft component to the pitching moment coefficient in cruise condition with a horizontal tail incidence angle of -2° (here thrust effects have been neglected). Fuselage instability has been estimated through a classical approach (Multhopp solution of Munk strip theory), as also reported in Roskam [12]. The chosen centre of gravity lies 25% of mean aerodynamic chord as longitudinal position and $0.25\bar{c}$ below the wing plane (which represents a reasonable aircraft centre of gravity vertical position) thus it also possible to appreciate the wing pendular stability, as it is shown by the wing contribution to the pitching moment coefficient (the dash dotted line). In order to check the aircraft trim capabilities, several elevator deflections have been considered and the aerodynamic moment coefficient has been computed for both cruise and landing flight condition for two horizontal tailplane incidence angles of 0° and -2° respectively. Fig.2.12 and Fig.2.13 show the complete aircraft pitching moment coefficient versus lift coefficient at several elevator deflections and for the above-mentioned stabilizer incidence angles in cruise and landing conditions (with the $x_{cg}/\bar{c}$ at the maximum forward position of 0.18). As it can be seen from Fig. 2.13, in landing condition (full flap deflection of about 40 degrees) and at low angles of attack, the chosen vertical position of the horizontal stabilizer can lead to a sensible reduction in the longitudinal stability(the estimated dynamic pressure ratio for the horizontal tailplane results in very low values being the stabilizer invested by the wing wake). However these flight conditions are not typical flight conditions for an aircraft (lower C_L, negative angle of attack at landing flap settings). Tab.2.2 summarizes some output data coming from the preliminary horizontal tail design such as the tail surface and span, the elevator effectiveness and the downwash.

The designed horizontal tailplane from the preliminary design phase is characterized by a surface area of about 6 square meters and a span of about 5.7 meters and an incidence angle of about -2°, and it is provided with a full-span elevator with a chord ratio of about 0.3 (c_e/c_h =0.3).

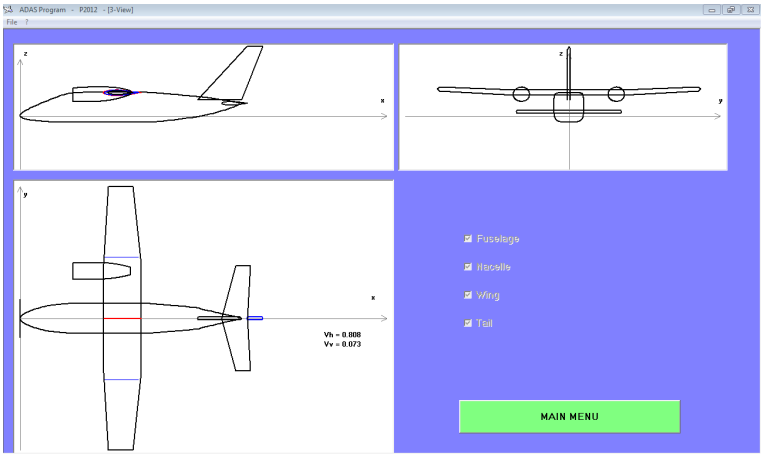

FIGURE 2.10: ADAS software framework, three view of the P2012 Traveller.

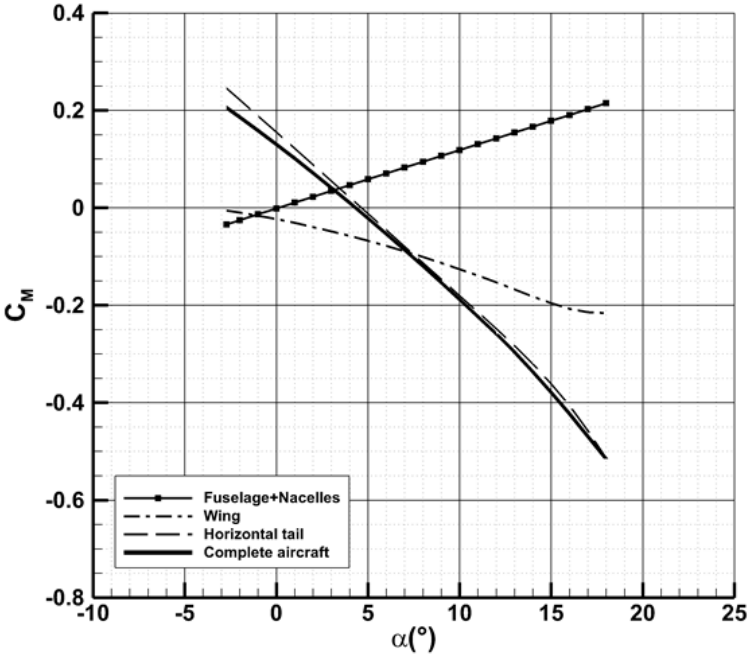

FIGURE 2.11: Semi-emipircal estimation of the pitching moment coefficient versus angle of attack ($x_{cg}/\bar{c}$=0.25, $z_{cg}/\bar{c}$=0.25).

TABLE 2.2: Horizontal tail and elevator output data.

	Value
S_h	6.08 m^2
b_h	5.7 m
τ_e	0.596
$\tau_e, \delta_{e_{max}}$	0.360
$d\epsilon/d\alpha$	0.347

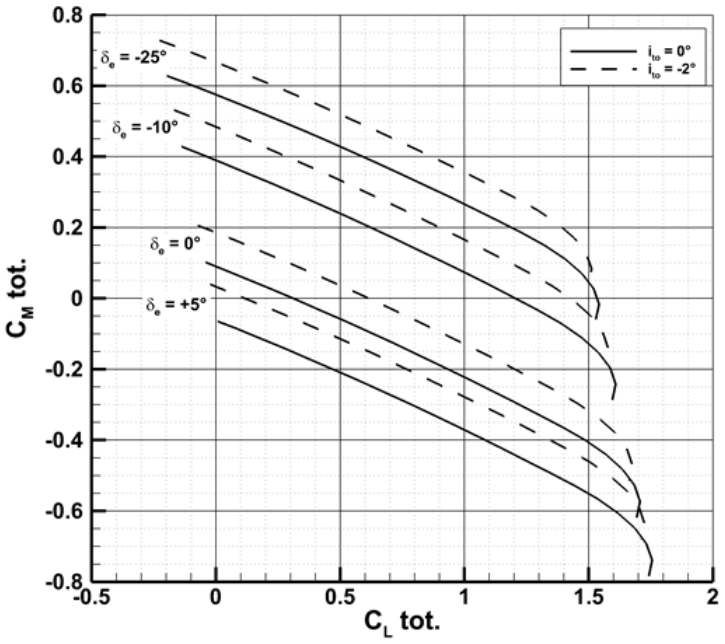

FIGURE 2.12: Semi-empirical trim analysis in cruise condition, $\delta_F = 0°$, maximum forward centre of gravity position ($x_{cg}/\bar{c}$=0.18, $z_{cg}/\bar{c}$=0.25).

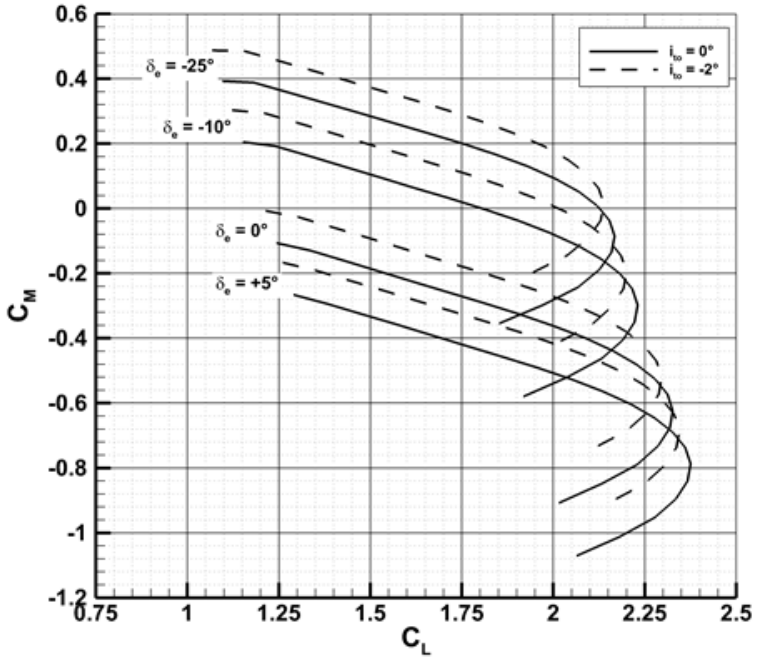

FIGURE 2.13: Semi-empirical trim analysis in landing condition, $\delta_F = 40°$, maximum forward centre of gravity position ($x_{cg}/\bar{c}$=0.18, $z_{cg}/\bar{c}$=0.25).

Particular attention has been posed to the vertical tail design which is crucial to achieve commercial success this aircraft category. As a matter of fact the minimum control speed, which strongly depends on the vertical tail sizing, has to be limited in order to reduce the accelerate stop distance (which depends on the engine failure speed VEF). Indeed the regulations [5] prescribe that the engine failure velocity VEF must be selected non less of 1.05VMC (which is the minimum control speed). Geometrical data and assumption made in order to perform the preliminary design of the vertical tail are summarized in Tab. 2.3 The vertical tail design has been carried out to grant the equilibrium during take-off in one engine inoperative condition (OEI), and also in order to accomplish with a good control efficiency of the rudder in presence of lateral gust (a well-designed vertical tail and rudder should assure that the ratio between the required rudder δ_{req} and sideslip angle β in steady sideslip should be slightly lower than 1 in the linear range to guarantee the possibility to equilibrate the aircraft up to 15-20 degrees of sideslip angle.). Fig. 2.14 shows the parametric investigation about the required vertical tail area to ensure the equilibrium in take-off phase with one engine inoperative, solid line represents the yawing moment due to the thrust of the remaining engine, while dashed lines show the yawing moment produced by the vertical tail with the maximum rudder deflection at zero sideslip angle, nonlinearities of the rudder effectiveness have been also considered. Once the vertical tail design has been carried out, a preliminary estimation of the aircraft components contribution to the lateral-directional stability has been performed, as it is shown in Fig. 2.15, where the solid line is the complete aircraft yawing moment coefficient. Fig. 2.16 shows instead the variation of the required rudder deflection to equilibrate the aircraft in sideslip conditions. As it can be noticed from the graph, the ratio between the required rudder and sideslip angle in the linear range (small β) is $\delta_{r,eq}/\beta \approx 0.70\text{-}0.75$.

In Fig. 2.17 main vertical tailplane geometric parameters are shown compared to similar aircraft with same configuration (high wing, horizontal tail body mounted). The final 3-view of the aircraft after the preliminary design process is shown in Fig. 2.18.

TABLE 2.3: Data and assumption for the vertical tail plane preliminary design.

	Value
AR_v	1.80
$\Lambda_{c/4}$	30.0°
λ_v	0.35
η_v	0.9
b_r/b_v	0.95
c_r/c_v(average value)	0.38
z_h/max. fus. height	0.643
x_{ac_v}/fus. length	86.0
z_{ac_v}/fus. length	0.75
$x_{cg}/\bar{c}$	0.25
$z_{cg}/\bar{c}$	0.25
V/VSTO	1.16
$\delta_{r_{max}}$	30°
l_T	2.23 m
Engine	Lycoming TEO540-A1A (350hp)
Propeller	Hartzell or MT 3 blades constant speed(2x)

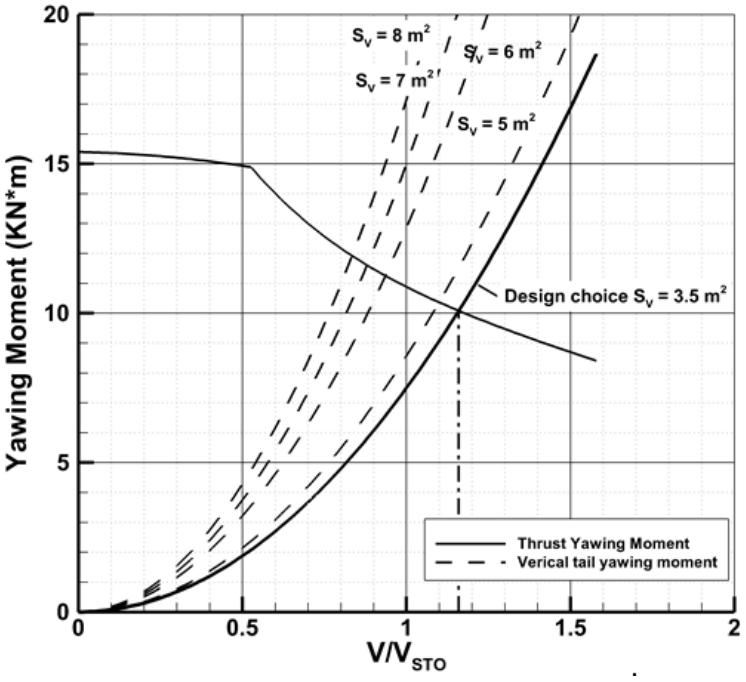

FIGURE 2.14: Design of the vertical tail surface.

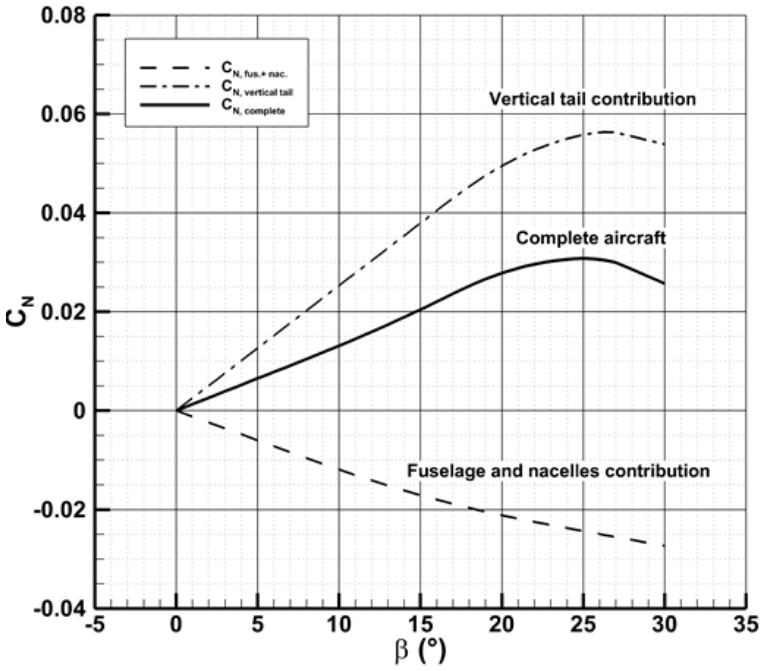

FIGURE 2.15: Semi-empirical yawing moment breakdown estimation.

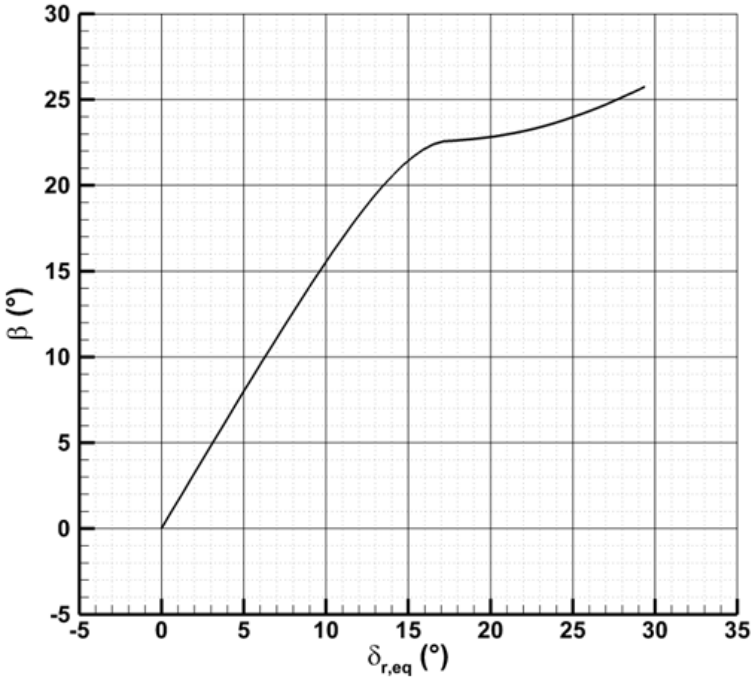

FIGURE 2.16: Required rudder deflection to grant the equilibrium in yaw with respect to the sideslip angle.

TABLE 2.4: Vertical tail and complete aircraft characteristics.

	Value
S_v	3.52 m^2
b_v	5.80 m
a_v	0.048 deg^{-1}
τ_r	0.387
$C_{N_{\delta_r}}$	0.0021 deg^{-1}
$C_{N_{\beta_{fus.}}}$	-0.0012 deg^{-1}
$C_{N_{\beta_{nac.}}}$	-0.0002 deg^{-1}
$C_{N_{\beta_{vert.}}}$	0.0025 deg^{-1}
$C_{N_{\beta_{tot.}}}$	0.0013 deg^{-1}
VMC	73 kts (37.6 m/s)

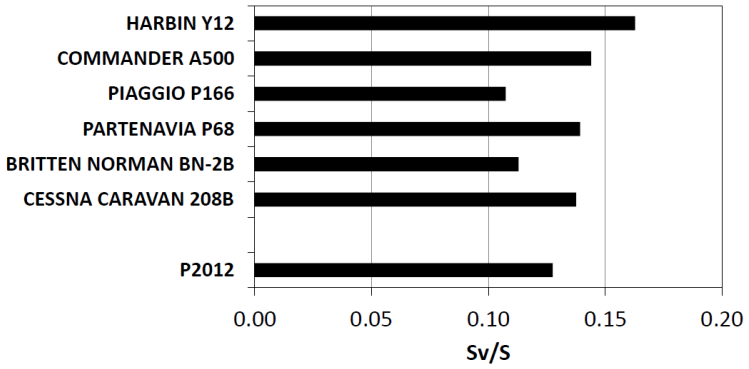

FIGURE 2.17: Vertical tail surface ratio comparison (source: Jane's [2]).

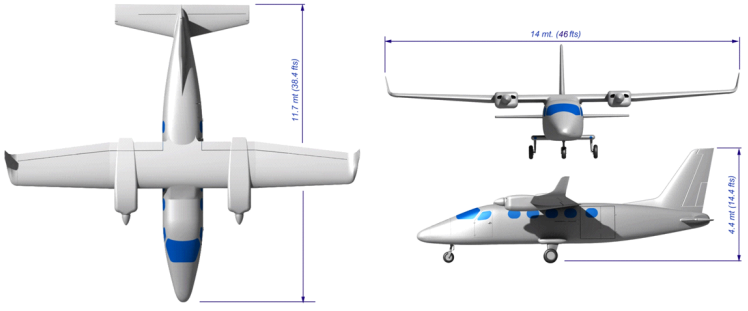

FIGURE 2.18: P2012 Traveller three-views and wing sizes (courtesy of Tecnam).

2.3 Preliminary Drag Polar Estimation

Once the ultimate aircraft configuration has been determined, in order to obtain a detailed data for aircraft design and preliminary flight performance estimation, an accurate and detailed aircraft drag polar calculation has been fulfilled. The aircraft zero lift drag coefficient has been calculated through the application of the methodologies proposed by Roskam [12, 20] and Raymer [16]. According to the used approaches the total drag coefficient of the aircraft can be assumed as the sum of the zero lift drag and induced drag coefficient. This assumption can be made when the approximation of a parabolic drag polar is considered, when the drag coefficient for lower incidence(i.e. cruise or climb condition) want to be estimated. The assumption of a parabolic drag polar is reliable until the lift coefficient becomes greater than 1. Tab. 2.5 summarizes the main characteristics and condition assumed to perform the estimation of the preliminary drag polar for this aircraft. The parabolic drag coefficient has been assumed as shown in Eq. 2.1 where AR is the wing aspect ratio and e is the induced drag factor of the complete aircraft. According to procedures of Ref. [12, 16, 20] the total zero lift drag coefficient is equal to 0.0306[4]. Fig. 2.19 and Fig. 2.20 show the drag breakdown of the aircraft zero lift drag coefficient. The main drag sources deal with the skin friction coefficient of the Wing, Fuselage, Nacelles and Tail planes), that can be estimated to be about 60%. The remaining 40% is due to drag sources difficult to evaluate, such as Wing-Fuselage interferences, Wing-Nacelle interference, wind-shield geometry, excrescences, engine cooling and gaps. Tab. 2.6 shows the zero lift drag coefficient of each aircraft component and of the main drag sources.

$$C_D = C_{D_0} + \frac{C_L^2}{\pi ARe} \tag{2.1}$$

Fig. 2.21 shows the drag polar estimated as illustrated in Eq. 2.1. The cruise condition is in a C_L range of 0.35-0.45 and the climb condition is the range of 0.8-1.0. As it is clearly shown in Fig. 2.21 in cruise condition the drag coefficient C_D is about 30% higher than the zero lift drag coefficient, whereas in climb condition it is almost twice as much the C_{D_0}. As it is well known the level flight performance(i.e. the maximum speed or fuel consumption) directly depend on the zero lift drag coefficient. Climb and ceiling performance are mainly influenced by the induced drag coefficient and they could be directly improved acting on this drag contribution. A solution to reduce the induced drag coefficient is the introduction of wing tip device such as the winglets.

[4]Assumption made to perform this estimation are: Mach number M=0.25, Reynolds number=$9.5e^6$, transition of the flow has not been fixed, thus the skin friction coefficient has been estimated both for laminar and turbulent flow according with the cut-off Reynolds number of each aircraft component. Wing, fuselage and tail surfaces are in treated metal alloy. Wind-shield is with flat with protruding and gaps are in flaps, ailerons, elevator and rudder.

TABLE 2.5: P2012 main characteristics and conditions.

Wing	
S_W	25.4 m^2
b_W	14.0 m
AR_W	7.72
Airfoil	NACA 23016
Horizontal tail	
S_h	6.08 m^2
b_h	5.70 m
AR_h	5.34
Airfoil	NACA 0012
Vertical tail	
S_v	3.52 m^2
b_v	2.56 m
AR_v	1.8 m
Fuselage	
S_f	14.8 m^2
l_f	11.7 m
w_f	1.6 m
Condition	
Reynolds number	9.5e^6
Mach number	0.2

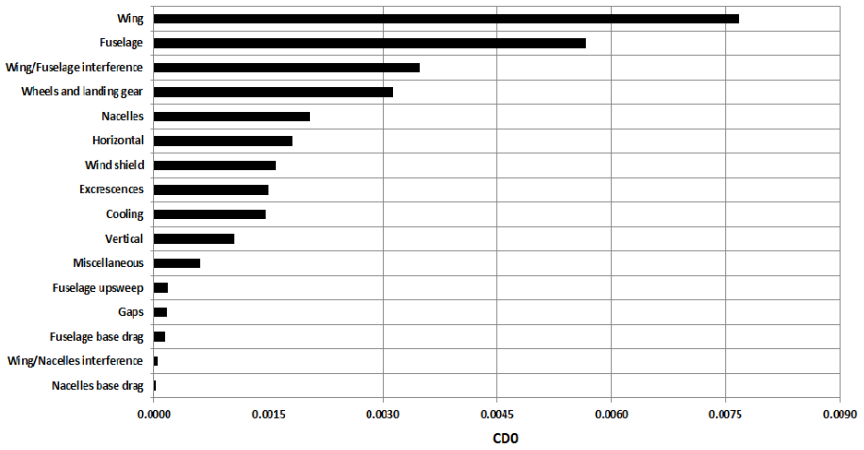

FIGURE 2.19: Preliminary drag breakdown estimation.

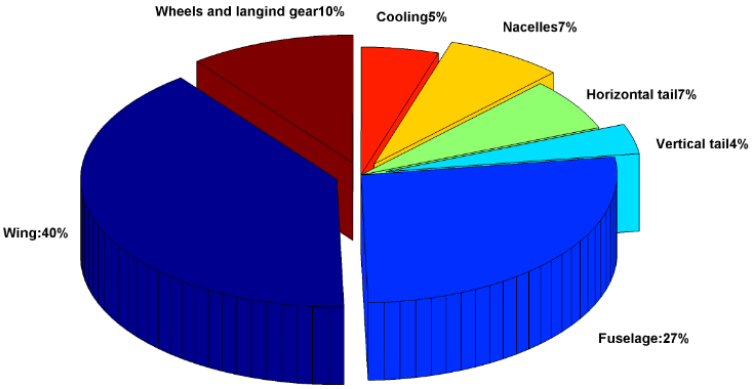

FIGURE 2.20: Preliminary drag contribution

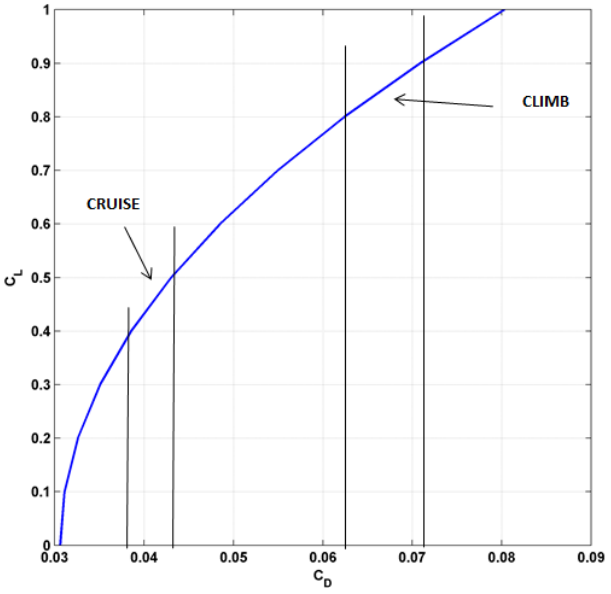

FIGURE 2.21: P2012 drag polar

TABLE 2.6: P2012 main characteristics and conditions.

Drag Source	C_{D_0}
Wing	0.00768
Fuselage	0.00567
Wing	0.00768
Wing-Fuselage interference	0.00348
Wheels and landing gear	0.00313
Nacelles	0.00204
Horizontal tail	0.00181
Wind shield	0.00160
Excrescences	0.00149
Cooling	0.00146
Vertical	0.00104
Miscellaneous	0.00060
Fuselage upsweep	0.00018
Gaps	0.00016
Fuselage base drag	0.00013
Wing-Nacelles interference	0.00005
Nacelles base drag	0.00002
Total	0.0306

2.4 Winglet design

Before introducing the design of the winglet for the P2012 Traveller, a brief description of the basic principles dealing with the aerodynamic of the winglet seems to be necessary to a better understanding. A wing moving in an airflow produces a lift force thanks the difference in the pressure between the lower and upper wet surfaces. In particular the wing upper surface is characterised by low pressure airflow while the wing lower surface is characterised by a high pressure flow field. Because of the wing finiteness an inward spanwise flow is generated on the wing upper surface and an outward on the lower surface. At the wing tip these two flows, having different directions, generate a vorticity. This is the origin of the induced drag (see Fig. 2.22). The aerodynamic load introduced by a winglet, or a simple tip end-plate, produces a flow field that interacts with the main wing flow reducing the span-wise flow [21]. The winglet spreads out the effect of the tip vortex (see Fig. 2.23) reducing the induced drag. The effect of the winglet can be also figured as a vertical diffusion of the vorticity at the wing tip. By introducing a winglet the efficiency of a wing can be grater than that of an elliptical loading (considering the same span), emulating the effect of a span increase [22].

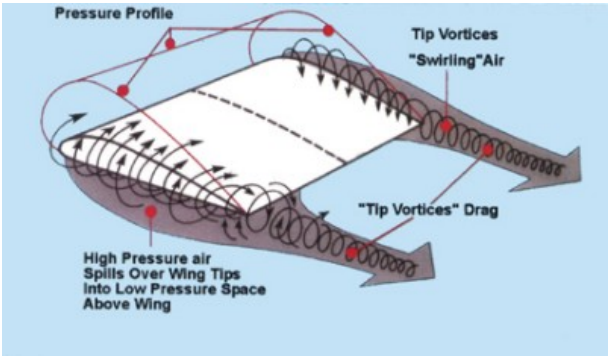

FIGURE 2.22: Vorticity du to finite wing

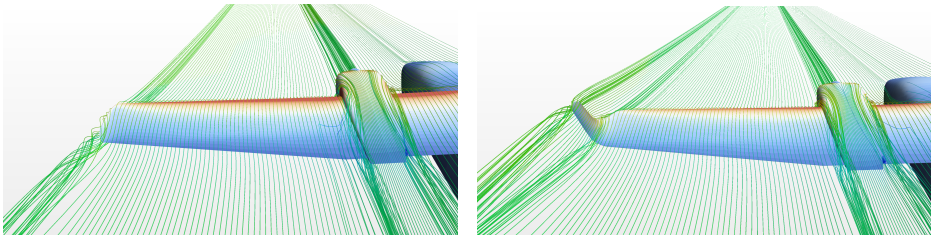

(a) Tip vortices on a finite wing.

(b) Tip vortex on a finite wing with winglet.

FIGURE 2.23: Effect of winglet on the tip vortices

It has been known for over a century that an end-plate at the tip of a finite wing can improve the induced drag. The first concept of a wing-tip device dates back to 1897 thanks to the English engineer Frederick W. Lanchester used wing end-plates as a method for controlling wingtip vortices [23]. Several years after, Vincent Burnelli, an American engineer, received an US patent for his *End Plating Wing Tips* [24] in 1930. The effect of the end plate at wing tip, especially in terms of wing lift distribution wer also investigated at NACA [25]. A great contribution in understanding the physical phenomena dealing with aerodynamic characteristics of wing tips was due to Sighard Hoerner [26]. During the seventies Whitcomb *et alii* [27–29] designed winglet for modern transport aircraft, highlighting the effects of the winglet on the aerodynamic forces and moments, especially the reduction of the drag coefficient at lifting conditions. Fletchner and Whitcomb indicated [28, 29] that the basic effect of the winglet is a vertical diffusion of the tip vortex flow just downstream of the tip, which leads to drag reduction. Following the remarkable successes reached by Whitcomb *et alii*, the study and implementation of end-tip devices had a wide distribution on several aircraft categories. Nowadays all transport aircrafts include wing tip devices, prevalently made of composite materials. These tip appendages (blended winglet, tip fences, raked wingtip and sharklet winglet) must achieve the goal of reducing induced drag. However, the requirements to be met by wingtip devices throughout the various flight conditions are different. As outlined in [30], it must be a compromise of these various conflicting requirements, resulting in less than optimal effectiveness in each flight condition (e.g. little or great additional surface for, respectively, low cruise parasite drag and high climb/descent performance). In general aviation, research on wing-tip devices was carried out for sailplanes, even though their wings have a large aspect ratio. Smith and Komerath [31] mention the development work of winglets for sailplanes, with wind tunnel testing of scale models. Another important application is the use in agricultural airplanes, as the wing-tip vortex is an important factor in the dispersion of pulverized fluid. In this field an important work is that of Coimbra [32], which compares several wingtip devices and analyses the effects on pulverization. Design, numerical analyses and tests of winglets have been conducted also at the Department of Industrial Engineering of the University of Naples Federico II [33, 34]. Winglet were design and tested in flight [35, 36] for the twin-engine four seater Tecnam P2006T aircraft. In this experience, calculations performed in the design and optimization of the winglet shown an increment of induced drag factor due to the winglet of about 0.09. In addition, wind-tunnel tests measured increment of the induced drag factor of 0.08 was noticed [34]. Finally flight tests gave an increment of the Oswald factor of about 0.09 [36] with a huge increment of climb performance and without any penalty of the cruise performance. Applications of winglet in turboprop and commuter aircraft is today a crucial item to reduce drag and improve performance [37].

2.4.1 P2012 winglet design

The design of a winglet must takes into account lots of variables. Fig. 2.24 illustrates the geometrical parameters for the design of a winglet. The primary parameters involved into design process are the winglet height, the toe angle, the cant angle and the winglet aspect ration and sweep angle (see 2.24). These parameters must be carefully managed because the design of a winglet it is also complicated by the operational profile of an aircraft. The mission profile of an aircraft involves several flight conditions combining low-speed and high lift conditions (e.g. the climb phase) with high-speed and low lift condition(e.g. the cruise phase) [38]. Thus the design of winglet should be the best compromise among maximizing the low speed improvement and affecting high speed performance (the introduction of a winglet leads to the increase of the wetted area affecting the zero lift drag coefficient of the aircraft).

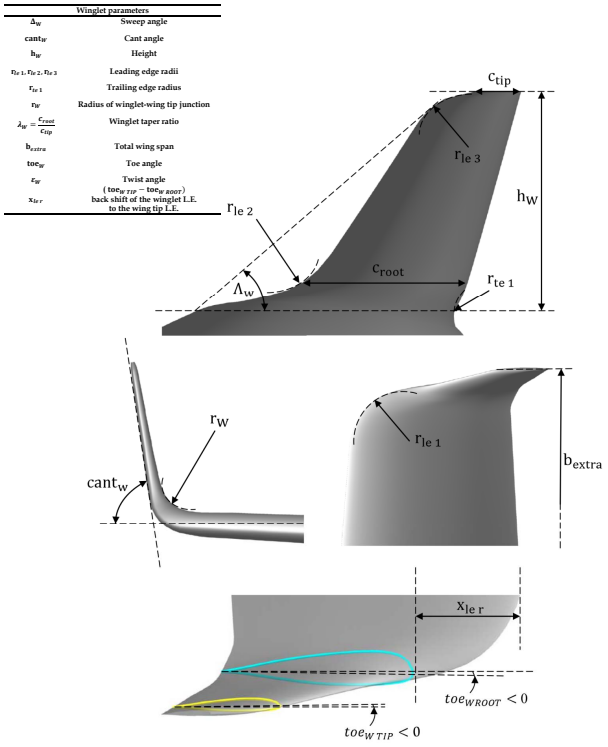

FIGURE 2.24: Winglet design parameters

The design and analyses of a winglet is structured in the following workflow:

1. Definition of the reference wing for which the winglet design is being performed;

2. Aerodynamic analysis of the reference wing execrating all the required parameters and coefficient (i.e. the induced drag factor, the wing span

load and lift span-wise distribution). These parameters will be the reference term for the design of the winglet;

3. Definition of the winglet parameters (the airfoil to be used, height, toe, sweep and cant angles, leading edge and trailing edge radii, etc.);

4. Generate several wing-winglet designs by varying the winglet geometry in order to perform a parametric investigation;

5. Compare results of the reference wing with the wing-winglet configurations and choose the best compromise among several considerations.

Dealing with the definition of the reference wing, the main data of the P2012 Traveller wing are summarized in Tab. 2.7 and the wing geometry is shown in 2.25. The wing aerodynamic analysis has been performed through a fast and reliable panel code solver available at the DII. This panel code solver has been widely tested and used Ref. [39–41]. The software allows the calculation of the nonlinear aerodynamic characteristics of arbitrary configurations in subsonic condition. The potential flow is analysed with a subsonic panel method; the program is based is based on the linearised equation of steady, compressible flow theory (Prandtl-Glauert equation), third Green's identity and indirect Dirichlet boundary conditions: zero perturbation potential is specified on the internal side of the body surface (outside the flow field). Linear source and quadratic potential (doublet) distribution on flat panels are applied. Nonlinear effects of wake shape are treated in an iterative wake relaxation procedure; the effects of viscosity are treated in an iterative loop coupling potential flow and integral boundary layer calculations. The compressibility effects are treated applying the Prandtl-Glauert rule.

Table 2.7: P2012 reference wing geometry.

Wing main geometrical characteristics	
c_{root}	2.0 m
c_{tip}	1.45 m
S_W	25.0 m^2
b_W	13.6 m
AR_W	7.4
root airfoil	NACA 23016
tip airfoil	NACA 23012

The reference wing has been appropriately meshed with about 2000 on-body panels and about 300 wake panels as shown in Fig. 2.26(a). Two different condition have been tested, a typical cruise and climb condition (see Tab. 2.8). Fig. 2.26(b) shows an example of the pressure coefficient contour on the reference wing at cruise condition.

In order to estimate the wing induced drag coefficient a parabolic drag polar formulation can be assumed, as shown in Eq. 2.2. The second term of

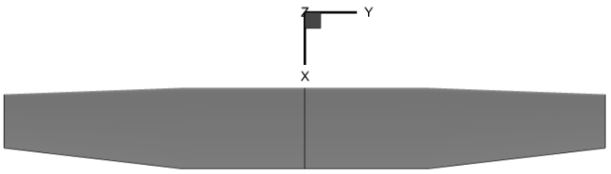

FIGURE 2.25: Reference wing geometry

TABLE 2.8: P2012 tested flight condition for winglet design.

	M	Re
Cruise condition	0.25	$9.5e^6$
Climb condition	0.11	$4.5e^6$

Eq. 2.2 is the induced drag coefficient ($C_{D_i} = kC_L^2$). Through the numerical analysis it is possible to calculate the value of k, which contains the induced drag factor as illustrated in Eq. 2.3.

$$C_D = C_{D_0} + kC_L^2 \tag{2.2}$$

$$e_w = \frac{1}{\pi A R_w k} \tag{2.3}$$

The constant k is the lift curve slope shown in Fig. 2.27, that show the variation of the square value of the lift coefficient with respect to the induced drag. The value of the induced drag coefficient for the reference wing is equal to 0.979 for cruise and 0.977 for climb condition. These values will be the reference values for evaluating the winglet effect on the induced drag factor. The analyses have been performed on the isolated wing without taking into account both fuselage and nacelles effects.

Fig. 2.28(a) and 2.28(b) show the lift distribution and wing span loading distributions at climb condition, respectively. Once the wing reference analysis has been terminated, the winglet geometry can be defined. A MATLab®code, developed at DII, allows to design and analyse several winglet geometries through the above mentioned panel code. Different winglet geometries have been analysed in order to improve the wing induce drag coefficient. The winglet design parameters useful to generate the winglet shape within the MATLab code are those illustrated in 2.24. Many of these parameters are dictated by experience and they are fixed at the very first step of the winglet design. The winglet shape design here is carried out evaluating the wing induced drag factor for several winglet geometries defined as the combination of the following parameters:

- *toe* (deg), toe angle;
- h_w (m), winglet height;

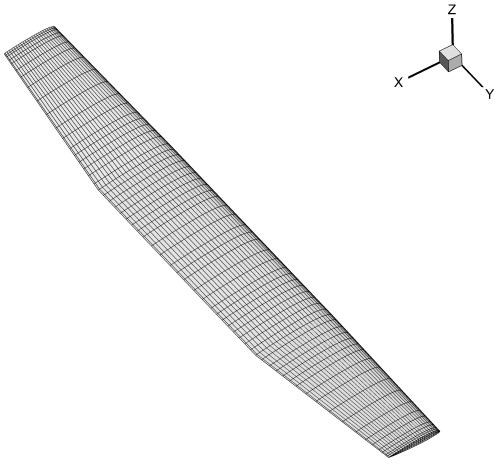

(a) Reference wing mesh.

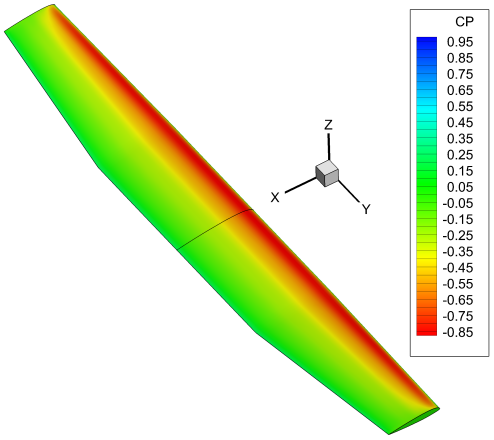

(b) Pressure coefficient contour on the reference wing.

FIGURE 2.26: Pressure coefficient contour

- δ_w (deg), winglet sweep angle;
- $cant_w$ (deg), winglet cant angle.

.

These can be assumed to be the main design parameters because they are directly involved into aerodynamic and structural items of the wing and flight performance. Due to structural reasons the winglet height should not exceed the 10% of the wing span. The variation of the δ_w is linked to the

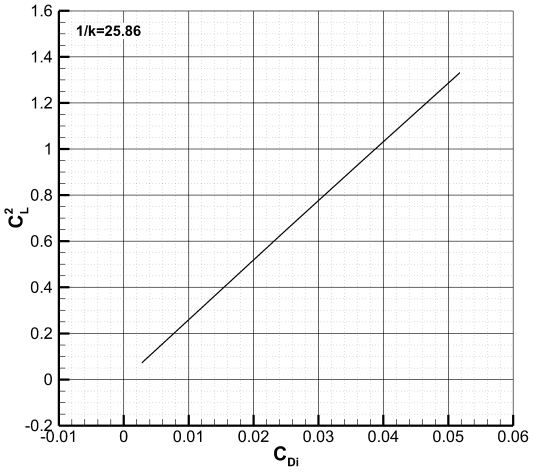

FIGURE 2.27: Reference wing, square lift coefficient variation with respect to induced drag, Climb condition

wing sweep angle in order to preserve the continuity and balancing of the wing shape. The cant angle $cant_w$ should be chosen in order to not add an excessive increase in the wing span. Finally a winglet developed airfoil (PSU[5]) has been chosen, see Ref. [42]. Tab. 2.9 are summarized the starting winglet reference parameters, whereas Tab. 2.10 shows the range of variation of these parameters in order to perform a parametric investigation among them and to reach the best winglet design. To supply the best winglet geometry many

TABLE 2.9: Winglet reference parameters.

Winglet reference parameters.	
Δ_w (deg.)	55
cant_w (deg.)	80
h_w (m)	0.7
$r_{le,1}$ $r_{le,2}$ $r_{le,3}$(m)	0.3, 0.45, 0.2
$r_{te,1}$ (m)	0.1
r_W (m)	0.2
λ_W	0.25
$b_{extra}/2$ (m)	7.245
toe (deg.)	-8.5
ϵ_W (deg.)	3

aspects must be considered. First of all the introduction of a winglet produces

[5]PSU airfoil is a winglet developed airfoil of the Pennsylvania State University. This airfoil is thin and highly cambered allowing good performance at higher angles and higher lower critical Mach number thus avoiding compressibility problems.

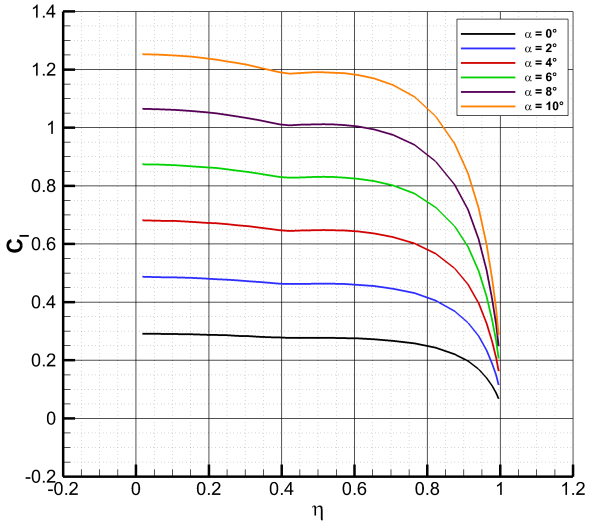

(a) Lift coefficient distribution.

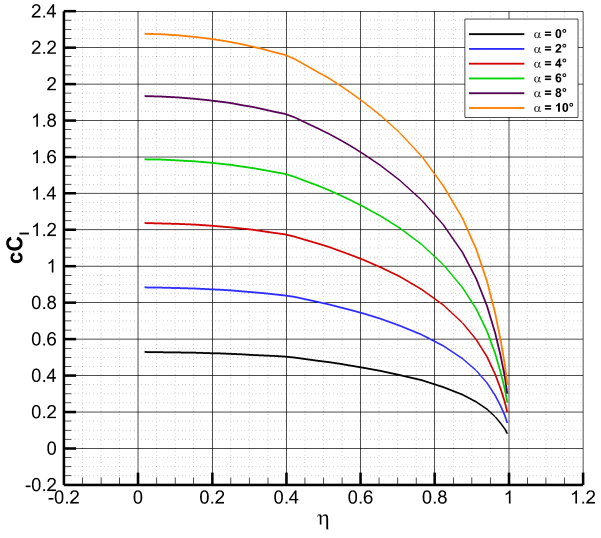

(b) Wing span loading distribution.

FIGURE 2.28: Pressure coefficient contour

variation in the lift distribution at the wing tip respect to the wing without winglet. This means that the lift distribution will present a peak in the local lift distribution as it is clearly shown in Fig. 2.31(a). The peak of the lift coefficient must be kept under control through the toe angle. Thus the first step for the winglet design deals with the choice of the toe angle. Fig. 2.31(a) and Fig. 2.31(b) show the lift coefficient distribution and the effect on the wing induced drag factor due to toe variation respectively. As it can been seen, while the peak in the lift coefficient at the wing tip is reduced increasing

TABLE 2.10: Winglet parameters variation range.

Winglet parameters variation range.	
δ_w (deg.)	$50 \leq \delta_w \leq 60$
cant_w (deg.)	$70 \leq \text{cant}_w \leq 80$
h_w (m)	$0.6 \leq h_w \leq 1.0$
toe (deg.)	$-12 \leq toe \leq -6$

the toe angle (in negative sign), on the other hand there is a reduction in the induced drag factor. Fortunately the variation of the induced drag factor with the toe angle is not so sensitive as shown in Fig. 2.31(b). From this analysis it can be concluded that a good choice for the toe angle is 10°, this value guarantees a good compromise between the need to reduce the lift peak at wing tip (restrained increase in the bending moment) and the need to have a good increment of the induced drag factor. Once the toe angle has been chose, a parametric investigation among the main winglet parameters has been performed (see Tab. 2.10). Fig. 2.29 graphically shows what the parametric investigation consists of. Fig. 2.30 shows how the winglet sweep angle

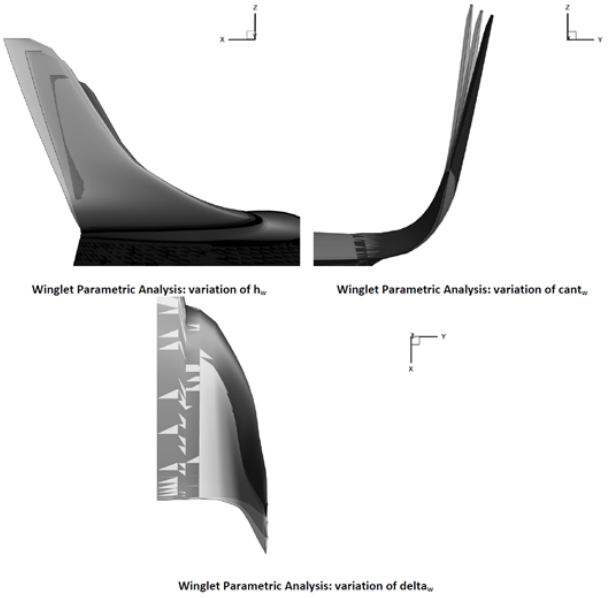

FIGURE 2.29: Examples of winglet design parameters on the winglet shapes.

(δ_w) affects the induced drag factor. It is clear how, for a given winglet height, that the sweep angle angle effect on the induced drag factor is lower than 1%. As it was expected, the main effect on the wing-induced drag factor is due to the winglets height (see Fig.2.32). It can be noticed that each winglets configuration gives an improvement of the wing-induced drag factor, which is maximum at the greatest analyse winglet height of 1.0 m. Another effect

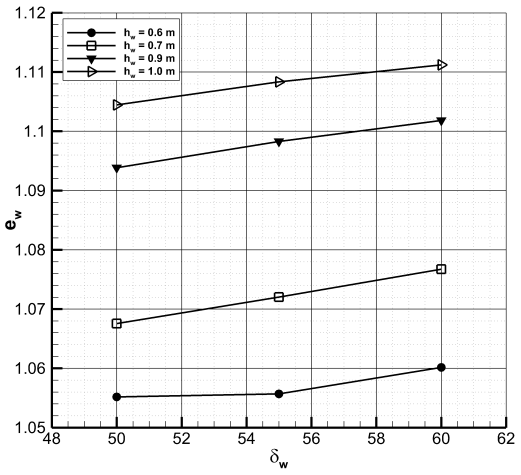

FIGURE 2.30: Winglet sweep angle effect on the wing induced drag factor $cant_w = 80°$.

to highlight is the cant angle effect. The angle of cant has not a high effect on the wing induced drag factor (as shown in Fig. 2.32) but it increase the wing geometrical aspect ratio as shown in Fig. 2.33 and Fig. 2.34. As matter of fact it is clear that a lower cant angle increase the wing aspect ratio (the wing span will be increased) leading to problems dealing with weight and structures. Data dealing with the effects of the winglet on the wing bending moment can be found in the literature, see Ref. [43, 44], where it is shown how a typical cant angle is no lower than 70° which produces an increment in the wing bending moment of about 3-5% [43, 44]. Also the winglet height has a typical value of 0.1 $b/2$ giving a bending moment increase of about 3-4% [43, 44]. Thus taking into account all the aerodynamic and structural issues, the best wnglet set of design parameters can be picked up from the wide amount of the available data. In the case of the P2012 Traveller the main issues in the choice of the best winglet design have been targeted to achieve an arrangement that could reduce at least the wing redesign (the wing design has been already defined), so the geometrical parameters of the new wing should be not so different from the reference wing, in terms of span and wing aspect ratio. Finally, at the end of this parametric investigation, the best choice of the winglet geometrical parameters is the following:

- *toe angle* = -10°;
- h_w = 0.7 m;
- $cant_w = 80°$;
- $\delta_w = 50°$.

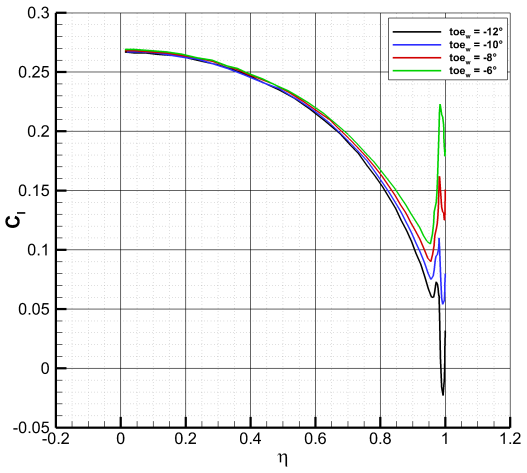

(a) Lift coefficient distribution, toe variation, $\alpha = 0°$.

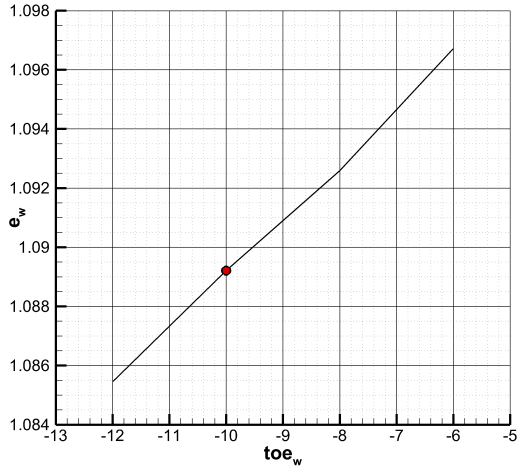

(b) Wing induced drag factor variation with respect to toe angle.

FIGURE 2.31: Effect of the winglet toe angle and the lift coefficient distribution and wing induced drag factor.

This choice gives a wing induced drag factor equal to e_w=1.107, which is about 10% higher than the corresponding value for the reference wing. Tab. 2.11 shows the results of the winglet design.

While the introduction of the winglet leads to a reduction of the wing induced drag factor, on the other hand the addition of the winglet surface gives an increment in the zero lift drag coefficient, due to the increment of

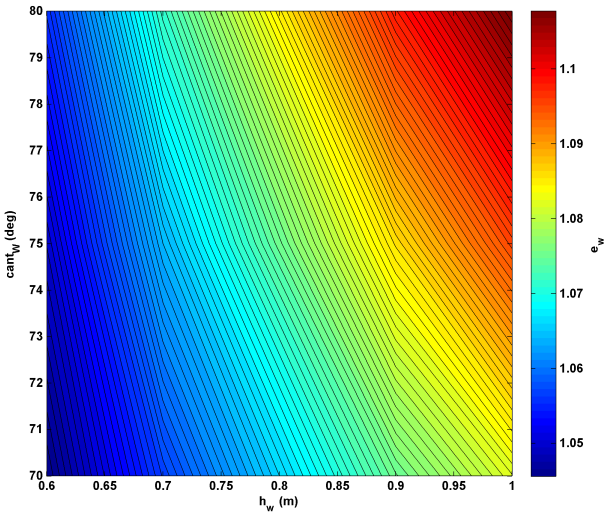

FIGURE 2.32: Cant and winglet height effect on the in induced drag factor e_w, $\delta_w = 55°$.

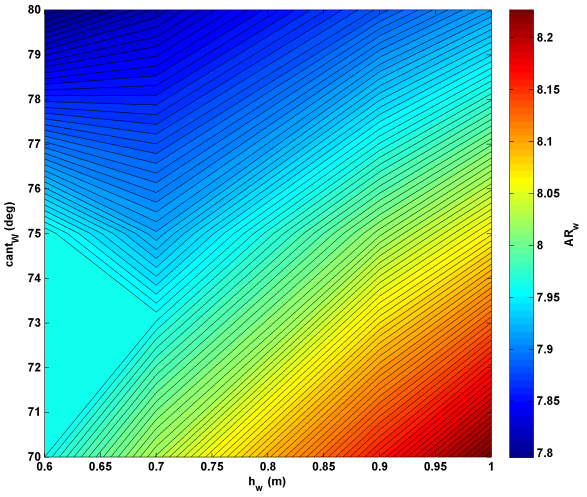

FIGURE 2.33: Cant and winglet height effect on the wing aspect ratio AR, $\delta_w = 55°$.

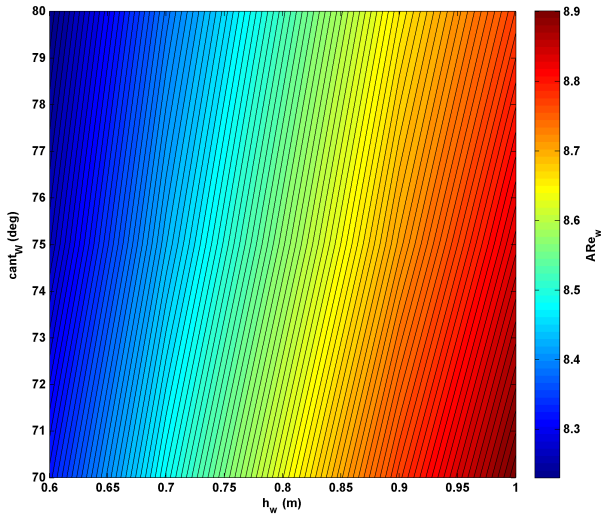

FIGURE 2.34: Cant and winglet height effect on the effective wing aspect ratio ARe_w, $\delta_w = 55°$.

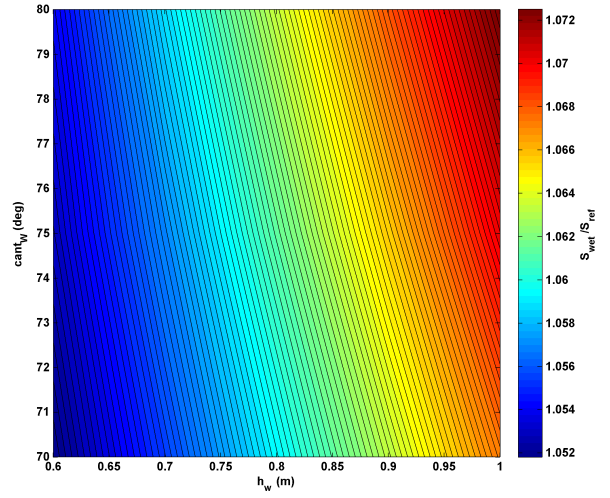

FIGURE 2.35: Cant and winglet height effect on S_{wet}/S_{ref}, $\delta_w = 55°$.

the wetted area. The increase of the zero lift drag coefficient given by the winglet surface can be estimated though the classical procedures shown in Ref. Roskam [12, 20] and Raymer [16], and already used in sec. 2.3, by considering the increment due to the winglet in the wing wetted area. This leads to an increment in the zero lift drag coefficient of about 5 drag counts, as shown in 2.11. How this affects the aircraft drag polar is shown Fig. 2.36 where the difference between the aircraft total drag coefficient in both winglet on and winglet off configuration is shown. It is interesting to appreciate how the winglet gives a reduction of the total drag coefficient in a wide range of lift

TABLE 2.11: Results for the winglet design.

	reference Wing	Wing with winglet	% of variation
b (m)	13.6	14	+3.28
S_w (m^2)	25.0	25.4	+1.60
S_{wet} (m^2)	26.5	27.88	+5.0
AR	7.4	7.72	+4.2
e_w	0.979	1.07	+10
ARe_w	7.2	8.2	+14.7
$Bending$			+3.5
C_{D_0} (drag counts)	306	311	+1.6

coefficient.starting from a $C_L = 0.32$. The major improvement due to the winglet are obtainable in the climb condition, where a drag reduction of about 30-40 drag counts can be appreciated. This is mainly impacting on the climb performance, in particular in the OEI condition. How the winglet affect the flight performance will be further discussed in this work, see chapter 5. Fig. 2.37 shows the final wing configuration with the winglet mounted at the wing tip.

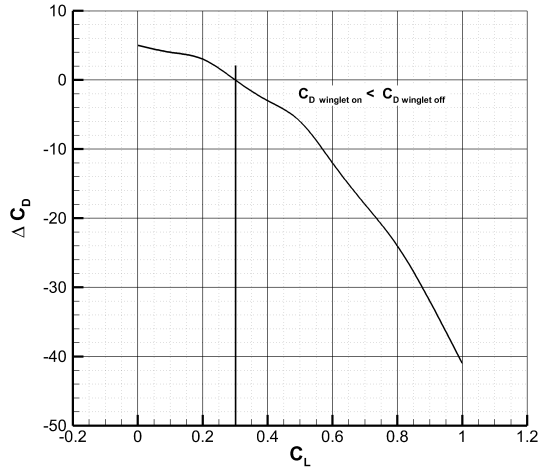

FIGURE 2.36: Complete aircraft drag coefficient variation due to the winglet.

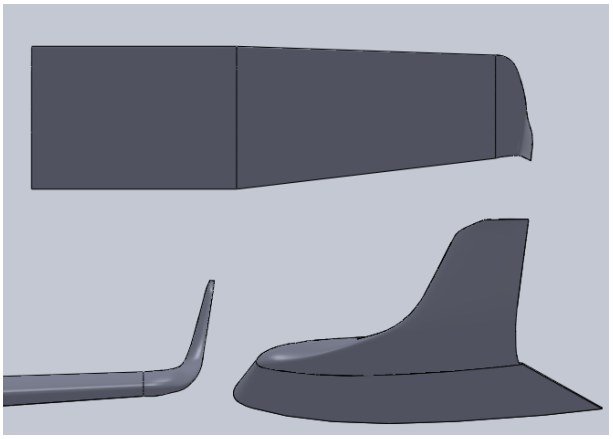

FIGURE 2.37: Wing with winglet, CAD drowing.

2.5 Preliminary Aerodynamic Analysis

The aerodynamic analyses, both for longitudinal and lateral-directional characteristics, have been also performed through a 3-D panel code available at DII (Department of Industrial Engineering-University of Naples). These analyses have been performed with two main goals. First of all in order to validate the conceptual design illustrated in sec. 2.2 dealing with the estimation of stability and control, and then with the aim to provide an accurate evaluation of the wing span load that could take into account the effect of the fuselage, winglet and nacelles. It is worth to notice that the estimation of wing span loading is a crucial aspect in order to perform a well-designed wing structure and the results are used for certification flight load assessment.

2.5.1 Longitudinal analysis

The longitudinal analyses have been performed on several modular configurations of the aircraft (i.e. isolated wing, wing-body, wing-body-nacelle, etc.), in order to estimate the contribution of each aircraft components to the longitudinal stability to be compared with the semi-empirical estimation previously discussed in sec. 2.2. The investigated configurations are the isolated wing, the wing body and nacelles and the complete aircraft. Fig. 2.38 shows the variation of the pitching moment coefficient respect to the angle of attack compared with the semi-empirical results carried out in sec. 2.2. The graph shows a good agreement between the two analyses confirming the reliability of semi-empirical methodology used during preliminary design phase. It must be highlighted that the analyses with the panel code solver have been limited within the range of angle of attack that goes from 0° up to 8°, where the nonlinearities effect are negligible, and also that no thrust effects have been considered. The aircraft centre of gravity was fixed in the same position assumed for the preliminary investigation of the sec. 2.2 (25% of the mean aerodynamic chord along the longitudinal axis and about 25% of the mean aerodynamic chord below the wing plane). Fig. 2.38 shows that fuselage instability (slope of C_M versus alpha for the fuselage contribution) estimated through numerical analysis with panel method leads to the same value that has been estimated through semi-empirical approach (Munk theory solved through Multhopp strip integration). The aerodynamic centre shift due to the fuselage and nacelle contribution is about 13% of the mean aerodynamic chord.

Particular attention has been posed on the estimation of the wing loads, thus several aerodynamic analyses have been performed on wing configuration (winglets on), wing-body configuration and wing-body-nacelles configurations. The main goal of the investigation has been the fuselage effect on wing lift close to wing-fuselage junction and to have more information about lift loss due to nacelles in terms of intensity and effect along wing span. In Fig. 2.39 and Fig. 2.40 the wing span lift coefficient and the wing span loading of the wing,

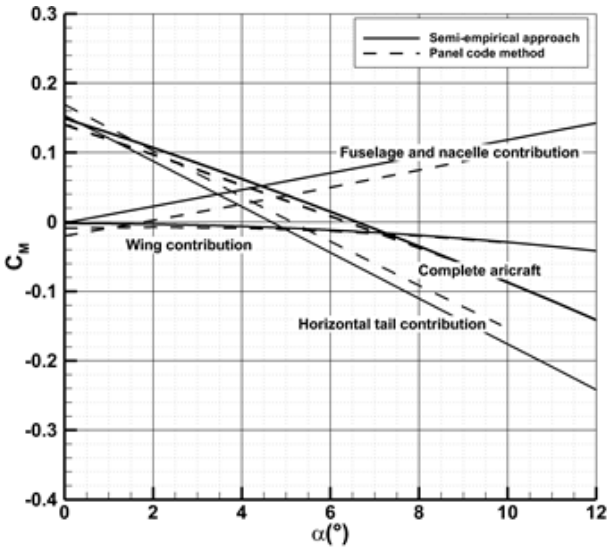

FIGURE 2.38: Pitching moment coefficient breakdown, panel method versus semi-empirical approach (cruise condition, $x_{cg}/\bar{c} = 0.25$ $z_{cg}/\bar{c} = 0.25$)

wing-body and wing-body-nacelles configurations are respectively depicted at different angles of attack. It is easy to see that the nacelle causes a lift loss in the wing zone where it is installed, but it has a positive effect on the wing-body interference. Fig. 2.41 shows the pressure coefficient distribution on the wing-body with nacelle at an angle of attack of 0°. As matter of fact, the nacelle geometry creates flow acceleration in the wing zone between the nacelle itself and the fuselage, leading to a slightly higher lift coefficient in this wing area especially at higher angle of attack (see Fig. 2.39). It is worth to observe that the wing span loading has an almost regular span-wise variation as shown in Fig. 2.40 and should not lead to excessive vortex intensity and lift loss, since the nacelle geometry has an higher local chord (respect to the wing chord, see Fig. 2.18). The graph in Fig. 2.39 clearly show that, especially at an angle of attack of 4 degrees, the spanwise lift distribution (and consequently the bending moment at wing-root) will not be significantly affected by the nacelle and the fuselage interference. The lift in the nacelle area does not take into account the flow separation on the lower surface of nacelle. Numerical calculations have been performed on a closed and streamlined nacelle shape and the propeller effect is not considered. Winglets span-wise effect has been carefully investigated during the winglets design, by controlling winglet toe and cant angles (see sec. 2.4), as it also done outlined in [33, 36]. The results in Fig. 2.39 show the lift coefficient in the winglet root area (at wing tip) with reasonable values, confirming the right design of toe angles, sweep and taper ratio for the winglet itself. The lift coefficient, also at high angles of attack, shows that winglet stall should be avoided for any condition of angle of attack and sideslip. Fig. 2.40 shows a very regular wing span loading, also in the

winglets area, confirming the good design that should lead, as estimated in sec. 2.4, to an increase of the induced drag factor (leading also to an increase of Oswald factor) of about 10% respect to a wing without winglet but with the same aspect ratio.

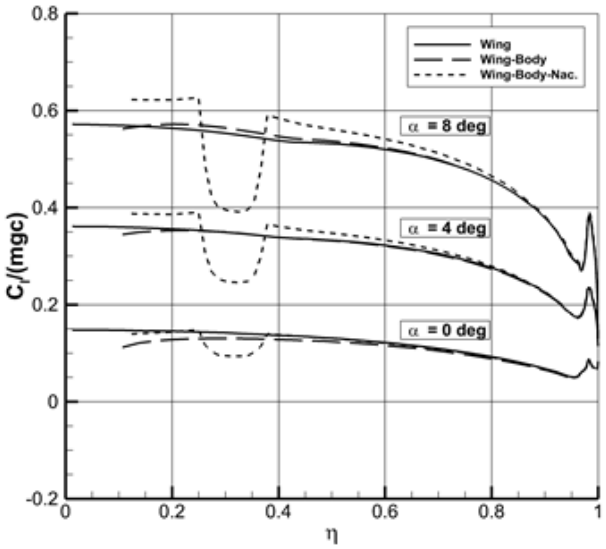

FIGURE 2.39: Wing span lift coefficient comparison of wing, wing-body and wing-body-nacelle configurations.

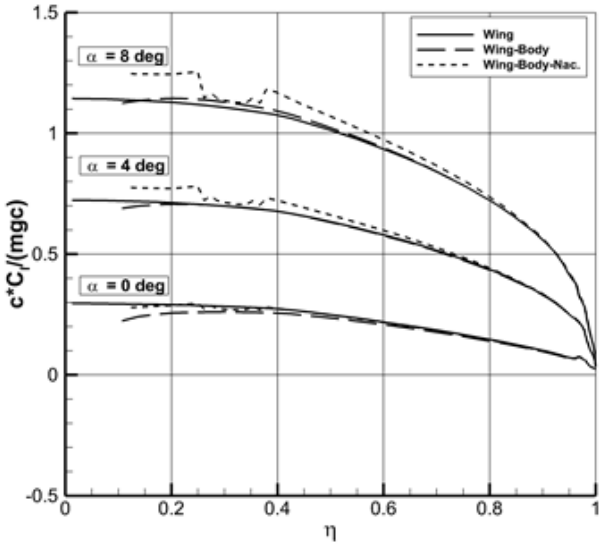

FIGURE 2.40: Wing span loading comparison of wing, wing-body and wing-body-nacelle configurations.

Another interesting result obtained from the panel code analysis has been the estimation of the wing wake position on the horizontal tail location. The

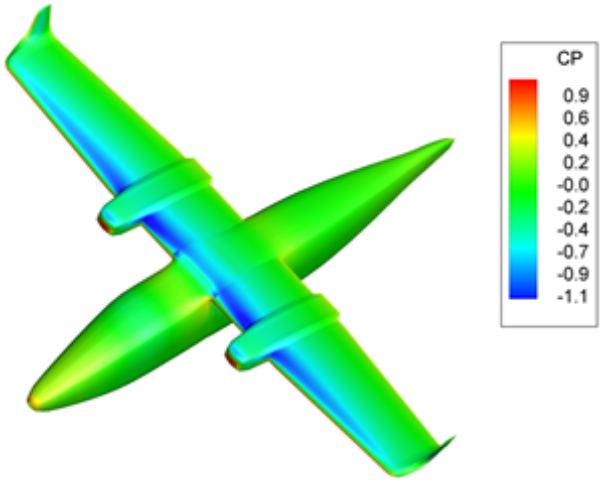

FIGURE 2.41: Pressure coefficient distribution over the wing-body-nacelles configuration, $\alpha = 0°$.

wing wake relaxation at two different angles of attack is shown in Fig. 2.42. It is clear how the wing wake is always clearly above the horizontal tail, moving away from it when the angle of attack increases. From the ratio between the horizontal tail lift slope in the body-horizontal configuration and the same lift slope in the wing-body-horizontal configuration it is possible to estimate the downwash effect, compared in Tab. 2.12 with the estimated value through the semi-empirical approach. Tab. 2.12 also summarizes the most relevant results dealing with the longitudinal stability carried out with the panel code method compared with the semi-empirical data already discussed in sec. 2.2.

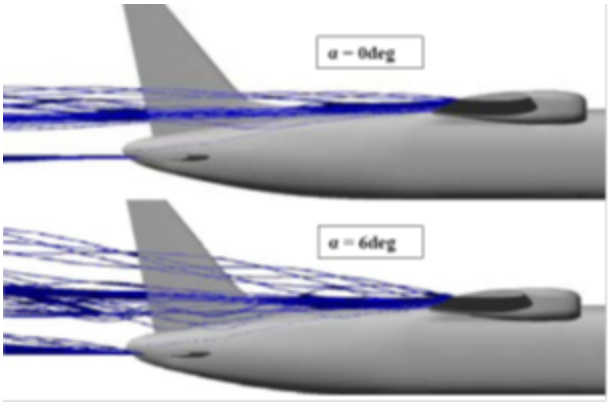

FIGURE 2.42: Wing wake relaxation at two different angle of attack (up: $\alpha = 0°$; down: $\alpha = 6°$).

TABLE 2.12: Longitudinal preliminary aerodynamic aerodynamic analysis results.

	Panel method	Semi-empirical
C_{L_α} complete	0.106 deg^{-1}	0.0920 deg^{-1}
C_{M_α} fus.+ nac.	0.0120 deg^{-1}	0.0120 deg^{-1}
C_{M_α} complete	-0.0223 deg^{-1}	-0.0228 deg^{-1}
Δx_{ac} fus.+nac.	11%$\bar{c}$	13%$\bar{c}$
$d\epsilon/d\alpha$	0.420	0.347

2.5.2 Lateral-directional analysis

The lateral directional aerodynamic analysis has been performed on the P2012 Traveller especially to investigate the vertical tail contribution to the directional stability. Particular care has been posed to the effects which the others aircraft components have on the vertical tail. This is crucial to lead to a correct design of the vertical tail and the rudder surface. However, also the lateral stability and dihedral effects have been estimated. The contribution of the vertical stabilizer on directional stability has been carefully estimated. As reported on many textbooks [12, 13, 45], and was well investigated in [46, 47], the contribution of the vertical tailplane on aircraft directional stability depends on many effects, among them the effect of the fuselage, the effect of the wing-fuselage combination also known as side-wash and the interference effect of the horizontal tailplane on the vertical stabilizer (the horizontal tailplane can act like an end-plate it can increase the vertical tailplane lift curve slope). To have an estimation of these effects several configuration (isolated vertical tail, body-vertical, wing-body-vertical and complete aircraft) have been analysed. The performed calculations show an indication of the above mentioned effects. In particular in Tab. 2.13 it can be observed a global increase of vertical stabilizer effectiveness (compared to that one relative to the isolated tail plane). This increment has been estimated to be about 1.25 concerning the stability and 1.35 concerning control derivatives. As also shown in [12, 45, 48], the main effects on the vertical tail is due to the fuselage, which amplifies the vertical tail lift capability of about 30%. The high wing configuration has the effect to decrease the vertical tail lift of about 10%, while the horizontal tail, although body mounted, gives an increment of about 15%. These results could be extremely useful to have a more accurate vertical tailplane sizing.

Fig. 2.43 shows the comparison between the breakdown of yawing moment coefficient with respect to sideslip angle carried out with both approaches (panel method, the dashed lines, and the semi-empirical methodologies, the solid lines). The graph shows the good agreement between the two methodologies providing a further validation of the vertical tail design carried out in sec. 2.2. Fig. 2.44 illustrates the variation of the complete aircraft rolling moment coefficient respect to the sideslip angle. Here the winglet on and winglet

TABLE 2.13: Estimation of vertical tail stabilizer and rudder effectiveness in stability and control (panel code method).

Configuration	$C_{N_{\beta_v}} deg^{-1}$	$C_{N_{\delta_{r_v}}} deg^{-1}$	Ratio $C_{N_{\beta_v}}$	$C_{N_{\delta_{r_v}}}$
V	-0.00235	0.00201	1.000	1.000
BV	-0.00291	0.00230	1.238	1.144
WBV	-0.00206	0.00226	0.877	1.124
BVH	-0.00335	0.00259	1.426	1.289
Complete	-0.00294	0.00263	1.251	1.308

off configuration are compared and it is very interesting to notice the large contribution to the dihedral effects introduced by the winglets. The winglet effect on the rolling moment coefficient cannot be evaluated with a classical semi-empirical approach, unless to define a wing equivalent dihedral angle. A method for predicting the winglet effect on the lateral stability can be found in Nickel and Wohlfahrt [48], where a formula for the estimation the wing equivalent dihedral angle is provided. A summary of the most meaningful derivatives is shown in Tab. 2.14 .

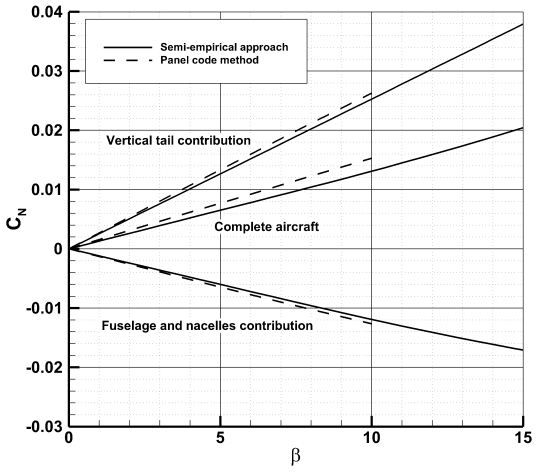

FIGURE 2.43: Yawing moment coefficient breakdown, panel method versus semi-empirical approach.

TABLE 2.14: Lateral directional aerodynamic analysis results.

	Panel Code	Semi-empirical
C_{N_β} complete	-0.00153 deg^{-1}	-0.00130 deg^{-1}
C_{roll_β} complete winglet on	0.00282 deg^{-1}	0.00251 deg^{-1}
C_{roll_β} complete winglet off	0.00155 deg^{-1}	0.00160 deg^{-1}

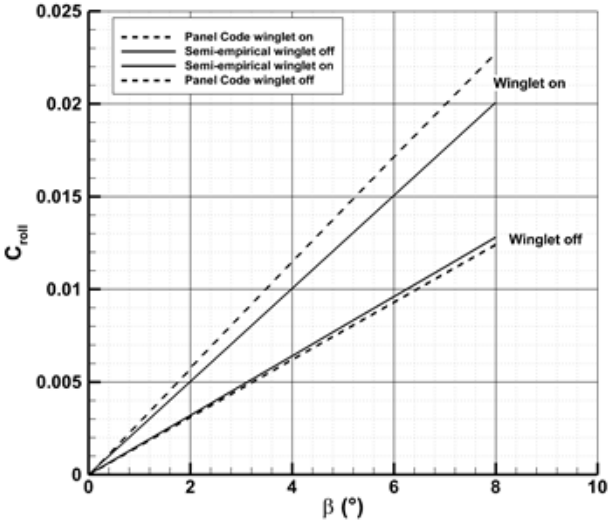

FIGURE 2.44: Rolling moment coefficient breakdown, panel method versus semi-empirical approach.

Chapter 3

Wind tunnel tests of the P2012 Traveller scale model

3.1 Introduction

This section deals with the experimental investigation of the aerodynamic characteristics of a scale model of the P2012 Traveller aircraft. Experimental tests have been focused on the estimation of both longitudinal and lateral-directional static stability and control derivatives, with the aim to verify the preliminary design and sizing of the aircraft shown in chapter 2.

The wind tunnels offer a rapid, economical and accurate means for aerodynamic research, because they make it possible to use models and because they are always available.

The earliest wind tunnels were invented towards the end of the 19th century, in the early days of aeronautic research. The wind tunnel was envisioned as a means of reversing the usual paradigm: instead of the air standing still and an object moving at speed through it, the same effect would be obtained if the object stood still and the air moved at speed past it. Benjamin Robins (1707-1751), an English military engineer and mathematician, invented a whirling arm apparatus to determine drag and did some of the first experiments in aviation theory. Sir George Cayley (1773-1857) also used a whirling arm to measure the drag and lift of various airfoils. However, at the end of the 19th century, the major fault of the whirling arm was apparent. This fault was due that the wing was forced to fly in its own wake. Francis Herbert Wenham (1824-1908), a Council Member of the Aeronautical Society of Great Britain, addressed these issues by inventing, designing and operating the first enclosed wind tunnel in 1871. Konstantin Tsiolkovsky built an open-section wind tunnel with a centrifugal blower in 1897, and determined the drag coefficients of flat plates, cylinders and spheres. In the early 1890s a Danish inventor, Poul la Cour, applied wind tunnels in his process of developing and the technology of wind turbines. Carl Rickard Nyberg used a wind tunnel when designing his Flugan from 1897 and onwards. In a classic set of experiments,

the Englishman Osborne Reynolds (1842-1912) of the University of Manchester demonstrated that the airflow pattern over a scale model would be the same for the full-scale vehicle if a certain flow parameter were the same in both cases. This factor, now known as the Reynolds number, is a basic parameter in the description of all fluid-flow situations. This comprises the central scientific justification for the use of models in wind tunnels to simulate real-life phenomena. The Wright brothers' use of a simple wind tunnel in 1901 to study the effects of airflow over various shapes while developing their Wright Flyer was in some ways revolutionary, Ref. [49]. In France, Gustave Eiffel (1832-1923) built his first open-return wind tunnel in 1909, running about 4000 tests between 1909 and 1912 and contributing to set new standards for aeronautical research. Eiffel's contribution into improvement of the open-return wind tunnel by enclosing the test section in a chamber was followed by a number of wind tunnels later built(Eiffels was also the first to design a flared inlet with honeycomb flow straightener). Subsequent use of wind tunnels proliferated as the science of aerodynamics and discipline of aeronautical engineering were established and air travel and power were developed. The US Navy in 1916 built one of the largest wind tunnels in the world at that time at the Washington Navy Yard, [50]. Until World War Two, the world's largest wind tunnel was built in 1932-1934 and located in a suburb of Paris, Chalais-Meudon, France. It was designed to test full size aircraft and had six large fans driven by high powered electric motors [51]. The Chalais Meudon wind tunnel was used by ONERA under the name S1Ch until 1976, e.g. in the development of the Caravelle and Concorde airplanes. Today, this wind tunnel is preserved as a national monument. During the Second World War large wind tunnels were built, and the development of wind tunnel science accompanied the development of the flying machines. In 1941 the US constructed one of the largest wind tunnels at that time at Wright Field in Dayton, Ohio [52]. The wind tunnel used by German scientists at Peenemünde prior to and during WWII is an interesting example of the difficulties associated with extending the useful range of large wind tunnels. By the end of World War Two, the US had built eight new wind tunnels, including the largest one in the world at Moffett Field near Sunnyvale, California [53], and a vertical wind tunnel at Wright Field [54]. Later on, wind tunnel study came into its own: the effects of wind on man made structures or objects needed to be studied when buildings became tall enough to present large surfaces to the wind, and the resulting forces had to be resisted by the building's internal structure. Determining such forces was required before building codes could specify the required strength of such buildings and such tests continue to be used for large or unusual buildings. Still later, wind-tunnel testing was applied to automobiles, not so much to determine aerodynamic forces per se but more to determine ways to reduce the power required to move the vehicle on roadways at a given speed.

3.2 Wind tunnel of the DII

The experimental tests campaign has been performed in the main subsonic wind tunnel facility of the DII. This subsonic wind tunnel is a closed circuit tunnel with rectangular cross section as shown in Fig 3.1. Main test section has a 4 meters length and a 2 m x 1.4 m. cross section with a maximum achievable speed of 50 m/s and low turbulence level equal to 0.1%. The main wind-tunnel characteristics are summarized in Tab. 3.1. The main components of the

(a) Main subsonic wind tunnel facility.

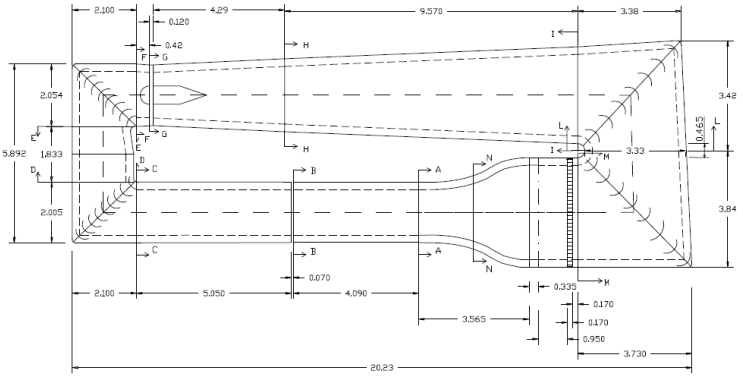

(b) Main subsonic wind tunnel diagram.

FIGURE 3.1: Main subsonic wind tunnel od the DII.

TABLE 3.1: Wind tunnel of the DII, main characteristics.

	Value
Test section dimensions	2.0 m x 1.4 m
Maximum available wind speed	50 m/s
Turbulence level	0.10%

closed circuit tunnel are the following:

- **Test section**: it has a 4 meters length and a 2 m x 1.4 m. Its cross sectional area is 2.68 m^2(the section is rectangular with blunted edges);
- **Diffuser**: there are three diffusers in order to slow down the airflow coming from the test chamber. The first diffuser has a length of about 5 m and an expansion angle of about 3° and links the last section of the test chamber to first corner. The second diffuser is placed between the first two corners and has a length of about 1.8 m. The last diffuser is the longest one (about 12.3 m) and increases the tunnel section having an expansion angle of about 3°, it is places between the second and third corner;
- **Screen**: it is placed immediately before the first corner with the aim to protect the turning vanes against any possible object or scraps that could be lost by the model in the test section. The screen has squared cells af about 13 mm.
- **Corners**: the first corner is placed behind the first diffuser and has a constant section with turning vanes having a chord of about 450 mm and a maximum thickness of about 14.4%. The second corner is placed behind the fan and is equipped with tabs having a chord of about 490 mm and maximum thickness of about 13.3%. The second corner section is slightly divergent such as for both the third and fourth corner. The third corner has diverters having a chord of 925 mm and maximum thickness of 17.3%, while the fourth corner tabs have a length of 875 mm with a maximum thickness of 18.3%.
- **Fan**: it is placed immediately ahead of the second corner. Before the six blades propeller a four blade flow straightener ring is placed. The ogive of the fan has a maximum diameter of 700 mm;
- **Honeycomb flow straighteners**: they are elliptical section cells placed at the beginning of the stagnation chamber;
- **Mesh screen**: it has the function to reduce the turbulence axial component of the flow in the test section allowing a turbulence level of 10%;
- **Stagnation chamber**: it has a length of 0.035 m and it is placed ahead of the nozzle;
- **Nozzle**: it has a length of 3.56 m with an inlet section of about 12.7 m^2 and an outlet section of 2.7 m^2, with a ratio of 4.83.

3.3 Instrumentation and calibration of the test section

The instrumentation used to perform the experimental test campaign can be divided in: measurement, control, data acquisition and elaboration.

3.3.1 Measurement instrumentation

This instrumentation consists of two internal strain gage balances for the measurement of aerodynamic forces and moments, a *Venturi* system to measure the dynamic pressure, an inclinometer to read the longitudinal attitude of the scale model and a potentiometer to measure the sideslip angle, and finally a temperature probe to measure the static temperature in the test section.

- **Internal strain gage balances**: two different internal strain gage balances with three channels each one, have been used to measure the aerodynamic forces and moments. Fig 3.2 shows both balances. The first balance (see Fig. 3.2(a)) has been used for the longitudinal measurements of lift, drag and pitching moment whereas a second balance (see Fig. 3.2(b)) has been used for the lateral-directional measurements of side force, yawing and rolling moment. Both balances have been subjected to a calibration procedure in order to perform a right estimation of the aerodynamic forces and moments, Ref [55]. It seems to be needed to supply a short overview about the calibration procedure to a better sake. Considering the case of applying a load into the lift direction, when the load to lift is applied, plots of lift load(on y axis) versus the reading on lift, drag and pitching moment (on x axis) are made. If the curves are slightly nonlinear, they are replaced by a linear approximation. When this has been done for all three components, the slopes of the nine curves are taken as $K_B = \Delta L_R / \Delta M_B$. The subscript B is the load applied to the balance and the subscript R is the balance output reading. If it is assumed to indicate as 1=lift, 2=drag and 3=pitching moment, thus for the lift reading one has:

$$L_R = K_{11} L_B + K_{12} D_B + K_{13} M_B \tag{3.1}$$

or in matrix form:

$$F_R = [K_{ij}] F_B \tag{3.2}$$

where F can be a force or a moment as required. The matrix equation expressed in Eq. 3.3 can be inverted to give:

$$F_B = [K_{ij}]^{-1} F_R \tag{3.3}$$

which is the required equation ot determine the forces and moments applied to the balance by the model from the balance output readings.

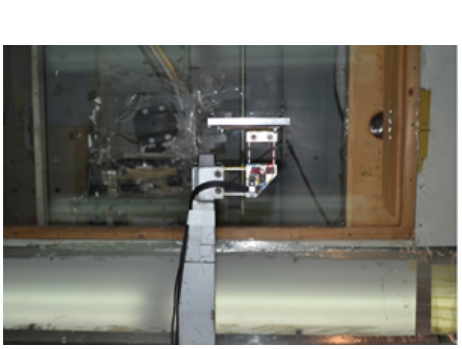

(a) Longitudinal strain gage balance.

(b) Lateral-directional strain gage balance.

FIGURE 3.2: Internal strain gage balances.

After a series of lading tests the final calibration matrix for both longitudinal and lateral directional balance have been found, in 3.4 the calibration matrix of the longitudinal balance is presented.

$$[K_{ij}]^{-1} = \begin{bmatrix} -12.78340689 & -0.099301901 & 0.036184436 \\ -0.004273371 & -2.068153696 & 0.004097878 \\ -0.052074693 & 0.158940964 & 4.938835907 \end{bmatrix} \tag{3.4}$$

Calibration procedure has been also essential in order to estimate both balance centre in order to apply the transportation of forces and moment from the balance centre to the desired reference pole for the reduction of the aerodynamic forces and moments. Tab. 3.2 summarizes the maximum error found for the balances reading after the calibration procedure. The maximum error in average is about 0.1% of the full scale maximum load of each measured force or moment.

TABLE 3.2: Strain gage balances margin of error.

Force/Moment	**Max. Error**	**Full scale**
Lift	0.05 kg (0.06%)	80 kg
Drag	0.03 kg (0.15%)	20 kg
Pitching moment	0.02 $kg \cdot m$ (0.1%)	20 $kg \cdot m$
Side force	0.02 kg (0.1%)	20 kg
Yawing moment	0.02 $kg \cdot m$(0.1%)	20 $kg \cdot m$
Rolling moment	0.02 $kg \cdot m$(0.1%)	20 $kg \cdot m$

- **Venturi**: the wind tunnel of the DII is equipped with 4 static pressure probe placed on both faces of both initial and final sections of the nozzle. A pressure transducer (with a F.S. of 2500 Pa and an accuracy of 2-3 Pa) measures the static pressure variation between these sections, and

through the continuity equation obtains the dynamic pressure and at the exit of the nozzle. Several tests without the model in the test section and at different air speeds, have shown that the dynamic pressure at the end of the nozzle is not equal to the test section dynamic pressure, but the linear fit shown in Eq. 3.5 has be found.

$$q_{eff} = q_{meas.} \cdot 1.09 \tag{3.5}$$

Because it is impossible to use a *Pitot* probe to measure the dynamic pressure in the test section in presence of the scale model[1], the only available measure of the dynamic pressure is obtained by the *Venturi*, thus the Eq. 3.5 is assumed to be valid also in presence of the scale model in the test section.

- **Inclinometer**: it is the uni-axial *Tilt Sensor* **CXLA01**, produced by **CrossBow** (San Jose, CA-USA). The sensor measures the component of the acceleration of gravity that lies in the plane of the instrument reference face. The inclinometer has been integral mounted with the sting on which the balance is fixed on. An accurate measurement of the off set angle has been performed in order to have the most accurate measurement of the model angle of incidence, see Fig. .

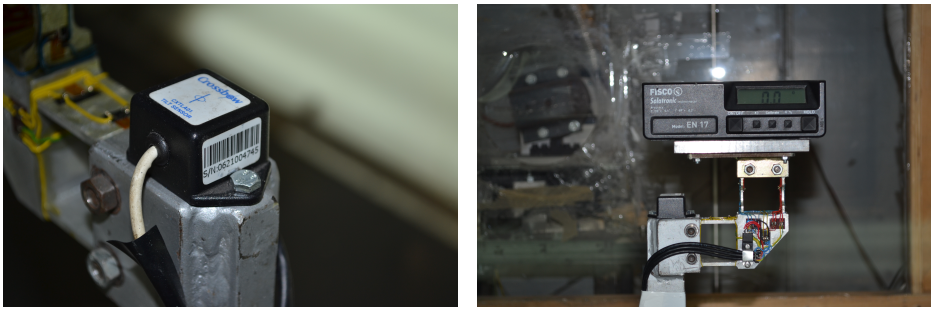

(a) The CrossBow inclinometer mounted on th balance sting.

(b) Estimation of the off-set angle for the pitch attitude.

FIGURE 3.3: Inclinometer used to measure the angle of incidence.

- **Potentiometer for the sideslip angle**: the sideslip angle has been measured through the use of a potentiometer with similar accuracy characteristics of the inclinometer described above. The available range for the sideslip angle is about -25°/+30° (the sideslip angle is assumed to be positive in sign when the airflow direction comes from the right hand of the model).

[1]The test section should be enough long to guarantee the *Pitot* probe measure to be not affected by pressure field produced by the model in the test section. This is not the case of the wind tunnel of the DII.

- **Temperature probe**: it consists of a flush wall-mounted probe for the measurement of the static temperature in order to determine the true test section speed through the use of Bernoulli's incompressible equation, and to obtain the mass density through the equation of state. The temperature measurements are also needed to take under control the heating of the strain gage sensors that are affected by temperature changes. As mater of fact in order to minimize the temperature changes the test procedures provides for a preliminary heating of the test section before each set of experimental tests[2].

3.3.2 Control instrumentation

Belonging to the control instrumentation are the longitudinal attitude and the sidelisp control systems. The first is an electromechanics system driven that could be remote controlled by PC, whereas the second one is basically a hand moved kinematic chain that allows to variate the sideslip angle of the assembly sting-balance-model.

- **Longitudinal attitude control system**: the pitching mechanism is an electromechanical system lead by PC. It is placed outside the model, below the floor of the test section and it is linked to the assembly of balance-model through the sting. It was internally made to the laboratory of the DII. The system consists of an electrical stepper, which allows a sting angular excursion from -3.5° up to 20°. The control is PC driven via a D/A converter 12 bit activating the electrical stepper. The system uses the above mentioned CrossBow Tilt sensor to measure the pitching attitude. The output signal of the inclinometer is acquired by an A/D converter and sent to the PC.

- **Lateral attitude control system**: it consists of a kinematic mechanism (manhandle by the operator) being a crank handle fixed at the end of a horizontal shaft acting as worm-screw. This shaft transmits the rotatory motion to the vertical axis of a small diameter gear wheel. The rotatory motion is then transmitted to a larger gear wheel through a steel chain reducing the angular velocity of the model. A steel plate being the sting base is fixed to the axis of the second gear wheel. The steel plate allows the whole assembly sting-balance-model to rotate, see Fig. 3.5

3.3.3 Acquisition and elaboration

This instrumentation consist of:

[2]A typical temperature range in the test section during a test is about 40-50°.

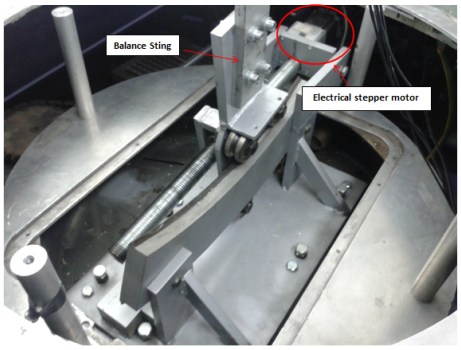

(a) Electrical stepper motor for pitching attitude control.

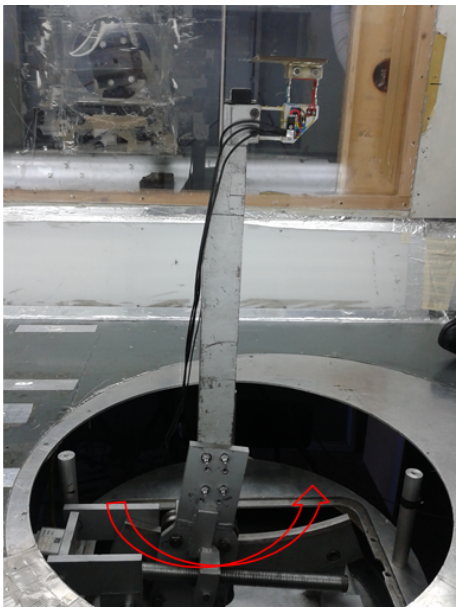

(b) Balance sting mounted on the pitching control system.

FIGURE 3.4: Longitudinal attitude control system.

(a) Sideslip control mechaniscm, the kinematic chain system.

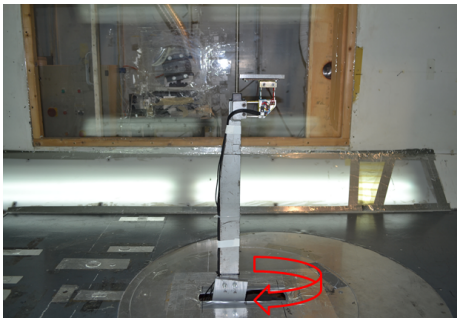

(b) Sideslip control mechaniscm, an inside test section view.

FIGURE 3.5: Lateral attitude control system.

- a 16 channels device for the acquisition and conversion into 16 bit (**SPARTAN** system, produced by ***Imc DataWorks***) of output data coming from the measurement instrumentation;
- a Desktop PC Windows XP based, provided with an interface software for the A/D converter;

- a software for the elaboration and visualisation of the acquired data. The software, named **WT6**, has been developed at the DII laboratory by **ADAG**[3] research group.

3.4 P2012 Traveller scale model and test section set-up

The experimental test campaign has been conducted on a 1:875 scale mode. The scale factor has been chosen in order to simulate the highest possible Reynolds number with respect to the tunnel dimensions. The ratio between the scale model wing span and the test section width is 0.8 while the ratio between the test section width and height is 0.7; this means that scaled model dimensions are within the range of wind tunnel walls correction effectiveness, as suggested by Rae and Pope [55]. The scale model has been manufactured at Tecnam factory and it consists of several disjointed components such as wing, fuselage, tailplanes, nacelles and winglet to allow tests of different configurations. The model is also provided with several movable surface being the both control surfaces (elevator and rudder), and flaps. The wing has been built shaping aluminium sheets on a several steel ribs, that have been welded on two steel rods placed at about 1/4 and 1/2 of the wing chord along the wing span. The fuselage has been built in similar way by welding a series of shape frames on four steel rods along the longitudinal direction. Both fuselage nose and tailcone shapes have been refined trough polyurethane foam. Winglets, wing tips, nacelles and tailplanes (also elevator and rudder surfaces) have been built in synthetic resin with a CNC machine. Finally the model surface has been refined, smoothed and painted. The wing-fuselage connection is granted by coupling the clutching plates of the two parts through four bolts, see Fig. 3.6(a). Winglet, wing tips, and tailplanes are secured to the wing or fuselage through steel plugs as shown in Fig. 3.6(b). The main geometrical characteristics of the scale model are summarized in Tab 3.3[4]. The fuselage is provided of a special compartment specifically designed to allow the housing of the internal strain gage balance. The scale model is placed in the test section by mounting the fuselage on the balance plate, which is fixed to a special sting that leads the model to be located at about the half of the test section. Fig. 3.9 shows the complete aircraft model in the test section. A wooden fairing, finished with modelling clay, that connects the wing to the fuselage,

[3] ADAG - Aircraft Design & AeroFlightDynamics Group, the Aircraft Design and AeroflightDynamics Group (ADAG) is a part of the Department of Industrial Engineering - Aerospace Engineering Division .
http://www.adag.unina.it.

[4] All distances are referred to a coordinate system with its origin placed in the fuselage nose, the x axis is corresponding to the reference fuselage line, downstream oriented, while y and z axes are orthogonal to the x axis, along the wing span and in the vertical direction respectively. The y axis is positively oriented in the right wing direction while z axis is positively oriented downward.

(a) Detail of the connection between the wing and fuselage.

(b) Detail of connection fo the wing tips to the wing.

FIGURE 3.6: P2012 at the Tecnam factory.

has been realized and fixed to the model, being careful to seal all the gaps in the wing and fuselage junction areas, as shown in Fig. 3.10. All the gaps due to the junction between the several aircraft components have been sealed through the use of tape or modelling clay. Different solutions have been used to allow the handling and the measurement of deflection angles of the movable surfaces(elevator, rudder and flaps). Two metal plates, fixed to the bottom surface of the rudder and the to the fuselage respectively have been used. The first plate is pierced to allow the fixing of a bolt provided with two small metal tabs, see Fig. 3.11(a), that allow to fasten this system to the metal plate fixed on the fuselage. The plate fixed to the fuselage is provided with a goniometer with its centre placed in the hinge of the rudder. The fuselage symmetry plane has been chosen as reference for the zero rudder deflection. A thin metal tip acting as indicator has been fixed on the rudder trailing edge, see Fig. 3.11(b). This system allows an accuracy of about $\pm 2°$ in measuring the rudder deflection. This system allows a range of rudder deflection between [-30°,+30°]. The solution used to change the elevator deflection consists of a thin metal plate with a buttonhole, fixed in the fuselage cone, and two tabs that clench together on the main metal plate locking the elevator in a certain position, see Fig 3.12(a). In order to read the elevator deflection an electronic bubble level, with an accuracy of $\pm 0.2°$, has been used. The level has been fixed on a wooden support specially shaped to fit on the elevator surface, see Fig. 3.12(b). The accuracy of this system also depends on the horizontal tail plane attitude angle and on the elevator deformation due to the weight force of the measurement system. Ultimately it can be stated that the accuracy of this system is about $\pm 1°$. This handling system allows a range of elevator angle of about [+10°;-25°]. A similar system has been also used to measure the flap deflection. In Fig. 3.13(a) and in Fig. 3.13(b) are shown the measured angles for the flap up and take off flap condition respectively. The accuracy of this system into measuring the flap deflection is about $\pm 3°$.

TABLE 3.3: P2012 Traveller scale model, main characteristics.

Wing	
S_W	0.331 m^2
b_W	1.6 m
c_{root}	0.219 m
c_{kink}	0.219 m
c_{tip}	0.165 m
c_{mac}	0.214 m
x_{ac}	0.558 m
y_{ac}	0.372 m
z_{ac}	0.144 m
Horizontal tail	
S_h	0.0794 m^2
b_h	0.651 m
c_{root}	0.143 m
c_{tip}	0.099 m
c_{mac}	0.121 m
l_h	0.704 m
Vertical tail	
S_v	0.046 m^2
b_v	0.289 m
c_{root}	0.218 m
c_{tip}	0.095 m
l_v	0.649 m
Fuselage	
l_f	1.321 m
w_f	0.183 m

3.5 Test Procedure

The typical experimental test is structured as follow:

1. **Calibration**: since the experimental target is the measurement of the aerodynamic forces and moments, a calibration procedure is needed in order to have the net aerodynamic forces acting on the model. Because the centre of gravity of a certain configuration does not correspond to the balance centre, the mass distribution of a configuration will affect the measurements of lift, drag and pitching moment. Thus in order to have the estimation of the net aerodynamic forces/moments, for each tested configuration, the weight contributions on each measured quantity must be estimated before the experimental test being performed (in tunnel off condition). The calibration procedure is stepped as follow:

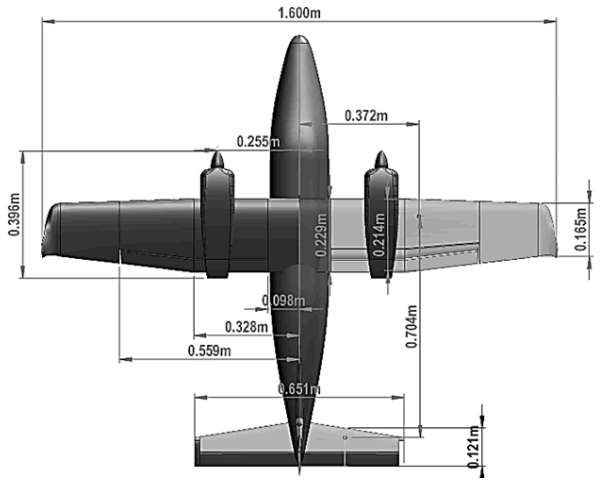

(a) Top view and main geometrical characteristics.

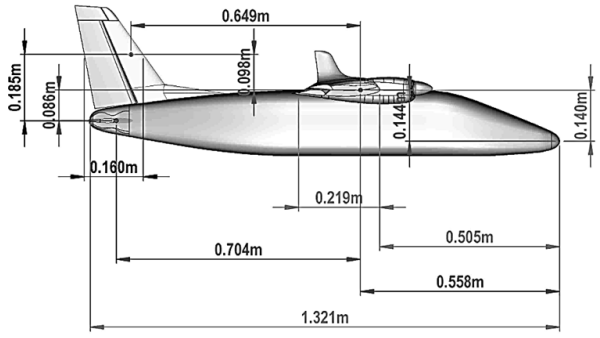

(b) Side view and main geometrical characteristics.

FIGURE 3.7: P2012 Traveller scale mode, top and lateral view (CAD).

- the model is placed at zero incidence angle (with a tolerance of $\pm 0,05°$);
- balance measurements are reset;
- the model is placed at the minimum angle of incidence (in this case about $-4°$);
- balance measurements are acquired at each model attitude (the used step for the calibration procedure in this case is $+1°$) till the maximum available angle of pitch[5] (in this case about $10°$);
- the acquired data are used to extract interpolation laws. This way the estimation of the contribution to each measured force/moment introduced by the weight of the tested model can be subtracted to obtain the net force/moment measurements.

[5]Although the maximum allowable pitch angle is about $20°$ tests have been limited within the range of $\alpha \in [-3.5°; +10°]$ because of structural reasons dealing with higher vibrations induced on the model by the large separated flow, especially in the flapped condition.

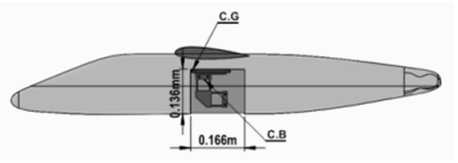

(a) Side view and sizes of the compartmente for the balance housing.

(b) Detail of the balance fixing in the fuselage.

FIGURE 3.8: P2012 Traveller scale mode, top and lateral view (CAD).

FIGURE 3.9: P2012 Traveller scale model in the test section.

2. **Data acquisition**: immediately after forces and moments have been reset, the tunnel is set on and led to the operative conditions. The operator acquires the data at each attitude after a waiting time of about 3 seconds to grant a stationary conditions of the flow. The acquisition software samplings data at 1000 Hz printing at video the mean value of the last 1000 acquired data, updating them each second. For the longitudinal tests, data have been acquired starting from the zero incidence angle then the model has been pitched down till -4° with a step of -0.5°. Once the minimum pitch attitude has been reached the model has been driven again at the zero incidence angle (acquiring again the set of data for this condition). Then the model has been driven to the maximum allowable pitch attitude (+0.5° step) . Dealing with the lateral-directional tests the model has been setted to the zero sideslip condition. Once the zero sidesplip conditions have been acquired the

(a) Wing-fuselage wooden fairing.

(b) Wing-fuselage junction sealed with modelling clay.

FIGURE 3.10: Wing-Fuselage fairing and gaps sealing.

(a) Handling and measurament system of the rudder, side view.

(b) Handling and measurament system of the rudder, rear view.

FIGURE 3.11: Rudder handling and deflection measurement system.

model has been driven at the minimum lateral attitude (about -25°) with a step of -2°, and then it has been bring back to the initial attitude and the sampling has been continued till the maximum available sideslip angle of about +30° has been reached, with a sampling step of about +2°. During a lateral directional test the operator must monitor the value of the incidence angle and if the variation of this angle is in excess must provide a correction of the model pitch attitude before the data acquisition.

3. **Data elaboration and storage**: the aerodynamic force and moment coefficients are calculated by the acquired measurements of forces and dynamic pressures. To these coefficients two different corrections have been applied:

   - **Moments transfer**

(a) Handling system of the elevator, rear view.

(b) measuring system of elevator deflection, $\delta_e = -10°$.

FIGURE 3.12: Elevator handling and deflection measurement system.

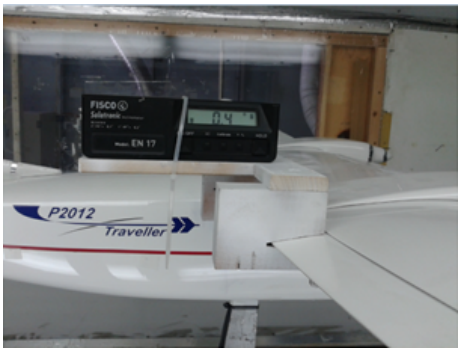

(a) Flap up condition, measured off set angle.

(b) Flap take-off, measured angle.

FIGURE 3.13: Flap handling and measurement system.

- **Wind tunnel corrections**

A point placed at 25% of the wing mean aerodynamic chord, along the longitudinal axis, and 25% of the wing mean aerodynamic chord along the vertical axis, below the wing mean aerodynamic chord plane, has been chosen as the reference point for the calculation of the aerodynamic forces and moments. Fig. 3.14 schematically illustrates the location of the reference point with respect to the fuselage nose. Since the

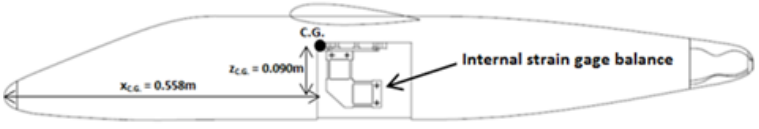

FIGURE 3.14: P2012 scale model, chosen centre of gravity.

centre of balance does not coincide with the chosen reference point the aerodynamic moments must be transfer to the desired reference point. Since the balance is integrated with the model, the transfer of the pitching, rolling and yawing moment form the balance centre to the chosen reference point can be expressed as shown in Eq. 3.6.

$$\begin{aligned} M_{y_{cg}} &= M_{y_{cb}} + F_z \cdot \Delta x + F_x \cdot \Delta z \\ M_{x_{cg}} &= M_{x_{cb}} - F_y \cdot [\Delta z \cdot cos(\alpha) + \Delta x \cdot sin(\alpha) + \Delta z] \\ M_{z_{cg}} &= M_{z_{cb}} - F_y \cdot [\Delta x \cdot cos(\alpha) - \Delta z \cdot sin(\alpha) + \Delta x] \end{aligned} \tag{3.6}$$

where the subscripts *cg* and *cb* indicate the chosen reference point and the balance centre respectively. The suffix x,y and z indicates that the force or moment is in the direction (or respect with) the longitudinal, lateral and vertical axis respectively. The quantities Δx and Δz are the longitudinal and vertical distances of the chosen reference point from the balance centre respectively. Forces and moments of Eq. 3.6 are intended to be the net aerodynamic forces and moments. Tab. 3.4 shows the coordinates of the chosen reference point and the longitudinal and vertical distances between this point and both balances centre. All the

Table 3.4: P2012 scale model, force and moments reference point location.

Reference point location		
x_{cg}	y_{cg}	z_{cg}
0.558 m	0.000 m	0.091 m
Longitudinal strain gage balance		
Δx_{cb}	Δy_{cb}	Δz_{cb}
-0.038 m	0.000 m	-0.029 m
Lateral-directional strain gage balance		
Δx_{cb}	Δy_{cb}	Δz_{cb}
-0.058 m	0.000 m	-0.077 m

required corrections to the acquired experimental data have been applied as suggested by Rae and Pope [55] to take into account the wind tunnel walls effects.

The wind tunnel walls presence produces a lateral constraint to the flow pattern about the body, this is known as solid blockage. The solid blockage leads to an increase of the dynamic pressure, increasing all forces and moments at a given angle of attack. Wind tunnel walls produce a lateral constraint to the flow pattern about the wake known as wake blockage, which increases with the wake size and this, in a closed test section, leads to an overestimation of the drag. The presence of lateral boundaries also produces an alteration of the normal curvature

of the flow about the wing so that the wing pitching moment and lift coefficient are increased. Moreover wind tunnel walls change the normal downwash behind the wing, so the measured longitudinal stability is too large in a closed test section. This is correction must be carefully taken into account because the complete scale model in the test section appears to be very much more stable than that it would be in free air, Ref. [55, 56]. All those effects are clearly outlined in Fig. 3.15 where comparison between the corrected and uncorrected experimental results for the complete aircraft lift, Fig. 3.15(a), drag Fig. 3.15(b) and pitching moment Fig. 3.15(c) coefficients is shown (the pitching moment shown in Fig. 3.15(c) is simply referred to the strain gage balance centre). Effects of wind tunnel walls must be taken into account also for the lateral-directional tests. The boundary effects of a closed test section could lead to an alteration of an asymmetrically loaded wing, see Fig. 3.15(d). The ratio between the scaled model wing span and the test section width is 0.8 while the ratio between the test section width and height is 0.7; this means that scaled model dimensions are within the range of wind tunnel walls correction effectiveness, as suggested by Rae and Pope [55]. Tab. 3.5 summarizes the aircraft components volumes

Table 3.5: P2012 scale model, voulumes and solid blockages.

Buoyancy Drag Coefficient	-0.0005
Volumes	
Wing volume (m^3)	0.0070248
Fuselage volume (m^3)	0.02736
Nacelle volume (m^3)	0.0016461
Horizontal tail volume (m^3)	0.000715
Vertical tail volume (m^3)	0.0008754
Solid blockages	
Wing volume (m^3)	0.001473698
Fuselage volume (m^3)	0.004983115
Nacelle volume (m^3)	0.000345327
Horizontal tail volume (m^3)	0.000141225
Vertical tail volume (m^3)	0.000173713
$dC_{M_{tail}}/d\alpha$ (deg^{-1})	-0.0435

and solid blockage coefficients useful to apply the wind tunnel corrections.

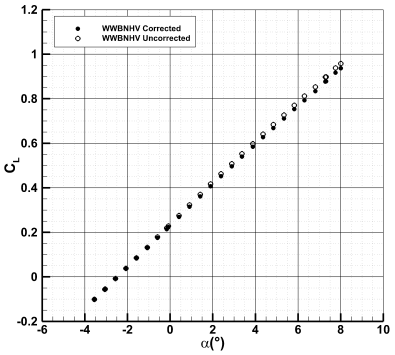

(a) Effect of wall corrections on lift.

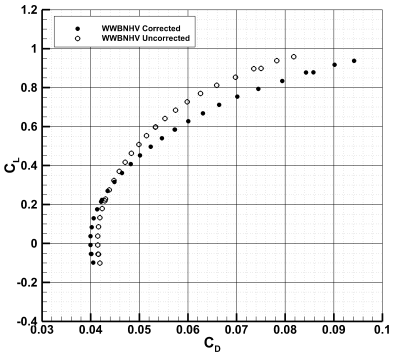

(b) Effect of wall corrections on lift.

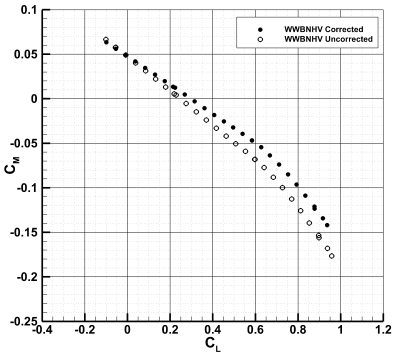

(c) Effect of wall corrections on pitch.

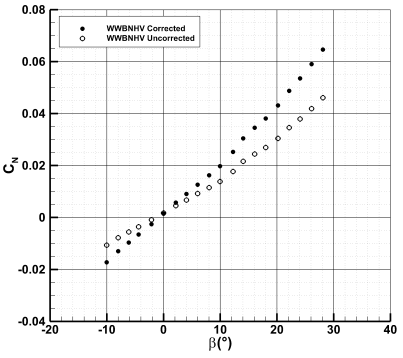

(d) Effect of wall corrections on yaw.

FIGURE 3.15: Effects of the wind tunnel walls corrections on the aerodynamic coefficients.

3.6 Transitional strips

All tests have been performed at a wind speed of about 40 m/s (the maximum available wind speed is about 50 m/s) with a Reynolds number of about 0.6 million (referred to the mean aerodynamic chord). It is well known that the Reynolds number effects can be profound on essentially all quantities of interest such as forces, stability moments, etc. Obviously, it behoves the tunnel engineer either to provide wind tunnel Reynolds number equal to flight (a procedure rarely possible), or to somehow make the model boundary layer duplicate that of the full scale aircraft. This is accomplished by the use of a transitional strip. A transitional strip is an artificial roughness added to the model in order to fix the location of the transition from laminar to turbulent boundary layer on the model, avoiding aerodynamic phenomena dealing with the low Reynolds number effects (such as laminar separation bubbles). Transitional strips have been placed on all components of the aircraft in order to promote the transition of the flow. The thickness and the right position of the transitional strips has been estimated by tests of flow visualization through the use of fluorescent oil (transitional strips have been placed about 5% of local chord, both on the lower and upper surfaces, of all components and have a thickness of about 0.3 mm). Fig. 3.16 shows a flow visualization (in this case, for major clarity of the picture, coloured oil has been used without the ultra-violet lamp) highlighting the transitional strip effects. As it can be seen a laminar bubble is clearly visible on the wing upper surface close to the leading edge and on the nacelle component, while on the right picture the three layers transitional strip avoids these phenomena. Moreover, due to the model scale factor, several aircraft components (flaps, winglets, control surfaces) have not completely representative geometrical dimensions and will not lead to a reliable aerodynamic condition. For example, flapped configuration tests were not mainly aimed to the right estimation of aircraft high lift performances, due to the very low dimension of gap and consequent possible chocked flow at test Reynolds number (the gap is lower than 9 mm in landing condition), but they were addressed to the estimation of stability and aircraft trim capabilities for take-off and landing flight conditions.

(a) Visualisation test, laminar separation bubble.

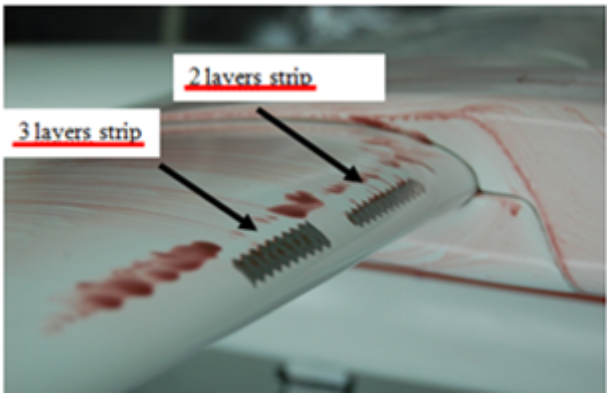

(b) Effect of the transitional strip thickness.

FIGURE 3.16: Effect of low Reynolds number, laminar separation bubble.

3.7 Longitudinal Wind Tunnel Tests

Longitudinal tests have been performed in order to evaluate aircraft stability and control characteristics and aerodynamic derivatives. Several aircraft configuration have been tested in order to evaluate the aircraft components effect on the longitudinal stability, in particular the fuselage and nacelles contribution. An experimental investigation about effects of the vertical position of the horizontal tailplane has been assessed by testing three different positions for the tailplane. Finally complete aircraft configuration at two horizontal tailplane incidence angles have been tested for two flap deflections (flap up and full flap deflection), in order to fulfil a trim analysis of the aircraft with the most forward centre of gravity position and check the right sizing of the tailplane.

3.7.1 Lift and pitching moment coefficient breakdown and downwash estimation

Tests have been performed on several configurations such as body isolated, wing-body, complete aircraft with and without nacelles and winglets with the aim to evaluate mutual effects on aircraft aerodynamics (in particular their effect about the longitudinal stability). In Fig. 3.17 the lift coefficient of several configurations is shown. As it can be seen the lift slope is slightly modified by the two nacelles. The measured wing-body lift slope is about 0.080 deg^{-1}, while the wing-body-nacelles configuration shows a lift slope of about 0.082 deg^{-1} (see also Tab. 3.6) highlighting an almost neutral effect of the nacelle, with a behaviour similar to a symmetrical airfoil also due to a higher nacelle length. Even though the nacelles contribution to the lift seems to be negligible, their contribution to the aircraft longitudinal stability is quite remarkable. Since about the 30% of the nacelles chord lies forward of the wing leading edge, and thus well forward of the chosen position for the aircraft centre of gravity, the nacelles contribution to the aircraft longitudinal stability is relevant. Fuselage contributes to an aft shift of the wing aerodynamic centre of 12% of the mean aerodynamic chord compared to the wing-body configuration[6]. The coupled effect of fuselage and nacelles in terms of aft shift of the aerodynamic centre, can be estimated by the ratio $C_{M_{\alpha_{WBN}}}/C_{L_{\alpha_{WBN}}}$, leading to a shift of about 15.5%. Thus, since the contribution due to the fuselage alone is 12%, it can be deduced that the nacelles contribution is of about 3.5% in terms of the shift of the aerodynamic centre. It is also interesting to notice the wing pendular stability, due to the low position of the CG with respect to the wing chord, where aerodynamic loads are applied. In Tab. 3.6, the summary of the experimental results in terms of aerodynamic derivatives is shown. Complete aircraft neutral point in clean configuration is about 47%

[6]The fuselage contribution in terms of shift aft of the wing aerodynamic centre has been estimated as $C_{M_{\alpha_B}}/C_{L_{\alpha_{WB}}}$

of the mean aerodynamic chord and the estimated downwash derivative is equal to 0.36. The neutral point can be estimated as shown in Eq. 3.7.

$$N_0 = \frac{dC_M}{dC_L} + \bar{x}_{cg} \tag{3.7}$$

The horizontal tail contribution to the complete aircraft lift and pitching moment coefficient can be expressed as shown in Eq. 3.8, whereas and Eq. 3.9 shows the tail contribution to lift and pitching moment in the winglet off condition (or without downwash effects).

$$\begin{aligned} (C_{L_h})_{wing,on} &= (C_{L_h})\eta_h \tfrac{S_h}{S_w}(1 - \tfrac{d\epsilon}{d\alpha})\alpha_h \\ (C_{M_h})_{wing,off} &= (C_{L_h})\eta_h \tfrac{S_h l_h}{S_w \bar{c}}(1 - \tfrac{d\epsilon}{d\alpha})\alpha_h \end{aligned} \tag{3.8}$$

$$\begin{aligned} (C_{L_h})_{wing,on} &= (C_{L_h})\eta_h \tfrac{S_h}{S_w}\alpha_h \\ (C_{M_h})_{wing,off} &= (C_{L_h})\eta_h \tfrac{S_h l_h}{S_w \bar{c}}\alpha_h \end{aligned} \tag{3.9}$$

Comparing Eq. 3.8 and Eq. 3.9 it is possible to estimate the downwash derivative. Assuming that the dynamic pressure ratio (η_h) in both wing on and wing off configurations is the same, the downwash factor can be estimated as illustrated in Eq. 3.10.

$$\begin{aligned} (1 - \tfrac{d\epsilon}{d\alpha}) &= \tfrac{(C_{L_h})_{wing,on}}{(C_{L_h})_{wing,off}} \\ (1 - \tfrac{d\epsilon}{d\alpha}) &= \tfrac{(C_{M_h})_{wing,on}}{(C_{M_h})_{wing,off}} \end{aligned} \tag{3.10}$$

Thus the estimation of lift and pitching moment curve slope of the horizontal tailplane in both wing on and wing off configuration is required. Those derivatives have been estimated by subtracting the body contribution from the complete (BH) configuration derivative and by subtracting the contribution of the (WWBN) configuration to the (WWBNHV) configuration (note that the WWVBN and WWBNV configuration can be considered equivalent in terms of longitudinal stability since the vertical tail contribution to the pitching moment is negligible). The downwash derivative has been estimated from both lift and pitching moment coefficient, the most accurate estimation should be

the one coming from the pitching moment slope, because the therms l_h leads to increase the sensitivity of the measurement of the downwash effects, the value of the downwash derivative is $d\epsilon/d\alpha = 0.360$.

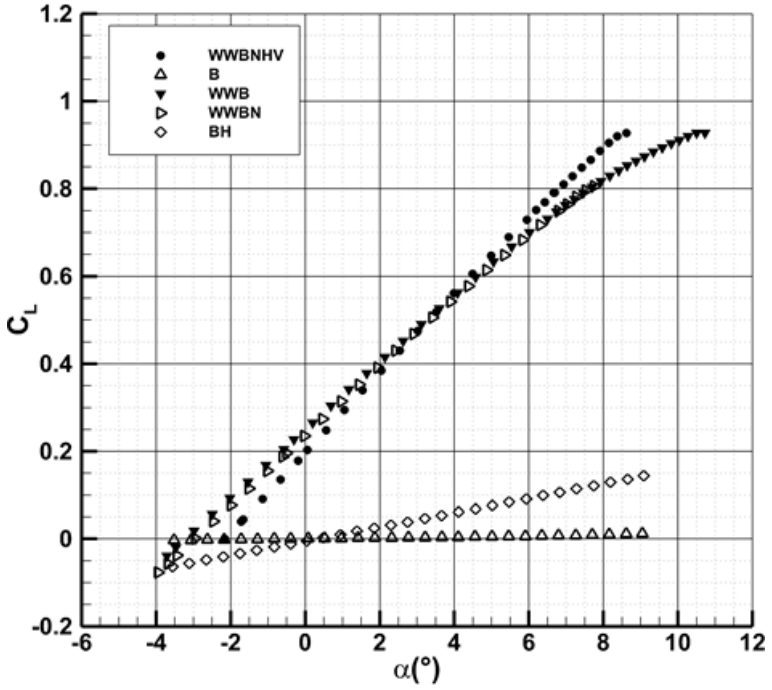

FIGURE 3.17: Lift coefficient breakdown.

TABLE 3.6: Lift and pitching moment curve slope breakdown, range of $\alpha \in [0 - 6°]$.

C_{L_α} complete	0.0911 deg^{-1}
C_{L_α} wing-winglet-body	0.080 deg^{-1}
C_{L_α} wing-winglet-body-nacelles	0.0820 deg^{-1}
C_{M_α} complete	-0.0200 deg^{-1}
C_{M_α} wing-winglet-body	0.00870 deg^{-1}
C_{M_α} wing-winglet-body-nacelles	0.0127 deg^{-1}
C_{M_α} body	0.0097 deg^{-1}
N_0	47% $\bar{c}$
$d\epsilon/d\alpha$	0.360
Δx_{ac} body	12% $\bar{c}$
Δx_{ac} nacelles	3.5% $\bar{c}$

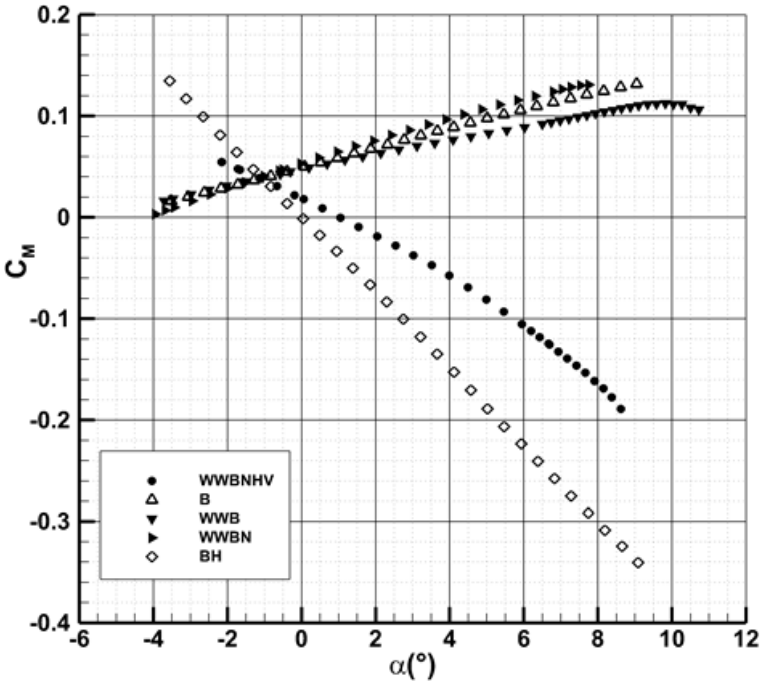

FIGURE 3.18: Pitching moment coefficient breakdown.

3.7.2 Drag Coefficient Breakdown and Induced Drag Factor

Drag coefficient variation with respect to the lift coefficient for several configurations is shown in Fig. 3.19. The aim of this investigation is to perform a drag coefficient breakdown in order to estimate aircraft components drag contribution in terms of percentage of influence and not to evaluate the real drag value because of the low Reynolds number during tests. Tab. 3.7 summarized the drag coefficient at zero lift condition. Results show a zero-lift drag coefficient for complete aircraft of about 400 drag count. Fuselage contribution is about 110 drag counts; the wing-winglet-body configuration shows a zero-lift drag coefficient of about 326 drag counts. Comparing the wing-body-winglet configuration with the isolated body it is possible to estimate that the wing-winglet plus the wing-body high-wing interference is about 216 drag counts. The contribution of the two nacelles is about 35 drag counts (obtained comparing the WWBN and the WWB configuration including also the interferences effects with the wing), showing a moderate drag contribution of the two nacelles. Both vertical and horizontal tailplanes add about 20 drag counts each one. It must be reminded that all experimental tests have been performed at a Reynolds number of 0.6e6 million (referred to the mean aerodynamic chord) thus the illustrated results dealing with the drag estimation cannot be considered representative of a typical flight condition (free flight Reynolds number in cruise is about 9.5e6). However an estimation of the components contribution to the drag coefficient of the aircraft can be

observed in Tab. 3.8, where is visible that wing component has more than 50% of zero-lift drag (wing plus WB interference), fuselage has about 30%, nacelles 8%, tailplanes 10% (vertical and horizontal) and winglet about 2%. A reliable estimation of the Reynolds number scaling effect, as suggested by Rae and Pope [55], and also by Patterson and Rizzi [57] through also the use of CFD computations, can be the application of the formula proposed by Prandtl and Schlichting, Ref. [58] , which correlates the flat plate skin friction coefficient to the Reynolds number. Assuming a free flight Reynolds number of about 9.5 million and under the assumption of a fully turbulent flow (a reliable assumption considering that the experimental tests have been conducted applying transitional strips on all the aircraft components) the application of the Prandtl-Schlichting formula leads to a C_{D_0} of about 244 drag counts at free flight conditions (this value does not take into account of the landing gear and wheels contribution and of the propulsion effects). Experimental

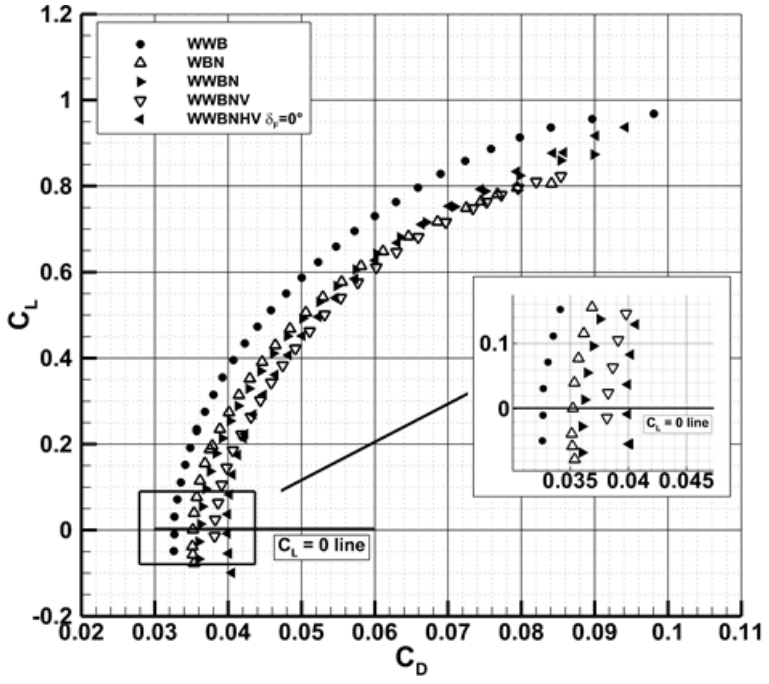

FIGURE 3.19: Drag coefficient breakdown.

tests have shown that the complete aircraft has an Oswald's factor of about 0.81, which is 10-11% higher than the complete aircraft without winglet as shown in Fig. 3.20 where the different slope at medium and high attitude represents winglet effect on drag coefficient. Doubtless the winglet introduces a drag penalty at low angles of attack of about 8 drag counts (at wind-tunnel Reynolds number) as shown in Tab. 3.7. This result is in accordance with the numerical estimation presented in section 2.4. Concerning winglet effects, it is relevant to highlight that winglets allow an overall drag coefficient reduction (the induced drag reduction becomes higher than the parasite drag penalty due

to the winglets) for lift coefficients higher than 0.50, as it can be observed from Fig 3.20. The experimental drag breakdown does not take into account of the

TABLE 3.7: Experimental drag coefficient breakdown.

B	0.0110
WWB	0.0326
WBN	0.0352
WWBN	0.0361
WWBNV	0.0381
WWBNHV $\delta_F = 0°$	0.0400
WWBNHV estimated at Re = 9.5e^6	0.0244

contribution of several additional drag sources, being wheels and landing gear, engine cooling, wind shield and excrescences. If a more reliable drag polar estimation would be performed, additional contributions can be added to the zero lift drag coefficient estimated by the wind tunnel tests and corrected to take into account of the Reynolds number effect. In sec. 2.19 the preliminary drag polar has been estimated through a classical semi-empirical approach, see Tab. 2.6. Thus if contributions to drag that are not available from the experimental tests will be added to the zero lift drag experimentally estimated a more reliable estimation of the complete aircraft zero lift drag coefficient could be obtained. Tab. 3.9 shows the result of this approach. Comparing the results of a pure semiempirical approach with the mixed approach it is possible to appreciate how both zero lift drag coefficients are in accordance, granting much more reliability to the predicted C_{D_0}.

TABLE 3.8: Experimental aircraft component contribution to the drag.

Component	C_{D_0}
Fuselage	27%
Wing plus Wing-Body interferences	52%
Nacelles	8%
Horizontal tail	5%
Vertical tail	5%
Winglets	2%

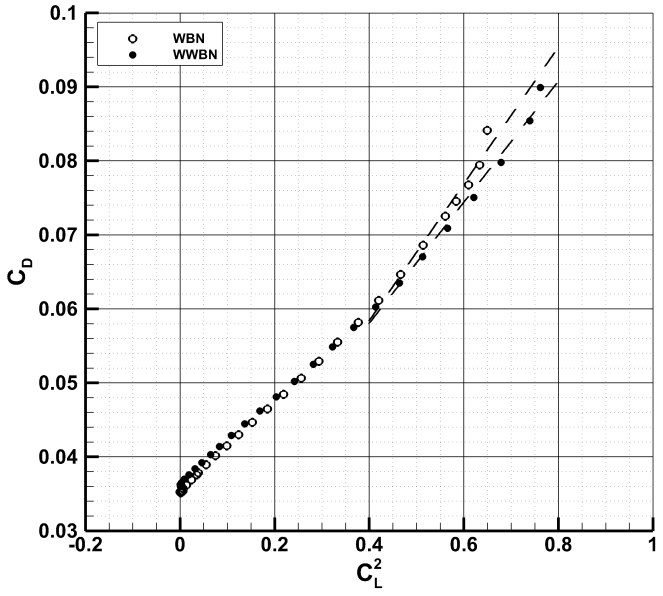

FIGURE 3.20: Winglet effect on induced drag coefficient, C_D vs. C_L^2.

TABLE 3.9: Experimental plus semi-empirical complete aircraft zero lift drag coefficient.

WWBNHV at Re = 9.5e^6	0.0244
Semi-empirical contribution of:	
Wheels and landing gear	0.00313
Wind shield	0.00160
Excrescences	0.00149
Total at Re = 9.5e^6	0.03062

3.7.3 Complete Aircraft at Several Flap Deflections

Complete aircraft configuration at three flap deflections have been tested in order to estimate the flap contribution to lift and especially to longitudinal stability characteristics. Tested flap deflections with flap up (retracted) configuration, flap deflection of 15° and full flap deflection of 40° are representative of cruise, take-off and landing condition respectively. Fig. 3.21 shows the

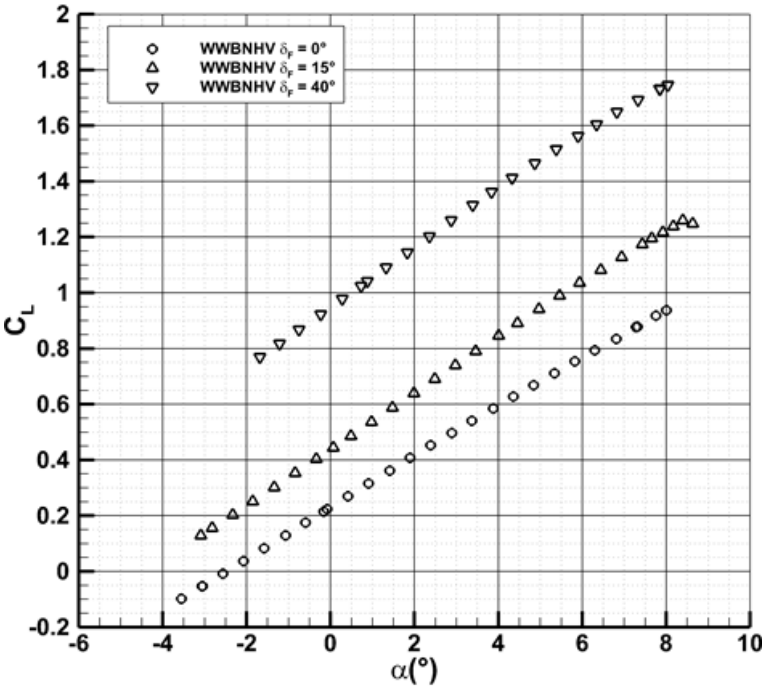

FIGURE 3.21: Complete aircraft at three flap deflection, C_L vs. α, $i_{t_0} = 0°$.

lift coefficient variation respect to the aircraft angle of attack highlighting the increase of the lift coefficient at zero angle of attack. The flap deflection leads to an increase of the lift curve slope of about 10%, as it is also outlined in Tab., since the single slotted flap is characterized also by a sensible (about 10%) increase of chord, with an effect similar to a fowler flap. Flap deflections lead to a lift coefficient increment of about 0.2 and 0.8 at zero angle of attack in take-off and landing condition respectively. Unfortunately the maximum lift coefficient and the angle of attack at which it occurs are strongly affected by the experimental Reynolds number. Tests with full flap deflection have been conducted up to angles of attack of about 9 degrees, but, as already pointed out, the flow separation observed (and consequent strong vibrations on the model) is indicative of incorrect flow conditions in the slot (choked flow) and consequent poor flap effectiveness due to low Reynolds number. Therefore, it is reasonable to expect maximum lift coefficients for the full scale aircraft at free flight Reynolds number (Reynolds number in landing conditions is about 4.5 million) much higher than these measured in the wind tunnel at low

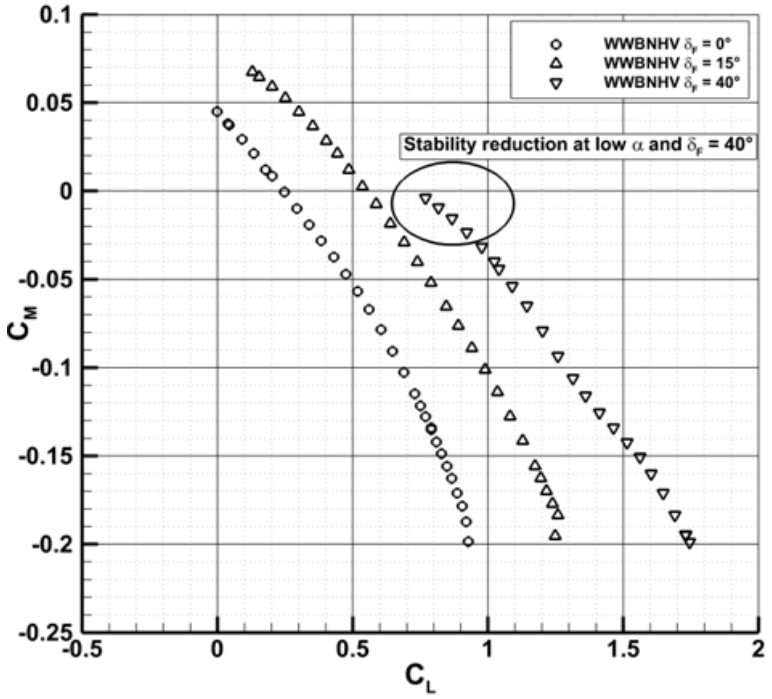

FIGURE 3.22: Complete aircraft at three flap deflection, C_M vs. C_L, $i_{t_0} = 0°$.

Reynolds number. Fig. 3.22 shows instead the pitching moment coefficient respect to the lift coefficient. Areas of a sensible reduction in the longitudinal stability can be found in the full flap condition and low angles of attack, where the interaction of the wing wake with the horizontal tailplane became stronger leading to both a reduction in the local dynamic pressure and an increased value of the downwash angle of the flow coming from the wing. Tab. 3.10 also illustrates the neutral point location in terms of mean aerodynamic chord at typical lift coefficients and outlines the effect of flap both in the zero angle of attack lift coefficient and in the zero lift drag coefficient (last column of Tab. 3.10).

TABLE 3.10: Experimental flap effect on complete aircraft configuration.

	$C_{L_\alpha}(deg^{-1})$	dC_M/dC_L	$N_0(\%\bar{c})$	ΔC_{L_0}	C_{D_0}
$\delta_F = 0°$	0.0911	0.205(at $C_L = 0.4$)	45.5	–	0.040
$\delta_F = 15°$	0.1010	0.297(at $C_L = 1.0$)	54.7	0.24	0.045
$\delta_F = 40°$	0.1050	0.251(at $C_L = 1.6$)	50.1	0.78	0.060

3.7.4 Experimental investigation about the vertical position of the horizontal tail

The original P2012 configuration layout provides for a body mounted horizontal tail with a symmetrical fuselage tailcone (see Fig. 2.18). This position for the horizontal tail plane could be interested by the wing wake in full flap and low angles of attack condition (as already outlined in sec. 3.7.3 and sec. 2.2.1); this and also considering that many similar aircraft such as the Cessna Caravan, see Fig.3.23(a), or the Britten Norman, see Fig. 3.23(b), provides the horizontal tail to be body mounted at the vertical tail plane root, has lead author to investigate about any possible alternative vertical position for the P2012 horizontal tailplane with the aim to minimize the wing wake interaction with the tail surface. Three different vertical positions for the horizontal tail

(a) Cessna Caravan 208B.

(b) Britten-Norman Islander.

FIGURE 3.23: P2012 competitors, horizontal tailplane position.

plane have been considered, referring to Fig. 3.24, these positions have been named as **POS. A**, **POS. B** and **POS. C**, progressively closed to the wing trailing edge. The vertical distances between the wing root trailing edge and the horizontal root leading edge are summarized in Tab. 3.11, where also the investigated configurations are shown. Position B and especially position C

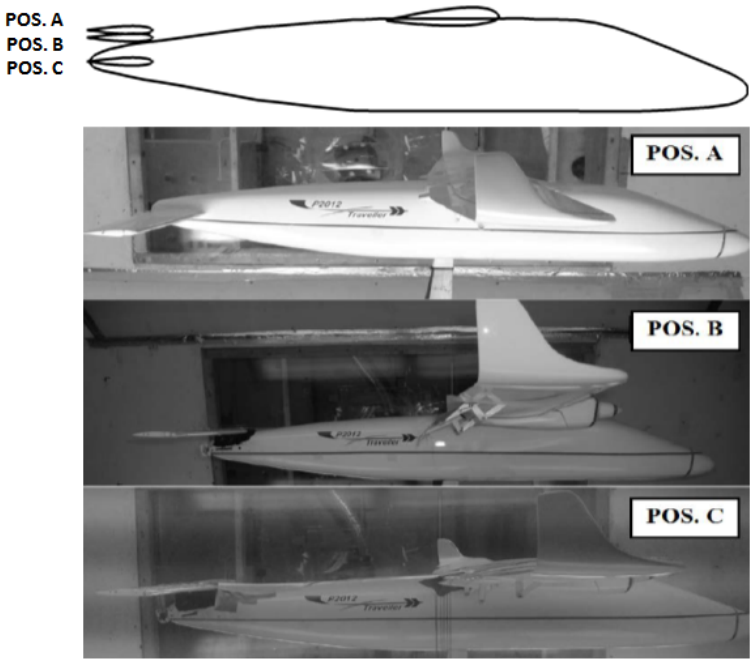

FIGURE 3.24: Layout of the three different vertical position of the horizontal plane experimentally investigated.

TABLE 3.11: Tested vertical position of the horizontal tail plane.

Vertical distance between wing root T.E. and horizontal tail L.E.		
	Scale 1:1	Scale model (1:8.75)
POS. A	0.72 m	0.082 m
POS. B	0.30 m	0.034 m
POS. C	0.17 m	0.019 m

could lead to better ground taxing (higher position of the horizontal tail and less possible interference with ground systems), and also could allow to increase slightly the fuselage upsweep and consequently increasing the possible rotation angle (limiting the main landing gear height) improving take-off performances. As negative aspects, these design solutions could lead to possible structural problems for horizontal tailplane connection (especially position C, with the horizontal tailplane structurally connected to the vertical tailplane) and could lead to problems coming from the possibility of the tailplane to be in the wing wake. Position A is optimal for fuselage drag (tailcone is almost symmetrical) but could lead to problems for ground taxing and low rotation angles. Also position A could be interested by the wing wake, but in full flap and low angles of attack conditions. A radical different design solution could also be identified in the T-tail arrangement, but for this aircraft has been not considered due to

increment in weight and costs due to the structural overload on the vertical tail and increment in complexity of all control systems belonging to the horizontal tailplane. Preliminary analysis have been performed in order to estimate the downwash angle and the wing wake characteristics (for power off condition) behind the wing both in clean condition (flaps up) and in flap down condition (take off flaps at about 15° and landing flap at about 40°). The investigation about the right positioning of the horizontal tail plane has been experimentally assessed. In order to evaluate the effect of the flap deflection on the horizontal tail, three flap conditions have been tested: flap up (cruise condition), flap 15° (take-off condition) and full flap 40° (landing condition). Tested tail positions are those previously illustrated in Tab. 3.11, the configuration under investigation is the complete aircraft. Results of those tests are shown in Fig. 3.25, Fig. 3.26 and in Fig. 3.27, where the pitching moment coefficient versus lift coefficient is plotted for the three vertical positions of the horizontal tail at the three considered flap deflections. As it is shown from graphs from Fig. 3.25 to Fig. 3.27, the longitudinal stability is variable with the lift coefficient range, and it is affected by the horizontal tail position especially for the flapped configurations, where the wing wake interaction with the tail surface became stronger, especially at low angles of attack and with POS. A. Tab. 3.12 shows the neutral point location, in percentage of the mean aerodynamic chord, for the highlighted typical lift conditions of Fig. 3.25, Fig. 3.26 and Fig. 3.27. Fig. 3.25 clearly shows how in the flap up condition the longitudinal stability gradually decreases as the horizontal tail is placed at reduced vertical distance from wing(from POS. A to POS. C), since the downwash became stronger and in some extreme condition the wing wake reduces the dynamic pressure acting on the tail. The POS. C is a critical position for the horizontal tail plane (see Fig. Fig. 3.25) since the tail surface is invested by the wing wake at high speed (cruise condition) with high risks of possible stick buffeting and structural fatigue for the horizontal tailplane structure. Fig. 3.26 shows how, in the take-off flap condition, POS. B is characterized by an area of sensible reduction of the stability due to the strong interaction of the wing wake with the tail surface. The neutral point moves forward from the 42% to the 37% of MAC (reduction of 5% of stability margin) at lift coefficient value of about 0.7. Fig. 3.27 shows how the POS. A, in the full flap configuration (landing condition), presents an area of a lower longitudinal stability at low angles of attack (alpha about -2°). However, these incidence are not typical flight condition for the aircraft with full flap deflected (landing condition) and should not lead to particular problems.

TABLE 3.12: Effect of vertical position of the horizontal plane, results.

Configuration		N_0 (% $\bar{c}$)	
FLAP = 0°	**POS. A**	**POS. B**	**POS. C**
$C_L = 0.2$	48.1	41.8	**39.2**
$C_L = 0.4$	47	45.2	42.3
$C_L = 0.6$	51.8	49.2	48.7
FLAP = 15°	**POS. A**	**POS. B**	**POS. C**
$C_L = 0.4$	44.7	41.9	39.6
$C_L = 0.7$	49.1	**37.2**	41.8
$C_L = 1.0$	54.7	49.4	43.8
FLAP = 40°	**POS. A**	**POS. B**	**POS. C**
$C_L = 1.0$	**43.9**	46.4	47.2
$C_L = 1.4$	47.0	44.3	49.8
$C_L = 1.6$	50.1	45.3	55.2

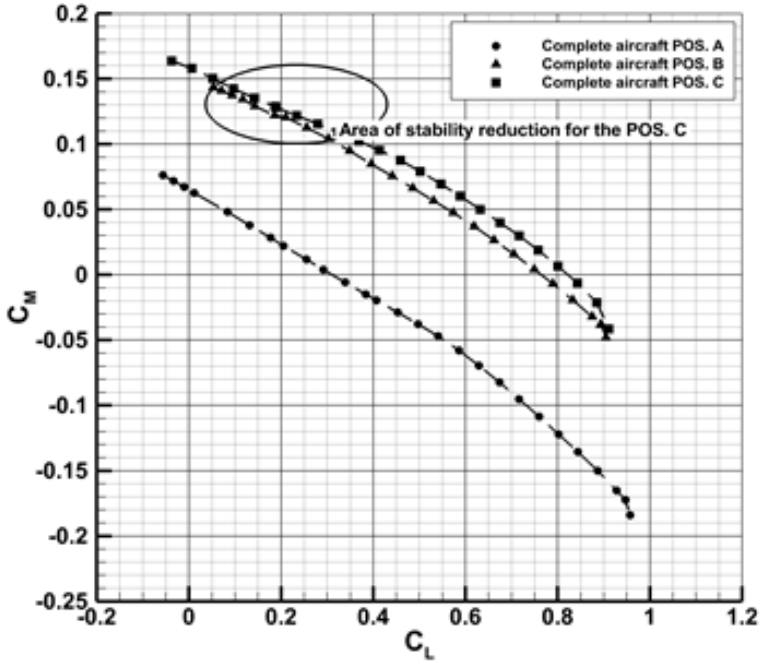

FIGURE 3.25: Pitching moment coefficient, Flap = 0°, $x_{cg}/\bar{c} = 0.25$, $z_{cg}/\bar{c} = 0.25$ and $i_{t_0} = 0°$.

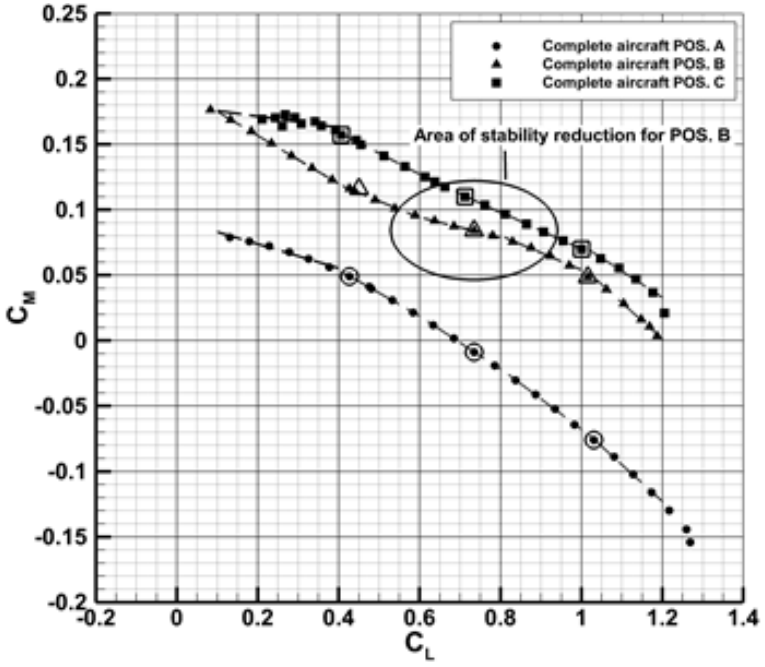

FIGURE 3.26: Pitching moment coefficient, Flap = 15°, $x_{cg}/\bar{c} = 0.25$, $z_{cg}/\bar{c} = 0.25$ and $i_{t_0} = 0°$.

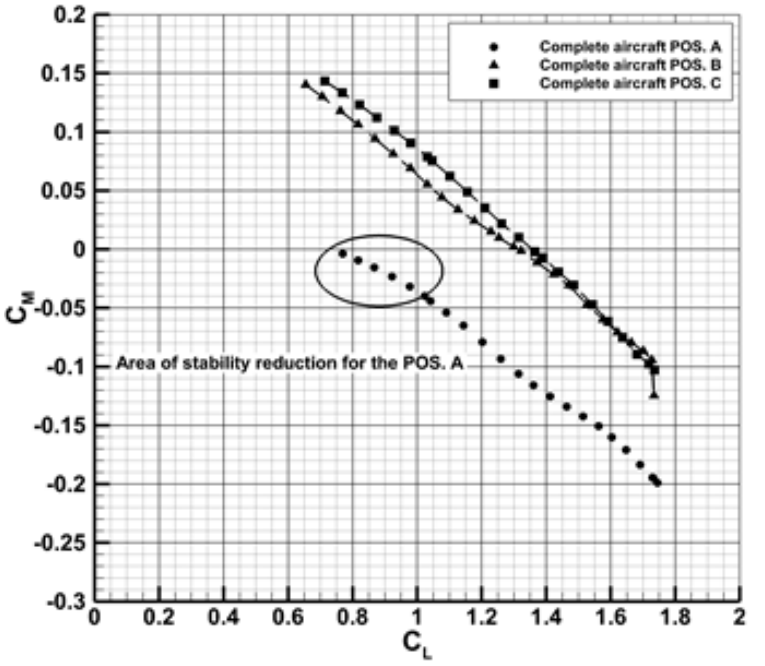

FIGURE 3.27: Pitching moment coefficient, Flap = 40°, $x_{cg}/\bar{c} = 0.25$, $z_{cg}/\bar{c} = 0.25$ and $i_{t_0} = 0°$.

This experimental investigation led to identify POS. A as the best position for the horizontal tail plane among all those tested.

3.7.5 Trim analysis

In order to have a validation of the aircraft trim capabilities, experimental tests have been performed on the complete aircraft configuration at several flap and elevator deflections. In particular the flap retracted and full flap deflections have been tested, typical of cruise and landing conditions respectively. Two different horizontal tail incidence angles have been considered, in particular $i_{t_0} = 0°$ and $i_{t_0} = -2°$. The most critical centre of gravity position has been considered, that is the most forward fixed at $x_{cg}/\bar{c} = 0.18$. Fig. 3.28 and Fig. 3.29 show the pitching moment coefficient with respect to the lift coefficient for the flap up and full flap condition, respectively, at several elevator deflections for two horizontal tail incidence angles. As it can be seen in Fig. 3.28 a horizontal tail plane incidence of -2° leads to trim the aircraft at about $C_L = 0.5$ without elevator deflection, value closer to cruise lift coefficient. In full flap configurations (Fig. 3.29), aircraft could be trimmed in the landing lift coefficient range of $1.2<C_L<1.8$ with about 0-10 degrees of deflection for the elevator. Experimental results for tests in full-flap landing configuration show that, especially considering a tail incidence of -2 degrees, the aircraft could be trimmed at lift coefficients up to 2.20 (extrapolation of upper solid circle line for intersection with x axis, $C_M=0$), with elevator deflection of -20 degrees. Considering these results, the final incidence for the horizontal stabilizer to be chosen for the full scale aircraft maybe slightly negative (i.e. -1 or -2 degrees). The negative incidence will then allow good pitch-up equilibrium and trim capabilities (useful for flight trim in landing, but also for take-off rotation phase).

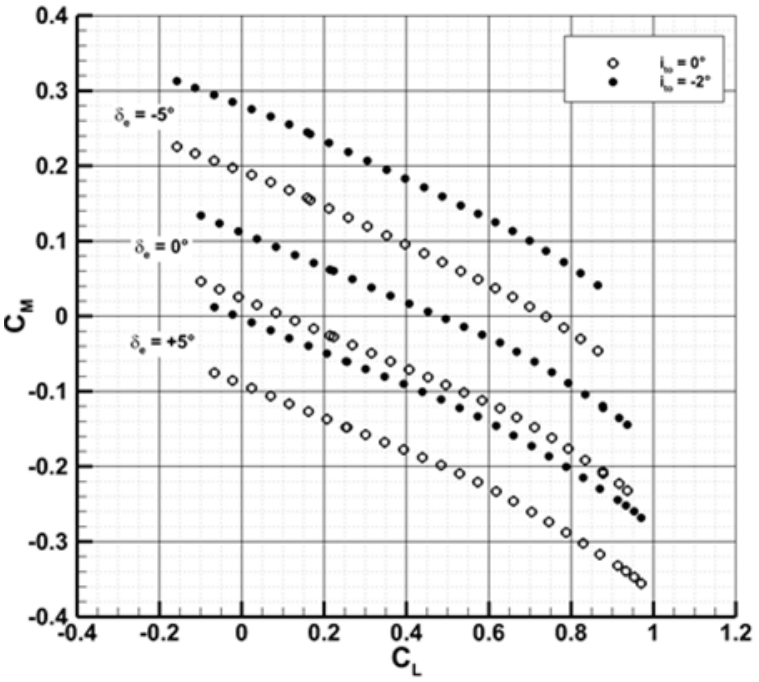

FIGURE 3.28: Experimental trim analysis, flap up, $x_{cg}/\bar{c} = 0.18$, $z_{cg}/\bar{c} = 0.25$.

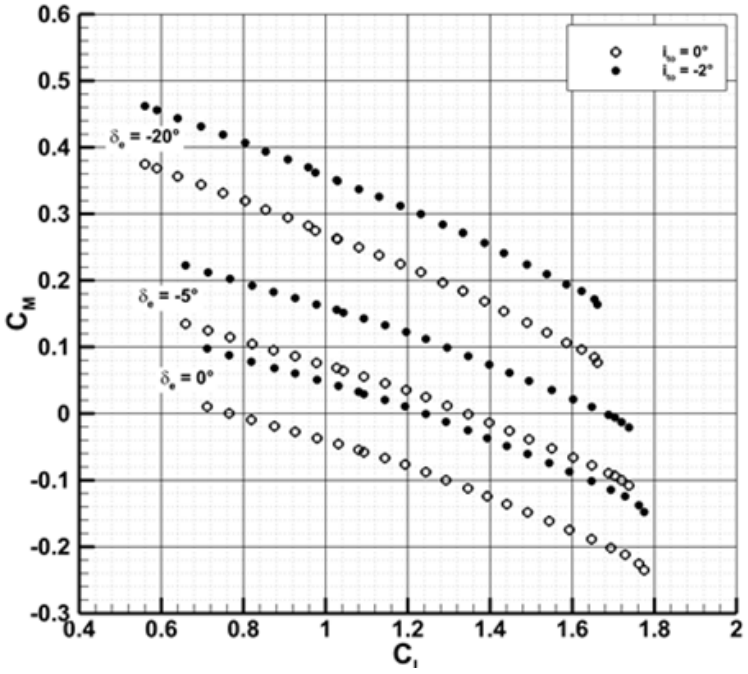

FIGURE 3.29: Experimental trim analysis, full flap, $x_{cg}/\bar{c} = 0.18$, $z_{cg}/\bar{c} = 0.25$.

3.8 Lateral-Directional Tests

Several wind-tunnel tests have been conducted in order to estimate the lateral-directional stability and control aerodynamic characteristics. During the preliminary design and sizing phase particular attention has been paid to the vertical tail design which is crucial to achieve commercial success of this aircraft category. As a matter of fact the minimum control speed (VMC), which strongly depends on the vertical tail sizing, has to be limited in order to reduce the accelerate stop distance (which depends on the engine failure speed VEF). The vertical tail design has been carried out to ensure equilibrium during take-off in one engine inoperative condition (OEI), and also in order to accomplish with a good control efficiency of the rudder in presence of lateral gust (a well-designed vertical tail and rudder should assure that the ratio between the required rudder $\delta_{r,eq}$ and sideslip angle β in steady sideslip should be about 0.8-1 in the linear range to guarantee the possibility to equilibrate the aircraft up to 15-20 degrees of sideslip angle, see sec. 2.2.1). Therefore several experimental tests have been conducted in order to estimate both aircraft directional and control derivatives. Tests to estimate the lateral stability of the aircraft have been also carried out highlighting for example, how the winglets affect the dihedral effect.

3.8.1 Yawing moment coefficient breakdown and directional control

Isolated vertical tail, isolated body, body-vertical, complete aircraft configuration and tailplanes off aircraft configuration have been tested in order to estimate the contribution to directional stability of each aircraft component and aircraft stability (see Fig. 3.30). Fig. 3.31 shows the yawing moment coefficient variation respect to the sideslip angle of the above mentioned aircraft configurations. Tests show that the complete aircraft has a derivative of about 0.00197 deg^{-1}, isolated vertical tail is characterized by a directional derivative C_{N_β} of about 0.00228 deg^{-1}, while the fuselage directional instability is about -0.00100deg^{-1}. Comparing both WWB and the WWBN configurations with the isolated body it is possible to appreciate an increment in the fuselage directional instability of about 10% due to the wing sidewash effect. The nacelles contribution is negligible (compare the WWB and the WWBN configurations). Tab. 3.13 shows the global directional derivatives of the tested configurations. The sidewash effect combined to the streamlined shape of the fuselage tail cone in the WWBNV configuration leads to a C_{N_β} of 0.0122 deg^{-1}. The body mounted horizontal tail plane increases the yawing moment derivative of about 60% by comparing the WWBNHV and WWBNV (horizontal tailplane off configuration. This large increment in the directional stability due to the horizontal tail is due to the non-linearity variation of the WWBNV yawing moment coefficient. In the chosen range of sidelsip angles $\beta \in [0°, 10°]$, where the directional derivative has been estimated, C_{N_β} of the WWBNV configuration

(a) Isolated Body configuration.

(b) Body-Vertical configuration.

(c) Complete aircraft configuration.

FIGURE 3.30: Several configuration experimental investigated in the lateral-directional test.

is quite lower than the one that could be estimated in a linear range of higher β (i.e. $[10°, 20°]$, the WWBNV directional control increase and the effect of the horizontal tailplane is about 26%. This aerodynamic behaviour has been confirmed also by the numerical investigation through CFD RANS approach shown in sec. 4. Complete aircraft configuration at several rudder deflection

TABLE 3.13: Yawing moment coefficient slope breakdown, range of $\beta \in [0, 10°]$.

Configuration	$C_{N_\beta} deg^{-1}$
V	0.00228
B	-0.00100
WWB	-0.00111
WWBN	-0.00109
WWBNV	0.00122
WWBNHV	0.00197

have been tested in order to estimate the control power derivative. Fig. 3.32

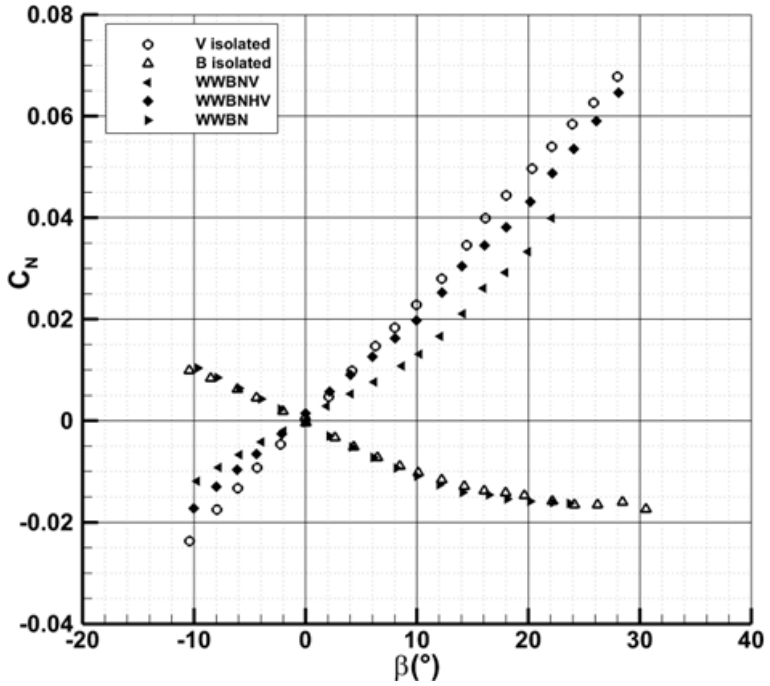

FIGURE 3.31: Yawing moment coefficient breakdown.

shows the yawing moment coefficient variation respect to the sideslip angle for the complete aircraft configuration at several rudder deflections. The aircraft shows a control power of about -0.00210 deg^{-1} that grants a minimum control speed (VMC) in take-off and one engine inoperative conditions of about 35 m/s (lower than the 38 m/s prescribed by regulations, being $1.2V_{STO}$ or 38 m/s, considering a maximum take-off weight of 3290 kg and a maximum lift coefficient of about 2). A minimum control speed lower than 38 m/s leads to a take-off distance lower than 700 m. Fig. 3.33 shows the required rudder deflection to grant the equilibrium in yaw with respect to the sideslip angle, as it can been seen from the graph the ratio between the required rudder deflection $\delta_{r,eq}$ and sideslip angle β in a steady sideslip is about 0.80 in the linear range (from 0° up to 10° sideslip angle) and with full rudder deflection allow the equilibrium with sideslip angles higher than 20 degrees.

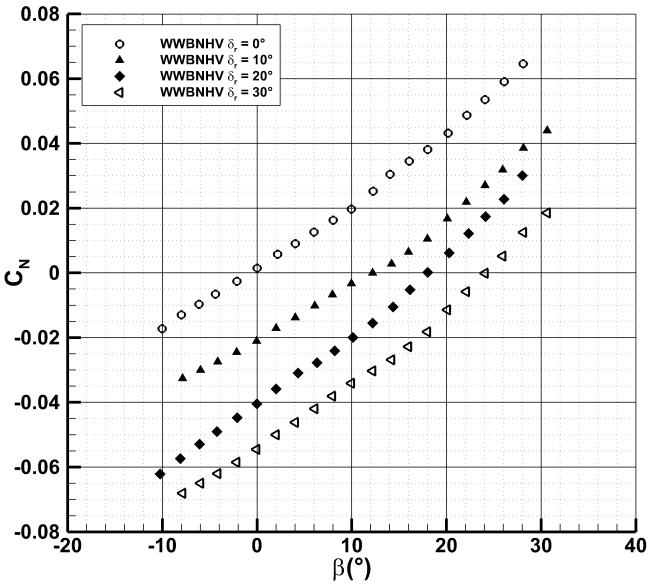

FIGURE 3.32: Complete aircraft at several rudder deflections.

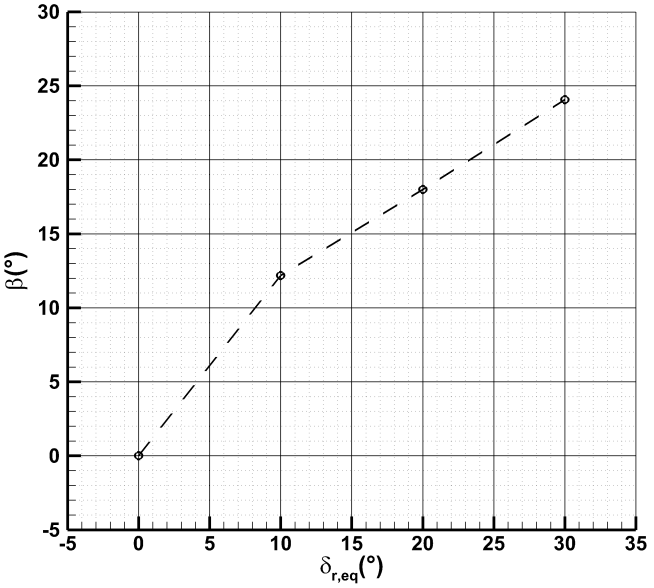

FIGURE 3.33: Required rudder deflection for the equilibrium in yaw.

3.8.2 Lateral stability

This section deals with the experimental estimation of the complete aircraft lateral stability characteristics. In particular, tests were also addressed to the evaluation of the winglet effect on the wing dihedral effect. Fig. 3.34 shows the rolling moment coefficient variation with respect to the sideslip angle for the tested aircraft configurations. The complete aircraft show a lateral stability derivative of about 0.0030 deg^{-1}. Referring to the graphs of Fig. 3.34 and in

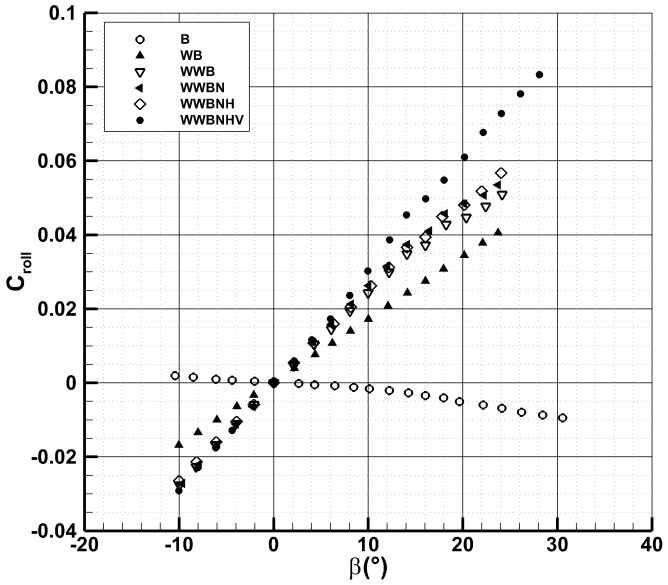

FIGURE 3.34: Rolling moment coefficient breakdown.

particular looking at the lateral stability derivatives summarized in Tab. 3.14, it is possible to appreciate how the two nacelles increase the lateral stability of about 8% (compare the WWB and WWBN configuration, marked with the unfilled gradient and filled left triangle in the graphs of Fig. respectively), this is a similar effect to the interference of the high wing configurations. The horizontal tail leads to a reduction of about 4% in the lateral stability (compare the WWBN and the WWBNH configuration, the filled left triangle and the unfilled diamond in the graphs of Fig. 3.34 respectively). The vertical tail contribution to the lateral stability can be estimated to be about 18% of the global value for the complete aircraft (compare the WWBNH and the WWBNHV curves of Fig. 3.34, marked with the unfilled diamond and the filled circle symbol respectively). Finally it is very interesting to highlight the winglet effect on the lateral stability derivative, by comparing the WB and the WWB configuration shown in Fig. 3.34. It is possible to appreciate that winglets increase of about 40% the lateral stability of the aircraft. This is

a very interesting results since during the preliminary design phase usually approached through the application of classical semi-empirical methodologies like those proposed by Roskam [12], Torenbeek [13], Perkins and Hage [14] and McCormick [15], no method to estimate the contribution of the winglets on the lateral stability can be found. The only way to take into account the winglet effect on aircraft lateral stability is to use the approach, as suggested by Nickel and Wohlfahrt [48], that provides adding the winglet effect estimating a wing equivalent dihedral angle, and it is strictly recommended to use it in preliminary design phase.

TABLE 3.14: Rolling moment coefficient slope breakdown, range of $\beta \in [0, 10°]$.

Configuration	$C_{roll_\beta} deg^{-1}$
B	-0.0002
WB	0.0017
WWB	0.0024
WWBN	0.0026
WWBNH	0.0025
WWBNHV	0.0030

3.9 Concluding remarks about wind tunnel tests

This chapter presents the most significant results of an extensive experimental wind tunnel test campaign made of more than 300 tests performed on several aircraft configurations. Wind tunnel tests led to the estimation of both longitudinal and lateral-directional stability characteristics, highlighting the contribution of each aircraft component, in particular those of the fuselage and nacelles. Experimental tests allowed to check the goodness of the aircraft trim capabilities also in both most critical centre of gravity position and flap deflection (full flap deflection, landing conditions). These tests have therefore also helped to choose the final incidence for the horizontal stabilizer in order to ensure good equilibrium and trim capabilities. Lateral-directional tests allowed to check the vertical tail sizing in order to grant the minimum control speed. It is clear that Balance Field Length (BFL) (which depends on minimum control speed) is one of the most crucial aircraft performance to have good opportunities of commercial success. It must be reminded that all experimental tests have been performed at a Reynolds number of about $0.6e^6$ while the free flight Reynolds number range should vary from $4.5e^6$ up to $9.5e^6$. Thus all the measured data suffer of the Reynolds number scaling effect. Nonetheless it is well known that Reynolds number does not affect aerodynamic coefficients curve slopes in the linear range. Despite this the estimation of the maximum lift coefficients and the angle of attack at which they occur are strongly dependent

on the Reynolds number. Concerning the longitudinal stability and control it is known that flight tests data are in general not so different from the wind tunnel tests, moreover, the discrepancy is usually in the direction of higher stability of the airplane coming from flight tests than was experimentally predicted in the tunnel. Finally dealing with the lateral stability it is known that in general the agreement between the flight and tunnel test is satisfactory. Literature offers several works in which is illustrated a general good correlation between the wind tunnel data (properly corrected to take into account the wind tunnel walls effects and the Reynolds number scaling effects) and the flight test data. Examples of correlations between experimental and flight test can be found in Ref. [59–61]. Concerning with the aircraft drag estimation, even though it can be argued that measuring drag is less important than stability and control, because drag affects aircraft flight performance and not safety, a method to predict the drag at free flight Reynolds number has been shown. Further investigations on aircraft longitudinal and lateral-directional aerodynamic characteristics through computational fluid dynamics tools (RANS approach) in order to take into account the Reynolds number effect have been performed and discussed in the next chapter. Finally it must be remarked that the experimental investigation has been addressed to the estimation of the static longitudinal and lateral-directional characteristics without thrust effects. Even if the estimation f the power effects on aerodynamic characteristics was not an object of this work, it seems reasonable to provide a brief discussion about those effects. Power effects on stability and control can be divided into direct and indirect effects. Belonging to direct effects are:

- Pitching and yawing moments due to thrust line not passing through the centre of gravity;
- The propeller normal force in its rotation plane that produces pitching or yawing moments. These effects adversely affect both longitudinal and lateral stability;
- For the multiengined aircraft there is a rolling an yawing moment due to the one engine inoperative condition (the critical condition for the rudder surface design).

In general these direct effect should be amenable to estimate and deal with thrust and moment arm, even if, in some cases, could be difficult to obtain data dealing with normal force variation with flow angles. Much more difficult to be estimated are the indirect effects that are due to the interaction of the slipstream with aircraft components. The indirect effects depend on the aircraft configuration and can be summarized as follow:

- Effect of the slipstream on moments of fuselage, wing and nacelles;
- Effect of slipstream on wing lift (due to the high local dynamic pressure);

- Effect of slipstream on downwash;
- Effect of slipstream on the dynamic pressure on the tail.

Effects of slipstream on fuselage and nacelles moments are small compared to other effects. Main effects are those on wing lift (especially in flap down configurations) that alter will alter the downwash changing the horizontal tail's angle of attack. A similar effect is produced by the propeller's normal force. The rotational component of the slipstream will change the the downwash across the horizontal tail, and finally the increase of the dynamic pressure due to the slipstream will change the contribution of the tail to the stability. The literature offers several works dealing with the experimental investigation about the power effects on aerodynamic characteristics. A semi-empirical approach to take into account thrust effect on the aerodynamic characteristics is suggested by Wolowicz and Yancey [[62, 63]], the method is based on experimental data of a full scale investigation of a light twin engine propeller driven aircraft. In these works the propulsion effects on both longitudinal and lateral-directional characteristics are mainly related to i) the lift (or side force) component of the propeller thrust vector, ii) the lift (or side force) component of the propeller normal force iii) the change in lift (or side force) due to power-induced change in dynamic pressure. Moreover according to number and engine configurations, the thrust effects have to be considered in the stability and control characteristics (thrust offset from the centre of gravity, downwash, sidewash and change of dynamic pressure on tail planes). These papers highlight that the lift slope C_{L_α} is slightly modified by power effects, while an increment of lift coefficient of about 12-15% can be appreciated along the entire lift curve. Moreover pitching, yawing and rolling moment coefficient variation due to the power effects are strictly related to the aircraft configuration (high-low wing and engine thrust axis location and tailplanes). Experimental and numerical investigation about the thrust effects on the lift and drag characteristics are also shown in Veldhuis [64], where the mechanisms and the phenomena that play a role in the aerodynamic interference between tractor propellers and a wing are presented. Quantitative results are also clearly explained highlighting effects on lift and drag coefficient. In particular power effect on lift curve is about 6% on the lift curve slope and an increment of 8% at the analysed angles of attack.

Chapter 4

CFD RANS Analysis

4.1 Introduction

The use of computational fluid dynamics (CFD) for industrial aircraft design started in the 1960s, and since then has grown from a tool used to supplement wind tunnel or flight experiments to an identifiable new technology standing on its own making important contributions to all stages of the design of a flight vehicle. Now it is possible to look back on 50 years experience in using CFD. Three main factors were instrumental in the CFD development: i) the increase in available computer resources, ii) the progress in development of efficient numerical methods, and iii) the progress in physical modelling. Many authors have extensively reviewed these aspects dealing with the CFD developments, some works can be found in [65–67]. In this chapter only a brief summary of the CFD development is provided, in order to set the stage of the current use of CFD approach in the aircraft design and in support of the wind tunnel data. In the 1960s and early 1970s, CFD applied to aircraft design consisted of simplified (linear) models, i.e. the Laplace or Prandtl-Glauert equation. Initially lifting-line and lifting-surface theories formulated these methods, then vortex-lattice procedures were developed representing the geometry by a mean surface and using vortex filaments as singularities. Since the mid-1960s panel methods arose that discretize the surface of geometry with either low-order (constant) or higher-order (linear or quadratic) singularity distributions. In the early 1970s, boundary layer methods to study viscous effects became mature to be applied in the design. In this decade, much work was done on coupling panel methods with boundary-layer methods. These non-linear inviscid methods were later coupled with boundary-layer computations, leading the development of several code, see Ref. [68]. The advent of vector supercomputers (Cray 1, Cyber 205) at the end of the 1970s, opened the way to using non-linear methods for applications more complicated than isentropic, irrotational flows. The first Euler codes for research associated with aircraft design appeared in the 1980s, followed by the further development of Euler methods coupled with boundary layer codes. These were applied mainly to steady aerodynamics,

while panel methods have been extended to handle unsteady problems. By the end of the 1980s, a further increase in computer capacity became available in the form of parallel computers. Massively parallel architectures were seen as a very promising way to solve realistic flow problems in an acceptable turn-around time for industrial design. Among others developments, parallel simulation contributed to the move from Euler to Navier-Stokes simulations for steady flows, and the use of the unsteady Euler formulation for studying transient phenomena. Since the mid 1990s efforts are underway to incorporate the extensive and existing body of CFD knowledge fully into methods and routines used in aircraft design. Numerical simulation has become a principal element in the aircraft design process because of the flexibility it provides for rapid and comparatively evaluation of alternative designs, and because it can be integrated in a simulation environment treating concurrently both multidisciplinary analysis and optimization. In carrying out a CFD simulation the designer faces a critical choice when selecting the underlying mathematical model. The selection must match the level of complexity needed to provide the accuracy necessary for his design intention with the level of cost and turnaround time allowed at this stage of the design. The development of the CFD methods and solvers and their application in the aircraft design is well illustrated in Ref. [69, 70], where the Boeing Commercial Air Group thirty years of development and application of CFD is shown. Today, the choice of model for steady state aerodynamics has grown from linear to Navier-Stokes (see Ref. [66, 71]), thanks to the ever-increasing power of computers and parallel architectures. For example with today's computer power a Reynolds-averaged Navier-Stokes simulation with a one-equation turbulence model for the steady flow around a wing-body-nacelle configuration is computed in a few hours. In summary, Navier-Stokes solvers have become a standard tool in industry at least for steady aerodynamics because:

- Navier-Stokes solvers have reached sufficient maturity and robustness for use on a daily base in an industrial design environment,
- the costs of Navier-Stokes simulations have been dramatically reduced in the last 5 years,
- Wind tunnel testing is costly, and rarely give the flight Reynolds number,
- other CFD methods (coupled Euler-boundary layer, panel methods) do not resolve the physics correctly.

Typical design applications of Navier-Stokes, currently underway are:

- vehicle shape i.e. design and analyse:
  - optimum airfoils, wings and empennage for external performance,
  - pylons, nacelles, inlets, diffusers and nozzles for engine integration and internal performance.

- performance: compute force and moment data to estimate lift, drag and moments for the performance dataset of the vehicle,
- systems integration: obtain flow field data to analyse the integration of engines or weapons with the airframe,
- control inputs: determine aerodynamic coefficients, force and moment data to evaluate stability, control and handling characteristics,
- loads for structural design: compute surface pressure to determine structural loading and aeroelastic impacts, including the likely loss of aerodynamic performance due to structural deformation under load and control-surface effectiveness (static aeroelasticity),
- aeroservoelastic design: compute surface pressure to study flutter and divergence; dynamic aeroelasticity simultaneously couples the aerodynamic loads with the structural response of the airframe and the control system with the aim to alleviate a degradation in aerodynamic performance and/or flying qualities resulting from deformation, e.g. active flutter control.

Several works, benchmark cases, test cases typically used for validating and certifying a solver, and other examples that indicate the current frontier of the use of Navier-Stokes solvers in aerospace engineering are extensively shown in Ref. [72].

In this work the Navier-Stokes approach has been used to support the experimental investigation about the P2012 Traveller configuration, and in particular to carry out information that are not available form the experimental test campaign, in order to verify the aerodynamics and stability of the airplane. The tunnel investigation has been accomplished on a scale model in a low Reynolds wind tunnel, this means that information of great interest such as the estimation of the maximum lift coefficient, the prediction of high lift characteristics and the understanding of the Reynolds number scaling effect are not experimentally available. Thus to supply these lack an extensively Navier-Sttokes investigation has been performed on the final layout of the P2012 Traveller. Longitudinal and lateral directional analysis have been computed simulating both experimental and free flight conditions. Complete aircraft and single parts in several configurations have been analysed to study interaction effects. Aerodynamic simulations have been carried out through the CD-adapco CFD software STAR-CCM+ leading to the evaluation of the characteristics of longitudinal and lateral-directional stability and for the complete aircraft and for many of the partial configurations. The 6 generalized components (forces and moments) of the aerodynamic actions depending on the attitude angles of the numerical model have been estimated to have an accurate prediction of the aircraft stability derivatives (both longitudinal and lateral-directional). Additional tests were made considering many partial

configurations in order to further investigate the contributions of the various components of the aircraft to the aerodynamic characteristics and have an estimation of their effects. Wing load distributions for different angles of attack of clean and flapped configurations have been extracted to accomplish the wing structural sizing, and in order to evaluate the stall and effects of winglets and nacelles on the wing loads. In order to validate the numerical results tests have been computed at wind tunnel conditions and compared with the available experimental results. To evaluate Reynolds number effects, on complete configurations, longitudinal and lateral directional analyses have been performed in both landing and cruise Reynolds number.

Aerodynamic analyses have been fulfilled through the software STAR-CCM+[1] (**??**), which is a commercial computer-aided engineering package developed by CD-adapco company. The software includes all the required features from the pre-processing (i.e. CAD modeler tool, CAD import tool), to the post-processing and data analyses tools.

4.2 Numerical model set-up

The 3D aircraft model used to perform the numerical simulations has been drown through external CAD software and imported into the STAR-CCM+ framework. Aircraft geometry has been divided into several components (such as Fuselage, Horizontal and Vertical tailplanes, Nacelles and Ogive and Wing), as shown in Fig. 4.1, in order to analyse different configurations and evaluate the contribution of each aircraft component and mutual interferences among them. Since many experimental data were available from the tunnel test campaign of a 1:8.75 scale model, the numerical model has been scaled to in order to compare numerical results with experimental data validating the goodness of the numerical simulation. The computational domain (or the fluid

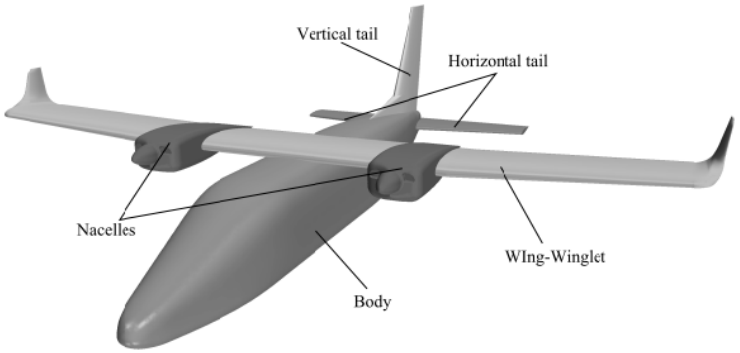

FIGURE 4.1: P2012 Traveller numerical CAD model.

[1]CD-adapco's official website.
http://www.cd-adapco.com

region around the aircraft to be simulated) has been defined as a block with dimensions of 10 fuselage lengths ahead the fuselage nose, 20 behind, 8 beside and 5 fuselage lengths above and below. The computational domain and the boundary condition settings are depicted in Fig. 4.2.

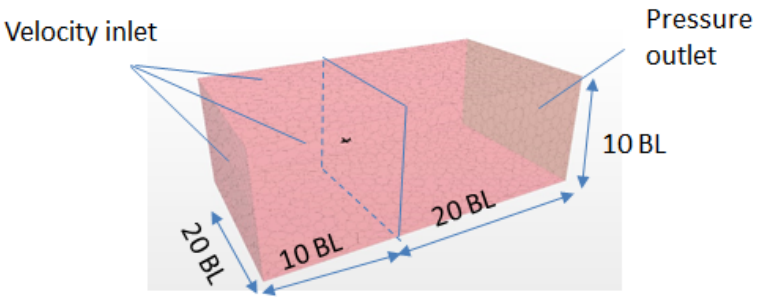

FIGURE 4.2: Computational domain and boundary conditions setting.

4.2.1 Mesh generation

The volume mesh is the mathematical description of the space or geometry of the problem being solved. STAR-CCM+ software provide several meshing strategies that are suitable for different applications. The meshing procedures start from the initial triangulation of the surfaces coming from the CAD representation. In order to improve the overall representation of the geometries being investigated, the *surface remesher* option has been activated, in this way the initial triangulation of the geometries CAD representation can be improved. A reference length parameter (the base size, BS), on which depends the surface mesh of the body to be simulated, has been defined, so it is possible to refine the mesh by changing a single parameter. The volume mesh has been built up using the *polyhedral mesher* tools instead of the tetrahedral. A polyhedral mesh could contains an amount of volume cells five times lower than a tetrahedral mesh, starting from the same surface mesh, and with the same accuracy of the solution. Tetrahedra are the simplest volume elements and tetrahedral meshes are also relatively easy to generate automatically. On the negative side, tetrahedra cannot be stretched too much, so in order to achieve a reasonable accuracy in boundary layers, long channels or small gaps, a much larger number of control volumes is needed than if structured (hexahedral) meshes are used. Tetrahedral control volumes have only four neighbours, and computing gradients at cell centres using standard approximations (linear shape functions) can be problematic. In order to achieve accurate solutions and good convergence properties on tetrahedral meshes, one needs special discretization techniques and a large number of cells. Polyhedra offer the same automatic meshing benefits as tetrahedra while overcoming these disadvantages. A major advantage of polyhedral cells is that they have many neighbours (typically of order 10), so gradients can be much better approximated than

is the case with tetrahedral cells.The fact that more neighbours means more storage and computing operations per cell is more than compensated by a higher accuracy. Polyhedral cells are also less sensitive to stretching than tetrahedra. Polyhedral cells are especially beneficial for handling recirculating flows. A more detailed analysis of properties of various mesh types and some results from test cases are published in an article by Peric [73].

To accurately simulate the boundary layer near walls (the aircraft surfaces has been defined as no-slip walls) the *prism layer option* has been enabled, so a layer of orthogonal prismatic cells near the walls can be created. Table II shows the main mesh parameters used to build up the mesh for the simulation. The prism layer thickness has been estimated as proportional to $1/\sqrt{Re}$ (the laminar boundary layer thickness of a flat plate), and it depends on the Reynolds number. Numerical simulations have been performed both at wind tunnel tests and at free flight Reynolds number (about $0.6e^6$ and $9.5e^6$ respectively). The parameters used to build up the mesh and the prism layer, for both simulated Reynolds number are shown in Tab. 4.1. In order to ease the

TABLE 4.1: Surface remesher and prism layer parameters.

Surface remesher	
Parameter	Value
Base size (BS)	0.6 m
Surface Growth Rate	1.3
Surface relative minimum size	0.1% BS
Surface relative target size	250%BS

Prism layer	
Parameter	Value
Stretching Function Geometric progression	
Number of prism layers	20
Prism layer stretching	1.1
Prism layer thickness (Re=$0.6e^6$)	0.00129 m
Prism layer thickness (Re=$9.56e^6$)	0.000324 m
Near wall thickness (Re=$0.6e^6$)	$2.1e^{-5}$ m
Near wall thickness (Re=$9.56e^6$)	$1.6e^{-6}$ m

solution convergence process, some volumetric controls have been designed with the aim to improve the mesh density in that area where the surface curvatures are high (such as the lift surfaces leading edge) and along the trailing edges of the wing and tailplanes surfaces, an example of volumetric control refinements is shown in Fig. 4.3, where the detail of the winglet is illustrated. Fig. 4.4 shows an example of the polyhedral mesh, while Fig. 4.5 shows instead the prism layer around both wing leading and trailing edge.

The final mesh (around the complete aircraft configuration) consists of about 9 million of polyhedral cells.

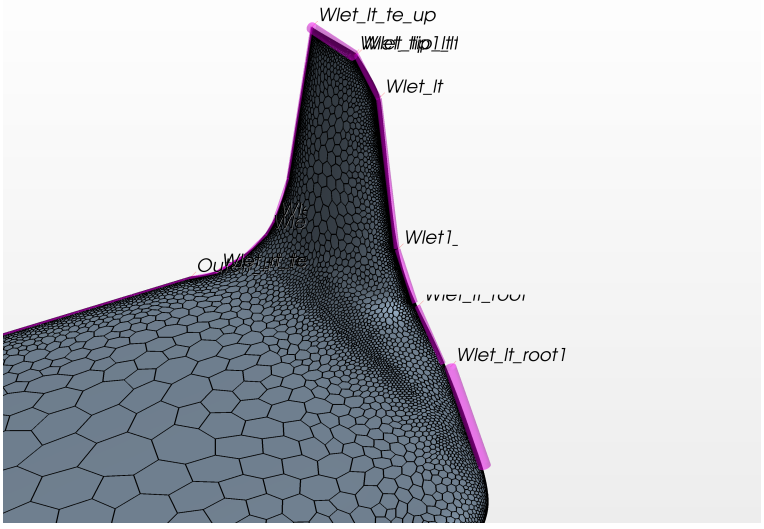

FIGURE 4.3: Volumetric controls on winglet surface.

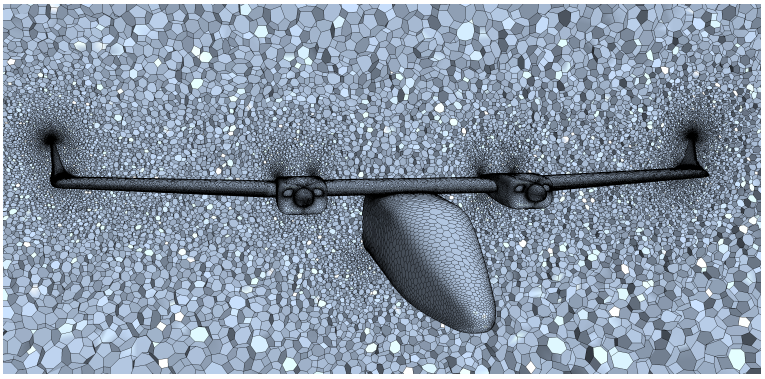

FIGURE 4.4: Polyhedral surface and volume mesh view.

4.2.2 Physic definition

Since all the simulated conditions (wind tunnel and free flight Reynolds number) lead the Mach number to not exceed 0.25 the flow has been considered to be incompressible ($M \ll 1$), the density has been considered to be constant and a segregated solver approach has been chosen. Moreover tests in compressible model have shown good agreement with Pradtl-Glauert correction. The Spalart-Allmaras turbulence model has been used, which is a recommended

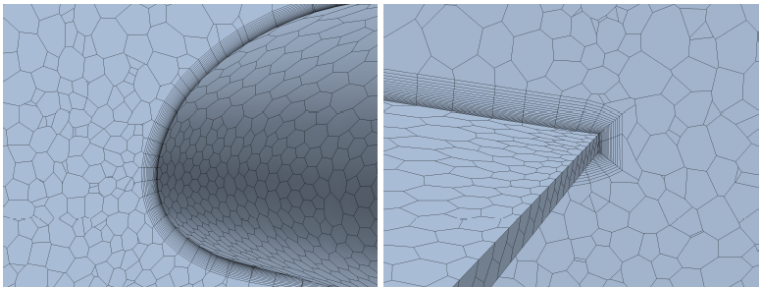

FIGURE 4.5: Prism layer around wing leading and trailing edge.

model for aerospace external flow applications. The basics of the Spalart-Allmaras turbulence model are illustrated in Ref. [74, 75], where also several validation test cases are shown. This model is particular recommended for unstructured grids, the model is robust enough to be applied in a variety of cases and physical situations, it has been demonstrated that the outright divergence of the iterative process rarely occurs, and the model seems to be reasonably friendly to the relaxation process, without any attention being paid to the initial conditions. Furthermore many works have shown the goodness of this model in many aerodynamic cases respect others turbulence model. Some validation cases can be found in Ref. [76, 77], where several turbulence models have been compared in order to predict the high lift characteristics of a trapezoidal wing.

Once the goodness of the numerical model to be simulated has been assessed (the CAD geometry has been defined, the mesh parameters have been checked, the solution convergence dependence on the mesh size has been assessed and results have been validated with respect to the available experimental data), the free flight conditions have been simulated on the same numerical scale model without convert it to the full scale but only by changing the fluid properties in order to grant the desired flight condition (in terms of Reynolds number and Mach number). This is possible thanks to the advantage of a numerical simulation to not work on a real fluid with a certain fluid properties that can not be changed or manipulated. Tab. 4.2 summarizes the fluid properties setted for both simulation of wind tunnel and free flight Reynolds number. In particular it can be appreciated how a free flight Reynolds number has been granted by changing the dynamic viscosity of the fluid. The right value of the dynamic viscosity has been estimated by considering the desired Reynolds number, the scale model mean aerodynamic chord and a fixed flow speed of 40 m/s (according to the wind tunnel tests). This way the free flight conditions can be simulated only by changing the fluid dynamic viscosity and the mesh parameters (the prism layer thickness and the near wall thickness discussed in sec. 4.2.1 and illustrated in Tab. 4.1) maintaining the same CAD geometry, the same mesh structure, the same force

and moment reports reducing the time required to set up of the cases to be studied at free flight conditions.

TABLE 4.2: Fluid properties.

Wind tunnel Reynolds, Re=$0.6e^6$	
Property	Value
Density	1.184 kg/m3
Dynamic viscosity	$1.855e^{-5}$ Pa-s
Reynolds number,cruise Re=$9.5e^6$	
Property	Value
Density	1.184 kg/m3
Dynamic viscosity	$1.067e^{-6}$ Pa-s
Reynolds number,landing and take-off Re=$4.5e^6$	
Property	Value
Density	1.184 kg/m3
Dynamic viscosity	$2.253e^{-6}$ Pa-s

4.3 The SCoPE grid infrastructure

To perform the large amount of numerical simulations discussed in this work, the University's computing grid infrastructure has been used. Sistema Cooperativo per Elaborazioni Scientifiche Multidisciplinari (SCoPE[2]) is a scientific data centre, based on a grid computing infrastructure, and it is a collaborative system for scientific applications in many areas of research. It is a project started in 2006 by the University of Naples Federico II. The data centre hosts about 300 eight-core blade servers, 220 terabyte of storage, and is already able to accommodate 500 more servers. Actually it has over 2400 CPUs. The data centre is located in the Monte S. Angelo Campus, which already hosts the Faculty of Sciences and it is close to the Faculty of Engineering, with kilometres of pre-existing optical fibres. The network infrastructure is shown in Fig. 4.7, while Fig. 4.8 shows some pictures of the fibre optic connection of the SCoPE facility. 128 license (one per CPU) were available for this work. Runs with several CPUs number have been performed, Fig. 4.6 shows how doubling the CPUs number the required time to convergence halves. A typical simulation, which may contain from 8 up to 16 million of polyhedral cells (according with the configuration being investigated), can be accomplished within few days (about 4-5 days to complete a set of incidence or sideslip angles with 2000-5000 iterations per case) using 32 CPUs.

[2]CD-adapco's official website.
http://www.scope.unina.it/default.aspx

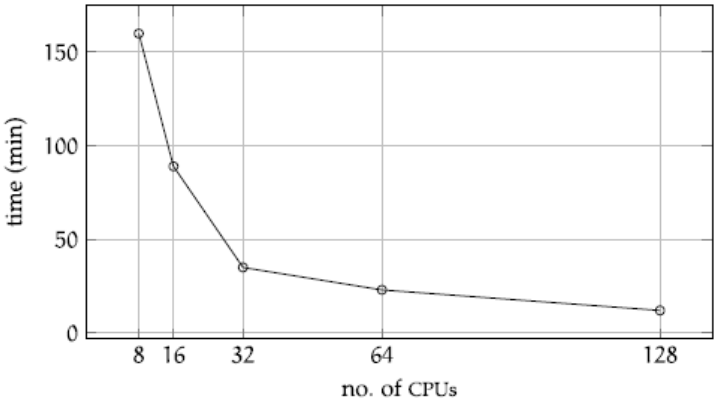

FIGURE 4.6: Time required to convergence vs. CPUs number.

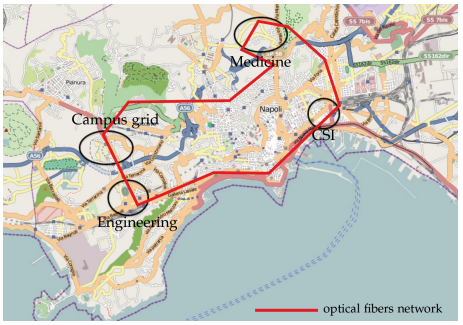

FIGURE 4.7: The SCoPE network infrastructure.

FIGURE 4.8: Three rack servers of the data centre

4.4 Solution convergence check

Several convergence analyses of the solution with the change of the number of cells and for different configurations have been made. Here results of the complete aircraft semi-model model with flap deflection of 40°, at both incidence and sideslip angles setted to zero, are illustrated. To increase uniformly the number of cells has been gradually decreased the base size from the initial value 1.6 (corresponding to the wingspan of wind tunnel model). Convergence analyses have been launched on SCoPE infrastructure, mesh has been generated in serial mode, while solution has been calculated in parallel, using 32 processors, the iterations number for each case has been set to 2000. In Fig. 4.9 the lift, drag and pitching moment coefficient at varying of the cells number are shown. These results highlight how reducing the base size further than 0.6 m would not produce significantly changes in the aerodynamic coefficients. Thus a base size of 0.6 m has been chosen as starting value for the mesh build up of each configuration to be investigated. Local surface

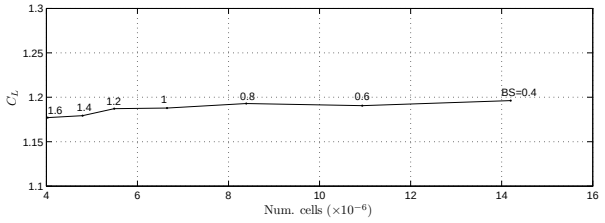

(a) Lift coefficient variation with respect of the cell number.

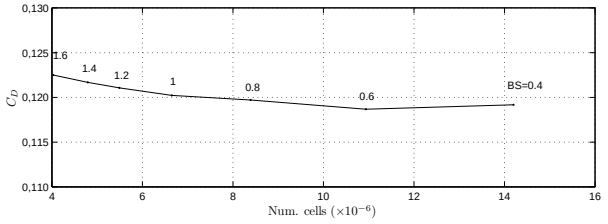

(b) Drag coefficient variation with respect of the cell number.

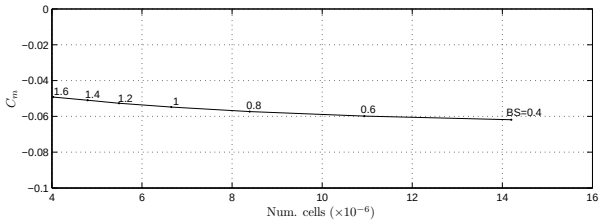

(c) Pitching moment coefficient variation with respect of the cell number.

FIGURE 4.9: Longitudinal aerodynamic coefficients at varying of the base size (m), complete aircraft flap 40°, $\alpha = \beta = 0°$

and volume mesh refinements in the most critical areas have been introduced for configurations of higher complexity such deflections of control surfaces or for the simulations of high lift conditions at higher attitudes where both geometry and wake must be discretized to reach a higher accuracy for the numerical simulation. In Fig. 4.10 shows an example of mesh refinement for the full flap deflection configuration. Convergence of the simulation is judged

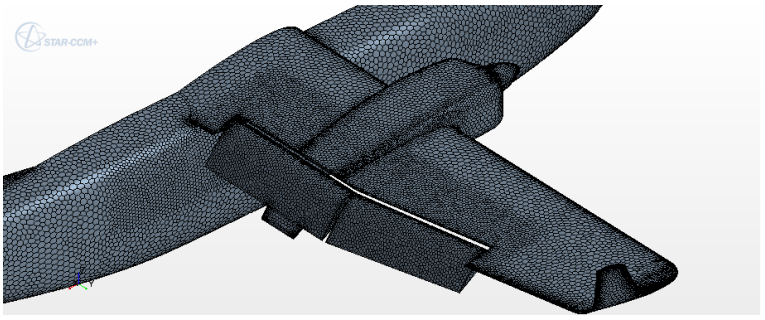

FIGURE 4.10: Surface and volume mesh refinement on flap.

by looking at the residual plot. Once the residuals drop to a very low value (usually around 10^{-7}), the aerodynamic coefficients are evaluated. Another parameters to consider is the dimensionless wall distance y^+. The choice of the Spalart-Allmaras turbulence model lead to verify if the y^+ is of order of magnitude as unity, allowing that the viscous sub layer is properly resolved. Fig. 4.11 and Fig. 4.12 show a typical residuals plot and the y^+ distribution on the complete aircraft in clean condition (cruise).

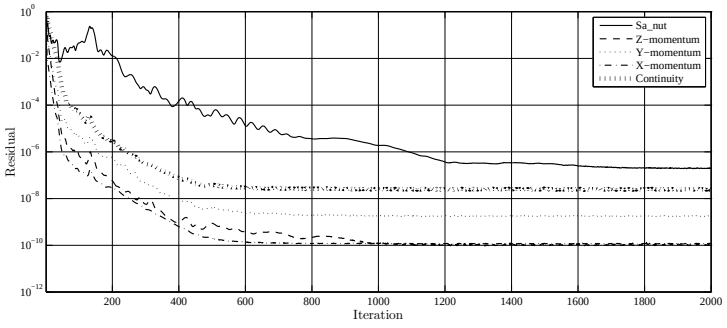

FIGURE 4.11: Typical residuals plot.

4.5 Longitudinal Analysis

In order to validate the numerical analyses by comparing CFD results with experimental data, several configurations have been analysed at the wind tunnel Reynolds number. Isolated body, wing-body both winglets on and off

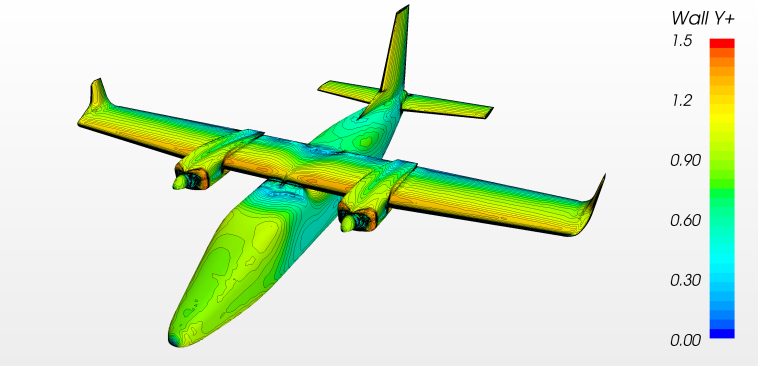

FIGURE 4.12: y^+ distribution on complete aircraft at Re=9.5e^6.

configurations, complete aircraft at several flap deflections have been simulated and compared with available experimental data. Once the goodness of the numerical simulation has been validated, the effects of the Reynolds number have been analysed. The lift, stability and control and drag characteristics have been evaluated for the complete aircraft at several flap deflections. Some of the analysed configurations are illustrated in Fig. 4.13.

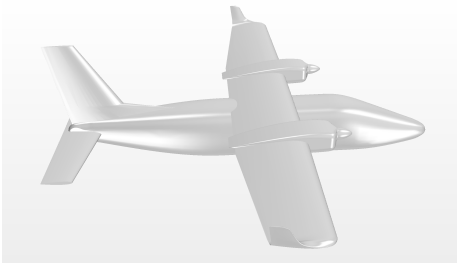

(a) Complete aircraft winglet on (WWBNHV).

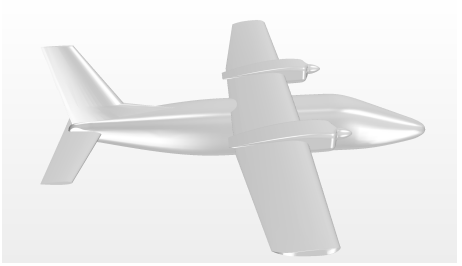

(b) Complete aircrft winglet off (WBNHV).

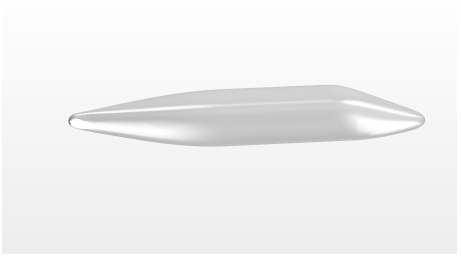

(c) Isolated body (B).

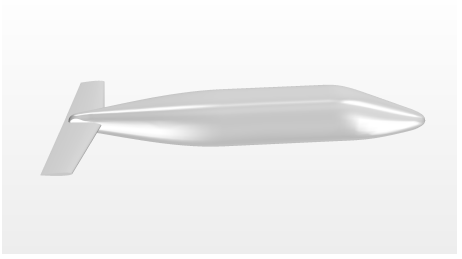

(d) Body and horizontal tailplane (BH).

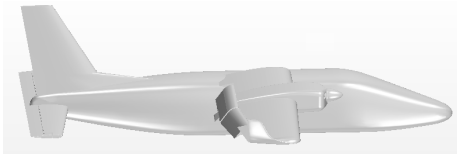

(e) Complete aircraft flap and elevator (WWBNHV $\delta_F = 40°, \delta_e = 0°$).

FIGURE 4.13: Some of the configurations analysed

4.5.1 Lift and pitching moment coefficient breakdown

In this section the lift and pitching moment coefficients breakdown is presented. The aim is to provide an estimation of the complete aircraft lift and stability characteristics evaluating the contribution of each aircraft component. Comparison with experimental data are shown both in terms of curve and derivatives in the linear range of incidence angles to provide the validation of the numerical simulations. In Fig. 4.14 the lift coefficient breakdown is presented . The measured wing-winglet-body (WWB) lift slope is about 0.080 deg^{-1}, while the wing-winglet-body-nacelles configuration (WWBN) shows a lift slope of about 0.082 deg^{-1} (see also Tab. 4.3) highlighting an almost neutral effect of the nacelle, with a behaviour similar to a symmetrical airfoil also due to a higher nacelle length. The fuselage produces an aft shif of the aerodynamic centre of about 12.3% very close to what has been experimentally estimated (see Tab. 4.3). The nacelles effect can be estimated by considering that the wing-winglet-body-nacelle (WWBN) configuration leads to an aft shift of the aerodynamic centre of about 13.7%, and since the contribution of the fuselage alone is about 12.3%, it can be estimated that the nacelles contribution to the aft shift of the aerodynamic centre is about 1.4%, quite lower than the experimentally estimation, as shown in Tab. 4.3. Complete aircraft neutral point in clean configuration is about 50% of the mean aerodynamic chord. This means that the CFD RANS approach leads to the aircraft configuration to be about 2% more stable than the experimental estimations. This is clearly due to the differences into the wing downwash estimation between the two approaches. In fact the numerically estimated downwash derivative is equal to 0.3, which is about 7% lower than the experimental estimation as shown in Tab. 4.3. The downwash derivative has been estimated by comparing the pitching moment curve slope of the horizontal tailplane in both BH and WWBNHV configuration. The neutral point location has been calculated as shown in Eq. 4.1.

$$\bar{x}_N = \bar{x}_{cg} + \frac{dC_M}{dC_L} \tag{4.1}$$

Winglets effect on the induced drag has been estimated by considering the slope of the linear regression of the drag coefficient versus the squared lift coefficient of both wing-body-nacelles (WBN) and wing-winglet-body-nacelles (WWBN), as it is shown in Fig. 4.16. The winglets reduced the induced drag factor of about 12% with a drag penalty of 5 drag counts, in good agreement with the estimation performed with the panel method approach discussed in sec. 2.4. Tab. 4.3 summarizes the most significant results of the lift and pitching aircraft characteristics and compares the CFD results with the experimental measured values. The comparison with the experimental data shows a remarkable agreement between the two different approaches, highlighting the goodness of the CFD simulations. Some little differences can be found in the stability estimation both in terms of pitching moment

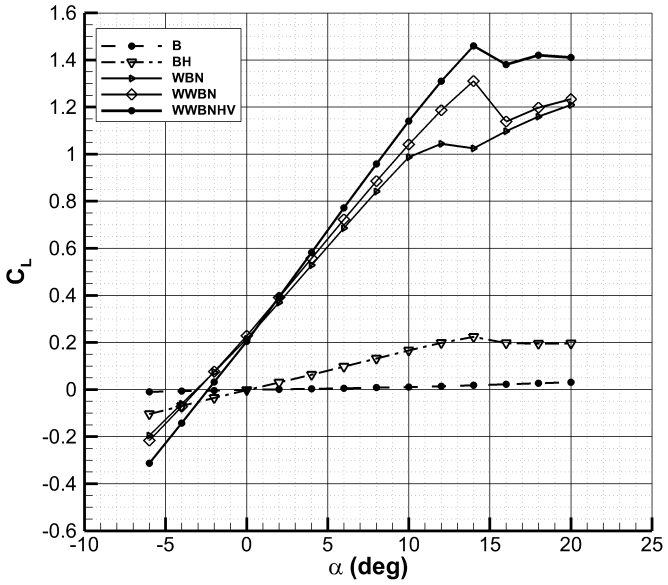

FIGURE 4.14: CFD lift coefficient breakdown,Re=$0.6e^6$.

coefficient slope with respect to the incidence angle and in the neutral point location, and in the estimation in the downwash derivative.

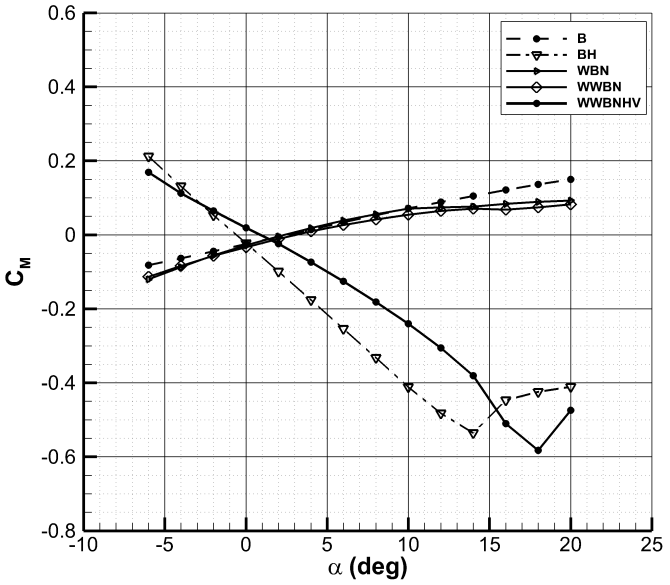

FIGURE 4.15: CFD pitching moment coefficient breakdown, Re=0.6e^6.

TABLE 4.3: Lift and pitching moment curve slope breakdown, at Re=0.6e^6, range of $\alpha \in [0 - 6°]$.

	CFD RANS approach	Wind Tunnel Data
C_{L_α} complete	0.0941 deg^{-1}	0.0911 deg^{-1}
C_{L_α} wing-winglet-body	0.080 deg^{-1}	0.080 deg^{-1}
C_{L_α} wing-winglet-body-nacelles	0.0820 deg^{-1}	0.082 deg^{-1}
C_{M_α} complete	-0.0236 deg^{-1}	-0.0200 deg^{-1}
C_{M_α} wing-winglet-body	0.0081 deg^{-1}	0.00870 deg^{-1}
C_{M_α} wing-winglet-body-nacelles	0.0112 deg^{-1}	0.0127 deg^{-1}
C_{M_α} body	0.0098 deg^{-1}	0.0097 deg^{-1}
N_0	50% $\bar{c}$	47% $\bar{c}$
$d\epsilon/d\alpha$	0.300	0.360
Δx_{ac} body	12.3% $\bar{c}$	12% $\bar{c}$
Δx_{ac} nacelles	1.4% $\bar{c}$	3.5% $\bar{c}$
Δe winglets	12.4%	10%
ΔC_{D_0} winglets	5 drag counts	8 drag counts

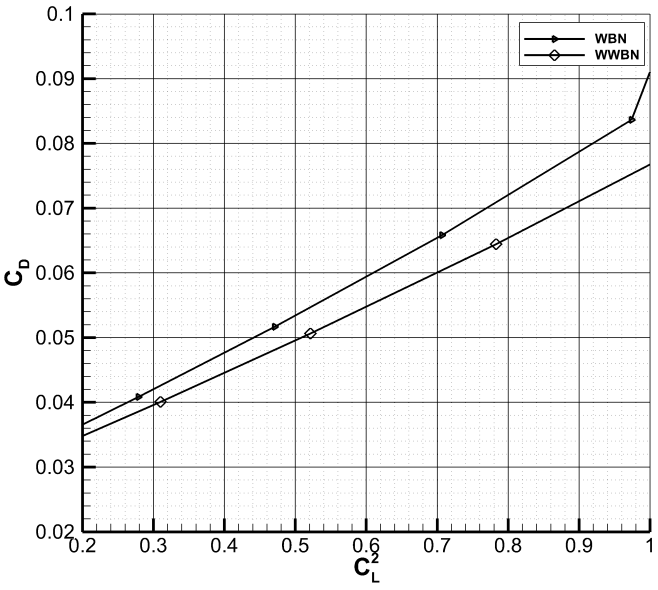

FIGURE 4.16: CFD C_D vs C_L^2 regression, Re=0.6e^6.

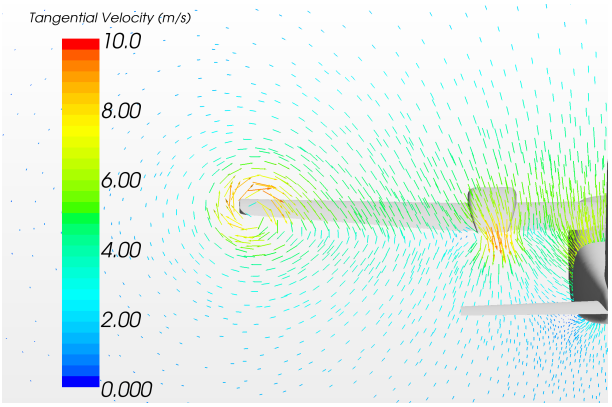

(a) Winglet off configuration.

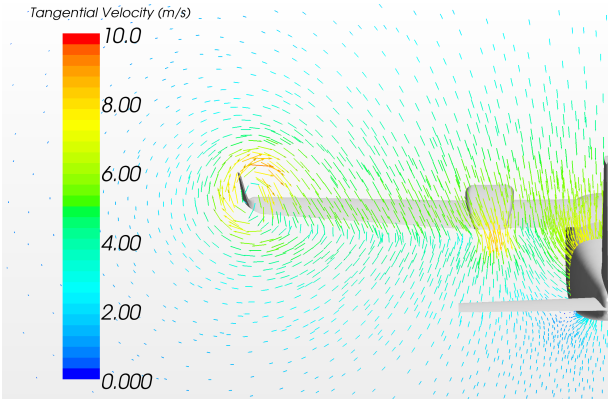

(b) Winglet on configuration.

FIGURE 4.17: Tangential velocity in a plane behind the wing, $\alpha = 10°$ at Re=0.6e^6.

4.5.2 Flap effects

The complete aircraft configuration has been tested at three different flap deflections: flap retracted, flap at 15° and full flap at 40° representative of cruise, take-off and landing conditions respectively. Fig. 4.18 shows the lift coefficient with respect to the angle of attack for the three flap deflections while Tab. 4.4 compares the numerical most significant derivatives and coefficient with the experimental data. The comparison between the numerical and experimental data is very remarkable in terms of lift curve slope. Experimental data dealing with the estimation of the maximum lift coefficient are not available thus a comparison with the numerical coefficients can not be effectuated. A good agreement is also shown dealing with the longitudinal stability in terms of the neutral point location. Differences can be appreciated in the estimation of the ΔC_{L_0}, those differences can be attributed to the uncertainty of the flap deflection angle of the experimental scale model. More in general it must be considered that there are some differences between the numerical and experimental tested geometry since the scale model of the aircraft has not been realised with a CNC machinery and thus the perfect matching of the simulated geometry with the tested one is not completely granted. Further discrepancies in the results can be due to uncertainty of the flap deflections measured during the experimental tests.

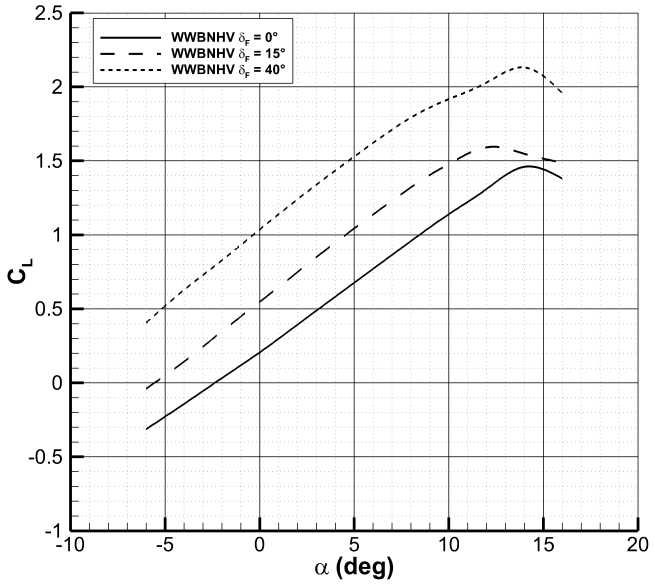

FIGURE 4.18: CFD complete aircraft lift coefficient at several flap deflections, Re=0.6e^6.

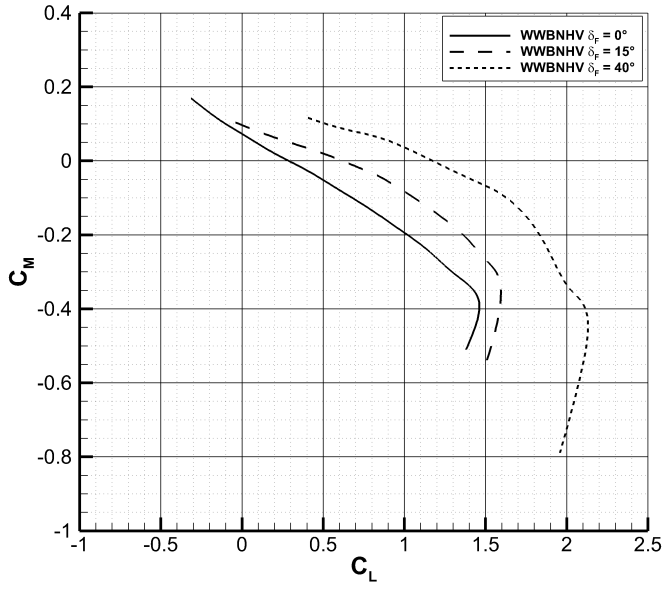

FIGURE 4.19: CFD complete aircraft pitching moment coefficient at several flap deflections, Re=0.6e^6.

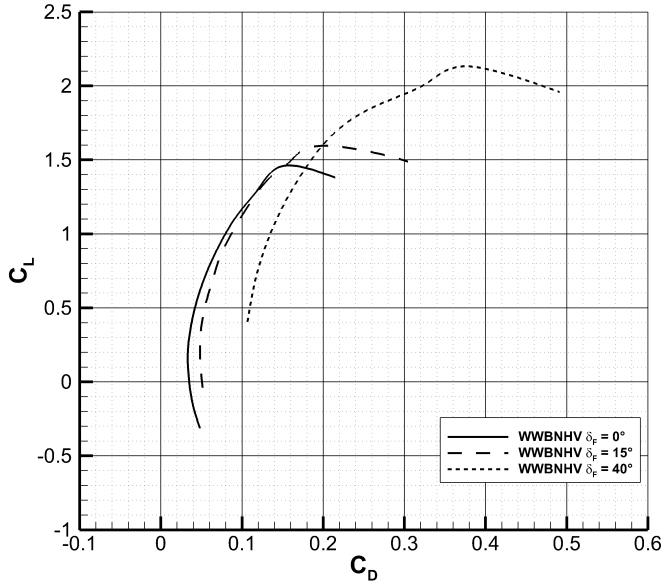

FIGURE 4.20: CFD complete aircraft drag coefficient at several flap deflections, Re=0.6e^6.

TABLE 4.4: CFD Flap effects summary results, at Re=0.6e^6.

	CFD RANS approach	Wind Tunnel Data
C_{L_α}, $\delta_F = 0°$	0.0941 deg^{-1}	0.0911 deg^{-1}
C_{L_α}, $\delta_F = 15°$	0.1000 deg^{-1}	0.101 deg^{-1}
C_{L_α}, $\delta_F = 40°$	0.1010 deg^{-1}	0.105 deg^{-1}
$C_{L_{max}}$, $\delta_F = 0°$	1.46	n.a.
$C_{L_{max}}$, $\delta_F = 15°$	1.60	n.a.
$C_{L_{max}}$, $\delta_F = 40°$	2.13	n.a.
ΔC_{L_0}, $\delta_F = 15°$	0.32	0.24
ΔC_{L_0}, $\delta_F = 40°$	0.83	0.78
C_{D_0} at $\alpha = 0°$, $\delta_F = 0°$	0.0334	0.0430
C_{D_0} at $\alpha = 0°$, $\delta_F = 15°$	0.0563	0.0576
C_{D_0} at $\alpha = 0°$, $\delta_F = 40°$	0.138	0.1160
N_0,$\delta_F = 0°$ (at $C_L = 0.4^*$)	50%	47%
N_0,$\delta_F = 15°$ (at $C_L = 1.0^*$)	53.3%	54.7%
N_0,$\delta_F = 40°$ (at $C_L = 1.6^*$)	50.1%	50.1%

*Calculated considering a linear regression of the curve C_M vs C_L near the considered lift coefficient.

4.5.3 CFD Longitudinal analysis validation

In previous sections a comparison between the longitudinal derivatives estimated both through experimental tests and numerical simulation has been shown. In this section the numerical longitudinal aerodynamic characteristics will be compared to the experimental ones in terms of curves, to better highlight how and how much numerical and experimental data agree. Fig. 4.21 shows the comparison of some tail off configurations, as it can be appreciated the matching between numerical and experimental data in terms of lift is very remarkable. Differences dealing with stability can be appreciated in terms of a shift in the C_M value due to discrepancies between the CAD geometry and the tested scale model, however the pitching moment curve slopes that can be estimated through both approaches are rather close. Fig. 4.22 shows instead the comparison among complete aircraft configuration at three flap deflections. The numerical lift curve slopes are very close to the experimental ones, a shift in terms of ΔC_{L_0} is due to uncertainty in the flap deflection angles measured in the wind tunnel. CFD results lead to a lightly larger longitudinal stability. Finally dealing with the drag estimation it is clear how the CFD approach underestimates the aircraft drag coefficient. Regarding this point it must be observed that experimental scale model has several gaps (i.e. control surfaces and flaps), flaps braces and many excrescences that are not present in the simulated numerical model, moreover, the experimental tests have been conducted by applying transitional strips on all aircraft components in order to avoid laminar separation bubbles. Other considerations to be made regard the wind tunnel wall presence, as matter of fact to take into account the effect of the tunnel walls all the required corrections have been applied to the experimental data, on the other hand the numerical simulations have been conducted in a simulated free stream conditions.

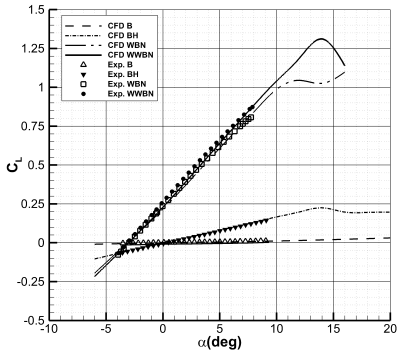

(a) Lift coefficient versus angle of incidence.

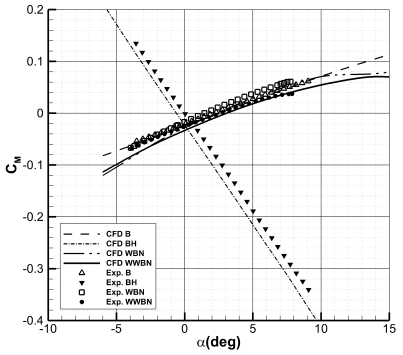

(b) Pitching moment coefficient versus angle of incidence.

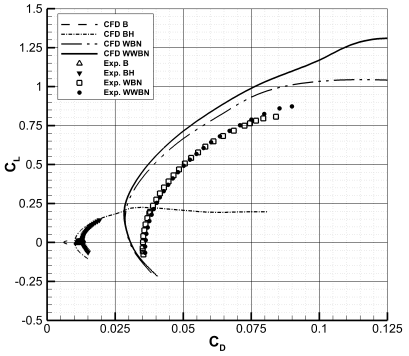

(c) Drag polar.

FIGURE 4.21: Comparison between CFD and wind tunnel results for tail off configurations, Re=$0.6e^6$.

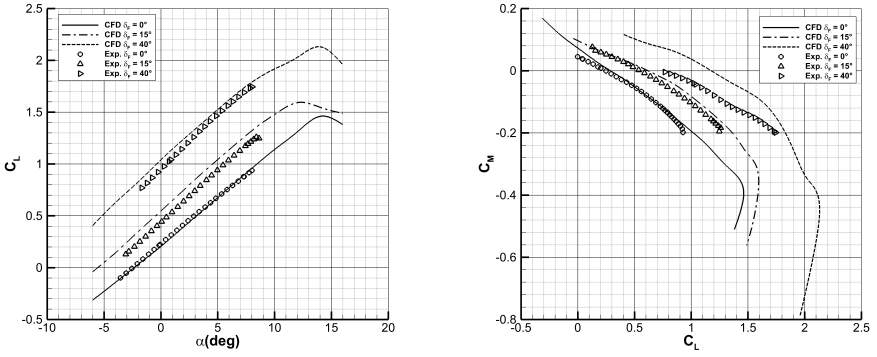

(a) Lift coefficient versus angle of incidence.

(b) Pitching moment coefficient versus angle of incidence.

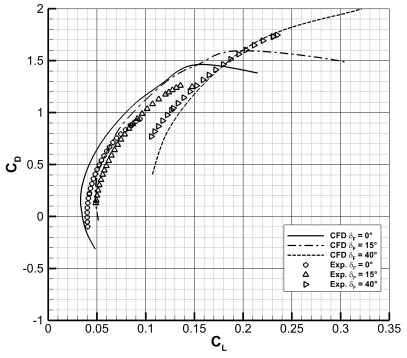

(c) Drag polar.

FIGURE 4.22: Comparison between CFD and wind tunnel results for complete aircraft at several flap deflections, Re=0.6e^6.

4.5.4 Reynolds Number Effects

In this section the effects of the Reynolds number on the longitudinal aerodynamic characteristics are illustrated. As already discussed in chapter 3 the main lacks in the experimental data are due to tests performed on a scale model in a low speed tunnel, making impossible to reply the free flight conditions in terms of Reynolds number. Moreover tests of flapped configurations have been limited to a maximum angle of attack of 9 degrees (due to structural reasons dealing with heavy vibrations of the scale model flap down configurations at higher attitudes), making impossible to extrapolate the maximum lift coefficients from tunnel Reynolds number to the free flight conditions by applying corrections procedures like those suggested by Rae and Pope [55]. The tested scale model was also missing of pressure probe along the wing span in order to provide the estimation of the wing loads. To supply those lacks several simulation at different Reynolds number have been performed. In addition to the wind tunnel Reynolds number other two conditions have been tested: Re=4.5e^6 and Re=9.5e^6 representative of landing (or take-off, these two flight conditions are very close in terms of Reynolds number) and cruise condition. In this section effects of Reynolds number, through CFD RANS analyses, on lift, drag, pitch characteristics and wing span loads are presented.

4.5.4.1 Reynolds number effect on lift and pitching moment on clean and full flap configurations

The tested configuration is the complete aircraft with flap retracted (clean configuration) and full flap (landing configuration), not trimmed, $i_{t_0} = 0°$. Fig. 4.23 shows the comparison of the lift curves at the three tested conditions. It is clear highlighted how the lift curve slope in the linear range of angle is slightly affected by the increasing Reynolds number, an increase of about 4.81% can be appreciated at cruise Reynolds number. The maximum lift coefficient and angle of attack at which it occurs increase according to what is predicted by theory and experimental results, see Ref. [12, 15, 55, 78, 79]. Fig. 4.24 shows instead the effects of the Reynolds number on the drag coefficient, as it could be expected by increasing the Reynolds number the viscous effects decrease leading to a reduction in the C_{D_0} (a more detailed analysis of the drag polar at varying of the Reynolds number is presented in sec. 4.5.4.2, where those effects on both pressure and skin drag coefficient are shown). Fig. 4.25 shows how the aircraft longitudinal stability derivatives in the linear range increases of about 2-3% (in terms of neutral point location in the range of cruise lift coefficient, $C_L \in [0.4, 0.5]$) increasing the Reynolds number. This is in accordance with what is also experimentally shown and discussed in Ref. [55], or the effect of higher Reynolds number is in the direction of a larger longitudinal stability than one measured at lower Reynolds number. Finally Fig. 4.26 shows the effect of increasing Reynolds number of the C_D versus the square lift coefficient C_L^2, how it is possible to appreciate the regression is almost linear in the whole

range of lift coefficient. Higher Reynolds numbers produce not only a shift in the curve (an almost constant ΔC_D applied on the whole curve) but also change the curve. This means that the estimations about the winglet effect on the induced drag (the slope of C_D vs. C_L^2 is the quantity used to estimate the Oswald's factor) carried out both through the experimental and numerical analyses, performed at the wind tunnel Reynolds number, are quite pessimistic if compared with those at higher Reynolds number. As shown in Tab. 4.6. This is not in accordance with what suggested by Rae ans Pope in [55], where it is stated that the induced drag factor estimation is independent by the Reynolds number. The landing flap configuration has been analysed at

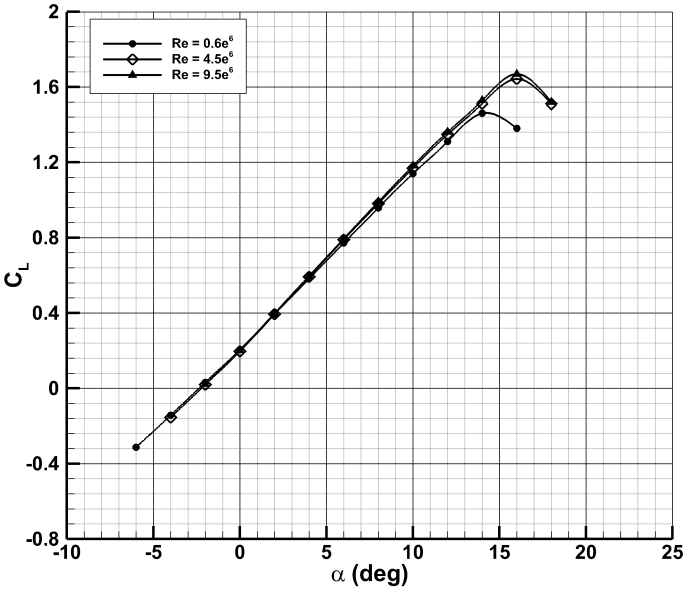

FIGURE 4.23: Reynolds number effect on lift coefficient for the complete aircraft in clean condition.

TABLE 4.5: Effect of Reynolds number on lift characteristics of the complete aircraft in clean condition.

Reynolds number	C_{L_0}	C_{L_α} (1/deg)	$\alpha_{z.L.}$ (deg)	$C_{L_{max}}$	$\alpha \mid_{C_{L_{max}}}$ (deg)	$\Delta C_{L_\alpha}\%$	$\Delta C_{L_{max}}\%$
0.6e^6	0.205	0.094	-2.4	1.46	14	-	-
4.5e^6	0.196	0.098	-2.2	1.64	16	4.0	12.5
9.5e^6	0.201	0.099	-2.2	1.67	16	4.8	14.3

Reynolds number of about $4.5e^6$ typical of landing conditions. Fig. 4.27 shows the effects of the Reynolds number on the longitudinal characteristics. Tab. 4.7

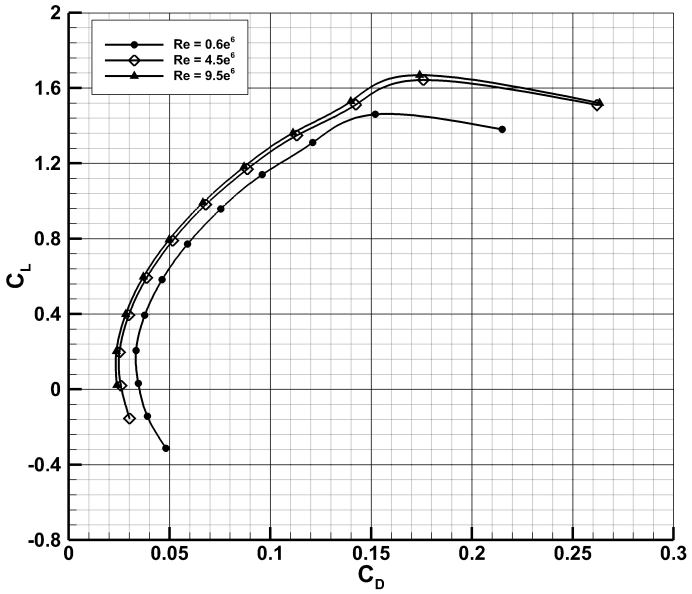

FIGURE 4.24: Reynolds number effect on the drag polar for the complete aircraft in clean condition.

TABLE 4.6: Effects of Re on drag polars

Reynolds number	C_{D_0}	$C_{D_{min}}$	$C_{L_{min.drag}}$	e	K	$\Delta C_{D_0}\%$	$\Delta e\%$
$0.6e^6$	0.0350	0.0334	0.205	0.820	0.04949	-	-
$4.5e^6$	0.0262	0.0251	0.196	0.861	0.04746	-25.2	4.3
$9.5e^6$	0.0239	0.0237	0.201	0.871	0.04661	-31.8	6.2

summarizes the main effects of the Reynolds number on the lift characteristics of full flap configuration.

TABLE 4.7: Effect of Reynolds number on lift characteristics of the complete aircraft in full flap condition.

Reynolds number	C_{L_0}	C_{L_α} (1/deg)	$C_{L_{max}}$	$\alpha\mid_{C_{L_{max}}}$ (deg)	$\Delta C_{L_\alpha}\%$	$\Delta C_{L_{max}}\%$
$0.6e^6$	1.036	0.101	2.13	14	–	–
$4.5e^6$	1.081	0.105	2.22	12	4.4	4.1

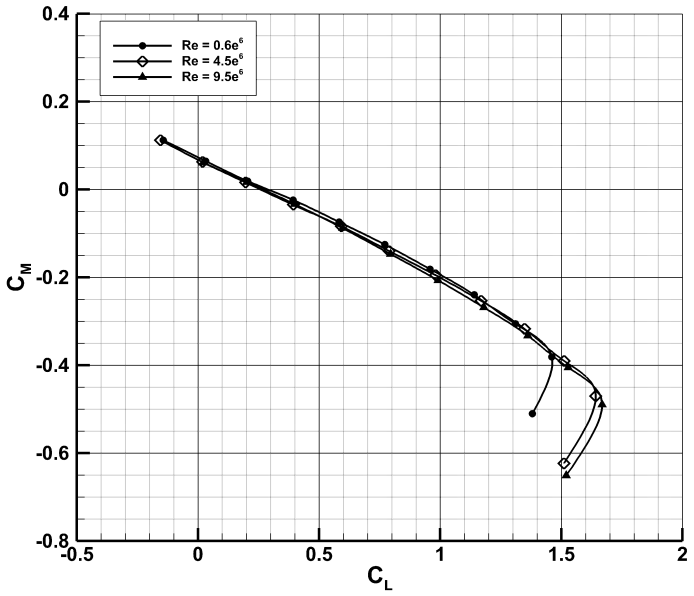

FIGURE 4.25: Reynolds number effect on longitudinal stability of the complete aircraft in clean condition.

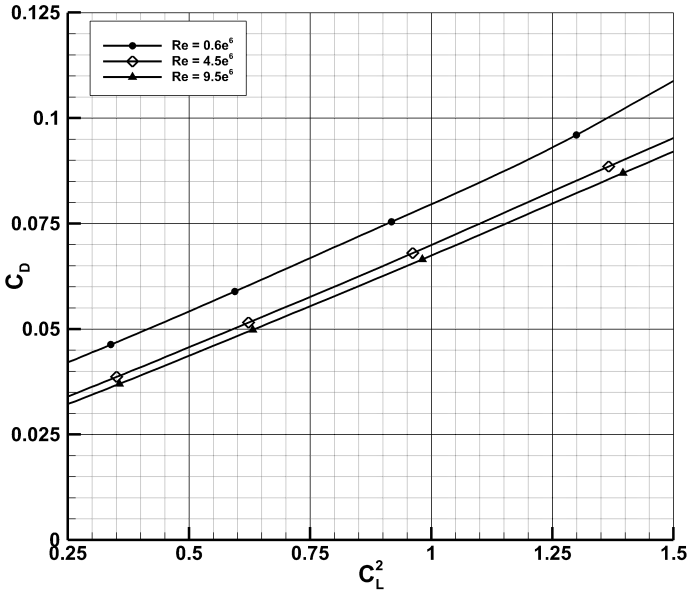

FIGURE 4.26: Reynolds number effect on the induced drag factor of the complete aircraft in clean condition.

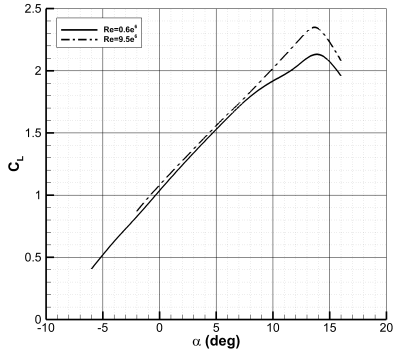

(a) Lift coefficient versus the angle of attack

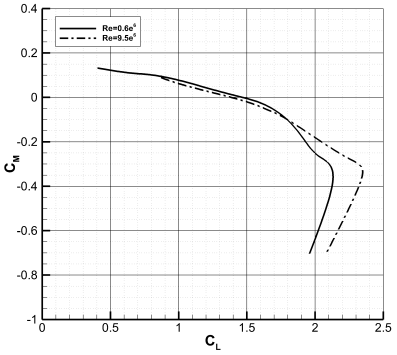

(b) Pitching moment coefficient versus the lift coefficient

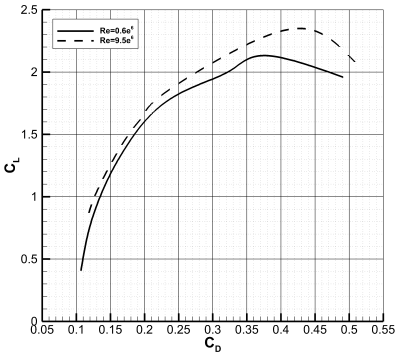

(c) Pitching moment coefficient versus the lift coefficient

FIGURE 4.27: Complete aircraft with full flap configuration, Reynolds number effects on longitudinal characteristics.

4.5.4.2 Reynolds number effect on drag coefficient

In this section a complete drag breakdown among the several aircraft components is shown and the effect of the Reynolds number is highlighted. Drag coefficient has been divided in its both contribution of skin friction and pressure in order to appreciate the Reynold number effect on both contribution to drag. In Tab. 4.8 and Tab. 4.9 are shown the percentage contribution of each aircraft component to the C_{D_0} for both Reynolds number. Nacelles

TABLE 4.8: Zero-lift drag coefficient breakdown at wind tunnel Reynolds number, $Re = 0.6e^6$.

Part	Pressure	Shear	Net	$\%C_D$	%Pressure	%Shear
Wing-Winglet	0.0039	0.0073	0.0112	32.5	35.2	64.8
Nacelles	0.0085	0.0019	0.0104	30.1	82.2	17.8
Body	0.0039	0.0049	0.0088	25.4	44.0	56.0
Horiz.tail	0.0005	0.0021	0.0025	7.4	19.0	81.0
Vert.tail	0.0003	0.0014	0.0016	4.7	15.9	84.1
Total:	0.0171	0.0174	0.0345	100.0	49.5	50.5

TABLE 4.9: Zero-lift drag coefficient breakdown at flight Reynolds number, $Re = 9.5e^6$.

Part	Pressure	Shear	Net	$\%C_D$	%Pressure	%Shear
Wing-Winglet	0.0012	0.0050	0.0062	26.0	19.4	80.6
Nacelles	0.0072	0.0013	0.0085	35.6	85.2	14.8
Body	0.0037	0.0030	0.0066	27.8	55.2	44.8
Horiz.tail	0.0002	0.0014	0.0015	6.4	11.2	88.8
Vert.tail	0.0001	0.0009	0.0010	4.2	10.8	89.2
Total:	0.0124	0.0115	0.0239	100.0	51.9	48.1

contribution to C_{D_0} is about 30% of its total amount, and the main about 80% of nacelles contribution is represented by the pressure drag. This contribution seems to be quite larger than it could be expected. It must be remarked that in the numerical model (and also the wind tunnel model) the nacelles air-intake and exhaust have been closed, thus stagnation areas will occur at the nacelles air intakes and heavy separation regions can be appreciated as it is shown in Fig. 4.29 where the streamlines on nacelles surfaces are depicted. In Tab. 4.10 and Tab. 4.11 the aircraft components contribution to the zero lift drag coefficient, estimated through both CFD and experimental approaches are compared. In section 3.7.2 a possible procedure to correct the experimental drag coefficient taking into account the Reynolds number scaling effect has been proposed. This procedure has led to a scaling factor of 0.61. As it can been appreciated by comparing the CFD results for the estimation of the C_{D_0}

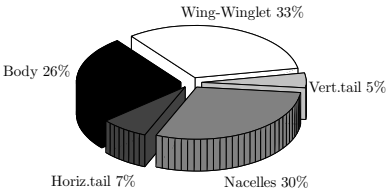

(a) $Re = 0.6e^6$.

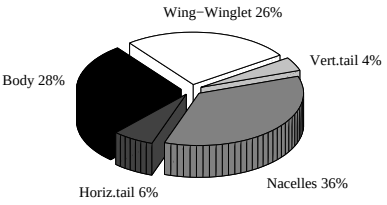

(b) $Re = 9.5e^6$.

FIGURE 4.28: Pie chart of percentage contribution of each aircraft component.

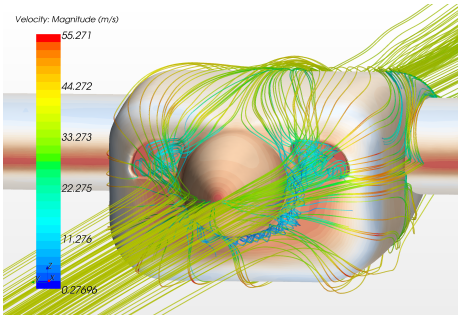

(a) Stagntion areas on air-intakes.

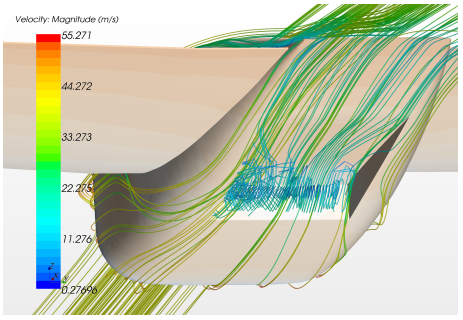

(b) Separation area on air-exhaust.

FIGURE 4.29: Streamlines on nacelles surface.

at both simulated Reynolds numbers, the correction factor is about 0.7 quite higher than that proposed in section 3.7.2. This is attributable to the fact that by applying the correction procedure based on the skin friction coefficient, it has been assumed that all the drag is due to friction forces, but, as it has been highlighted in this section, the pressure contribution to the drag is quite remarkable. Indeed, considering the CFD results shown in Tab. 4.8 and Tab. 4.9, the ratio between the skin friction contributions at two Reynolds number is about 0.66 and thus very close to what has been estimated in section 3.7.2, but comparing the pressure contributions to drag, the ratio is about 0.73. However the complete aircraft zero lift drag coefficients estimated through both CFD and wind tunnel approaches are very close. A comparison among the several aircraft component contributions estimated with both approaches is hard to perform since it was impossible to experimentally measure each contribution independently as it can be performed in the numerical simulation.

TABLE 4.10: Drag breakdown comparison between CFD and tunnel data, $Re = 0.6e^6$.

Component	C_{D_0} CFD	C_{D_0}Experimental
Wing-Winglet	0.0112	0.0216
Nacelles	0.0104	0.0035
Body	0.0088	0.0110
Horiz.tail	0.0025	0.0019
Vert.tail	0.0016	0.0020
Total:	0.0345*	0.0400

*No wing-fuselage fairing

TABLE 4.11: Drag breakdown comparison between CFD and tunnel data, $Re = 9.5e^6$.

Component	C_{D_0} CFD	C_{D_0}Experimental*
Wing-Winglet	0.0066	0.0132
Nacelles	0.0085	0.0024
Body	0.0066	0.0067
Horiz.tail	0.0015	0.0012
Vert.tail	0.0010	0.0012
Total:	0.0239	0.0244

*Estimated for each component as suggested in sec. 3.7.2.

**No wing-fuselage fairing

4.5.4.3 Reynolds number effect on wing loads

The estimation of wing span loads is a relevant information in order to supply the right sizing of wing structure and for the preparation of the wing structure static tests. In this section will be illustrated the procedure used to extract the wing loads from the CFD numerical simulations, and the effect of Reynolds number on wing loads will be shown. The procedure used to evaluate the wing loads consists of extracting both pressure and skin friction coefficient on several wing sections, as it is shown in Fig. 4.30. The local lift coefficient, C_l, can be expressed as shown in Eq. 4.2. In order to calculate both longitudinal and normal forces coefficient (C_x and C_z respectively), the pressure (C_P) and the skin friction coefficient (C_f), acting on a wing section, can be integrated as shown in Eq. 4.3. This procedure has been completely automated in a MATLab®code.

$$C_l = C_z \cos\alpha - C_x \sin\alpha \tag{4.2}$$

C_x and C_z are calculated as shown by Eq. 4.3.

$$\begin{aligned} C_x &= \int_0^1 \left(C_{p_{upper}} - C_{p_{lower}}\right) d\left(\tfrac{z}{c}\right) + \int_0^1 \left(C_{f_{upper}} + C_{f_{lower}}\right) d\left(\tfrac{x}{c}\right) \\ C_z &= \int_0^1 \left(C_{p_{lower}} - C_{p_{upper}}\right) d\left(\tfrac{x}{c}\right) + \int_0^1 \left(C_{f_{upper}} + C_{f_{lower}}\right) d\left(\tfrac{z}{c}\right) \end{aligned} \tag{4.3}$$

The fuselage contribution to the lift coefficient has been estimated by subtracting the contribution of the wing to the wing-body configuration lift coefficient, as shown in Eq. 4.4, where root coordinate is $\eta_r = \frac{D_f/2}{b/2}$.

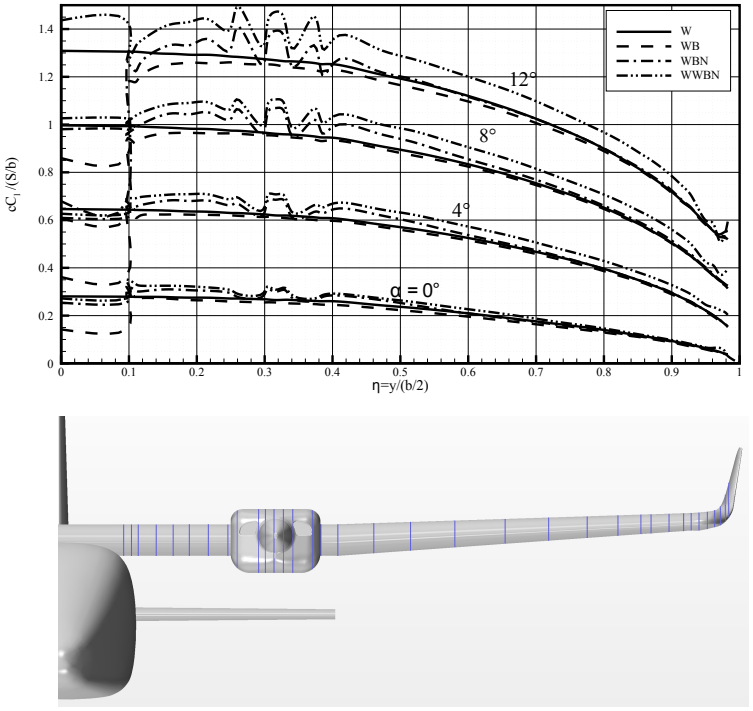

FIGURE 4.30: Wing span load distribution, $Re = 0.6e^6$.

$$\begin{aligned} C_{L_{body}} &= C_{L_{wing-body}} - \tfrac{b}{S} \int_{\eta_r}^1 cC_l d\eta \\ C_{l_{body}} &= \frac{C_{L_{body}} S}{bc_r \eta_r} \end{aligned} \tag{4.4}$$

Fig. 4.31 shows some example of wing section used to perform the estimation of the wing span loads. Fig. 4.32 is shown the comparison among the wing load distributions of several configurations,it is possible to appreciate the effects of the fuselage, nacelle and winglet. Wing loads can be extracted also for the flapped configurations as shown in Fig.4.32, in this case, for the

flapped sections, the local lift coefficient has been calculated by integrating the pressure and skin friction coefficient on both parts of the section or the main and the flap surfaces, as it can be appreciated in Fig. 4.34 and in Fig. 4.35. Fig. 4.36 shows the comparison between the wing span loads at two Reynolds number. Within the linear range no appreciable differences can be highlighted both in terms of global coefficient (lift coefficient in the linear rang is almost unaffected by the Reynolds number) and wing load distributions. Outside the linear variation of the lift curve, where the different viscous behaviour of the two tested flow conditions became remarkable strong differences can be appreciated. In effect, as it is shown in Fg. 4.36 stall path changes: the incidence angle at which the stall occur grows up to 18° for the free flight Reynolds number, and the first section to be affected by stall moves from the outer to the inner side of the nacelles. This investigation highlights how, if experimental data, concerning with lift spanwise distributions, were available, they can be considered to be a reliable prediction of a full scale aircraft only within the linear range of the lift curve, where, Reynolds number does not affect in a sensible way the aerodynamic behaviour of the flow. No experimental data are available from the tunnel tests campaign since the tested scale model was not provided of pressure probes along the wing span. Thus a comparison between the estimated wing loads through the CFD RANS approach cannot be performed to validate the goodness of the numerical prediction of this parameter. However many works have been validated the RANS approach capability into prediction of section pressure distribution also for high lift configuration, see Ref. [76], and in particular Ref. [80], where precisely the solver $STAR-CCM+$ has been used to predict the high lift characteristics of a trapezoidal wing. In Ref. [80] many comparisons, in terms of pressure distribution along spanwise, have shown the good agreement between the experimental and numerical results.

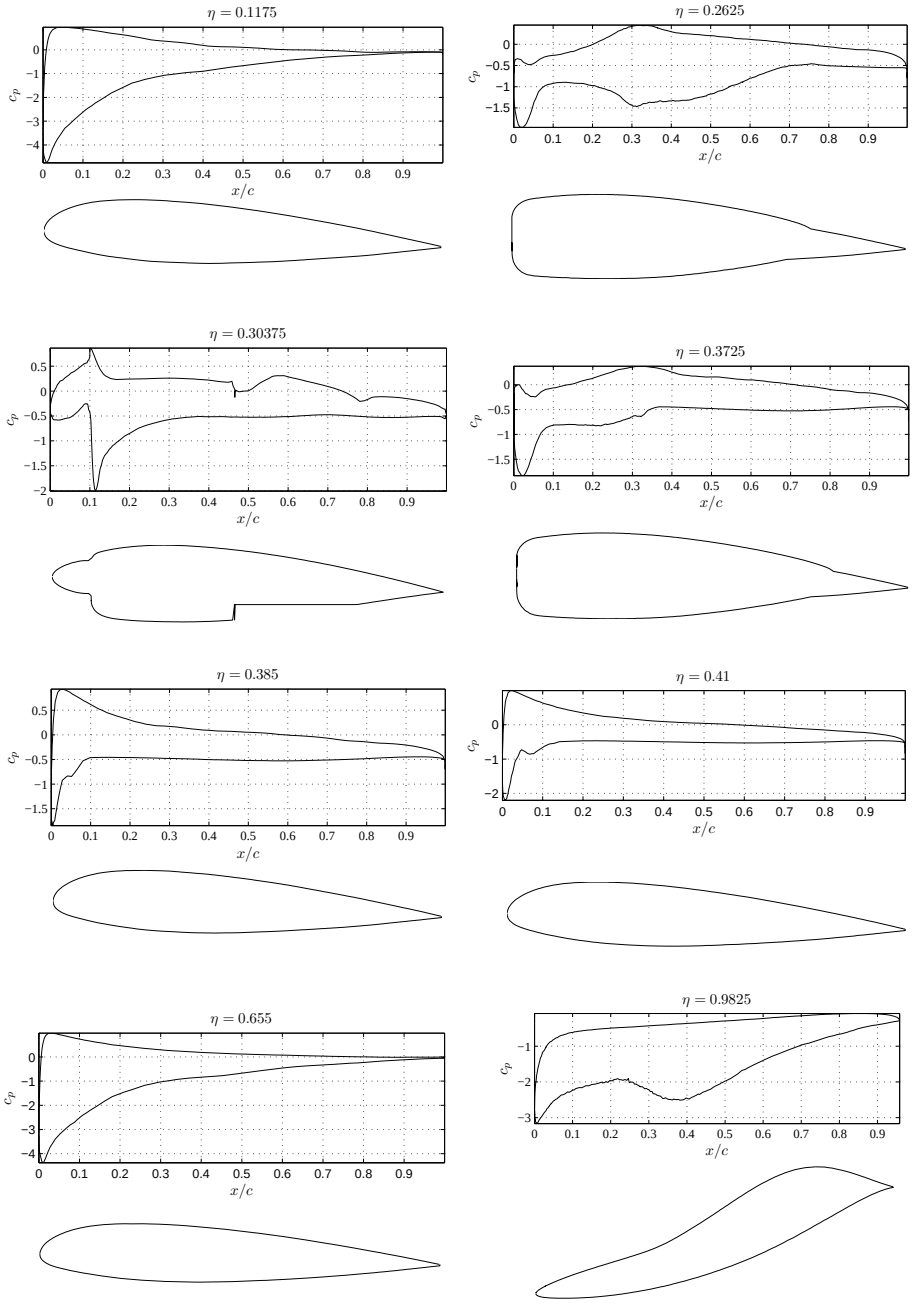

FIGURE 4.31: Pressure distribution on some sections of clean wing at $\alpha = 16°$, $Re = 0.6e^6$.

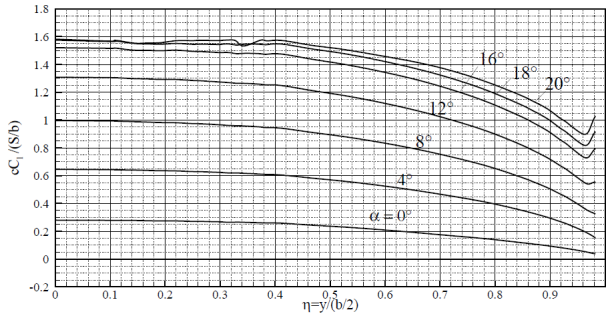

(a) Wing.

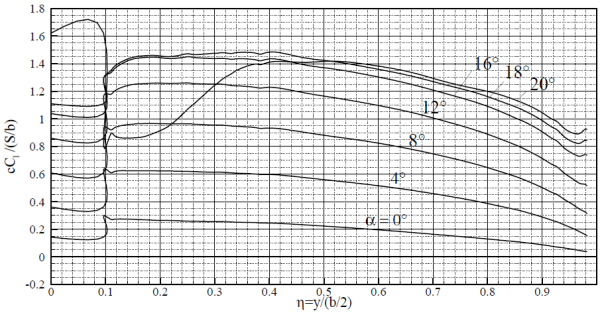

(b) Wing-Body.

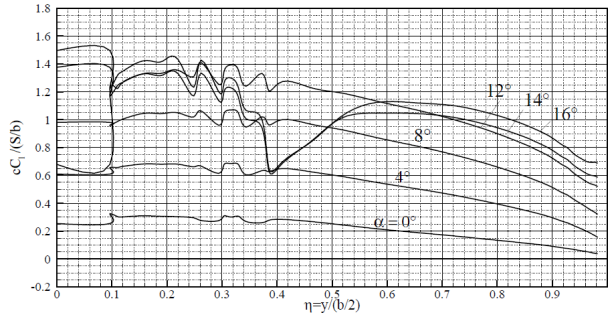

(c) Wing-Body-Nacelle.

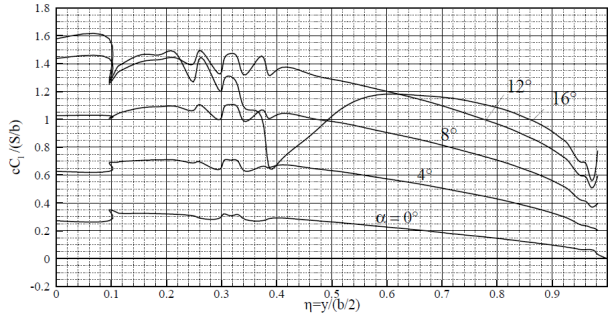

(d) Wing-Winglet-Body-Nacelle.

FIGURE 4.32: Wing Load Distribution along wingspan. $Re = 0.6^6$.

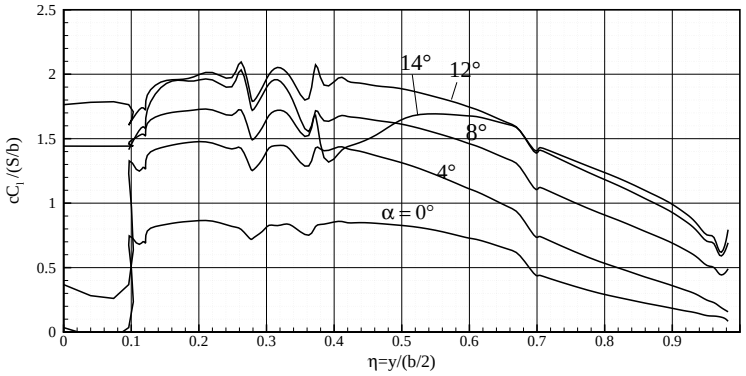

(a) Flap deflection 15°.

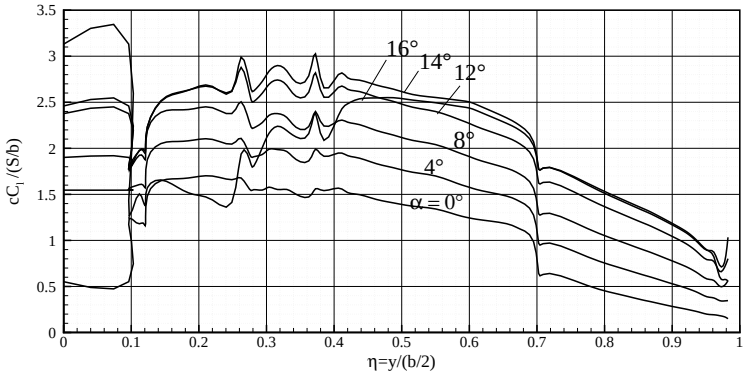

(b) Flap deflection 40°.

FIGURE 4.33: Wing load distribution in take-off and landing configuration, $Re = 0.6e^6$.

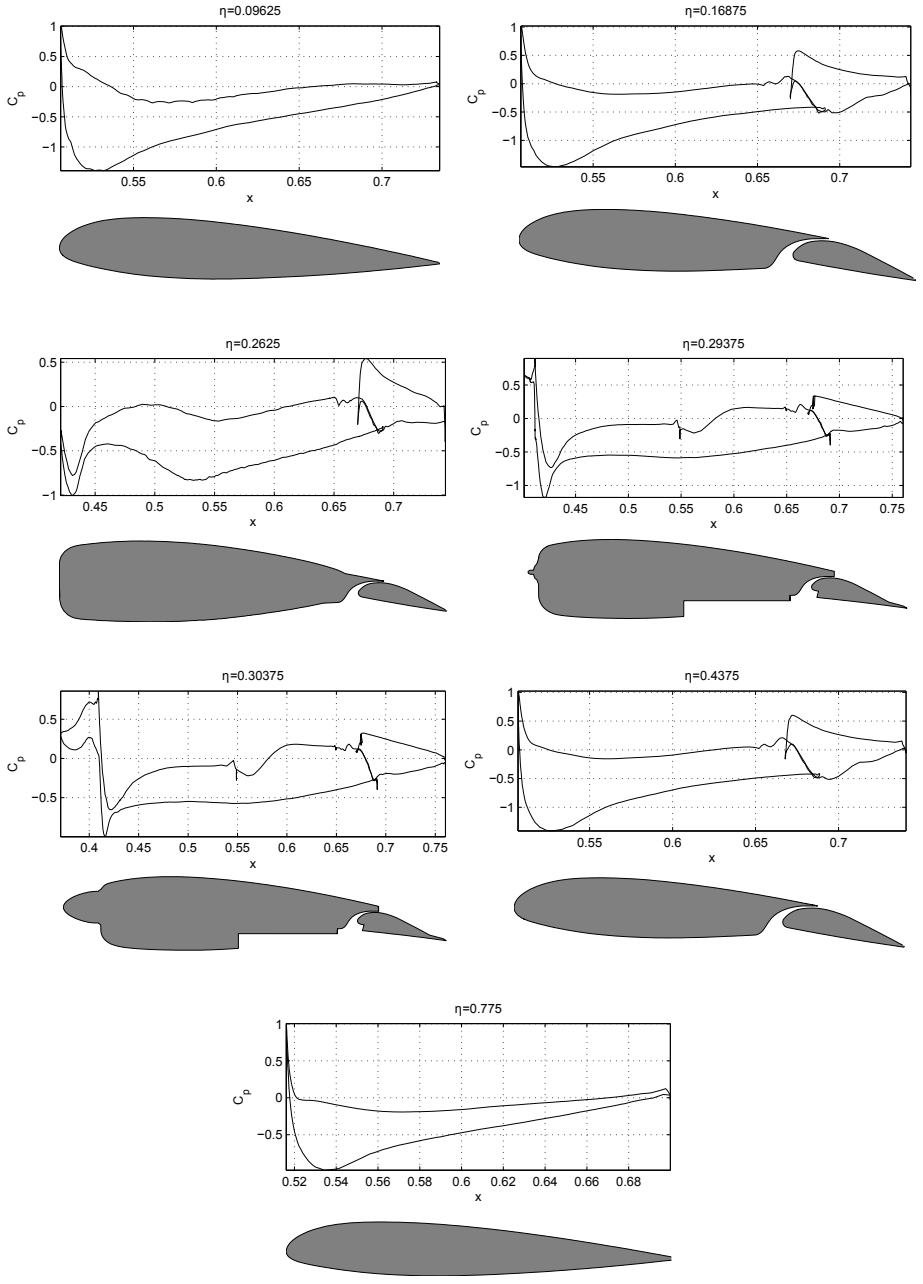

FIGURE 4.34: Pressure distribution of some wing sections at $\alpha = 0°$, flap deflection 15°. $Re = 0.6e^6$.

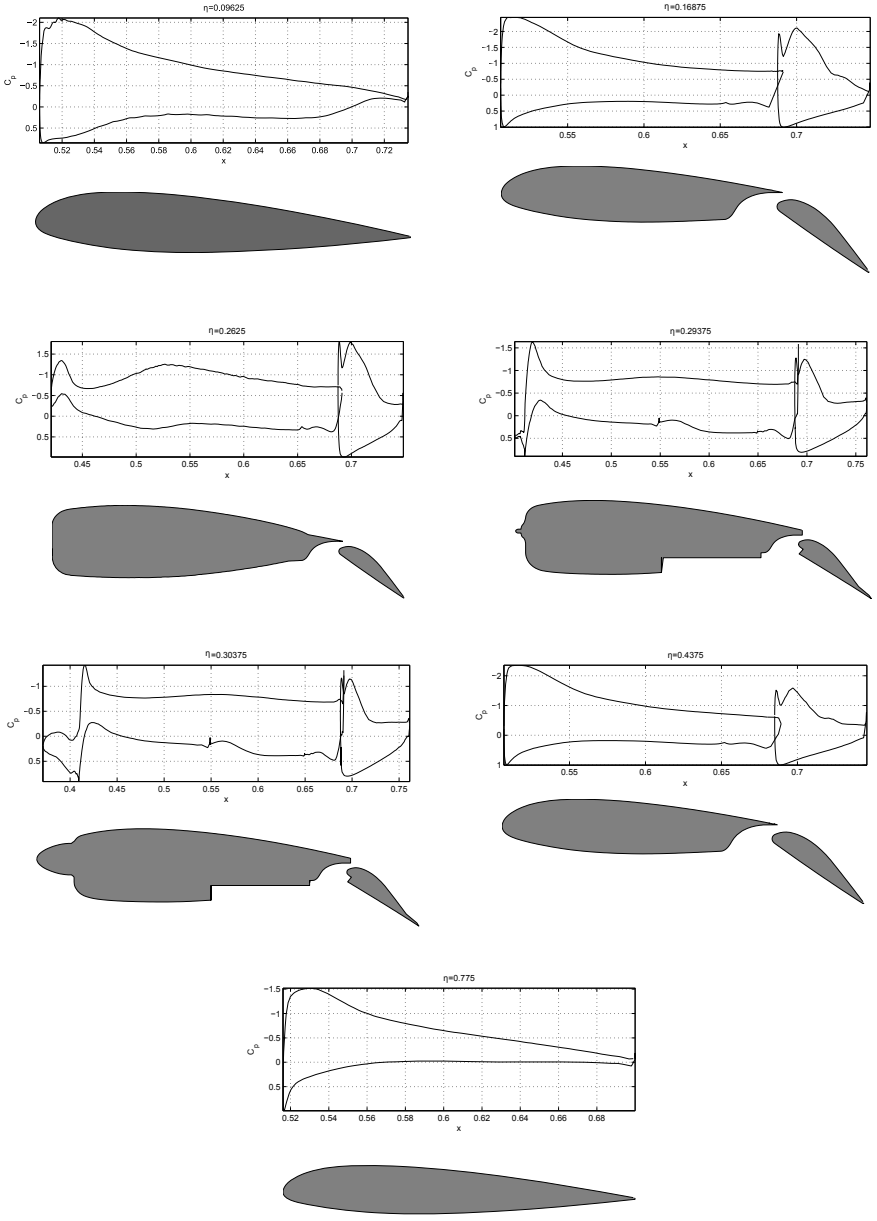

FIGURE 4.35: Pressure distribution of some wing sections at $\alpha = 0°$, flap deflection 40°. $Re = 0.6e^6$.

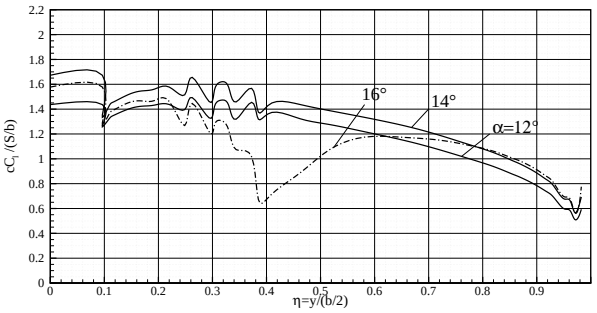

(a) Wing loads at $Re = 0.6e^6$

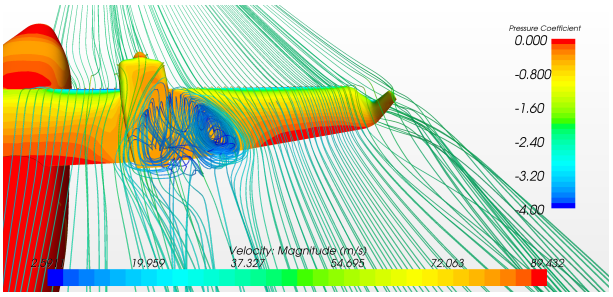

(b) Contour of C_P and streamlines at the stall angle, $Re = 0.6e^6$

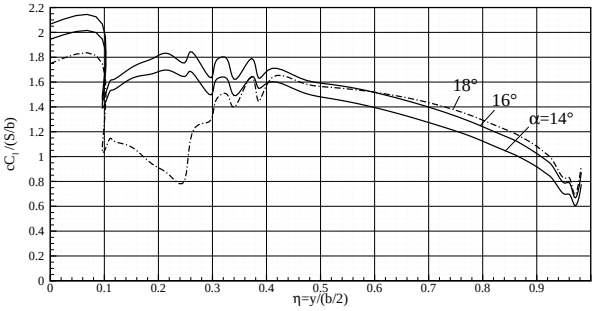

(c) Wing loads at $Re = 9.5e^6$

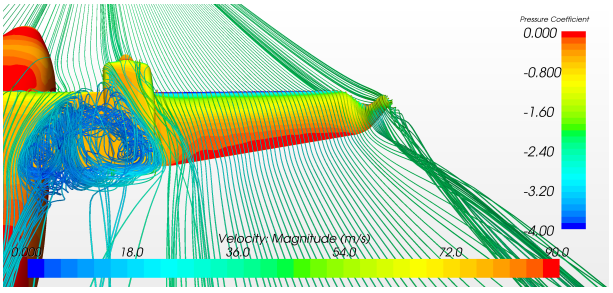

(d) Contour of C_P and streamlines at the stall angle, $Re = 9.5e^6$

FIGURE 4.36: Effect of Reynolds number on stall path and wing loads, flap up configuration.

4.5.5 Trim analysis, downwash estimation and wing wake displacement

A trim analysis of the complete aircraft at two flap deflections has been performed in order to validate the estimation assessed through both semi-empirical and experimental data, dealing with trim capabilities and the required horizontal tail incidence angle. As was already assumed for the experimental and semi-empirical approaches, the most critical condition for the trim analysis as been considered the maximum forward position of the centre of gravity at 18% of the mean aerodynamic chord. Two angle of incidence for the horizontal tail plane has been considered, $i_{t_0} = 0°$ and $-2°$. Fig. 4.37 and Fig. 4.38 show the variation of the pitching moment coefficient with respect to the lift coefficient at three elevator angles and for both considered horizontal tail incidence angles. The CFD results, estimated at free flight Reynolds number, and the experimental data, at wind tunnel Reynolds number, are compared. The chosen horizontal tail incidence angle of -2° leads to the aircraft to be trimmed at about $C_L = 0.5$ without elevator deflection. The numerical and experimental results shown a very good matching, highlighting the goodness of the numerical approach. Numerical results for the full flap configuration

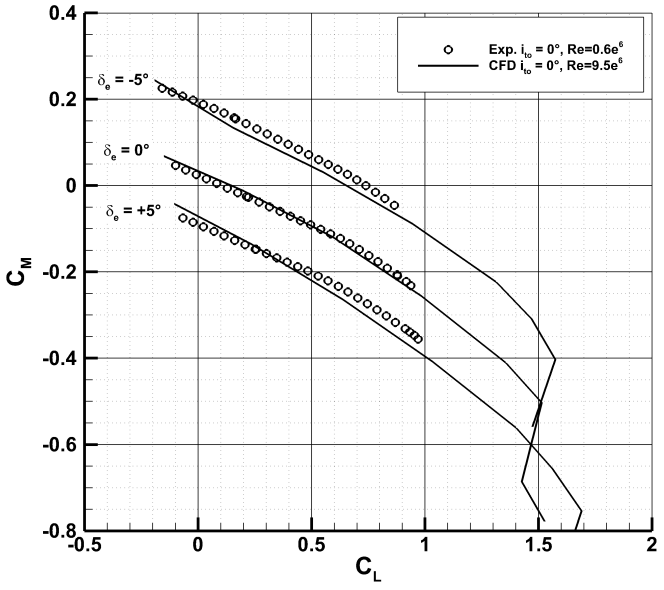

FIGURE 4.37: Trim analysis, flap up and $i_{t_0} = 0°$.

are shown in Fig. 4.39 and Fig. 4.40 for $i_{t_0} = 0°$ and $-2°$ respectively. The numerical analyses shows how in the full flap and with most forward centre of gravity condition, the aircraft could be trimmed in the landing lift coefficient range of $1.3 < C_L < 1.9$ with about 0-10 degrees if elevator deflection. The

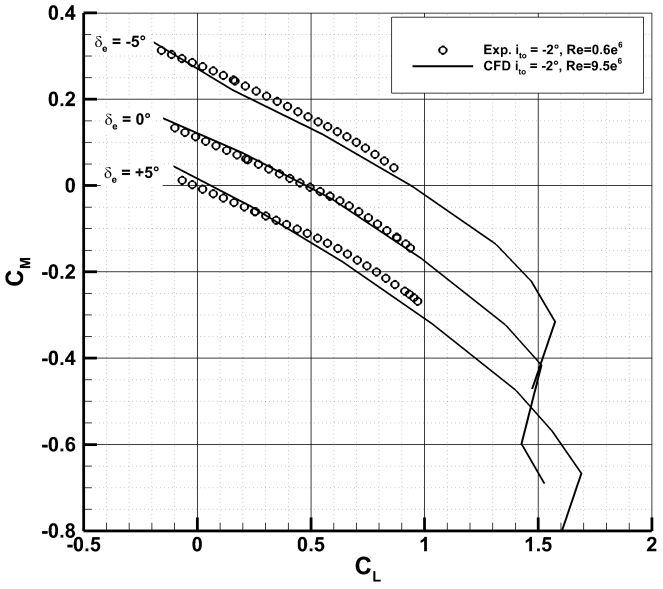

FIGURE 4.38: Trim analysis, flap up and $i_{t_0} = -2°$.

numerical simulation, at flight conditions, shows how with a horizontal tail incidence of $-2°$ the aircraft could be trimmed at lift coefficient up to 2.1. This is well in accordance with the experimental estimation and no extrapolation are required unlike the tunnel data. Horizontal tail lift coefficients in several configurations are plotted in Fig. 4.41. In Tab. 4.12 the derivatives $(dC_L/d\alpha)_h$ and $(dC_m/d\alpha)_h$, estimated in the linear range of $\alpha \in [0°, 6°]$, are shown. C_{L_h} has been normalized with respect to the wing surface. In Fig. 4.42 are plotted downwash angles variation with respect to the angle of attack. They have been calculated as the $\Delta\alpha$ at fixed C_{L_h}, assuming the dynamic pressure ratio $\eta_h = 1$. The curves slope decreases at higher incidence angles since the wing wake moves away from the tail surface, as it is confirmed by the the estimation of the wing wake displacement shown in Fig. 4.46. Tab. 4.13 shows the downwash derivative, $d\epsilon/d\alpha$, estimated through the application of the Eq. 4.5, where $\left(\frac{dC_L}{d\alpha}\right)_{h0}$ represents the contribution to the lift curve slope of the horizontal tail in the configuration under investigation.

$$\frac{d\epsilon}{d\alpha} = 1 - \frac{(dC_L/d\alpha)_h}{(dC_L/d\alpha)_{h0}} \tag{4.5}$$

As it can be shown in Tab. 4.13 the winglets do not affect in a sensible way the wing downwash, an increase of the downwash derivatives of about 2% can be appreciated. This is due to the winglet effects on the wing load distribution, as it is clearly outlined in Fig. 4.30, where it is possible to appreciate how

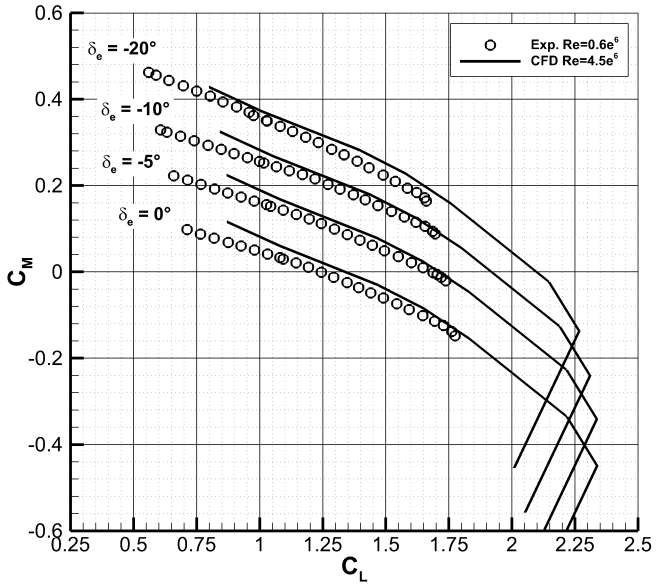

FIGURE 4.39: Trim analysis, full flap $i_{t_0} = 0°$.

the winglets lead to and increase in the overall wing load distributions. A larger contribution to the downwash is due to the nacelles, which contribute to increase the downwash derivatives on the tail plane of about 9%. This is clearly due to the effect produced by nacelles on the wing loads, as it is outlined in Fig. 4.30, moreover, the nacelles wake invests a large part of the horizontal tail plane, see is Fig. 4.46. Fig. 4.46, Fig. 4.47 and Fig. 4.48 show a three dimensional view of the wing wake displacement along a plane close to the wing trailing edge for different incidence angles at several flap deflections.

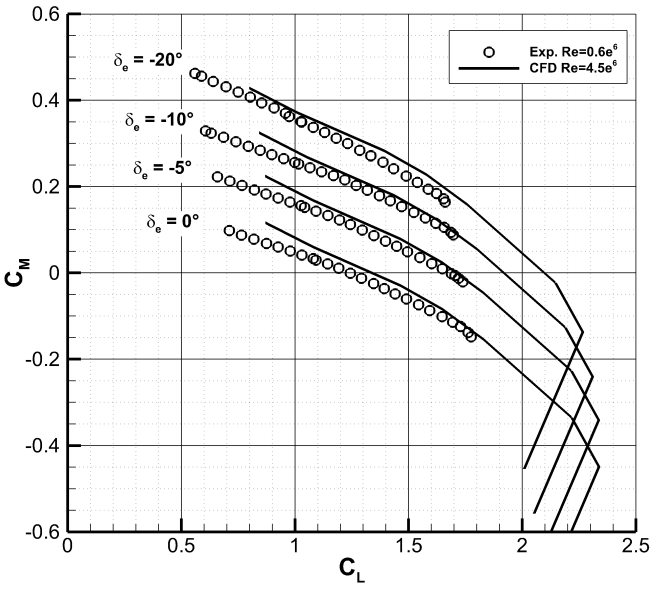

FIGURE 4.40: Trim analysis, full flap and $i_{t_0} = -2°$.

TABLE 4.12: Horizontal tail lift and moment coefficients derivatives, $Re = 9.5e^6$.

Configuration	$(dC_L/d\alpha)_h$ (1/deg)	$(dC_m/d\alpha)_h$ (1/deg)	$\alpha_{z.L_h}$ (deg)	$(C_{L_h})_{max}$	$\alpha\|_{(C_{L_h})_{max}}$ (deg)
H	0.0171	-0.0539	0.0	0.247	16
WH	0.0123	-0.0390	1.6	0.236	20
WNH	0.0118	-0.0375	1.7	0.224	18
WWH	0.0122	-0.0387	1.7	0.235	20
WWHN	0.0120	-0.0381	1.8	0.226	18
BH	0.0140	-0.0442	0.1	0.184	14
BHV	0.0139	-0.0438	-0.3	0.187	14
WBHV	0.0102	-0.0324	1.3	0.182	18
WBNHV	0.0099	-0.0314	1.5	0.183	18
WWBNHV	0.0099	-0.0317	1.7	0.187	18

TABLE 4.13: Downwash angle on horizontal tail. $Re = 9.5^6$.

Configuration	ϵ_0 (deg)	$d\epsilon/d\alpha$ (eq. 4.5)	$d\epsilon/d\alpha$ (fig. 4.42)	$\Delta d\epsilon/d\alpha\%$ (eq. 4.5)
WH	1.097	0.266	0.283	-
WNH	1.145	0.293	0.310	9.7
WWH	1.157	0.272	0.289	2.1
WWHN	1.237	0.282	0.300	6.0
WBHV	1.174	0.264	0.268	-
WBNHV	1.281	0.288	0.290	8.1
WWBNHV	1.363	0.280	0.284	6.1

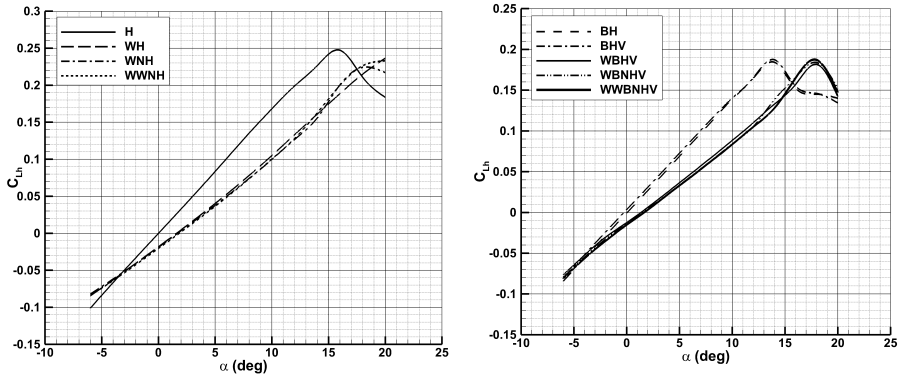

(a) Wing-Horizontal configuration (b) Wing-Body-Horizontal configuration

FIGURE 4.41: Horizontal tail lift coefficient variation with respect to the angle of attack for different configurations. $Re = 9.5e^6$.

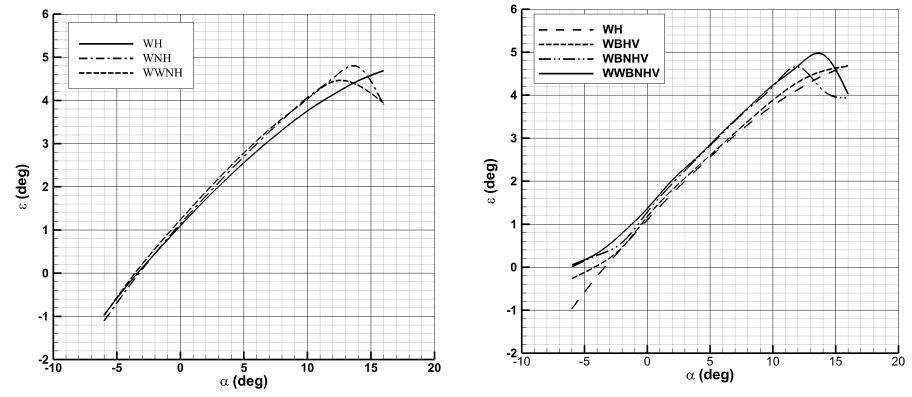

(a) Wing-Horizontal configuration (b) Wing-Body-Horizontal configuration

FIGURE 4.42: Downwash angle variation with respect to the angle of attack for complete aircraft. $Re = 9.5e^6$.

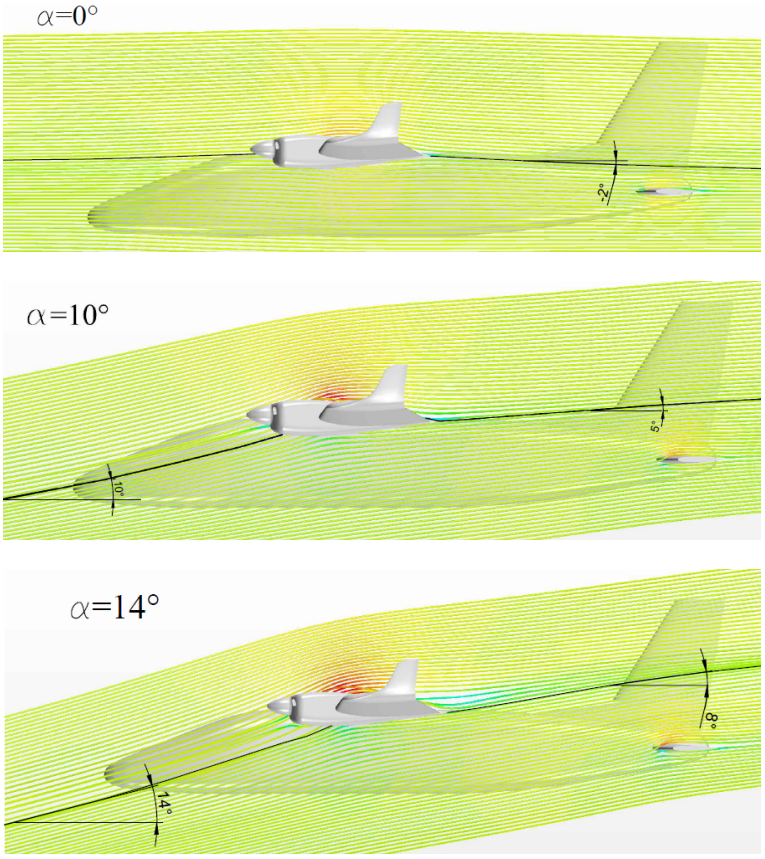

FIGURE 4.43: Lateral view of the wing wake displacement in flap up configuration, $Re = 9.5e^6$.

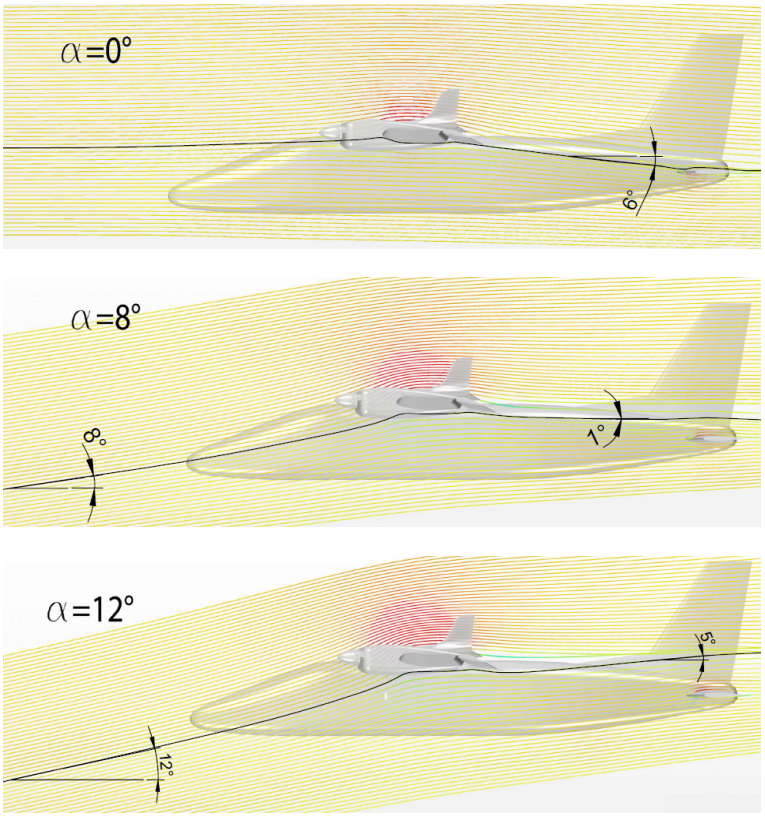

FIGURE 4.44: Lateral view of the wing wake displacement in take-off flap configuration, $Re = 9.5e^6$.

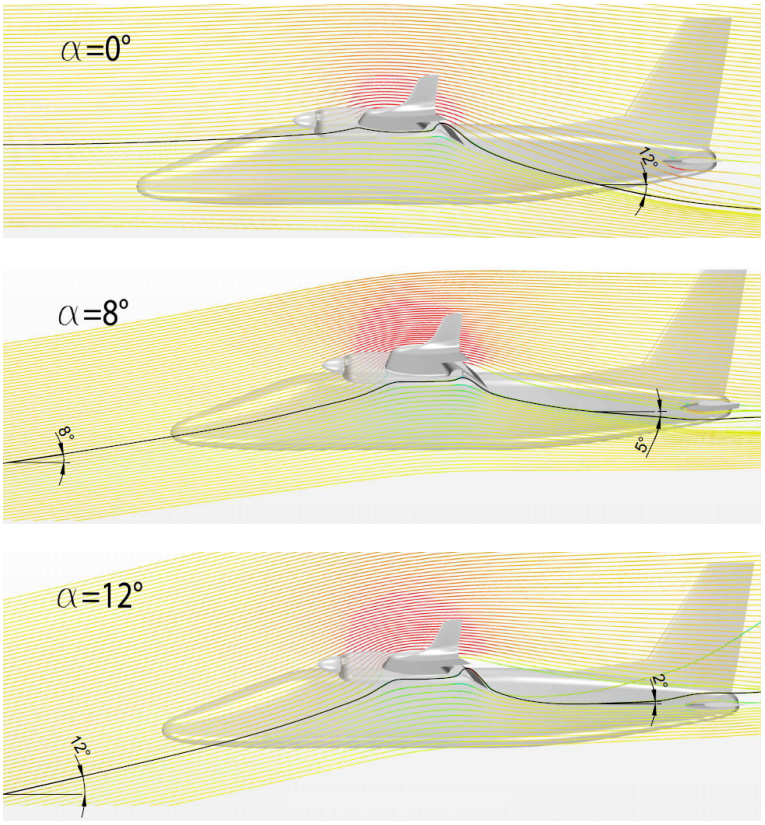

FIGURE 4.45: Lateral view of the wing wake displacement in landing flap configuration, $Re = 9.5e^6$.

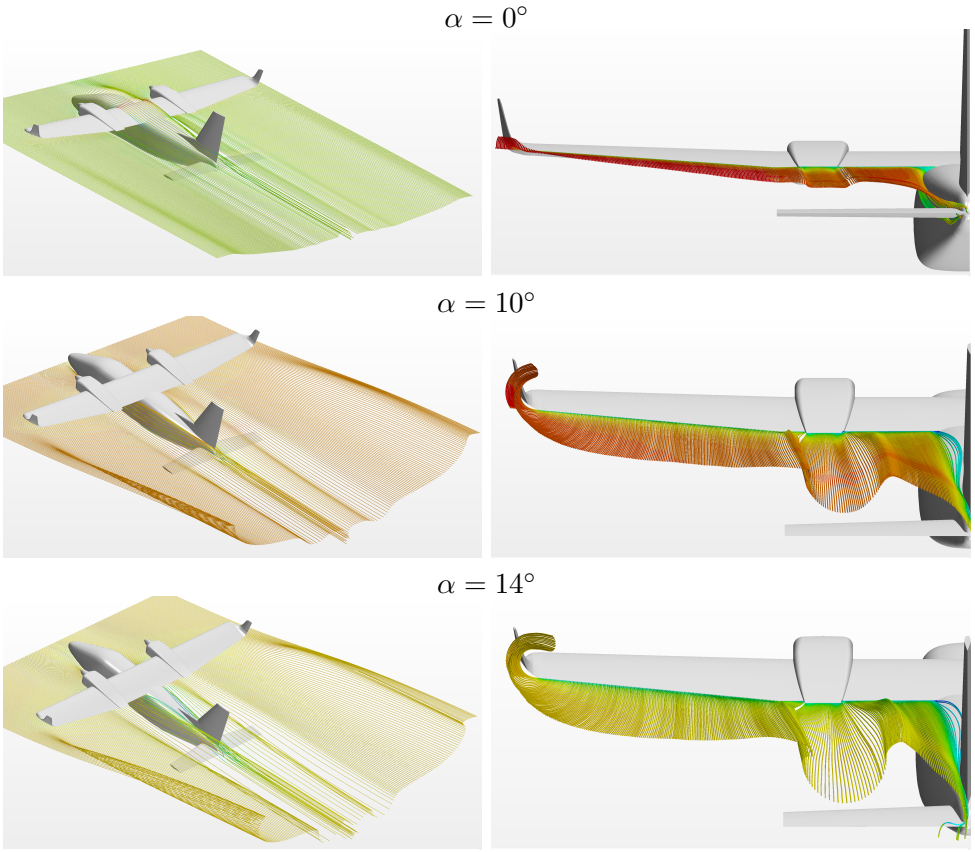

FIGURE 4.46: Wing wake displacements in flap up configurations, 3D views, $Re = 9.5e^6$.

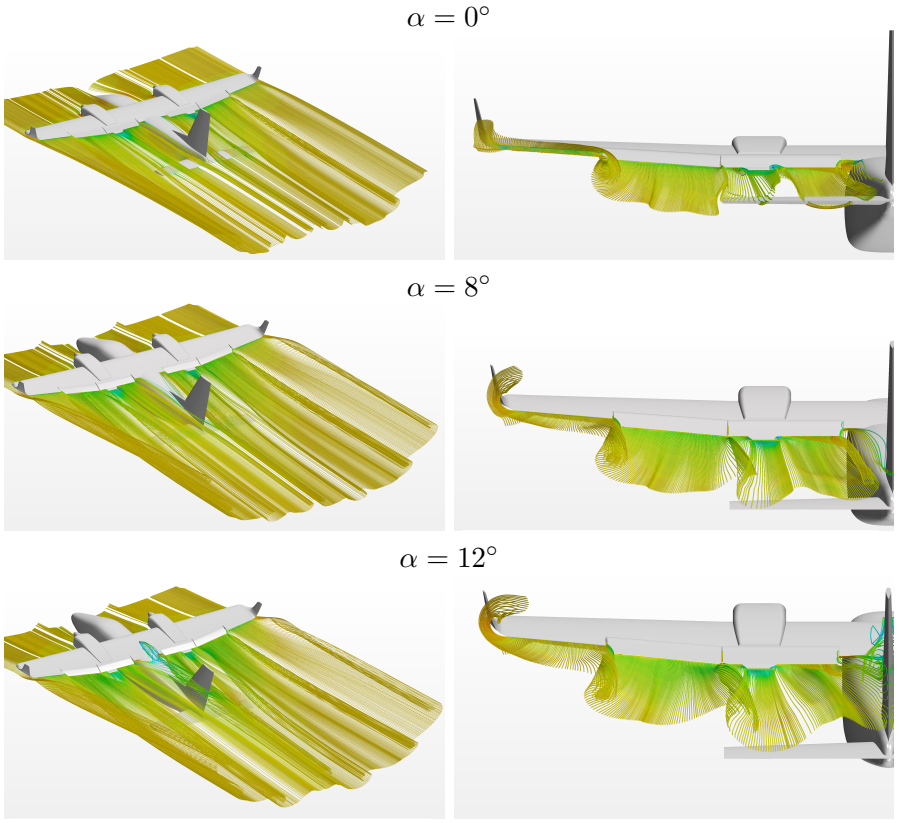

FIGURE 4.47: Wing wake displacements in take-off flap configurations, 3D views, $Re = 9.5e^6$.

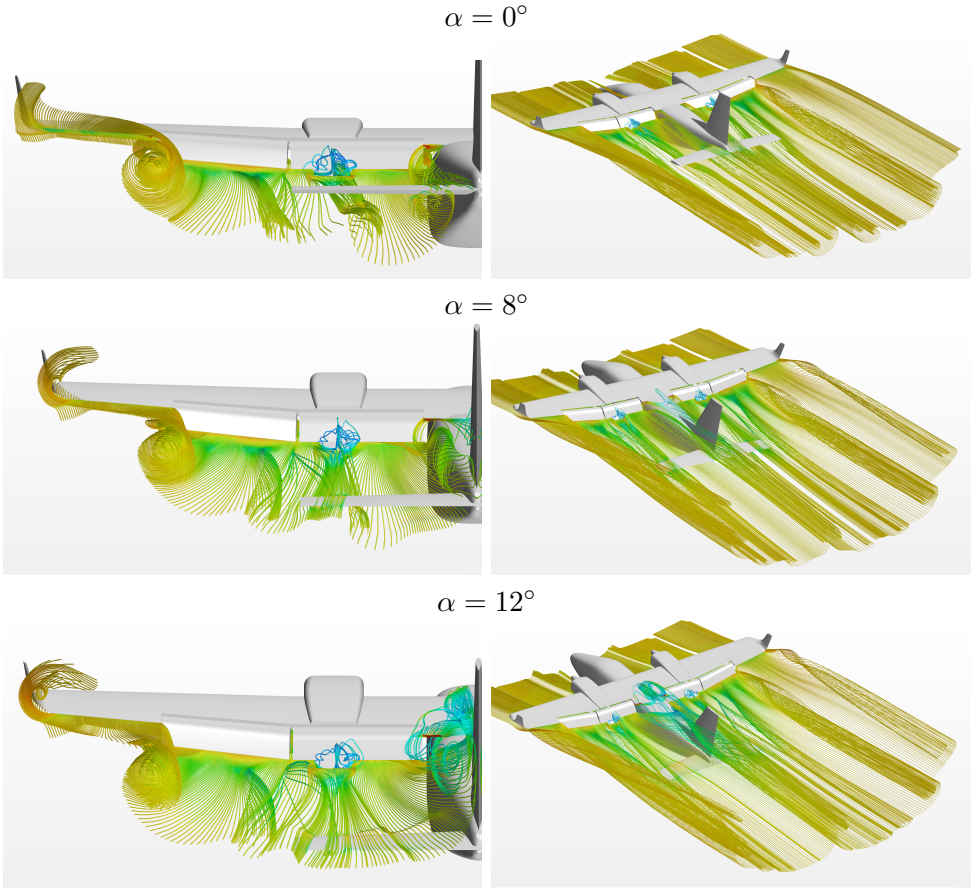

FIGURE 4.48: Wing wake displacements in landing flap configurations, 3D views, $Re = 9.5e^6$.

4.5.6 Fairing effects

The wing-fuselage junction induces strong interactions between these components. The combined boundary layers cause complex flow phenomena really difficult to describe and simulate, this is well explained in Simpson [81], Hoerner [82] and Schlichting [83]. Suggestions to achieve improvements, as highlighted by Siegel [84], deal with flow manipulation around the junction: i) optimize the relative wing-body position; ii) adapt the junction shape with fillets and fairings; iii) manipulate the flow with active installations.

Experimental research was done in the past at NACA, such as the experiential investigation conducted by Jacobs and Ward [85] about the relative wing-body position or the fillet-specific investigation by Muttray [86]. Hoerner [82] and Schilicthing and Truckenbrodt [83] have summarized the wing-fuselage drag characteristics. Remarkable investigations were made by Fleming et al. [87], extensive measurements can be found in Oelcmen [88] and a detailed summary is given in Simpson [81]. Detailed investigations about the influence on lift and drag of the relative wing-body position have been performed by Jacobs [85]. His research has shown how the drag coefficient gradient C_{D_α} increases for the high-wing configuration, especially in the case where the wing bottom surface is tangent to the fuselage surface. Jacobs [85] has shown that providing a fitting curvature of the intersection lines through fairings, fillets and fuselage shape design, it is possible to reduce drag to acceptable magnitudes similar to middle or far outer wing mount position. More recent works have been related to jet aircraft, see [89], where both experimental and numerical investigation of two wing-body fairings have been investigated for the DLR-F6 model geometry in order to alleviate or completely remove the side-of-body separation near the wing upper-surface trailing-edge. Other works have numerically investigated the optimisation of the wing-fuselage fairings for large regional turboprop, see Ref. [37, 41, 90], the main results has been a reduction of about 3 drag count of the zero lift drag coefficient for both cruise and climb conditions. Light twin-engine commuter aircraft with high wing configuration, such as Cessna Caravan or Britten-Norman Islander, reduce the junction drag by optimizing the relative wing-fuselage position, as shown in Fig. 4.49. But this could lead ot a sensible reductions of the cabin height. Thus, since one of the main design tasks for the P2012 Traveller is to provide a better cabin comfort, to reduce the wing-fuselage interferences for the P2012 Traveller, the adoption of fairing between wing and body has been suggested. Moreover the adoption of fairings and fillets is the most useful approach to reduce fuselage drag.

In this section will be illustrated a preliminary investigation about the effects of the fairing between the wing-fuselage junction for the P2012 Traveller. All the experimental tests, shown in chapter 3, have been performed with a wooden hand shaped fairing and all gaps between wing-fuselage junction have been sealed with plaster or tape. The adoption of a fairing and the need of sealing all gaps, was addressed to avoid interferences between the airflow

(a) Cessna Caravan (b) Britten-Norman

FIGURE 4.49: Wing-Fuselage junction of similar commuter aircraft.

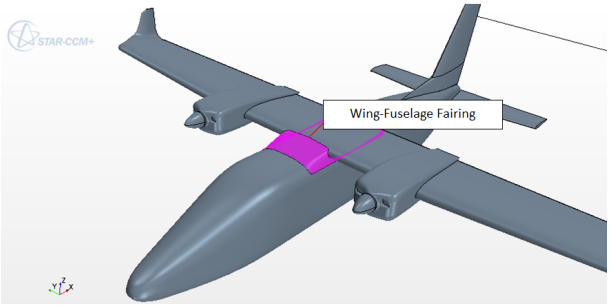

FIGURE 4.50: [A preliminary shape for the P2012 Traveller wing-fuselage fairing.

and strain gage balance housed within the model. RANS simulations have been performed without the fairing geometry, as it has been illustrated in previous sections. But since the drag coefficient could be largely affected by the wing-fuselage intersection, a preliminary analysis of a first fairing shape, here is presented. Fig. 4.50 shows a view of a preliminary shape for the wing-fuselage fairing design. This fairing has been added to the complete aircraft configuration and simulated at cruise Reynolds number of $9.5e^6$, being the effects on the drag coefficient the objective of this investigation. Fig. 4.53 shows how the effect of the fairing on the lift and pitching moment coefficient is negligible. This means that the adoption of the fairing for the wing-fuselage junction will not affect the maximum available lift coefficient and the aircraft stability. The major effect, as it would be though, is on the drag coefficient. Fig. 4.52 shows how the fairing could reduce the zero lift drag coefficient of about 10 drag counts. The complete aircraft without wing-fuselage fairing is characterised by a $C_{D_0} = 0.0239$ (239 drag counts), while the complete configuration with fairing on shows a $C_{D_0} = 0.0229$ (229 drag counts). Fig. 4.52 also illustrated how the fairing is particularly effective in a range of low angles of attack (typical of the cruise phase, where the aircraft flies most of

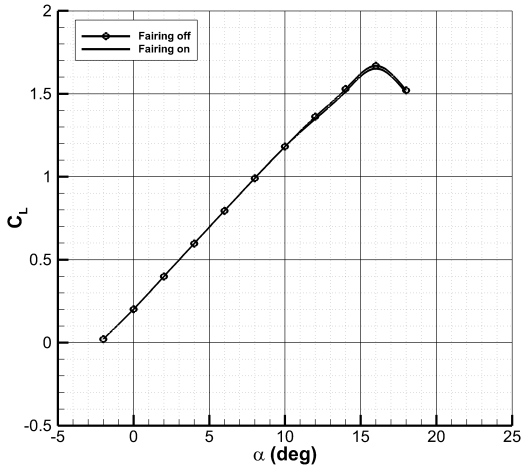

(a) Lift coefficient vs. α

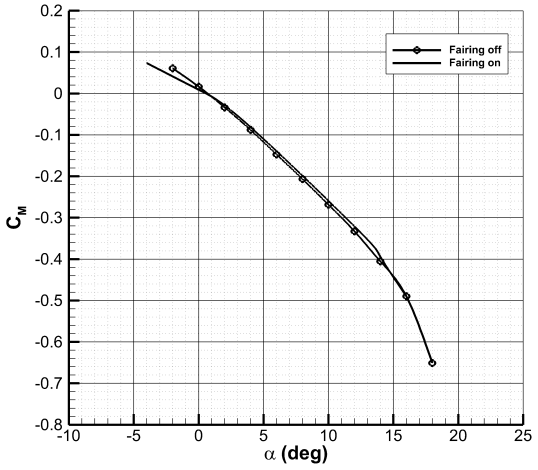

(b) Pitching moment coefficient vs. α

FIGURE 4.51: Fairing effects on lift and pitching moment coefficient, Re=$9.5e^6$.

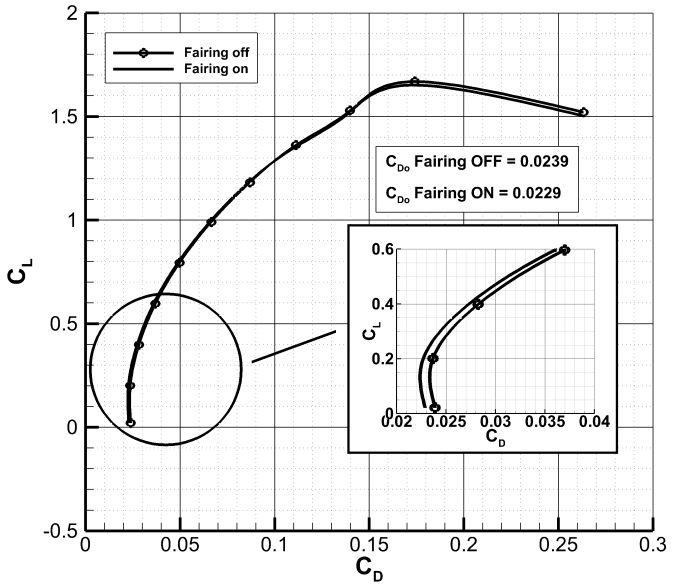

FIGURE 4.52: Fairing effect on drag coefficient, Re=$9.5e^6$.

the time during a typical mission profile). The reduction of the zero lift drag coefficient is clearly due to the ramp angle provided from the faring that avoids the flow separation in the froward area of wing-fuselage junction, reducing the pressure gradient. Moreover the fairing contributes to grant an attached flow also on lower wing surface, especially in the trailing edge area, as shown in Fig. 4.53. This preliminary investigation about the fairing design shows how the zero lift drag coefficient could be reduced of about 10 drag counts also with the adoption of a very simple fairing shape. Several studies, like those of Jacobs [85] and Vassberg, Sclafani and DeHaan [89] have shown how the drag due the wing-fuselage interference could be reduced also by designing fillets and fairing for the rear wing-fuselage junction, that for this preliminary shape for the fairing design have not be taken into account. Moreover several numerical investigations about typical large regional turboprop wing-fuselage fairings optimisation, like those of Della Vecchia [37, 41], have show how the optimisation of this component could lead to further reductions of the zero-lift drag coefficient. The zero lift drag coefficient reduction affects the aircraft flight performance is shown in chapter 5.

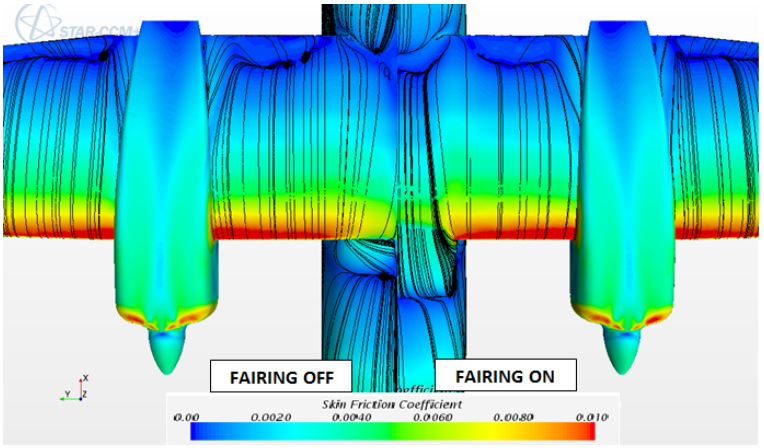

(a) Fairing effects on flow separation in the wing fuselage junction, top view

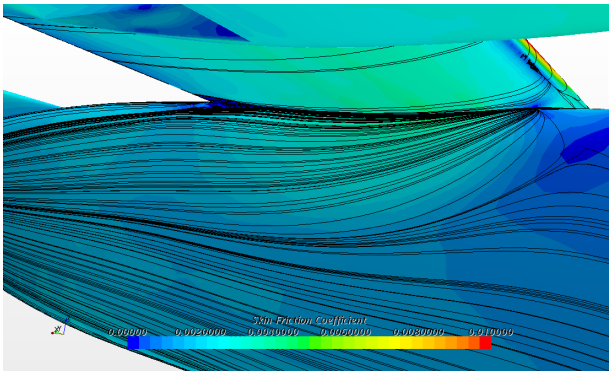

(b) Wing-fuselage junction at wing trailing egde, fairing off

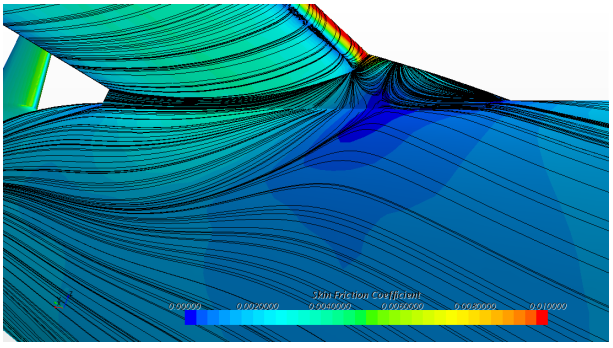

(c) Wing-fuselage junction at wing trailing egde, fairing on

FIGURE 4.53: Wing-fuselage fairing effects, $\alpha = 4°$ at Re=$9.5e^6$.

4.6 Lateral-Directional Analysis

Several aircraft configurations have been investigated in order to evaluate how each component contributes to lateral-directional characteristics of the aircraft. Simulations at both wind tunnel and free flight Reynolds number have been performed in order to validate the reliability of the RANS approach through a comparison with the available experimental data, and then to investigate about the Reynolds number scaling effects in order to provide a more reliable estimation of the aerodynamic characteristics.

4.6.1 Yawing moment coefficient breakdown and directional control

In this section the breakdown of the yawing moment coefficient among the aircraft components is illustrated. The aim is to investigate and estimate how aircraft components affect the directional stability. All the investigated configurations are described in Tab. 4.14. Fig. 4.54 shows the yawing moment

TABLE 4.14: Analysed configurations for the lateral-directional investigation

Abbreviation	Configuration
WWBNHV	Wing-Winglet-Body-Nacelles-Horizontal-Vertical tail
WBNHV	Wing-Body-Nacelles-Horizontal-Vertical tail
WBHV	Wing-Body-Horizontal-Vertical tail
WBNV	Wing-Body-Nacelles-Vertical tail
WBN	Wing-Body-Nacelles
WBV	Wing-Body-Vertical tail
WV	Wing-Vertical tail
WB	Wing-Body
B	Body
BHV	Body-Horizontal-Vertical
BV	Body-Vertical
V	Vertical

coefficient breakdown. For a better figure clearness only the most significant configurations have been reported in terms of yawing moment coefficient curves, as shown in Fig. 4.54. Directional stability derivatives C_{N_β}, for all the analysed configurations are reported in Tab. 4.15. The complete aircraft configuration shows a stability derivative, C_{N_β}, of about 0.00201 deg^{-1}, which is close to the experimental results. Tab. 4.54 highlights how the nacelles are almost neutral in terms of lateral stability thanks to the reduced side area. Winglets contribute to increase the directional stability of about 9% (compare WBNHV and WWBNHV configuration of Tab. 4.15). This effect is in accordance with the results discussed by Jacobs and Flechenr in Ref. [91], where an experimental investigation about the effect of winglets on

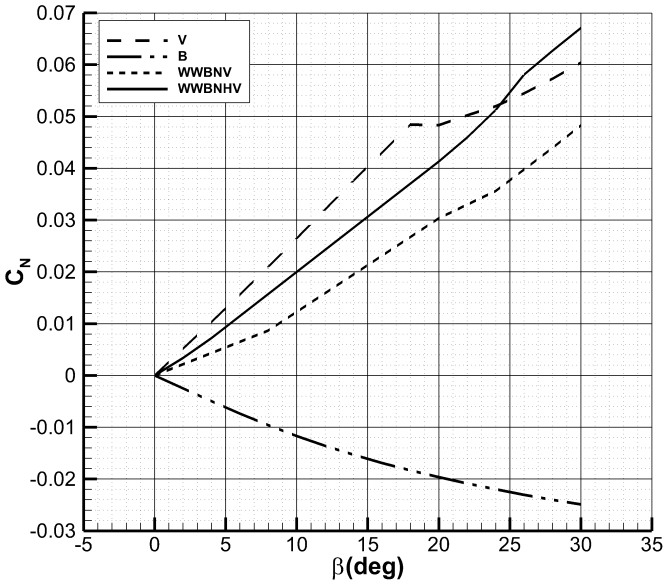

FIGURE 4.54: Yawing moment coefficient breakdown, CFD analysis, $Re = 0.6e^{\circ}$.

the static aerodynamic stability characteristics of a representative second generation jet transport model, shows an increase of directional stability derivative even of 20% with respect to the winglet off configuration. For lower sideslip angle the contribution of the horizontal tail in terms of increment of the directional stability is about 60% (compare the WWBNV and WWBNHV configurations). This large contribution is due to the non linearity of the yawing moment curve variation with respect to the sideslip angle as it can bee seen from graph of Fig. 4.54. If the C_{N_β} for the WWBNV configuration, is estimated in the linear range of $\beta \in [8^{\circ}, 12^{\circ}]$, the horizontal tail leads to an increment of directional stability of about 26%. This contribution is quite in accordance with what has been found by Brewer and Lichtenstein [92], where has been found that the effect on vertical tail effectiveness for horizontal tailplane positioned on the fuselage leads to an increase of about 15%. Similar results have been found also by Nicolosi, Della Vecchia and Ciliberti in [47], where a deep investigation on the aerodynamics of the vertical tailplane and the correct estimation of its contribution to aircraft directional stability and control has been performed. Similar results has been found by Della Vecchia [37], where a new method to design a vertical tail for commuter and turboprop aircraft has been proposed and where also the an application on the P2012 Traveller configuration is provided. The horizontal tail modifies both fuselage and vertical tail contributions to the side-force and thus the yawing moment coefficient. The horizontal tail body mounted (in fuselage) or

TABLE 4.15: Side force and yaw moment coefficients derivatives, $\beta \in [0°, 10°]$, at $Re = 0.6e^6$

Configuration	CFD. $C_{N_\beta}(deg^{-1})$	Exp. $C_{n_\beta}(deg^{-1})$
V	0.002618	0.00228
WV	0.002636	n.a.
BV	0.001714	0.00170
BHV	0.002257	0.00242
WBV	0.001111	n.a.
WBHV	0.001790	n.a.
WBNV	0.001081	0.00122
WBNHV	0.001840	n.a.
WWBNHV	0.002014	0.00197
W	0.00006	0.00005
B	-0.00120	-0.00100
WB	-0.00121	-0.00112
WBN	-0.00121	-0.00111

fin mounted (in the vertical tail plane, in particular in T-tail configuration), acts like and end-plate increasing the effectiveness of the vertical surface; on the other hand the horizontal surface contributes to increase the pressure distribution in the fuselage area affected by the tail surface, reducing the fuselage directional instability. The wing reduces the directional stability of about 20%, as it can be appreciated by comparing the derivative of the isolated vertical tail with one of the complete configuration and taking into account that the instability contribution due to body-horizontal combination is about 13%. To a better comprehension of the mutual interference effects among aircraft components, in Tab. 4.16 and in Tab. 4.17 the vertical tail and body contributions to C_{N_β} derivative in all tested configuration are reported. By comparing the C_{N_β} of the vertical tail (see Tab. 4.16) it is possible to appreciate how the high wing configuration in the wing-vertical tail configuration (no fuselage) reduce the vertical tail effectiveness of about 1.6%, which is consistent with the estimations that can be performed with the most known and used semi-empirical method (see USAF DATCOM [93] and ESDU [94]) and with experimental results, see [85, 95], that provide for a mean reduction of about 1% of the directional stability for to the high wing configurations. The wing contribution dramatically changes when the combination of fuselage-wing is considered. As matter of fact, by looking the vertical tail contribution in the WBV, it is possible to appreciate how the wing reduce the vertical tail effectiveness of about 18%. This is due to the combined effect of the wing sidewash and the streamlined shape of the fuselage. Fig. 4.55 depicts the combined effect of the high wing and streamlined fuselage on the direction of the flow coming from the wing and investing the vertical

TABLE 4.16: Vertical tail contribution to directional derivative in several configurations.

Configuration	$C_{N_{\beta_V}}$ (1/deg)	$\Delta C_{N_{\beta_V}}$ %
V	0.00262	-
BV	0.0026	-0.5
BHV	0.00301	15
WV	0.00258	-1.6
WBV	0.00216	-17.4
WBNV	0.00214	-18.4
WBHV	0.0027	3.1
WBNHV	0.00266	1.6
WWBNHV	0.00278	6.1

TABLE 4.17: Body contribution to directional stability derivative in several configurations.

Configuration	$C_{N_{\beta_B}}$ (1/deg)	$\Delta C_{N_{\beta_B}}$ %
B	-0.00120	-
BV	-0.00089	-26.2
BHV	-0.00079	-34.7
WB	-0.00127	5.4
WBN	-0.00120	-0.1
WBV	-0.00110	-8.4
WBHV	-0.00097	-19.8
WBNHV	-0.00093	-22.5
WWBNHV	-0.00090	-25.1

tail. The effects of the fuselage shape on the vertical tail effectiveness have never been investigated, and in the classical semi-empirical approaches no method to take into account the fuselage shape are provided. By looking at derivatives illustrated in Tab. 4.16), it is possible to appreciate how the fuselage does not affect the vertical tail C_{N_β} in a sensible way, this effect is not in accordance with the prediction carried out by applying classical semi-empirical procedure. Della Vecchia [37] has shown how the application of classical methodologies like those proposed in USAF DATCOM [93], ESDU [94] or also by the application of a new method for the vertical tail design, based on CFD approach, leads the fuselage contribution to be estimated as an increment of about 26% in the vertical tail effectiveness. This is mainly due to the dorsal fin that reduces the cross-flow on the vertical tail and to the fuselage cross sectional shape. The fuselage acts as a cylinder at the vertical

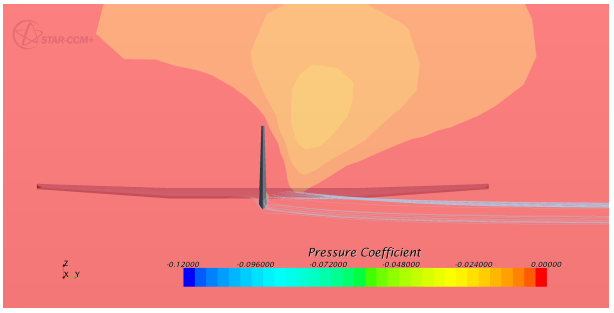

(a) Wing-Vertical tail

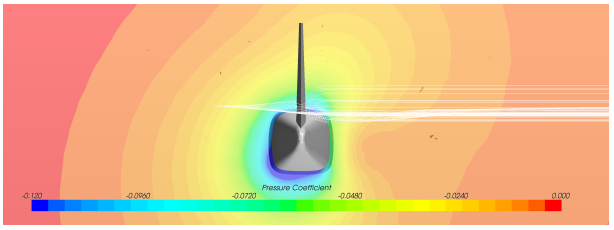

(b) Body-Vertical tail

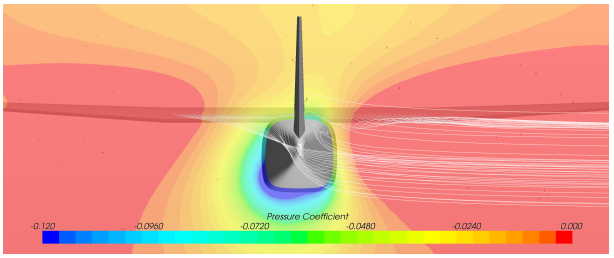

(c) Wing-Body-Vertical tail

FIGURE 4.55: Effects of the combination of the high-wing sidewash and streamlined fuselage shape on the flow investing the vertical tail.

tail root, accelerating the flow and increasing the sideforce on the vertical tail root region close to the fuselage junction. But, in that case, the dorsal fin and the square-shaped fuselage section reduce this effects leading the fuselage to be almost neutral in terms of vertical tail effectiveness. The effects of the dorsal fin and the cross section shape of the fuselage have never been investigated an thus no methods are available in the literature to confirm or compare the estimation of those effects. Finally the horizontal tail contributes to increase the vertical effectiveness of about 20%, very consistent with the mean value that can be found in literature for an horizontal tail body mounted, see [92, 96]. Tab. 4.17 shows instead the C_{N_β} derivative of the fuselage in several configurations. It is interesting to highlight the main interference effects acting on the fuselage. The vertical tail (and the dorsal fin) contributes into reducing the fuselage directional instability of about 26%, as i can be estimated

by comparing the isolated body (B) and the body-vertical tail combination (BV). The horizontal tail leads to a further reduction of the fuselage instability of about 8%. Those effects are connected to the over-pressure in the zone of intersection of the tail surfaces with the fuselage as illustrated in Fig. 4.56. In all the classical semi-empirical methodologies, the mutual interference effects between the vertical tail and the fuselage provide method to predict only the fuselage effects on the vertical surface and do not consider the mutual effect of the vertical tail on the fuselage. The complete aircraft configuration at several rudder deflections has been analysed in order to estimate the directional control power derivative. Comparisons with experimental data in terms of $C_{N_{\delta_r}}$ derivative is presented in Tab. 4.18, the control power derivatives has been estimated in the linear range of sideslip angle $\beta \in [0°, 10°]$, where the numerical data is very close to the experiential estimation. Instead, Fig. 4.57 shows the yawing moment coefficient variation with respect to the sideslip angle at several rudder deflections and the required rudder deflection to trim the complete aircraft with the change in sideslip. Differences in the control power derivatives between the numerical and experimental data have been found as the rudder angle increase. This is due to the uncertainties in the experimental measurement of rudder deflection angles. Since the matching between experimental and numerical investigation is remarkable at low rudder deflections, it seems reliable to state that the measured deflection of the rudder during the wind tunnel test was underestimated.

TABLE 4.18: Directional control derivative, $Re = 0.6e^6$.

Configuration	CFD. $C_{N_{\beta_B}}$ (1/deg)	Exp. $C_{N_{\beta_B}}$ (1/deg)
Complete aircraft	-0.00220	-0.00210

4.6.2 Lateral stability and winglet effect

Fig. 4.6.2 shows the rolling moment coefficient variation with respect to the sideslip angle for different configurations, derivatives C_{roll_β}, estimated in the linear range of $\beta \in [0°, 10°]$, are summarized in Tab. 4.19. The complete aircraft shows an lateral stability derivative of 0.00254 $deg{-}1$, which is about 16% lower than the experimental measured one. The most interesting effect dealing with the aircraft lateral stability is due to the winglet surface. As already highlighted and discussed in previous sections, the winglet increase the wing dihedral effect. The CFD RANS approach shows an increase of about 65% while the experimental data have shown an increase of about 40%.

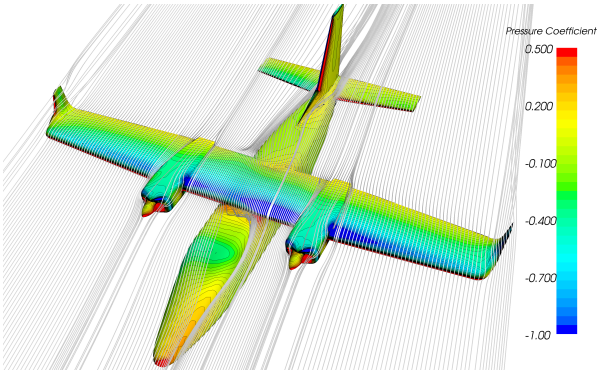

(a) Complete aircraft

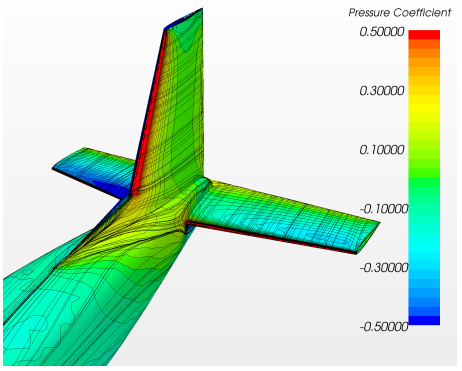

(b) Body-Horizontal-Vertical tail

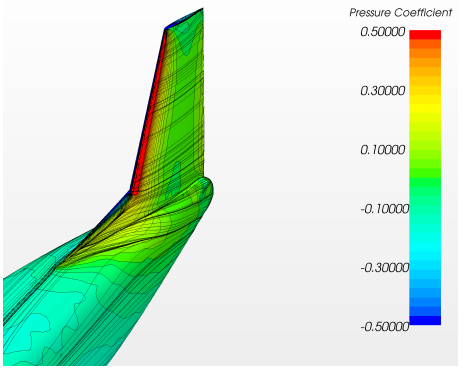

(c) Body-Vertical tail

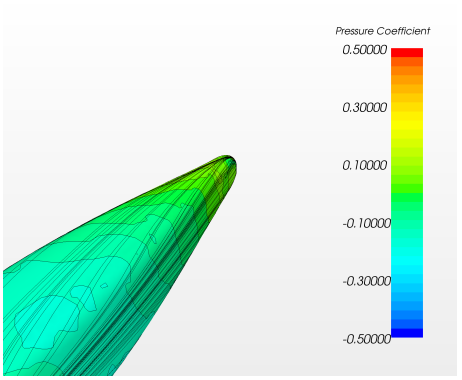

(d) Body

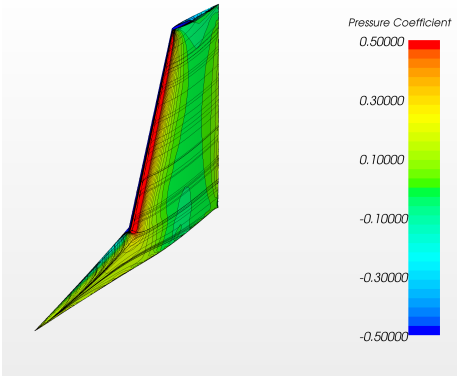

(e) Vertical tail

FIGURE 4.56: Streamlines and contour of pressure coefficient on tail assembly at $\alpha = 0°$, $\beta = 10°$.

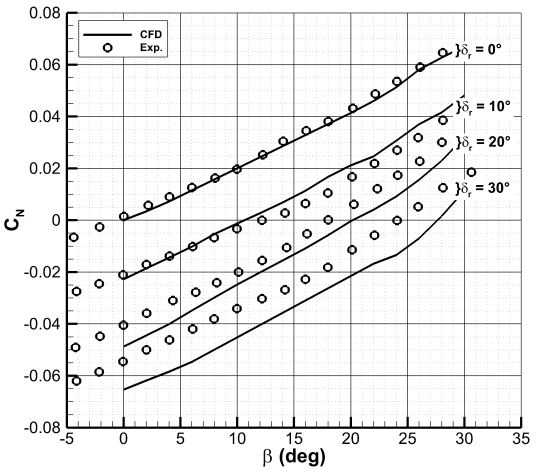

(a) Yawing moment coefficient variation with respect to the sideslip angle at several rudder deflections

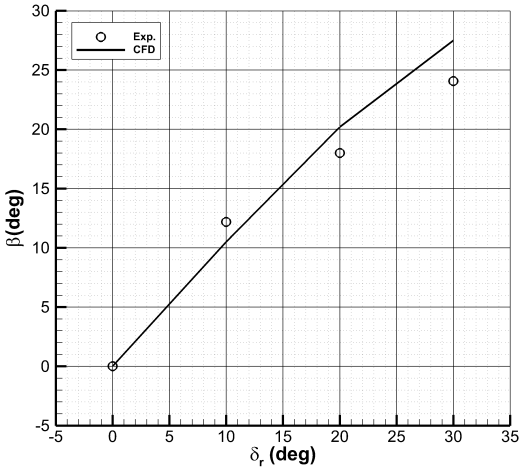

(b) Required rudder deflection to trim sideslip angle

FIGURE 4.57: Complete aircraft configuration at several rudder deflections, $Re = 0.6e^6$.

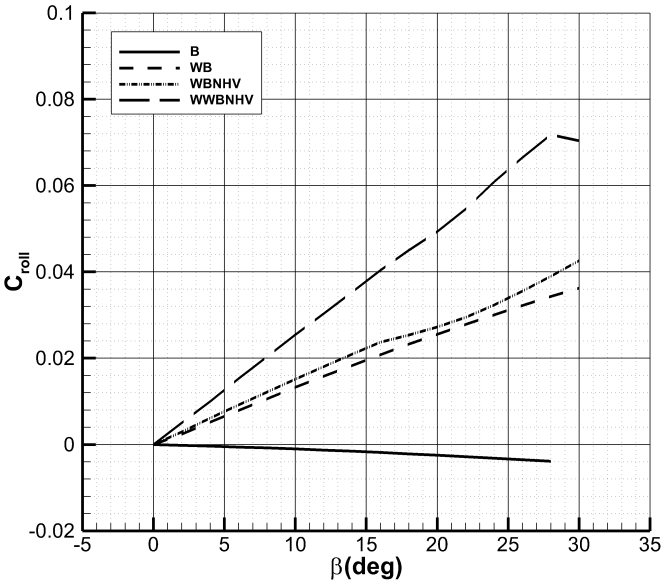

FIGURE 4.58: Rolling moment coefficient breakdown, CFD analysis, $Re = 0.6e^6$.

TABLE 4.19: Body contribution to directional stability derivative in several configurations.

Configuration	CFD $C_{roll_{\beta_B}}$ (1/deg)	Exp. $C_{roll_{\beta_B}}$ (1/deg)
W	0.00061	n.a.
WB	0.00133	0.0017
WBV	0.00186	n.a
WBHV	0.00153	n.a.
WBNHV	0.00154	n.a.
WWBNHV	0.00254	0.0030
BV	0.00051	0.00043
WV	0.0012	n.a.
B	-0.0001	-0.0002

4.6.3 CFD Lateral-directional analyses validation

Comparisons with experimental data have already been shown in previous sections in terms of stability and control derivatives characteristics. The complete aircraft at several rudder deflections has been also compared with experimental data in terms of yawing moment coefficient curve in Fig. 4.57. In this section other several configuration, that have been numerically investigated,

will be compared with the experimental counterpart in terms of curves of variation of both yawing and rolling moment coefficient with respect to the sideslip angle.

4.6.4 Reynold number effect on lateral-directional stability and control

In this section the effects of Reynolds number on both yawing moment and rolling moment coefficients will be illustrated. Reynolds number effects have been investigated on the complete aircraft configuration a t several rudder deflections. Fig. 4.61 shows the comparison of yawing and rolling moment coefficient at two Reynolds number, $Re = 0.6e^6$ and $Re = 9.5e^6$ respectively. The Reynolds number effects does not affect neither the directional stability nor the lateral stability derivative. Fig. 4.61 shows how the vertical tail at high sideslip angle (30°)the vertical tail is not stalled yet. This is due to dorsal fin surface. The adoption of a dorsal fin introduces a discontinuity in the leading edge of the vertical tail, that at non zero sideslip angles generates a vortex, as shown in Fig. 4.62. This vortex splits in two halves the vertical surface,a s clearly outlined in Fig. 4.62. The upper half of the vertical tail has an higher aspect ratio than the lower one, thus will stall at lower sideslip angles. The lower half instead is a low aspect ratio surface stalling at higher β. This allows the vertical tail to maintain the C_{N_β} also at high sideslip angles.

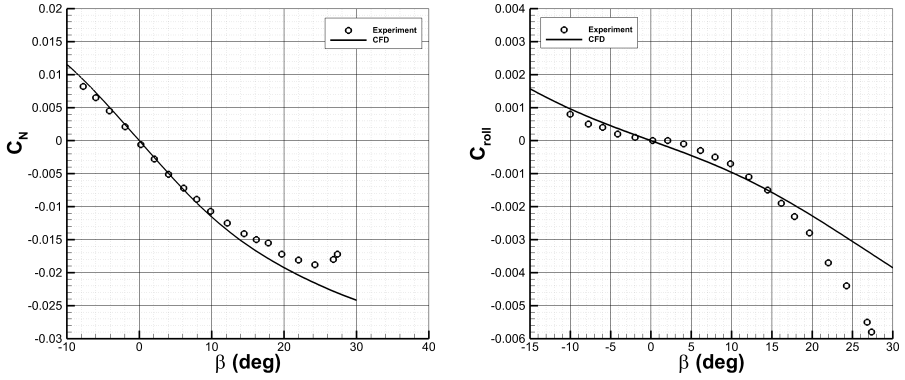

(a) Yawing moment coefficient variation with respect to the sideslip angle

(b) Rolling moment coefficient variation with respect to the sideslip angle

FIGURE 4.59: Isolated body configuration, $Re = 0.6e^6$.

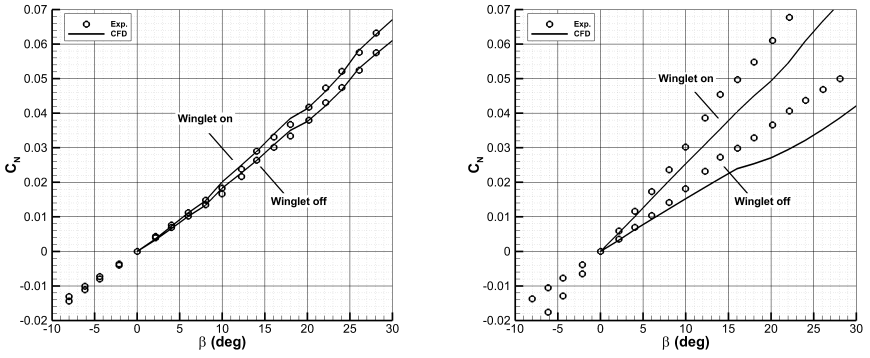

(a) Yawing moment coefficient variation with respect to the sideslip angle

(b) Rolling moment coefficient variation with respect to the sideslip angle

FIGURE 4.60: Complete aircraft with winglet on and off configurations, $Re = 0.6e^6$.

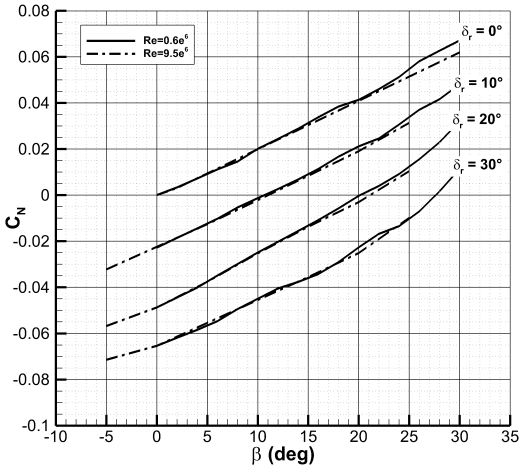

(a) Yawing moment coefficient variation with respect to the sideslip angle

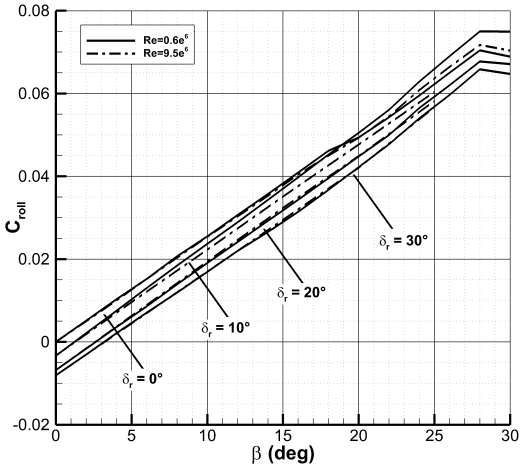

(b) Rolling moment coefficient variation with respect to the sideslip angle

FIGURE 4.61: Complete aircraft configuration, Reynolds number effects on yawing and rolling moment coefficients.

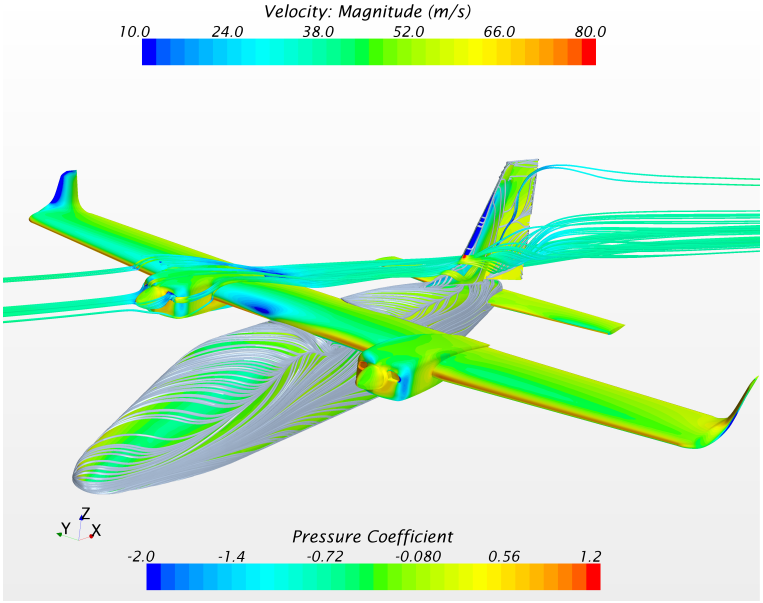

FIGURE 4.62: Streamlines on complete aircraft, $\delta_r = 30°$, $\beta = 25°$ and $Re = 9.5e^6$.

4.7 Concluding remark about CFD RANS analysis

In this chapter a summary of hundreds numerical simulations performed by the means of the software STAR-CCM+ has been presented. This wide investigation has been addressed to supply the experimental investigation about the determination of all static and in power off condition, longitudinal and lateral-directional stability and control characteristics of the P2012 Traveller. Validation of the numerical approach, in terms of mesh accuracy, solution convergence has been provided. Simulations have been performed also at low Reynolds number (equal to one of the experimental wind tunnel tests) in order to validate the matching and the goodness of RANS approach. A good fitting with the experimental data in terms of lift, longitudinal and lateral-directional stability and control has been found, supplying the goodness of the numerical approach. Sensible differences between the experimental and numerical results occurs where the discrepancies between the scale model experimentally investigated and the numerical model used for the RANS analysis are remarkable, especially in flap down configurations where the measured flap deflections during the tunnel could be affected by not negligible errors (2-3°). RANS simulations have also provide to extend the investigation about the aerodynamic characterisation of the P2012 Traveller to higher Reynolds number (about 9.5 million typical of cruise condition for this aircraft), supplying the lack of the experimental data performed in a low-speed tunnel. Estimation of maximum lift coefficients (clean and flap down configurations) has been provided. Numerical investigations have been also helpful into the estimation of the wing flight loads at free flight conditions. Wing flight loads were not available from tunnel tests, and their estimation is of a crucial importance for the planning of the static loading tests of the wing structure. Moreover the investigation about Reynolds number effect on wing loads has revealed that at higher angles of attack wing flight loads, and especially the stall path could be quite different. RANS approach has been also useful into the estimation of wing-fuselage fairing effects, highlighting how paying attention into design of this component a sensible improvements into complete aircraft drag coefficient can be achieved. Further investigations, that have been planned deals with the estimation of power effects on the aerodynamic behaviour of the aircraft, optimisation of wing-fuselage fairings (both wing-fuselage and landing gear pods-fuselage).

Chapter 5

Performance evaluation

Performance analysis of the P2012 Traveller has been performed to evaluate the effects of the improvements due to the drag reduction dealing with the introduction of the winglets and the wing-fuselage fairing, illustrated in previous sections. In sec. 2.4 has been shown how the introduction of a winglet surface having a height of about 10% of the wing semi-span could lead to an improvement of the Oswald factor of 10%. This result has been also confirmed by experimental and numerical investigation discussed in previous sections. Discussion about the wing-fuselage intersection, shown in sec. 4.5.6, has highlighted how, by introducing a fairing surface for the wing-fuselage junction and optimising its shape, a possible reduction of the zero lift drag coefficient of about 10 drag counts can be achieved (or a C_{D_0} reduction or aerodynamic improvements). Thus in this chapter will be presented the estimation of the effects of the improvements in the aircraft zero lift drag coefficient and Oswald factor in order to appreciate how these benefits affect flight performance, essentially the maximum speed, the maximum rate of climb and the fuel burned during the mission profile. The performance analysis is based on the evaluation of required and available power. The P2012 Traveller is equipped with 2 Lycoming TEO 540 engines and Hartzell or MT three blade constant speed propellers with maximum horse power $P_0 = 350$ hp and a propeller efficiency of $\eta_p = 0.82$ (see Tab. 5.1). The propeller efficiency has been estimated as a typical Clark-Y three blade as suggested in the NACA report No. 650 Ref. [97]. Typical turbocharged engine shaft horse power (SHP) ratio (for a cruise rating) used for performance evaluation is shown in Fig. 5.1. Fig. 5.2 shows some possible routes of a reliable future Italian Small Aircraft Scenario. Let's suppose the 222 nm route Napoli-Lecce, or the route Providence-Philadelphia (a typical CapeAir flight) as a possible mission profile for the Tecnam P2012 Travller, and let's assume it as the reference mission profile on which perform an estimation of the flight performance. The

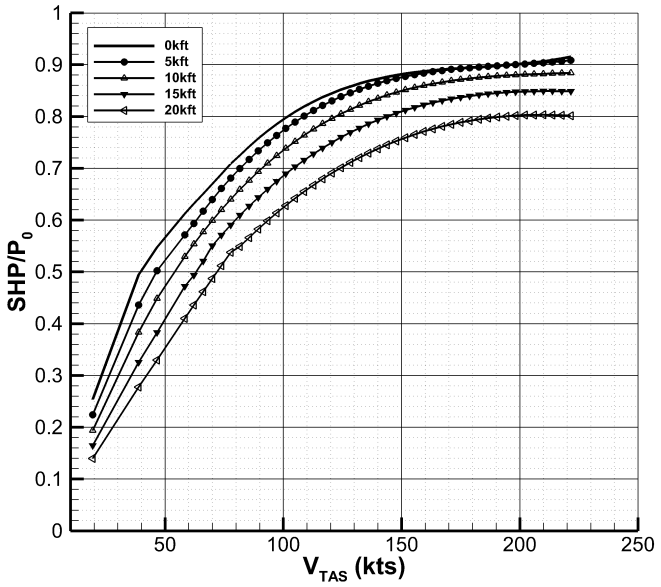

FIGURE 5.1: Typical turbocharged power ratio, coupling engine and propeller.

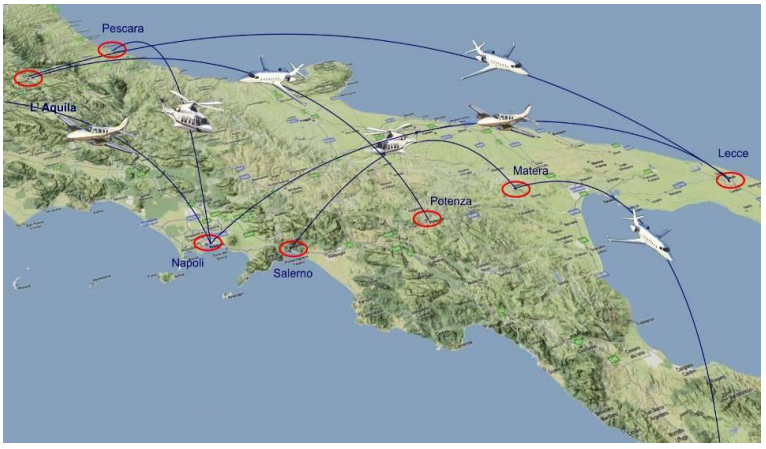

FIGURE 5.2: Example of a reliable SAT scenario, source [4].

estimated performance are summarized in Tab. 5.2[1]. Ground performance have been estimated in standard condition at sea level and fuel consumption has been evaluated also considering weight variation during the mission profile. To show the effects of the improvement of the Oswald factor a value of

[1]Performance have been evaluated according to Ref. [98]. All the assumed data are summarized in Tab. 5.1. Engine rating during Climb is about 10% higher than cruise shown in Fig. 5.1

$e = 0.83$ as been assumed, which is a typical value for this aircraft category. As reference zero lift drag coefficient the $C_{D_0} = 0.0306$, estimated by applying the semi-empirical procedure, experimental investigation and RANS analysis presented in sec. (**??** has been assumed.

TABLE 5.1: P2012 Traveller main characteristics and conditions.

W_{TO} (kg)	3290
Engine	Lycoming TEO 540
SHP (hp)	350
SFC (lb=hph)	0.45
η_p	0.82 (Clark-Y 3 blade propeller, see Ref. [97])
Geometry	
Fuselage length (m)	11.5
Fuselage diameter (m)	1.6
$S_w(m^2$ 25.4	
$b_w(m)$	14
AR_w	7.72
root airfoil 6 NACA 23016	
tip airfoil	NACA 23012
Oswald factor	0.83*
C_{D_0}	0.0306**
Conditions	
M	0.25
Re	9.5e^6
Cruise Altitude (ft)	8000

*Typical Oswald factor for this aircraft category, no winglet

**Estimated through semi-empirical approach as shown in sec. 2.3

5.1 Performance improvements due to drag reduction

Assuming as reference values for the zero lift drag coefficient a $C_{D_0} = 0.0306$ as estimated by the semi-empirical method, and Oswald factor $e = 0.83$, the influence of these two parameters on the performance has been investigated. The variation of maximum speed and fuel consumption has been estimated by considering a cruise altitude of 8000 ft.

5.1.1 Zero lift drag coefficient reduction

Aircraft performance have been evaluated according to Ref. [98] varying the zero lift drag coefficient of ± 10 drag counts. Fig. 5.3 and Fig. 5.4 show the variation of maximum true airspeed and fuel consumption respect to the

TABLE 5.2: P2012 Traveller main characteristics and conditions.

Performance	
Take-off distance, (ft)	1410
Landing distance (ft)	1840
R/C s.l. AEO (ft/min)	1743
R/C 8 kft AEO (ft/)min)	1580
R/C s.l. OEI (ft/min)	315
R/C 8 kft OEI (ft/min)	186
Maximum VTAS at 8kft (kts)	200
Fuel consumption for a 222 nm mission (kg) (Cruise at max. power)	332
Time required to cover a 222 nm mission (min.)	75
Fuel consumption for a 222 nm mission (kg) (Cruise at 75% of power)	205

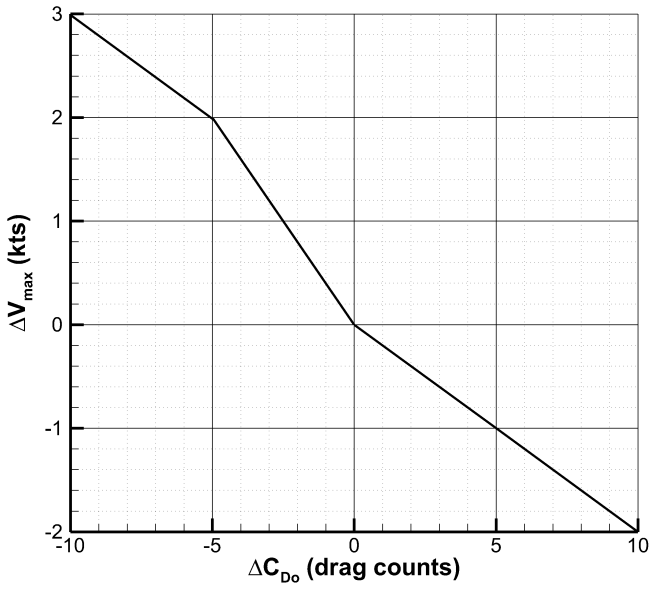

FIGURE 5.3: Maximum true airspeed variation due to zero lift drag coefficient, at cruise altitude of 8 kft.

reference conditions shown in Tab. 5.1. A C_{D_0} reduction of 10 drag counts leads to a maximum speed improvement of about 3 knots at typical cruise flight altitude of 8 kft and a reduction of 3 kg of the fuel mass burned. It is possible to say that for each knot of maximum true airspeed improvement a drag reduction of about 3 drag counts is required. The effect of reduction of the C_{D_0} of 10 drag counts, as shown in Fig. 5.4, leads to a fuel consumption

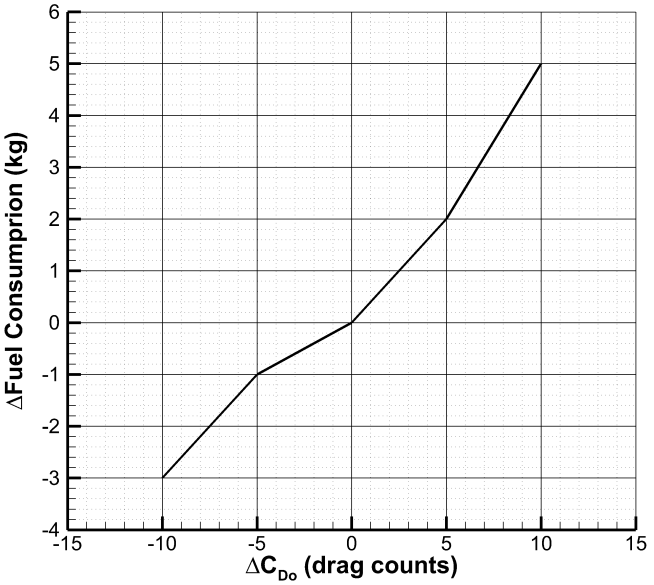

FIGURE 5.4: Fuel consumption variation due to zero lift drag coefficient on a mission profile of 222 nm with a cruise altitude of 8 kft.

reduction of about 2% on the mission profile of 222 nm. Climb and ground performance are slightly modified in the range of C_{D_0} variation with values lower than 1%.

5.1.2 Oswald factor improvement

In sec. 2.4 the winglet design has shown how an improvement of about 10% of the induced drag factor is achievable thanks to the use of this wing tip device, this value has also been confirmed by the experimental and numerical RANS analyses. Thus in this section a variation of $\pm 10\%$ of th Oswald factor will be consider, and effects of this parameter on the main flight performance will be shown. The estimated performance are summarized in Tab. 5.2 Engine rating during Climb is 10% higher than cruise shown in Fig. 5.1. Fig. 5.5 shows the maximum true airspeed variation due to Oswald factor percentage variation. As it can be noted the effects are non linear at high reductions of e. It is clear that the induced drag depends on the C_L^2 and thus the improvements of V_{MAX} are smaller than the reductions estimated on the same Oswald factor range of variation. It has also to be noted that a certain gain of e it is associated in the practice to an increase of the zero lift drag coefficient (due to the introduction of an additional surface). This has been taken into account by considering that to reach an increase of 10% of e an increase of 5 drag counts of the C_{D_0} must be considered, as has been found through numerical and

experimental investigations. Results presented in sec. 2.4 show that an Oswald factor improvement of 10% could increase the maximum speed of about 2 knots and leads to a fuel consumption reduction of about 1% during the whole mission profile, as shown in Fig. 5.6. The major improvements due to the Oswald factor could be achieved in climb condition, as shown in Fig. 5.7, where the percentage variation of the maximum rate of climb for both AEO and OEI conditions at an altitude of 8 kft are illustrated. It is clear that the higher variations are in the one engine inoperative conditions, in particular the maximum rate of climb at 8 kft in OEI condition can be improved of about 27% by a 10% improvement of the Oswald factor, as illustrated by the dashed line of Fig. 5.7

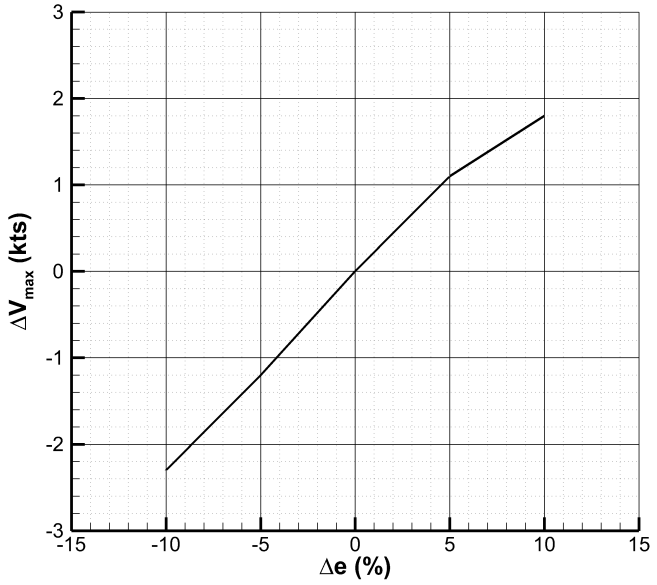

FIGURE 5.5: Maximum true airspeed variation due to Oswald factor e, at cruise altitude of 8 kft.

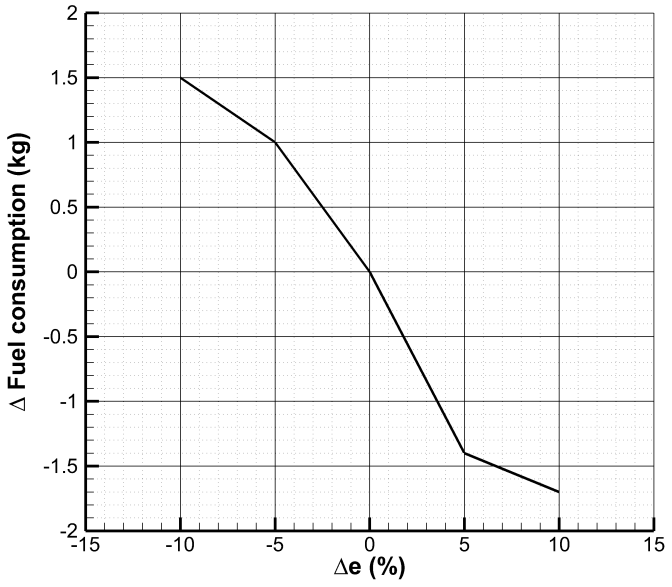

FIGURE 5.6: Fuel consumption variation due to Oswald factor e, on a mission profile of 222 nm with a cruise altitude of 8kft.

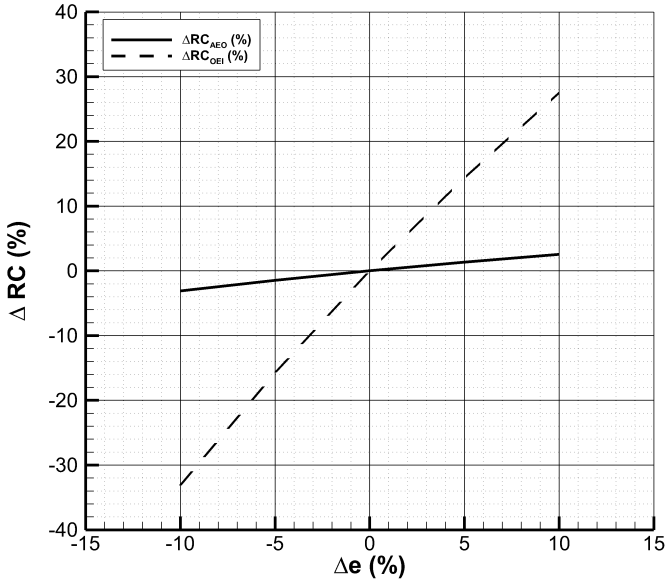

FIGURE 5.7: Maximum rate of climb variation due to Oswald factor e, at of 8 kft.

Chapter 6

Conclusions

Main objectives of this research work have been:

- the individuation of the main design specifications for a new twin engine eleven seats commuter aircraft;
- the individuation of possible solutions to reduce both zero lift drag coefficient and induced drag;
- the complete characterization of the static longitudinal and lateral-directional characteristics of stability and control in thrust off conditions;
- evaluation of the main flight performance and the effects of drag reduction on the main flight performance.

A commuter aircraft market analysis has shown how the most commercial successful twin-engined commuter aircraft design moves around the following main characteristics:

- high wing
- all aluminium alloy main structure
- piston powered
- reduced take-off and landing distances

In addition to this main design specification, to ensure the aircraft to have a good opportunities of success replacing some heritage aircraft, the design of the Tecnam P2012 Traveller has been accomplished also to provide for the following additional tasks:

- Easy cabin access and cabin comfort;
- Streamlined symmetrical fuselage tail shape (low drag);
- Spacious luggage compartment;

- Reduced take-off run (<1900 ft) and take-off from not prepared runways;
- Cruise flight speed of about 200 kts at flight altitude of 8000 ft;
- Range higher than 600 nm;
- TEO-540 Turbocharged Engine dual fuel capable (AVGAS/MOGAS) with low fuel consumption (114 l/h for 2 engines).

The design of the aircraft has been accomplished through the application of the most commonly used semi-empirical methods and has been also supported by a preliminary numerical aerodynamic analyses performed through a three dimensional panel code. Once the preliminary design of the aircraft has been accomplished, to improve the flight performance, especially for the climb phase, the design and optimisation of the wing-tip device has been performed. The optimal design of the winglet has led to a possible improvement of the aircraft induced drag factor of about 10%. Once the P2012 Traveller design and sizing has been defined a complete characterisation of the aerodynamic behaviour has been performed with the aim to estimate as accurate as possible both longitudinal and lateral-directional stability and control characteristics. The aerodynamic characterisation of the aircraft has been accomplished through both experimental and numerical RANS simulations. A scale model of the aircraft has been widely tested (more than 300 tests have been performed) in the main subsonic wind tunnel of the DII. Many aircraft configurations have been tested in order to better understand how and how much each aircraft components contributes to the aircraft aerodynamic characteristics and estimate the mutual interference effects in order to provide an accurate estimation of these effects for a right sizing of vertical tail, crucial for the minimum control speed estimation. The experimental investigation has also highlighted another crucial aspect to which pay a attention into design of tailplanes for this aircraft category: the right positioning of the horizontal tail with respect to the wing wake. As matter of fact several vertical positions for the horizontal tail have been investigated in order to provide design guidelines that could take into account effects of the wing wake on the tail. To supply the lacks due to the low Reynolds number at which the experimental tests have been performed, numerical simulations by the means of a RANS solver have been performed. The goodness of the numerical simulations have been validated by comparing numerical results of several configurations at wind tunnel Reynolds number. The agreement between the experimental and numerical results has been really good in terms of stability and control derivatives. Larger differences between numerical and experimental data are due to discrepancies between the scale model tested in the tunnel and the CAD geometry used for the numerical simulations. Moreover some uncertainties in the measured control surfaces angles have led to larger discrepancies between the numerical and experimental results dealing especially with the effects of flap and rudder deflections. The using of a RANS solver has led to estimate the Reynolds number scaling effects

on the aircraft aerodynamic characteristics. Simulations performed at several Reynolds number have highlight that the Reynolds number does not affect in a sensible way the aerodynamic derivatives in their linear range variation with respect to the incidence or sideslip angle. The simulations performed at high Reynolds number have led to the estimation of the maximum lift coefficients and stall path, where no reliable experimental data could be provided from the performed tunnel tests. Moreover numerical simulations have provided the estimation of the wing flight loads, which are a crucial data for the right design and sizing of the wing structure and for the planning of the wing static loads tests for certification issues. This work has shown how the adoption of winglets for this aircraft category could lead to an increase of the Oswald factor of about 10% with significant improvements in the climb performance. The maximum rate of climb in AEO condition could be improved of 3% while the maximum rate of climb in OEI condition can be about 30% higher than the winglets off configuration. Moreover the winglet device could also lead to an increase of the maximum available cruise speed (at a cruise altitude of 8 kft) of about 2 knts, since the benefits of this wing tip device in terms of drag reduction could be afford also in cruise condition ($C_L \in [0.4, 0.5]$) as shown in sec. 2.4. This shows how the adoption of the winglets on these aircraft category should became a main topic for new designs, according to author opinion. The numerical simulations have also led to the estimation of the effects of the wing-fuselage junction, highlighting how the design of a fairing for the intersection areas between the wing and the fuselage could lead to a zero lift drag coefficient reduction of 10 drag counts (about 3% of the total zero lift drag coefficient). This drag reduction has led to an increase of the maximum true airspeed (at a cruise altitude of 8 kft) of about 2 knots and a possible fuel consumption reduction of 3 kg on a mission profile of about 200 nm (this means a free flight every 100 flights).

Future works will be focused essentially on four main topics: i) the optimisation of the wing-fuselage fairing by the means of the RANS approach; ii) the estimation of power effects on aerodynamics characteristics through RANS approach; iii) numerical and experimental investigation about the landing gear (pods, legs and wheels) effects on aerodynamic characteristics, especially on drag; iv) modelling and simulation of flight through a flight dynamics model (FDM) software (*JSBsimt* or *Flightgear*) .

Bibliography

[1] GAMA (General Aviation and Manufacturer Assosiacion). General aviation statistical databook & industry outlook. Washington, DC 20005 2011.

[2] Jane'e Information Group Limited. Jane's all the world's aircraft, 2004-2005. (ISBN 978-88-906484-1-0), 163 Brightnon Raod, Coulsdon, Surrey CR5 2YH, UK 2004.

[3] A. Silverstein and S. Katzoff. Design charts for predicting downwash angles and wake characteristics behind plain and flapped wings. *NACA Report No. 648*.

[4] M. Amato. *Workshop on Small Aircraft Transport (SAT) Mode 5 June CIRA*.

[5] European Aviation Safety Agency CS23. Certification specifications for normal, utility, aerobatic and commuter category airplanes. Koeln, Germany 2003.

[6] C. R. Frlschtak. Learning, technical progress and competitiveness in the commuter aircraft industry: an analysis of embraer. *The World Bank Industry and Energy Department, OSP*, (11195), June,15 1992.

[7] Williams J.P. Small transport aircraft technology. *NASA SP-460*, 1983.

[8] R. Simpson. Airlife's world aircraft. *Airlife Publishing Ltd*, (ISBN 1-84037-115-3), Shrewsbury, England, 2001.

[9] J.W. Olcotto and S. Wilkinson. Musclebird: The duke b60. *Flying, World's Most Widely Read Aviation Magazine*, January, 1974 .

[10] The encyclopedia of world aircraft. *Donald Devid (editor)*, (ISBN 1-85605-375-X), Leicesrer, UK:Blitz Editions, 1997.

[11] Pattillo D.M. A history in the making: 80 turbulent years in the american general aviation industry. (ISBN 0-07-049448-7), New York: McGraw-Hill, 1998.

[12] J. Roskam. Preliminary calculation of aerodynamic, thrust and power characteristics. *DARcoporation*, Airplane Design, Part VI(2nd Edition), Lawrence, Kansas, 2000.

[13] E. Torenbeek. Synthesis of subsonic airplane design. *Delft University Press*, (ISBN 90-298-2505-7), 1976.

[14] C. D. Perkins and R. E. Hage. Airplane performance stability and control. *Wiley, New York*, (ISBN 0-471-68046-X), 1949.

[15] B. McCormick. Aerodynamics aeronautics and flight mechanics. *Wiley and Sons, 1994*.

[16] D. P. Raymer. Aircraft design: A conceptual approach. *AIAA Education Series*, (3rd Edition), Reston, Virginia, 1999.

[17] L. Pascale and F. Nicolosi. Design and aerodynamic analysis of a twin engine propeller aircraft. *26th ICAS conference, Anchorage (Alaska, US), 14-19 September, 2008*, (ISBN 0-9533991-9-2).

[18] Della Vecchia P. Nicolosi F., De Marco A. Flight tests, performances, and flight certification of a twin-engine light aircraft. *Journal of Aircraft, Vol. 48, No.1, 2011, pp. 177-192*, (ISSN 0021-8669, doi: 10.2514/1.C031056).

[19] Paduano G. Nicolosi, F. Development of a software for aircraft preliminary design and analysis. *3rd CEAS (Council of European Aerospace Societies Congress)*, (ISBN 978-88-96427-18-7), Venice (Italy), 24-28 October 2011 .

[20] J. Roskam. Methods for estimationg drag polars of subsonic airplanes. *The Univeristy of Kansas*, Lawrence, Kansas, 1971.

[21] J. A. Jr Blackwell. Numerical method to calculate the induced drag or optimum loading for arbitrary non-planar aircraft. *NASA SP-405*, 1976.

[22] J. E. Yates and C. P. Donaldson. Fundamental study of drag and assessment of conventional drag-due-to-lift reduction devices. *NASA CR 4004*, 1986.

[23] G. S. Langevin and P. Overbey. Concept to reality: Winglets. *NASA Langley Research Center*, Hampton, VA 2003.

[24] V. J. Burnelli. End plating wing tips. *U.S. no 1,775,474*, 1930.

[25] W. Mangler. The lift distribution of wings with end plates. *NACA TM 856*, 1938.

[26] S. Hoerner. The aerodynamic shape of the wing tips. *Air Materiel Command, Wright-Patterson Air Force Base, Dayton, Ohio*, 1952.

[27] R.E. Bower. Opportunities for aerodynamic-drag reduction. *NASA/University Conference on Astronautics. NASA SP-372*, pages 323–352, 1975.

[28] S.G. Flechner, P.F. Jacobs, and R.T. Whithcomb. A high subsonic speed wind-tunnel investigation of winglets on a representative second-generation jet transport wing. *NASA TN D-8264*, 1976.

[29] R.T. Whithcomb. A design approach and selected wind-tunnel results at high subsonic speeds for wing-tip mounted winglets. *NASA TN D-8260*, 1976.

[30] L. Falcao, A. Gomes, and A. Suleman. Multidisciplinary design optimisation of a morphing wingtip. *2nd International Conference on Engineering Optimization, Lisbon, Portugal*, 2010.

[31] R. Ames O. Wong M. J. Smith, N. Komerath and J. Pearson. Performance analysis of a wing with multiple winglets. (AIAA Applied Aerodynamics, AIAA 2001-2407), 2001.

[32] R. Coimbra and F. Catalano. Estudo experimental sobre pontas de asa para uma aeronave agrìcola. *Revista Brasileira de Engenharia Agrìcola e Ambiental,vol. 3, pp. 99-105, 1999.*

[33] L. Pascale and F. Nicolosi. Design and aerodynamic analysis of a light twin-engine propeller aircraft. *26th ICAS Conference*, Anchorage, Alaska (ISBN: 9781605607153), 14-19 September 2008.

[34] D.P. Coiro, F. Nicolosi, F. Scherillo, and U. Maisto. Single versus multiple winglets: Numerical and experimental investigation. *26th ICAS Conference*, Anchorage, Alaska(ISBN: 9781605607153), 14-19 September 2008.

[35] F. Nicolosi, A. De Marco, and P. Della Vecchia. Flight tests of a twin-engine flight aircraft: performances, stability and parameter estimation. (20th AIDAA Congress), June-July 2009.

[36] F. Nicolosi, A. De Marco, and P. Della Vecchia. Flight tests, performances, and flight certification of a twin-engine light aircraft. *Journal of Aircraft*, 48(1):177–193, January 2011.

[37] P. Della Vecchia. Developement of methodologie for the aerodynamic desing and optimization of a new regional turboprop aircraft. *PhD thesis, Univeristy of Naples Federico II, Italy*, (ISBN 978-88-98382-02-6), 2013.

[38] M. D. Maughmer. The design of winglets for high-performance sailplanes. *AIAA Paper 2001-2406*, 2001.

[39] F. Nicolosi and P. Della Vecchia. Aerodynamic guidelines in the design and optimization of new regional turboprop aircraft. *3rd CEAS and 21st AIDAA Congress*, (ISBN: 9788896427187):577–587, 24-28 October 2011.

[40] F. Nicolosi, P. Della Vecchia, and S. Corcione. Aerodynamic analysis and design of a twin engine commuter aircraft. *28th ICAS Conference*, (ISBN: 9780956533319), 23-28 September 2012.

[41] P. Della Vecchia and S. Serino. Aerodynamic analysis and optimization of a regional transport aircraft. *AIAA Pegasus Conference*, page 11, April 2010.

[42] Jane'e Information Group Limited. The desing and testing of a winglet airfoil for low-speed aircraft. *Journal of Aircraft*, Vol. 39 No. 4, July-August 2002.

[43] L. C. Montoya, S. G. Flechner, and P. F. Jacobs. Effects of winglets on a first generation jet trasport aircraft. ii-pressure and spanwise load distributions for a semispan model at high subsonic speeds. *NASA TN D-8474*, (Dryden Flight Research Center), July 1977.

[44] R. R. Meyer and P. F. Covell. Effects of winglets on a first generation jet trasport aircraft. vii-sideslip effect on winglets loads at subsonic speeds for a full span model. *NASA Technical paper 2619*, (Ames Research center), 1986.

[45] J. Roskam. Airplane design, part i: Preliminary sizing of airplanes. *DARcoporation*, (2nd Edition), Lawrence, Kansas, 2000.

[46] F. Nicolosi, P. Della Vecchia, and D. Ciliberti. An investigation on vertical tailplane design. *Research and Education in Aircraft Design*, 17-19 October 2012.

[47] F. Nicolosi, P. Della Vecchia, and D. Ciliberti. An investigation on vertical tailplane contribution to aircraft sideforce. *Aerospace Science and Technology*, (DOI:10.1016/j.ast.2012.12.006), 2013.

[48] K. Nickel and M. Wohlfahrt. Tailless aircraft in theory and practice. *American Institute of Aeronautics and Astronautics*, (ISBN: 1563470942), Washington D.C., 1994. .

[49] Dodson M.G. An historical and applied aerodynamic study of the wright brothers' wind tunnel test program and application to successful manned flight. *US Naval Academy Technical Report*, (USNA-334), 2005.

[50] Us navy experimental wind tunnel. *Aerial Age Weekly, 17 January 1916, pages 426-427*, (USNA-334), 2005.

[51] Man made hurricane tests full size planes. *Popular Mechanics, January 1936, pp.94-95*, (USNA-334).

[52] Vertical wind tunnel. *Popular Science, February 1945, p. 73*, (USNA-334), .

[53] Wind at work for tomorrow's planes. *Popular Science, July 1946, pp. 66-72*, (USNA-334), .

[54] Vertical wind tunnel. *Popular Science, February 1945, p. 73*, (USNA-334), .

[55] W.H. Rae Jr. and A. Pope. Low-speed wind tunnel testing. *John Wiley & Sons, Inc.*, (ISBN 978-88-906484-1-0), 163 Brightnon Raod, Coulsdon, Surrey CR5 2YH, UK 1984.

[56] I. Lotz. Correction of downawash in wind tunnel of circular and elliptical sections. *TM 801, 1936.*

[57] K. Patterson and A. Rizzi. Estimating reynolds number scaling and wind tunnel boom effects with the help of cfd methods. *24th Applied Aerodynamic Confere, AIAA, San Francisco USA, 2006*, (AIAA 2006-3162).

[58] L. Prandtl and H. Schlichting. Das widerstandsgesetzrauherplatten. *Weft, Reederei, Haften*, 1934.

[59] Neal R.D. Correlation of small-scale and full-scale win tunnel data with flight test data on the lear jet model. *SAE National Business Aircraft Meetings, 1970*, (Paper 700237).

[60] Hockman M.T. and Esiminger R.E. The correlation of wind-tunnel and flight test stability and control data for an sb2c-1 airplane. *JAS, January 1948.*

[61] McKinney L.W. and Baals D.D. Wind-tunnel/flight correlation-1981. (NASA CP 2235), 1982.

[62] Wolowicz C.H. and Yancey R.B. Longitudinal aerodynamic characteristics of light, twin-enigne, propeller-driven aircraft. *National Aeronautics and Space Admnistration, Washington, D.C. June 1972*, (NASA Technical Note TN D-6800), .

[63] Wolowicz C.H. and Yancey R.B. Lateral-directional aerodynamic characteristics of light, twin-enigne, propeller-driven aircraft. *National Aeronautics and Space Admnistration, Washington, D.C. October 1972*, (NASA Technical Note TN D-6949), .

[64] Veldhuis L.L.M. Propeller wing aerodynamic interference. *Delft University of Technology, Delft, Holland, 2005*, (ISBN 90-9019537-8).

[65] W. H. Jou. A systems approach to cfd code development. *21th International Council of Aeronautical Science, ICAS, Melbourne, Australia, 1998*, (ICAS-98-2,7,5).

[66] Jameson A. The present status, challenges, and future developments in computational fluid dynamics. *In: Progress and Challenges in CFD Methods and Algorithms, AGARD-CP-578, 1996.*

[67] Raj P. Cfd at a crossroads: An industry perspective. *In: Caughey DA, Hafez MM, editors. Frontiers of computational fluid dynamics, 1997*, .

[68] Young D.P. Melvin R.G. Bieterman M.B. Holmes C.L. Huffman W.H., Jou W.H. and Johnson F.T. Practical considerations in aerodynamic design optimization. *AIAA Paper 95-1730-CP, June 1995.*

[69] Tinoco E.N. Johnson F.T. and Yu N.J. Thirty years of development and application of cfd. *In: Computers & Fluid 34 (2005) 1115-1151, Elsevier Ltd.*, (doi: 10.1016/j.compfluid.2004.05.005).

[70] Tinoco E.N. The changing role of computational fluid dynamic in aircraft development. *AIAA Paper 98-2512, 1998.*

[71] Raj P. Aircraft design in the 21st century: implications for design methods. *AIAA Paper 98-2895, 1998*, .

[72] Darraq D. Vos J.B., Rizzi A. and Hirshel E.H. Navier-stokes solvers in european aircraft design. *Progress in Aerospace Science 38 (2002) 601-797, Elsevier Science Ltd.*

[73] Peric M. Flow simulation using control volumes of arbitrary polyhedral shape. *ERCOFTAC Bulletin, No. 62, September 2004.*

[74] Spalart P.R. and Allmaras S.R. A one-equation of turbulence model for aerodynamic flows. *30th Aerospace Sciences Meeting and Exhibit, Janaury 6-9, 1992, Reno, NV, USA*, (AIAA-92-0439).

[75] Della Vecchia P. and Ciliberti D. Numerical aerodynamic analysis on a trapezoidal wing with high lift devices: a comparison with experimental data. *21th AIDAA Conference, Naples, Italym September 9-12, 2013*, (ISBN 9788890648427), .

[76] Stuever R.A. RumseyC. L., Long M. and Wayman T.R. Summary of the first aiaa cfd high lift prediction workshop. *49th AIAA Aerospace Sciences Meeting including the New Horizons Forum and Aerospace Exposition, 4-7 January, 2011, Orlando, Florida, USA*, (AIAA 2011-939).

[77] da Silva R.G. Antunes A.P. and Azevedo J.L. On te effects of turbulence modelling and grid refinement on high-lift configuration aerodynamic simulations. *28th International Congress of teh Aeronautica Sciences, 23-28 September 2012,Brisbane, Australia*, (ISBN 9780956533319).

[78] I. H. Abbott and A.E. Von Doenhoff. Theory of wing sections: Including a summary of airfoil data. (ISBN 978-0486605869), 1959.

[79] E. Obert. Aerodynamic design of trasport aircraft. *IOS Press TUDelft Amsterdam*, (1st ed.), 2009.

[80] Shankara P. and Snyder D. Numerical simulation of high lift trap wing using star-ccm+. *30th AIAA Applied Aerodynamics Conference ,25-28 June 2012, New Orleans, Louisiana*, (AIAA 2012-2920), .

[81] R. Simson. Junction flows. *Annual Review of Fluid Mechanics*, 33, 2001.

[82] S. F. Hoerner. Fluid dynamic drag. *Hoerner Fluid Dynamics*, 1965.

[83] H. Schlichting and E. Truckenbrodt. Aerodynamics of the aeroplane. *McGraw Hill*, 2nd edition 1979.

[84] S. Siegel. Comparison of design rules regarding the wing-body junction flow of a subsonic aircraft. *University of Technology Dresden*, Dep. of Aerodynamics, 30 June 2011.

[85] E. Jacobs and K. Ward. Interference of wing and fuselage from tests of 209 combinations in the naca variable-density test tunnel. *NACA Technical Report No. 540*, 1935.

[86] H. Muttray. Aerodynamic aspects of wing-fuselage
llets. *NACA Technical Memorandum No.764*, 1935.

[87] J. Fleming, R. Simpson, J. Cowling, and W. Devenport. An experimental study of a turbulent wing-body junction and wake flow. *Experiments in Fluids*, 14, 1993.

[88] S. Oelcmen and R. Simpson. Some structural features of a turbulent wing-body junction vortical flow. *Report No. VPI-AOE-238*, Virginia Polytechnic Institute and State University Blackburg, 1996.

[89] A. Sclafani J. Vassberg and M. DeHaan. A wing-body fairing design for the dlr-f6 model: A dpw-iii case study. *AIAA Conference paper 2005-4730*, 2005.

[90] Della Vecchia P. and Nicolosi F. Aerodynamic guidelines in the design and optimization of new regional turboprop aircraft. *Aerospace Science and Technology, Vol. 38 October 2014, Pages, 88-104*. URL http://dx.doi.org/10.1016/j.ast.2014.07.018.

[91] Jacobs P.F and Flechner S.G. The effect of winglets on the static aerodynamic stability characteristics of a representative second generation jet transport model. *NACA Technical Note TN D-8267*, 1976.

[92] J. D. Brewer and J. H. Lichtenstein. Effect of horizontal tail on low-speed static lateral stability characteristics of a model having 45 deg. sweptback wing and tail surfaces. *Technical Note 2010, National Advisory Committee for Aeronautics*, 1950.

[93] R. D. Finck. Usaf stability and control datcom. *AFWAL-TR-83-3048*, Wright-Patterson Air Force Base, McDonnell Douglas Corporation, Ohio 1978.

[94] R. W. Gilbey. Contribution of fin to sideforce, yawing moment and rolling moment derivatives due to sideslip, $(y_v)f$, $(n_v)f$, $(l_v)f$, in the presence of body, wing and tailplane. *Item 82010, Engineering Science Data Unit*, 1982.

[95] R. O. House and A. R. Wallace. Wind-tunnel investigation of effect of interference on lateral-stability characteristics of four naca 23012 wings, an elliptical and circular fuselage and vertical fins. *Report 705, National Advisory Committee for Aeronautics*, 1940.

[96] W. D. Wolhart M. J. Queijo. Experimental investigation of the effect of the vertical-tail size and length and of fuselage shape and length on the static lateral stability characteristics of a model with 45 deg. sweptback wing and tail surfaces. *Report 1049, National Advisory Committee for Aeronautics*, 1950.

[97] Biermann D. and Hartman E. The aerodynamic characteristics of six full-scale propellers having different airfoil sections. (NACA Report No. 650).

[98] J. Roskam and C. T. E. Lan. Airplane aerodynamics and performance. *DARcoporation*, (ISBN 1-884885-44-6), 1st Edition Lawrence, Kansas, 1997.